

# Studies on Dynamics of Space Charge Dominated Beam in a Low Energy Beam Transport System

*By*

**PARITOSH SING BABU**  
**VARIABLE ENERGY CYCLOTRON CENTRE**  
**Kolkata-700064, India**

*A thesis submitted to the*  
*Board of Studies in Physical Sciences*  
*In partial fulfillment of requirements*  
*For the Degree of*  
**DOCTOR OF PHILOSOPHY**  
*of*

**HOMI BHABHA NATIONAL INSTITUTE**  
**Bhabha Atomic Research Centre**  
**Mumbai-400085, India**



September, 2012

# Homi Bhabha National Institute

## Recommendations of the Viva Voce Board

As members of the Viva Voce Board, we certify that we have read the dissertation prepared by Paritosh Sing Babu entitled ‘Studies on dynamics of space charge dominated beam in a low energy beam transport system’ and recommend that it may be accepted as fulfilling the dissertation requirement for the Degree of Doctor of Philosophy.

**Date:**

---

Chairman: Dr. Alok Chakrabarti

**Date:**

---

Guide/Convener: Dr. V. S. Pandit

**Date:**

---

Member: Dr. S. Krishnagopal

**Date:**

---

Member: Dr. P. R. Sarma

**Date:**

---

Technical Advisor: Shri Gautam Pal

**Date:**

---

External Examiner: Dr. D. Kanjilal

Final approval and acceptance of this dissertation is contingent upon the candidates submission of the final copies of the dissertation to HBNI.

I hereby certify that I have read this dissertation prepared under my direction and recommend that it may be accepted as fulfilling the dissertation requirement.

**Date:**

**Time:**

**Guide:** \_\_\_\_\_

Dr. V. S. Pandit

## STATEMENT BY AUTHOR

This dissertation has been submitted in partial fulfillment of requirements for an advanced degree at Homi Bhabha National Institute (HBNI) and is deposited in the Library to be made available to borrowers under rules of the HBNI.

Brief quotations from this dissertation are allowable without special permission, provided that accurate acknowledgement of source is made. Requests for permission for extended quotation from or reproduction of this manuscript in whole or in part may be granted by the Competent Authority of HBNI when in his or her judgment the proposed use of the material is in the interests of scholarship. In all other instances, however, permission must be obtained from the author.

PARITOSH SING BABU

## DECLARATION

I, hereby declare that the investigation presented in the thesis has been carried out by me. The work is original and has not been submitted earlier as a whole or in part for a degree / diploma at this or any other Institution / University.

PARITOSH SING BABU

## DEDICATIONS

**To my parents**

*Shri Krishna Prasad Sing Babu*

*and*

*Smt. Ujjala Sing Babu*

## ACKNOWLEDGEMENTS

I would like to express my sincere gratitude to my thesis supervisor Dr. V. S. Pandit for his continuous guidance, inspiration and his constant support throughout my thesis work. I am highly obliged to him for his constructive criticism and valuable suggestions, which helped me to present the scientific results in an efficient and effective manner in this thesis.

I am extremely thankful to Dr. R. K. Bhandari (Former Director, VECC, Kolkata) and Dr. D. K. Srivastava (Director, VECC, Kolkata) for their valuable guidance and encouragement.

I would like to take this opportunity to thank the members of my doctoral committee, Dr. Alok Chakraborty, Dr. S. Krishnagopal, Dr. P. R. Sarma and Sri Gautam Pal for their support, encouragement and discussions during the annual reviews. I wish to give special thanks to Dr. P. R. Sarma for the pleasure of working with and learning from him.

I would like to thank Shri A. Goswami for many helpful discussions and full co-operation towards me. I also thank Shri S. Srivastava, Shri A. Mishra, Dr. S. Pal, Shri S. Mukhopadhyay, Shri D. Pandit, Shri S. Kundu, Shri J. K. Nayek, Shri H. Pandey, Shri S. Dechoudhury, Shri S. C. L. Srivastava, Shri P. Chauhan for their help and full co-operation towards me.

This thesis would not have been possible without the support and care of my family. I appreciate my relatives and my friends for their encouragement and support. I am eternally grateful to my parents for their love and care, for everything what they have done for me in my life. I am thankful to my wife Mitali for her love and support. Her understanding and care were so important to me in my work and every-day life. I fondly remember the cheerful face of my

little daughter Ankita who have been my constant source of energy and delight.  
I appreciate the support from my parents-in-law who inspired me immensely to  
pursue this thesis work.

# Contents

<b>SYNOPSIS</b> . . . . .	xii
<b>List of Figures</b> . . . . .	xviii
<b>List of Tables</b> . . . . .	xxvi
<b>1 Introduction</b>	<b>1</b>
1.1 Applications of Charged Particle Beams . . . . .	1
1.2 Parameters of 10 MeV Cyclotron . . . . .	3
1.3 Injection System of 10 MeV Cyclotron . . . . .	4
1.3.1 Ion Source and Extraction System . . . . .	4
1.3.2 Low Energy Beam Transport Line . . . . .	5
1.4 Space Charge Dominated Beams . . . . .	7
1.5 Theoretical Models of Intense Beams . . . . .	8
1.5.1 Vlasov Equilibrium for Space Charge Dominated Beams	10
1.5.2 Beam Envelope Model . . . . .	11
1.5.3 Beam Dynamics during Bunching . . . . .	12
1.5.4 Self-consistent Approach . . . . .	13
1.6 Thesis Overview . . . . .	14
<b>2 Beam Dynamics in the Aligned and Misaligned LEBT System</b>	<b>18</b>
2.1 Introduction . . . . .	18
2.2 Vlasov Equilibrium in Misaligned Focussing Channel . . . . .	20
2.3 Numeical Results . . . . .	27
2.3.1 Computation of Solenoid Field and its Derivatives . . . . .	28
2.3.2 Vlasov Equilibrium in Misaligned Channel . . . . .	29

2.3.3	PIC Simulation in Aligned Solenoid System . . . . .	31
2.3.4	PIC Simulation in Misaligned Solenoid System . . . . .	36
2.4	Summary and Discussion . . . . .	42
<b>3</b>	<b>Dynamics of Multispecies Beam in the LEBT System</b>	<b>44</b>
3.1	Introduction . . . . .	44
3.2	Envelope Model for Multispecies Beam . . . . .	45
3.2.1	Space Charge Field . . . . .	46
3.2.2	Single Particle Equation . . . . .	47
3.2.3	Equation of Motion in the Larmor Frame . . . . .	48
3.2.4	Beam Envelope Equation . . . . .	49
3.2.5	Beam Selection by Slit . . . . .	51
3.3	Numerical Results . . . . .	52
3.3.1	Results using Envelope Model . . . . .	53
3.3.2	Results of PIC Simulation . . . . .	58
3.4	Summary and Discussion . . . . .	69
<b>4</b>	<b>Optimisation of LEBT Parameters for Multispecies Beam</b>	<b>71</b>
4.1	Introduction . . . . .	71
4.2	Mathematical Model . . . . .	73
4.2.1	Dynamics of Multispecies Beam . . . . .	73
4.2.2	Boundary Condition . . . . .	75
4.2.3	The Reference Trajectory and Cost Functional . . . . .	76
4.3	Optimisation using Random Search Method . . . . .	77
4.4	Numerical Results . . . . .	79
4.5	Summary and Discussion . . . . .	86
<b>5</b>	<b>Beam Bunching in the Presence of Space Charge</b>	<b>87</b>
5.1	Introduction . . . . .	87
5.2	Theory . . . . .	90
5.3	Numerical Results . . . . .	94

5.4	Summary and Discussion . . . . .	101
<b>6</b>	<b>Dynamics of Intense Beam during Bunching</b>	<b>103</b>
6.1	Introduction . . . . .	103
6.2	Longitudinal Dynamics . . . . .	104
6.2.1	Beam Energy Spread . . . . .	104
6.2.2	Average Longitudinal Electric Field . . . . .	106
6.2.3	Fixed Shape Density Profile $\sigma(r, R)$ . . . . .	107
6.2.4	Evaluation of $\langle E_{ij} \rangle$ for Fixed Shape Density Profile . . . . .	109
6.2.5	Equation of Motion . . . . .	110
6.3	Transverse Dynamics . . . . .	111
6.3.1	Beam Envelope Equation . . . . .	111
6.3.2	Evaluation of the Axial Derivative of $\langle E_{ij} \rangle$ . . . . .	113
6.3.3	Emittance Growth due to RF Field . . . . .	115
6.4	Numerical Results . . . . .	116
6.4.1	Simulation Results using Analytical Model . . . . .	117
6.4.2	Simulation Results using PIC Model . . . . .	130
6.5	Summary and Discussion . . . . .	134
<b>7</b>	<b>PIC Simulation Methods for Space Charge Dominated Beam</b>	<b>135</b>
7.1	Introduction . . . . .	135
7.2	Computational Procedure for PIC Method . . . . .	136
7.3	2D PIC Method for Single Species . . . . .	136
7.3.1	Charge Assignment to the Grid Points . . . . .	137
7.3.2	Poisson Solver . . . . .	138
7.3.3	Interpolation of Fields to the Particle Location . . . . .	140
7.3.4	Particle Distribution Generator in Phase Space . . . . .	140
7.3.5	Equation of Motion . . . . .	143
7.4	PIC Model for Multispecies Beam . . . . .	144
7.5	3D PIC Method for Beam Bunching . . . . .	146
7.5.1	Equation of Motion . . . . .	147

7.5.2	Charge Assignment to the Grid Points . . . . .	147
7.5.3	Calculation of the Space Charge Electric Field . . . . .	148
7.5.4	Interpolation of Fields to the Particles Position . . . . .	150
7.6	Convergence Test and Benchmarking . . . . .	151
7.7	Summary and Discussion . . . . .	157
<b>8</b>	<b>Conclusions and Future Research</b>	<b>158</b>
8.1	Conclusions . . . . .	158
8.2	Future Research . . . . .	163
	<b>Appendix A</b>	<b>166</b>
A.1	Calculation of $f(r_j, r_k)$ and $g(r_j, r_k)$ . . . . .	166
A.2	Beam Selection through Circular Slit . . . . .	167
A.3	Runge-Kutta Method . . . . .	169
	<b>Appendix B</b>	<b>172</b>
B.1	Evaluation of $\langle E_{ij} \rangle$ for Bell Shape Density Profile . . . . .	172
B.2	Evaluation of $\langle E_{ij} \rangle$ for Hollow Shape Density Profile . . . . .	174
	<b>Bibliography</b> . . . . .	<b>177</b>
	<b>List of Publications</b> . . . . .	<b>185</b>

# SYNOPSIS

The field of intense charged particle beams is a rapidly growing field due to many important applications ranging from accelerator driven systems, neutron spallation sources, heavy ion fusion, high intensity accelerators for basic research in high energy and nuclear physics, to mention a few examples. For most high intensity accelerators, at the lower energy part, particularly near the ion source, the self-field of the beam plays an important role in determining the beam behaviour from there onwards. For the optimal design and stable operation of high intensity accelerators and their beam transport systems, it is therefore necessary to develop a basic understanding of the beam dynamics with space-charge effects particularly at low energy.

The Variable Energy Cyclotron Centre at Kolkata has undertaken a project of development of a 10 MeV, 5 mA compact radial sector proton cyclotron. This project is a part of the activity of high intensity accelerator development for accelerator driven subcritical systems. The injection line of the cyclotron consists of 2.45 GHz microwave ion source, two solenoids to transport and match the beam, a slit between the solenoids to reject the unwanted component of the beam and a sinusoidal buncher to bunch the beam. The ion source and the solenoid based low energy beam transport line have been designed, fabricated and commissioned and are presently under testing for beam characterization. The ion source will produce proton beam at an energy of 80–100 keV and beam current in the range of 10–20 mA. The extracted beam will first be collimated by slits to remove the undesired ions ( $H_2^+$ ,  $H_3^+$  etc.) and will be bunched using a sinusoidal buncher. It will then be injected axially in the central region where a spiral inflector will place the beam on the proper orbit of a cyclotron. The main aim of the project is to study the physics of space-charge-dominated beams

and technological problems associated with the generation, transport, bunching, injection, extraction, etc. of the high intensity proton beams.

In this thesis, detailed analytical and numerical studies have been performed to study the dynamics of space-charge-dominated beams (single species and multispecies) propagating through the low energy beam transport line. Main emphasis has been put on the matching, rejection of unwanted component and detailed analysis of the physical phenomena associated with the transport of intense beams.

In an uncoupled and perfectly aligned lattice, the Kapchinskij-Vladimirskij (K-V) distribution is the only known exact self-consistent solution of the nonlinear Vlasov-Maxwell equations for intense beams. In the first part of the thesis, a self-consistent kinetic description has been used to understand the dynamics of a space-charge-dominated single species beam in the aligned and misaligned solenoidal based transport system. A general equation for the centroid motion is derived using the nonlinear Vlasov-Maxwell equation. It has been shown that there exists a self-consistent Vlasov equilibrium distribution in the case of a uniform beam density. The beam envelope equation that determines the evolution of the outer radius of the equilibrium beam is similar in form to the well known K-V envelope equation and is independent of the centroid equation when the conducting beam pipe is considered very far away from the beam.

The microwave proton sources used in the injection system of cyclotrons produce a proton fraction of the order 80-85% of the total beam. The other major unwanted components are  $H_2^+$  and  $H_3^+$ . The presence of these unwanted species in an intense beam alters the dynamics of the primary species during the transport and thus the behavior of the beam envelope relative to the usual situation where the unwanted species are not present.

In this thesis, a multispecies beam envelope model for the evolution of an axisymmetric space-charge-dominated multispecies beam has been developed, for the evolution of the radius of each species along the transport line. For the selection of a particular species, circular slits are introduced in the beam line. The effective values of the current and emittance of each species after the slit are taken into account in the beam envelope model for further transport in case the radius of any species is larger than the slit size. Numerical results of the beam selection and transport have been presented for various values of the total beam current and different fractions of  $p$ ,  $H_2^+$ ,  $H_3^+$  species. It has been observed that the envelope of the proton beam behaves differently in the presence of different fractions of the other components. The simple envelope model presented in this thesis can be successfully utilized for a more precise estimate of the beam envelope, without the use of large simulations in the case of a multispecies beam.

An optimization method has also been developed to find the optimal beam line settings for the transport and matching of the desired primary beam using the developed multispecies beam envelope model. It is based on the random search technique where the parameters are varied randomly during the optimization. Using this method, the primary beam is matched at the final position and the loss of unwanted species is maximized at the location of a circular slit. In the optimization two cost functionals have been defined, one for the primary beam and the other for the unwanted species. The major advantage of this method is that it is very simple to apply, easy to include any number of constraints without calculating any differentiation of the cost functional and is very fast.

In order to improve the capture efficiency in a defined phase width of the cyclotron, it is necessary to bunch the beam in the beam injection line. The physics of the bunching process of intense beams is not yet well understood. Therefore, a systematic study of the beam dynamics during the longitudinal

beam compression will be helpful in better understanding of the beam bunching and in improving the design of the system.

In the thesis, a detailed theoretical analysis has been carried out for the longitudinal and transverse beam dynamics of the beam bunch as it evolves under the influence of space charge and external forces during the bunch compression. The longitudinal dynamics and transverse dynamics have been studied using disc model and envelope model respectively for various types of fixed shape beam density profiles. The beam envelope equation has been modified to take into account the longitudinal space-charge effect on transverse motion which arises when the bunch size is comparable to beam size. It has been shown that the location of the buncher from the time focus is a very crucial parameter in the case of high beam current. For a given beam current, there is an optimum drift length of time focus from the buncher beyond which the bunching efficiency decreases rapidly and is independent of buncher voltage. It has been observed that for intense beams different parts of the bunch evolve differently due to the unequal amounts of space-charge force experienced during the bunch compression. This kind of behaviour does not appear when the beam current is very small. For beams with bell shaped distribution, it has been observed that the increased nonuniformity in the density distribution reduces the total projected rms emittance as well as sharpness of the beam pulse at the time focus and the effect is reversed for hollow shape distributions.

Though the linear beam envelope model based on K-V distribution or on equivalent rms quantities, generally used for studying the average beam behavior in the injection line, predicts the envelope behavior with reasonable accuracy, it does not provide any information on emittance growth due to nonlinear external or self forces. In the more general case, where nonlinear forces from both the applied fields as well as from the space-charge fields are present, the

analytical investigation is very difficult, and one takes help of computer simulations. For the self-consistent description of an intense beam, particle-in-cell (PIC) simulation methods are widely used to understand the beam dynamics in beam transport systems.

In order to understand the detailed dynamics of space-charge-dominated beams with different density distributions in the injection line, a two-dimensional PIC code has been developed. To include the effect of bunching a three dimensional PIC code has also been developed for the self-consistent study during the longitudinal compression. In the PIC method a beam is represented as a collection of a large number of macroparticles. The equations of motion for the macroparticles are integrated using the leap-frog algorithm. The region occupied by the ensemble of particles is divided into uniform meshes. At every time step, the space-charge forces acting on the beam particles are calculated using the particle-in-cell method, in which the charge of the macroparticles is deposited onto a nearest grid points, followed by solving Poisson's equation using the fast Fourier transform method. The computer code developed on the above philosophy can handle the misalignment (displacement as well as tilt), higher order nonlinearity of the focusing element and the off-centering of the beam.

The PIC code has been used to investigate the evolution of phase space distribution, rms emittances, rms size, and centroid for different types of beam distributions particularly in the cases where the focusing magnets are misaligned with respect to the symmetry axis. In addition, the beam loss during the transport has also been estimated numerically for various beam parameters.

The PIC code has also used to get detailed information about the evolution of the beam distribution and emittance growth caused due to nonlinear effects

in the case of multispecies beams. The evolution of beam size and emittance growth of the primary species has been investigated in the presence of unwanted species for various beam parameters. The formation of beam hollow of unwanted species is observed due to nonlinear space-charge effect. It has been shown that the rejection of unwanted species is very effective when the slit is placed after the hollow formation of the unwanted species.

# List of Figures

1.1	<i>Layout of the high voltage deck, source and LEBT line. . . . .</i>	5
1.2	<i>Drawing of the ion source and extraction system (left). Developed ion source (right). . . . .</i>	6
1.3	<i>Beam transport line. . . . .</i>	7
2.1	<i>Schematic of a misaligned solenoid described by a two-step transformation. First, translation of center by <math>\vec{\Delta} = \Delta_x \hat{x} + \Delta_y \hat{y}</math>, and then a rotation of the axis of symmetry in the translated system. . . . .</i>	21
2.2	<i>A schematic of beam transport system with misaligned solenoid magnets showing the laboratory coordinate system <math>(x, y, z)</math> and the local coordinate system <math>(x_D, y_D, z_D)</math> of the solenoids. . . . .</i>	28
2.3	<i>Variation of axial (<math>r = 0</math>) (a) normalised axial magnetic field <math>B_n</math> of solenoid obtained from simulation (dotted) and analytical approximation (solid) (b) first <math>B1 = dB_n/ds</math>, (c) second <math>B2 = d^2 B_n/ds^2</math>, and (d) third <math>B3 = d^3 B_n/ds^3</math> derivatives along the length of the solenoid. . . . .</i>	29
2.4	<i>Plots show the evolution of (a) beam centroid <math>\langle x \rangle</math> and <math>\langle y \rangle</math> (b) percentage change in rms beam emittances and (c) rms beam sizes <math>X_{rms}</math> and <math>Y_{rms}</math> as a function of drift distance <math>s</math>. . . . .</i>	31
2.5	<i>Evolution of (a) rms beam size <math>X_{rms}(s)</math> and (b) ratio of rms emittance <math>\varepsilon_{rms}(s)/\varepsilon_{rms}(0)</math> in Larmor frame as a function of drift length <math>s</math> using the self-consistent particle-in-cell method for five different initial distributions K-V (KV), waterbag (WB), parabolic (PA), semi-Gaussian (SG) and Gaussian (GA) of the beam. . . . .</i>	33
2.6	<i>Evolution of rms beam size and rms emittance in Larmor frame for axisymmetric (solid) and non-axisymmetric (dashed) beam with Gaussian distribution. The input parameters are: (i) axisymmetric: <math>X_{rms}(0) = Y_{rms}(0) = 0.125</math> cm and <math>\varepsilon_{x_{rms}}(0) = \varepsilon_{y_{rms}}(0) = 13\pi</math> mmmrad, (ii) non-axisymmetric: <math>X_{rms}(0) = 0.125</math> cm, <math>Y_{rms}(0) = 0.2</math> cm, <math>\varepsilon_{x_{rms}}(0) = 13\pi</math> mmmrad and <math>\varepsilon_{y_{rms}}(0) = 19.5\pi</math> mmmrad. . . . .</i>	34

2.7	Plots of transverse (a) real space $(x, y)$ and (b) phase space $(x, x')$ of the beam at locations $s = 0$ cm and $s = 277$ cm for five initial distributions K-V (KV), waterbag (WB), parabolic (PB), semi-Gaussian (SG), and Gaussian (GA). . . . .	35
2.8	Evolution of the beam centroid $\langle x \rangle$ and $\langle y \rangle$ in laboratory frame using self-consistent model in the case of initial K-V distribution for four different cases: ideal $[0, 0, 0, 0]$ for S1 and $[0, 0, 0, 0]$ for S2, case (i) $[2, -2, 0, 0]$ for S1 and $[0, 0, 0, 0]$ for S2, case (ii) $[5, 0, 0, 0]$ for S1 and $[0, 0, 0, 0]$ for S2, case (iii) $[2, 2, 20, 0]$ for S1 and $[2, 2, 20, 0]$ for S2. Centroid motion for a given set of misalignment is independent of beam distribution. . . . .	37
2.9	Real space and phase space distributions of initial 10 mA beam with Gaussian distribution at the second waist ( $s = 277$ cm) in the case (a), (b) aligned and (c), (d) misaligned solenoids of case (iii) $[2, 2, 20, 0]$ for S1 and $[2, 2, 20, 0]$ for S2. . . . .	38
2.10	Evolution of rms beam envelope $X_{rms}$ in Larmor frame around the centroid with drift length $s$ in the case of misaligned solenoids for (a) K-V and (b) Gaussian distributions. Misalignment parameters are: ideal $[0, 0, 0, 0]$ for S1 and $[0, 0, 0, 0]$ for S2, case(i) $[2, -2, 0, 0]$ for S1 and $[0, 0, 0, 0]$ for S2, case(ii) $[5, 0, 0, 0]$ for S1 and $[0, 0, 0, 0]$ for S2, case(iii) $[2, 2, 20, 0]$ for S1 and $[2, 2, 20, 0]$ for S2. . . . .	39
2.11	Beam loss as a function of drift length $s$ for five distributions with misalignment parameters of case (iii): $[2, 2, 20, 0]$ for S1 and $[2, 2, 20, 0]$ for S2. . . . .	40
2.12	Evolution of the beam centroid in the laboratory frame for different misalignment parameters set (i) $[0, 2, 0, 0]$ for S1 and $[2, 0, 20, 0]$ for S2, set (ii) $[2, 0, 20, 0]$ for S1 and $[2, 0, 0, 0]$ for S2, set (iii) $[2, 2, 20, 0]$ for S1 and $[2, 2, 20, 0]$ for S2. . . . .	41
3.1	Evolution of the envelope radii of proton beam having three different fractions 60%, 80% and 100% in the total beam of 10 mA at 100 keV, for an axisymmetric beam in the transport line. The initial beam parameters are $r(0) = 2.5$ mm, $r'(0) = 0$ . The centres of the solenoids S1 and S2 are located at $s = 60$ cm and $s = 210$ cm respectively. The orientations of the phase ellipses at the slit location are also shown for the three different fractions of proton. . . . .	54
3.2	Variation of envelope radii of a) $H_2^+$ beam and b) $H_3^+$ beam without slit (dashed line) and with slit of radius 5 mm (solid line). Slit is located at $s = 135$ cm. The strengths of the solenoids S1 and S2 are 3.035 kG and 2.833 kG respectively. The evolution of $H_2^+$ and $H_3^+$ envelope radii after selection by three different slit sizes are also shown. The dotted curves represent the proton envelope. . . . .	55

3.3	<i>Evolution of envelope radii of <math>p, H_2^+</math> and <math>H_3^+</math> having fractions of 80%, 15% and 5% respectively in the total initial beam current of 10 mA at 100 keV. The initial beam parameters are <math>r(0) = 2.5</math> mm, <math>r'(0) = 0</math> for all the species. Beam spots of <math>p, H_2^+</math> and <math>H_3^+</math> near the second waist of proton beam are also shown.</i>	56
3.4	<i>The orientation of phase space ellipses of different species of the beam at the position of the slit for various beam parameters. In each case the phase space region occupied between the two dotted lines (representing the edges of the slit in phase space), will pass through the slit of radius 5 mm.</i>	57
3.5	<i>Comparison of the evolution of (a) rms beam sizes and (b) rms emittances of <math>p, H_2^+</math> and <math>H_3^+</math> obtained from the multispecies envelope model (solid curve) and the self-consistent PIC simulation (dashed curve) for <math>I = 10</math> mA. A slit of radius 5 mm is placed at <math>s = 135</math> cm.</i>	60
3.6	<i>Plot shows the comparison of the variation of (a) rms beam size and (b) rms emittance of initially K-V distributed proton beam and with different types of beam distribution for <math>H_2^+</math> and <math>H_3^+</math>. We have considered five different types of distribution for <math>H_2^+</math> and <math>H_3^+</math>: K-V (KV), waterbag (WB), parabolic (PA), semi-Gaussian (SG) and Gaussian (GA) distributions.</i>	61
3.7	<i>Evolution of rms beam size of proton along the distance <math>s</math> with different types of initial distribution for all the species. We have considered five different types of distributions for all the species <math>p, H_2^+</math> and <math>H_3^+</math>: K-V (KV), waterbag (WB), parabolic (PA), semi-Gaussian (SG) and Gaussian (GA) distributions.</i>	62
3.8	<i>The variation of the rms beam size of (a) <math>H_2^+</math> and (b) <math>H_3^+</math> along the beam transport line. A circular slit of aperture 5 mm is placed at a distance <math>s = 135</math> cm.</i>	63
3.9	<i>The variation of the rms emittance of (a) <math>H_2^+</math> and (b) <math>H_3^+</math> along the beam transport line before and after a slit of aperture 5 mm with different distributions of species. Slit is located at <math>s = 135</math> cm.</i>	64
3.10	<i>Phase space <math>(x, x')</math> and real space <math>(x, y)</math> distributions of <math>p, H_2^+</math> and <math>H_3^+</math> at <math>s = 277</math> cm without any slit in the beam line for K-V and Gaussian distributions of all the species. Species fractions are: <math>p = 80\%</math>, <math>H_2^+ = 15\%</math> and <math>H_3^+ = 5\%</math>.</i>	65
3.11	<i>Comparison of phase space and real space distributions of <math>p, H_2^+</math> and <math>H_3^+</math> at location <math>s = 277</math> cm for circular and square aperture placed at <math>s = 135</math> cm. We have considered K-V and Gaussian distributions of all the species.</i>	66

3.12	<i>Evolution of (a) rms envelope size and (b) rms emittance of proton having different species fractions in the total beam of 10 mA at 100 keV. Different percentage fraction in 10 mA are (1): [60, 20, 20], (2): [70, 20, 10], (3): [80, 10, 10], (4): [80, 15, 5] and (5): [100, 0, 0]. . . . .</i>	66
3.13	<i>Phase space <math>(x, x')</math> and real space <math>(x, y)</math> distributions of <math>p, H_2^+</math> and <math>H_3^+</math> at different locations during the beam transport for two types of distributions (A) K-V and (B) Gaussian for all the species. . . . .</i>	67
4.1	<i>The flow chart of the optimisation code using random search technique.</i>	78
4.2	<i>Schematic diagram of the matching system. . . . .</i>	80
4.3	<i>Plots of unmatched (dash-dotted line) and matched (solid line) beam envelopes of proton for total initial beam current of 10 mA at 100 keV. Dashed line represents the reference trajectory of the proton beam. The initial beam parameters for all the species are <math>r(0) = 2.5</math> mm, <math>r'(0) = 0</math>. The fractions of <math>p, H_2^+</math> and <math>H_3^+</math> are 80%, 15% and 5% respectively. The initial beam transport parameters are: <math>B_1 = 3.97</math> kG, <math>B_2 = 2.47</math> kG, <math>ld_1 = 97</math> cm, <math>ld_2 = 144</math> cm and <math>ld_3 = 39</math> cm. The optimised beam transport parameters are: <math>B_1 = 3.09</math> kG, <math>B_2 = 2.87</math> kG, <math>ld_1 = 59</math> cm, <math>ld_2 = 150</math> cm and <math>ld_3 = 71</math> cm. The optimised locations of solenoid magnets are also shown by solid curve. . . . .</i>	80
4.4	<i>Plots of envelope radii of <math>H_2^+</math> beam (dotted line), <math>H_3^+</math> beam (dashed line) before optimisation and <math>H_2^+</math> beam (solid), <math>H_3^+</math> beam (dash-dotted) after optimisation of the beam line parameters. The initial and optimised transport parameters are same as in Fig. 4.3. . . . .</i>	82
4.5	<i>Evolution of envelope radii of <math>p, H_2^+</math> and <math>H_3^+</math> beams for 10 mA and 20 mA beam current for two different fractions. The initial beam parameters for all the species are <math>r(0) = 2.5</math> mm, <math>r'(0) = 0</math> in both the cases. . . . .</i>	83
4.6	<i>Cost functional of proton beam and total beam current of unwanted species just after selection by the slit for different fractions 1, 2, 3 and 4 of species as mentioned in Table 4.1. Results are presented for the optimised and unoptimised beam transport parameter for 10 mA and 20 mA. . . . .</i>	85
5.1	<i>Normalised electric field <math>E_{ij}/E_0</math> as a function of the disc separation. The bunch spacing <math>\beta\lambda_{rf}</math> is equal to 10.5 cm. . . . .</i>	95
5.2	<i>Optimised bunching efficiency of a sinusoidal buncher as a function of the drift length for various values of the beam current of 100 keV proton beam. The beam radius is 5 mm and the phase width at time focus is <math>30^\circ</math> of rf for all the cases. . . . .</i>	96

5.3	Variation of the optimum drift length and buncher voltage as a function of the beam current. The beam phase width at the time focus is $30^0$ of rf. . . . .	97
5.4	Variation of the parameters of a two harmonic buncher with the beam current. The bunch width at the time focus is $30^0$ of rf and the beam radius is 5 mm. . . . .	98
5.5	Variation of the bunching efficiency for a double drift buncher as a function of $l/L$ for three different values of the beam current. The beam bunch width at the time focus is $30^0$ of rf and the beam radius is 5 mm. . . . .	98
5.6	$K(s)/K$ as a function of drift length showing the effect of increasing beam current in the bunch on the perveance. . . . .	99
5.7	Beam envelopes for 10 mA proton beam in the injection line. (a) dash-dotted line: without buncher, magnetic field of S1 and S2 are 3.034 kG and 2.88 kG respectively, beam radius at time focus is 2.85 mm. (b) dashed line: with buncher on and unoptimised, (c) solid line: with buncher on and optimised, magnetic field of S1 and S2 are 3.034 kG and 2.96 kG respectively and the beam radius at time focus is 6.03 mm. The beam phase width is $30^0$ of rf. . . . .	100
5.8	Density distribution of discs at the time focus for beam phase width of $30^0$ of rf. (a) Without space charge: buncher voltage $V_1 = 5.32$ kV and bunching efficiency is equal to 54%. (b) With space charge (10 mA beam current): optimized buncher voltage $V_1 = 5.6$ kV and bunching efficiency is 47%. The restricted energy width $\Delta E = \pm 2.0$ keV. . . . .	101
6.1	A schematic illustration of beam frame and laboratory frame. . . . .	105
6.2	Plot of distribution function $f(r/R)\pi R^2$ as a function of $r/R$ for (a) bell shape and (b) hollow shape distributions with $p = 0, 1, 2, 3$ . . . . .	109
6.3	(a) Evolution of the quantity $\langle \Lambda(s) \rangle$ due to the axial variation of longitudinal electric field during the bunch compression for 100 keV, 10 mA beam at various values of energy spread. (b) Variation of the perveance $\langle K(s) \rangle$ of the beam bunch during longitudinal bunch compression, with and without the inclusion of $\langle \Lambda(s) \rangle$ . The optimised drift length $L = 77$ cm and buncher voltage $V_b = 6$ kV are used in the simulation. . . . .	118
6.4	Evolution of the emittance growth during the beam transport with bunch compression for three different values of beam current and at different energy spread ; $\sigma_E = 0, 80, 160, 240, 320$ eV. The beam injection energy is 100 keV. . . . .	119

6.5	Relative density distribution of discs at the time focus as a function of phase $\phi$ for 100 keV beam at beam current of $I = 0$ mA ( $L = 100$ cm), $I = 5$ mA ( $L = 87$ cm) and $I = 10$ mA ( $L = 77$ cm) and for three different values of initial beam energy spread (column 1 for $\sigma_E = 0$ eV, column 2 for $\sigma_E = 80$ eV and column 3 for $\sigma_E = 320$ eV). . . . .	120
6.6	The longitudinal phase space distribution of the beam at the time focus for three different value of beam current and energy spread at 100 keV. The indicated bunching efficiencies $\eta$ are for bunch width $\Delta\phi = 30^\circ$ of rf. . . . .	121
6.7	Variation of (a) rms radius and (b) rms divergence of beam in one $\beta\lambda_{rf}$ consisting of 72 slices at the entrance of the buncher gap. The slices in the chosen bunch width are indicated by dark shades. . . . .	122
6.8	Variation of rms radius and rms emittance of different slices in the bunch width as a function of drift length for $I = 0$ mA and $I = 10$ mA. Six slices of the bunch are numbered as 1 to 6 starting from the beginning of the bunch to the end. The location and length of solenoid magnet S2 together with strengths are also indicated. . . . .	123
6.9	Evolution of (a) projected rms emittance due to space-charge effect and (b) total effective rms emittance for different distributions. The total effective rms emittance (Eq. (6.44)) includes the thermal and growth due to the space charge and rf fields. . . . .	124
6.10	The rms radius, rms divergence and orientation of the phase ellipses of the slices 1 to 6 at the buncher location and at the time focus for $I = 0$ mA. . . . .	125
6.11	Plots show (A) rms radius and (B) rms divergence of slices 1 to 6 of the beam bunch at the time focus at 10 mA beam current having different density distributions in the radial direction. The term initial indicates the values at the buncher location. . . . .	126
6.12	(A) Phase space ellipse and (B) current $I(Z, s)/I(Z, 0)$ of all six slices in the bunch at the time focus for bell shape and hollow shape density distributions of the beam at three different values of parameter $p$ . Initial indicates values at the buncher location. Slices in the specified bunch width of $30^\circ$ of rf are shown in dark colour. . . . .	128
6.13	Variation of (a) current in the slices $I(Z, s)/I(Z, 0)$ around the bunch centre and (b) the parameter $\Lambda(Z, s)$ at four different axial locations $s$ from the buncher gap in the case of uniform density profile. The shaded regions indicate the extent of specified bunch width ( $30^\circ$ of rf). . . . .	129
6.14	Comparison of the evolution of (a) the rms beam size and (b) the relative increase in bunch current $\langle I(s) \rangle / I(s = 0)$ along the drift length during the bunching obtained with PIC simulation (solid) and analytical formulations. . . . .	131

6.15	<i>Evolution of the (A) slice emittances and (B) slice current as a function of drift distance <math>s</math> with initial K-V and Gaussian distributions. The thick solid line indicated by average represents the average value of parameter of the bunch. . . . .</i>	132
6.16	<i>Transverse and longitudinal phase space distributions at the time focus with initial K-V and Gaussian distributions. . . . .</i>	133
7.1	<i>Particle-in-cell simulation algorithm. . . . .</i>	137
7.2	<i>Charge deposition in two dimensional rectangular grid. . . . .</i>	138
7.3	<i>2D Cartesian grid for the solution of Poisson's equation for continuous beam in the case two dimensional problem. . . . .</i>	139
7.4	<i>Generation of particle distributions in real, phase and momentum spaces for K-V (KV), waterbag (WB), parabolic (PA), semi-Gaussian (SG) and Gaussian (GA) distributions. . . . .</i>	142
7.5	<i>Leap-frog method. . . . .</i>	143
7.6	<i>Computational grid for the solution of Poisson's equation with beam spot of three different species. . . . .</i>	146
7.7	<i>Charge deposition in three dimensional rectangular grid. . . . .</i>	148
7.8	<i>3D rectangular grid for the solution of Poisson's equation for continuous beam and bunched beam respectively. . . . .</i>	149
7.9	<i>Variation of error in the generation of emittance against number of macroparticles. . . . .</i>	152
7.10	<i>Plots of the beam density profiles along the <math>y</math> axis for different values of number of grids and macroparticles. . . . .</i>	153
7.11	<i>Evolution of (a) rms beam size and (b) rms emittance of an initial Gaussian distributed beam along the beam transport line for different values of <math>N</math>, <math>N_x</math> and <math>\Delta s</math>. . . . .</i>	154
7.12	<i>Variation of charge density, potential and <math>y</math>-component of electric field for different distributions. . . . .</i>	154
7.13	<i>Contour plot for the charge density, potential and <math>y</math>-component of the electric field <math>E_y</math> for K-V and Gaussian distributions. . . . .</i>	155
7.14	<i>Three dimensional plot for the charge density, potential and <math>y</math>-component of the electric field <math>E_y</math> for K-V and Gaussian distributions. . . . .</i>	156
7.15	<i>Plots of rms beam envelopes obtained with PIC method and envelope equation as a function of path length for <math>I = 10</math> mA. Beam input parameters are: rms beam size <math>X_{rms}(0) = 1.25</math> mm and rms divergence <math>X'_{rms}(0) = 0</math>, beam energy <math>E_0 = 100</math> keV, normalised rms emittance <math>\epsilon_{rms} = 0.2\pi</math> mmmrad. . . . .</i>	157

A.1 *Plot shows a typical phase space ellipse at the slit position. The edges of the slit are shown by two vertical solid lines. . . . .* 168

# List of Tables

3.1	Emittances and currents of different components of the beam after the slit of radius 5 mm. The initial emittances in $\pi$ mmmrad are; 54.7948 ( $p$ ), 38.7463 ( $H_2^+$ ) and 31.6376( $H_3^+$ ). . . . .	58
4.1	Optimised parameters for 10 mA total beam current with different fraction of $p$ , $H_2^+$ and $H_3^+$ . The initial emittances in $\pi$ mmmrad are; 54.7948 ( $p$ ), 38.7463 ( $H_2^+$ ) and 31.6376 ( $H_3^+$ ). ( $ld_1 + ld_2 + ld_3 = 280$ cm) . . . . .	84

# Chapter 1

## Introduction

### 1.1 Applications of Charged Particle Beams

High intensity charged particle beams are used in many areas of scientific research, as well as for a variety of applications. To mention a few examples, high-intensity charged particle beams are used in applications such as accelerator driven subcritical systems (ADSS) [1], neutron spallation sources [2], heavy ion fusion [3] and high intensity accelerator for basic research in high energy and nuclear physics [4, 5]. In recent years activities on ADSS has gained momentum for production of clean energy through controlled nuclear fission. Basically, a particle accelerator is used to deliver a continuous high energy  $\sim 1$  GeV proton beam of the order of 10 mA to produce neutrons by spallation to feed a fuel/moderator assembly where the neutrons multiply by fission chain reactions. Unlike a conventional reactor, in ADSS the fission reaction is not self-sustaining and is subcritical. It needs a continuous supply of neutrons from external source. If the accelerator stops, the reaction stops as well. The expectation is that such systems could be a possible source of energy for coming decades with Thorium as breeding fuel which has considerable advantages when compared with Uranium. Thorium is more abundant than Uranium. It gener-

ates much less Pu and transuranic actinides among the radioactive waste. The primary fuel is completely burnt after a number of fuel cycles. Moreover, operation in an accelerator driven mode eliminates the possibility of a criticality accident. Among the different options for the accelerator complex for ADSS are either a system of linacs or cyclotrons [6, 7, 8].

In practical realization of ADSS, the most challenging task is the development of a high energy ( $\sim 1$  GeV) and high current ( $\sim 10 - 15$  mA) proton accelerator to produce neutrons by spallation to drive the sub-critical reactor assembly. Cyclotron is an excellent option for delivering high power high current beam because of compact structure, low beam losses, operation in the cw mode and the most important cost factor for the beam power levels  $\leq 10$  MW.

Cyclotrons operating presently at various laboratories around the world were designed preliminarily for research in nuclear and particle physics. The beam powers available from these machines are at least one order of magnitude lower than needed for ADSS. The overall efficiency of these machines is also very low. Much larger efficiency can be achieved by designing the accelerator properly keeping in mind the power dissipation in RF and magnet. At present cyclotron is the highest beam power accelerator at PSI producing proton beam of 1.3 MW in cw mode at 590 MeV [9, 10]. In order to achieve 10 mA proton beam at 1 GeV using cyclotron, certain critical issues are required to be studied in detail, particularly at low energy regime where the space-charge forces dominate. Before reaching the prototype stage of a driver accelerator for ADSS plant much R & D works are needed to be carried out using proton beam of lower energy and lower current.

The Variable Energy Cyclotron Centre at Kolkata has undertaken a project to develop a 10 MeV, 5 mA compact radial sector proton cyclotron. This project

is a part of the activity of the high intensity accelerator development for ADSS. The main aim of the project is to study the physics of space-charge-dominated beams and technological problems associated with the generation, transport, bunching, injection, extraction etc. The ion source and the solenoid based low energy beam transport line have been designed, fabricated and commissioned. It is presently under testing for beam characterization.

In this thesis, detailed analytical and numerical studies have been performed to understand the dynamics of space-charge-dominated beams (single species and multispecies) propagating through the low energy beam transport line. Main emphasis has been put on the matching, rejection of unwanted components and detailed analysis of the physical phenomena associated with the transport of intense beam. In the following section we briefly describe the salient features of the 10 MeV cyclotron and present status of the injection system.

## 1.2 Parameters of 10 MeV Cyclotron

Detailed design philosophy of the four sector 10 MeV compact cyclotron is given in Ref. [11, 12, 13]. The maximum magnetic field at the hill centre is 1.5 T, and an average magnetic field is 0.689 T, which correspond to a particle revolution frequency of 10.5 MHz for proton. The hill gap is 4 cm and the valley gap is 64 cm, same as the distance between the upper and lower return yokes. For the injection system, one hole is provided at the center. We have provided four holes in the four valleys, two of which will be used for vacuum pumps and the rest two will be used for the RF cavities. Apart from using a high dee voltage, we have chosen a low average magnetic field and hence a large extraction radius ( $\sim 65$  cm) for 10 MeV cyclotron to have a reasonable turn separation at the extraction radius. Though this method increases the cost of the cyclotron, it gives more flexibility and a clear advantage for injection and extraction. The

harmonic mode  $h$  of operation is equal to 4. The magnet design combines the advantages of solid pole cyclotron and separated sector cyclotron. A high flutter provides strong focusing in the vertical direction. The main idea was to provide the vertical betatron tune  $> 0.5$  in the acceleration zone. This is necessary for handling the space-charge defocusing force at an average beam current of  $\sim 5$  mA.

### 1.3 Injection System of 10 MeV Cyclotron

In order to study injection of space-charge-dominated beam in the compact cyclotron and to characterize the beam, we have developed a microwave ion source and a beam transport line [14]. Ion source with adjustable solenoid, its power supplies, microwave generator (2.45 GHz, 1.2 kW), a high precision gas flow system etc., all float at  $\sim 100$  kV. High voltage deck at 100 kV is separated from the ground through polypropylene insulators. A two-segment ceramic insulators ( $\text{Al}_2\text{O}_3$ ) column, which supports the beam extraction electrodes, separates the high voltage deck and the beam line at the ground potential. Three turbo pumps having pumping speed of 520 l/s are used to evacuate the entire system. Two pumps are placed close to the extraction and other one in the transport line. Two motor controlled independent slits, one for  $x$ -plane and other for the  $y$ -plane are placed in the beam line to control the size of the beam and to reject the molecular hydrogen beam. Figure 1.1 shows the layout of the injection system.

#### 1.3.1 Ion Source and Extraction System

The design of the ion source is based on the principle of microwave discharge off resonance. The main advantage of this type of the source is the low emittance, stable high yield with large proton fraction. The schematic of ion source

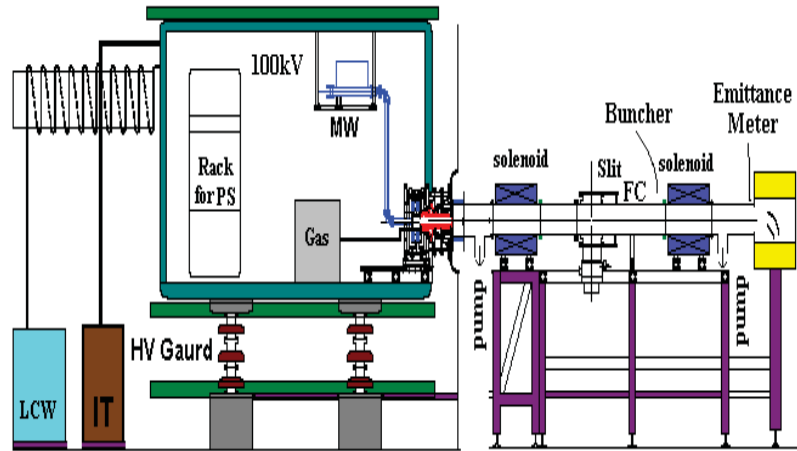


Figure 1.1: Layout of the high voltage deck, source and LEBT line.

is shown in Fig. 1.2. The plasma chamber is a double walled water-cooled cylindrical stainless steel chamber of 100 mm length and 90 mm diameter. The microwave power from the 2.45 GHz, 1.2 kW magnetron is coupled to the chamber through a three stubs tuning unit and ridged wave guide. The microwave window for vacuum sealing is placed behind a bend to avoid any damage due to back streaming electrons. Two motor controlled movable magnetic coils with separate power supply provide the desired magnetic field. There is a provision for adjustment of coils parallel to the source axis online with two motors. The diameter of the apertures in the plasma electrode, accelerating electrode and de-accelerating electrode are 7 mm, 8 mm and 8 mm respectively.

### 1.3.2 Low Energy Beam Transport Line

The injection beam line as shown in Fig. 1.3 consists of two solenoid magnets each having physical length 40 cm to transport and match the proton beam and two steering magnets to steer the beam. The beam from the ion source is expected to contain  $H_2^+$  and  $H_3^+$  species along with primary proton beam.

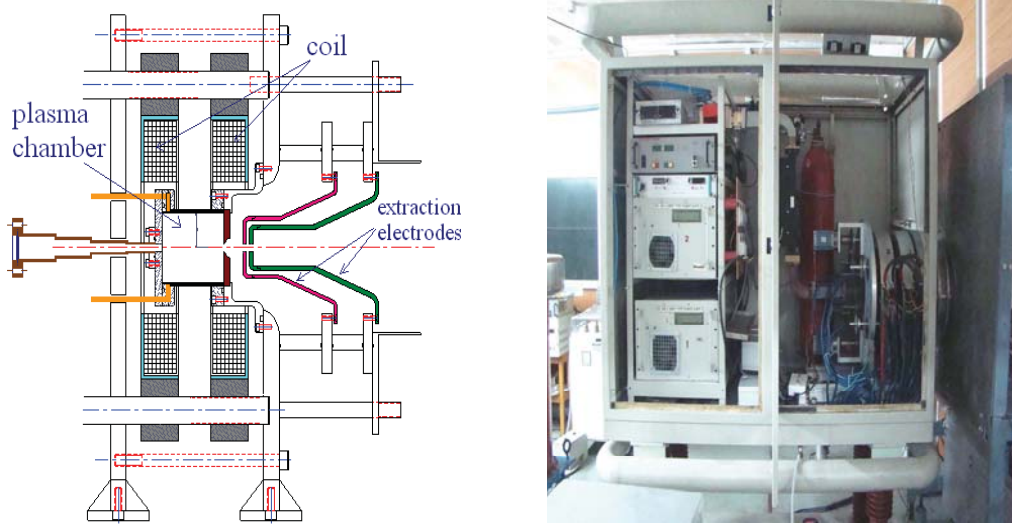


Figure 1.2: Drawing of the ion source and extraction system (left). Developed ion source (right).

We have provided a slit at the waist position of the proton beam after the first solenoid to reject most of  $H_2^+$  and  $H_3^+$  species. Beam current measuring equipments used in the beam line are: a water-cooled faraday cup with secondary electron suppresser, a DCCT and a beam dump cum faraday cup at the end of the beam line. A pressure of the order of  $3.5 \cdot 10^{-7}$  mbar has been achieved in the beam line. At present we are testing the source for performance and beam quality improvement. In order to study the inflection and transmission of the high beam current through the spiral inflector, we have designed and fabricated a small magnet having a similar characteristics as the central region of 10 MeV cyclotron.

The main body of this thesis consists of analytical, numerical and particle-in-cell (PIC) simulation study of intense single and multispecies beam behavior through low energy beam transport line. Detailed analysis of beam behavior has also been studied under various conditions such as misalignments and with different beam distributions.

Figure 1.3: *Beam transport line.*

## 1.4 Space Charge Dominated Beams

As mentioned earlier, the main work presented in this thesis is the study on the dynamics of space-charge-dominated beams propagating through the low energy beam transport line. In the following we present a general discussion on the space-charge effect. A beam is a collection of large number of charged particles moving along a straight or curved orbit, in which the longitudinal velocity is much greater than the transverse velocities. Depending on the nature of the source, there is always a spread in kinetic energy and velocity distribution in a charged particle beam. The quality of the beam can be described by the beam emittance which is related to the width and divergence of the beam. The divergence of the beam is due to the random velocity spread. The most widely used beam emittance is the normalized root-mean-square (rms) emittance defined in one direction (say, the  $x$ - direction) as [15]

$$\tilde{\epsilon}_n = \beta\gamma\tilde{\epsilon} \tag{1.1}$$

where  $\tilde{\varepsilon}$  is the unnormalized rms emittance in the  $x$ -direction, defined as

$$\tilde{\varepsilon} = (\langle x^2 \rangle \langle x'^2 \rangle - \langle xx' \rangle^2)^{1/2} \quad (1.2)$$

where  $\langle \dots \rangle$  indicates the average over the beam distribution. In the case of a uniform distribution the total normalised emittance  $\varepsilon_n = 4\tilde{\varepsilon}_n$ . It is to be pointed out here that emittance alone is not enough to define the quality of a beam. The figure of merit is therefore known as the normalized brightness of the beam, commonly defined as beam current divided by the square of normalised emittance. In order to have a good quality beam for a given current one always tries to get the beam emittance as minimum as possible. When the brightness of the beam is very high, the beam becomes space-charge dominated. In the space-charge dominated regime, the space-charge force is much greater than the emittance force which can be described by the relation  $KR^2 > \varepsilon^2$ , where  $K = 2I/(I_0\beta^3\gamma^3)$  is the self-field perveance of the beam and  $R$  is the radius of the beam [15].

## 1.5 Theoretical Models of Intense Beams

For most of the machines near the ion source the self field is important in determining the beam characteristics. In order to have optimal design and stable operation it is essential to have a basic understanding of the beam dynamics with space-charge. As the beam current increases the interaction between the particles become more important. The charges produce mutually repulsive electric force and also magnetic fields that produce attractive forces. The magnetic forces are much smaller than the electric forces at low velocity and are unimportant except for relativistic particles. The total Coulomb field experienced by any particle is the sum of the fields due to all other particles. The self interaction of particles can be classified into two categories, the collisional regime and the collective or space-charge regime. The collisional regime is dominated by binary

collisions caused by close encounters. The space-charge regime is dominated by the self field produced by the particle distribution that can be represented by a smooth field as a function of space and time. The space-charge regime occurs when there are enough neighbouring particles to shield the effects of density fluctuations, a phenomenon known in plasma physics as Debye shielding. In order to distinguish the two regimes a parameter  $\lambda_D$  known as Debye length is used and is given by [15]

$$\lambda_D = \left( \frac{\varepsilon_0 \gamma^2 k_B T}{q^2 n} \right)^{1/2} \quad (1.3)$$

where  $k_B$  is the Boltzmann constant,  $n$  is the number density of particles,  $q$  is the charge,  $T$  is the temperature,  $\varepsilon_0$  is the free space permittivity and  $\gamma$  is the usual relativistic parameter. If the Debye length is large compared with the beam radius  $R$  ( $\lambda_D \gg R$ ), the single particle behaviour dominates. On the other hand, if the Debye length is small compared to the beam radius ( $\lambda_D \ll R$ ), collective behaviour of the beam dominates and smooth functions for charge and field distributions can be used. In such cases self fields can be treated as an applied force. In the absence of collisions, a complete description of collective processes for intense charged particle beams in terms of external field and smooth self fields is provided by the Vlasov-Maxwell equations. These equations provides self-consistent nonlinear evolution of the beam distribution function  $f(\mathbf{x}, \mathbf{p}, t)$  and the self-generated fields and are given by [15, 16]

$$\frac{\partial f}{\partial t} + \frac{\partial}{\partial \mathbf{x}} \cdot (\mathbf{v}f) + \frac{\partial}{\partial \mathbf{p}} \cdot (q(\mathbf{E} + \mathbf{v} \times \mathbf{B}))f = 0 \quad (1.4)$$

The total electric and magnetic fields  $\mathbf{E}(\mathbf{x}, t)$  and  $\mathbf{B}(\mathbf{x}, t)$  are determined self-consistently from Maxwell's equations

$$\nabla \cdot \mathbf{E} = \frac{1}{\varepsilon_0} q \int f(\mathbf{x}, \mathbf{p}, t) d^3 \mathbf{p} + \rho_{ext}(\mathbf{x}, t), \quad (1.5)$$

$$\nabla \times \mathbf{E} = -\partial \mathbf{B} / \partial t, \quad (1.6)$$

$$\nabla \cdot \mathbf{B} = 0, \quad (1.7)$$

$$\nabla \times \mathbf{B} = \mu_0 \mathbf{J}_{ext}(\mathbf{x}, t) + \mu_0 q \int \mathbf{v} f(\mathbf{x}, \mathbf{p}, t) d^3 \mathbf{p} + \mu_0 \varepsilon_0 \partial \mathbf{E} / \partial t. \quad (1.8)$$

here  $\rho_{ext}(\mathbf{x}, t)$  and  $\mathbf{J}_{ext}(\mathbf{x}, t)$  are the external volume charge density and current density respectively. For a multispecies beam, each species can be defined by separate distribution function and evolution of each distribution is provided by Vlasov equation. A variety of theoretical and numerical methods are employed based on the above Vlasov-Maxwell equation to describe the collective effects in charged particle beams such as beam envelope model, 1D model for longitudinal dynamics and more rigorous self-consistent methods.

### 1.5.1 Vlasov Equilibrium for Space Charge Dominated Beams

The equilibrium states of a distribution of collisionless low energy charged particle beams are defined by time independent solutions of the Vlasov-Maxwell equations by setting  $\partial f / \partial t = 0$  in Eq. (1.4). The equilibrium distribution function can then be used to investigate beam equilibrium properties over a wide range of system parameters and beam intensities. Of particular concern are emittance growth and beam losses, which arise due to the evolution of distribution function in their non equilibrium states. The solution of Vlasov-Maxwell equations obviously has many solutions which depend on the form of the distribution functions and the parameters of the system. The usual approach is to choose a distribution function which depends on the constants or integrals of the single particle motion and therefore is a solution of the Vlasov equation. In an uncoupled and perfectly aligned lattice, the Kapchinskij-Vladimirskij (K-V) distribution function is the only known exact self-consistent solution of the nonlinear Vlasov-Maxwell equations for high-intensity beams [17]. There also exists a rigid-rotor Vlasov equilibrium for an intense axisymmetric beam with uniform density in the radial direction propagating through an aligned periodic

solenoidal focusing field [18]. In a recent article, Moraes *et al.* [19] have studied the propagation of off-axis intense beam in an aligned periodically focusing solenoidal channel and obtained a Vlasov equilibrium distribution.

### 1.5.2 Beam Envelope Model

The Kapchinskij-Vladimirskij (K-V) envelope equations are often employed as a simple model of the transverse evolution of intense ion beams. These equations are coupled ordinary differential equations. They describe the evolution of the beam edge in response to applied linear focussing forces and defocussing forces resulting from space-charge and emittance [17]. The K-V beam envelope equations are given by

$$X'' + k_x(s)X - \frac{2K}{(X+Y)} - \frac{\varepsilon_x^2}{X^3} = 0 \quad (1.9)$$

$$Y'' + k_y(s)Y - \frac{2K}{(X+Y)} - \frac{\varepsilon_y^2}{Y^3} = 0 \quad (1.10)$$

where  $X$  and  $Y$  are the beam envelope sizes and  $\varepsilon_x$  and  $\varepsilon_y$  are the emittances in  $x$  and  $y$  directions respectively.  $k_x(s)$  and  $k_y(s)$  are the external focussing forces in  $x$  and  $y$  directions respectively and  $K$  is the perveance of the beam. Later Sacherer and Lapostolle extended the work for the elliptically symmetric more general beam density distributions [20, 21]. They introduced rms quantities and the concept of equivalent beams. According to this concept, two beams composed of the same species, current and kinetic energy are equivalent if the second moments of the distributions are the same. The evolution equations for the rms beam size are same for all the distributions. The rms envelope equations are given by

$$\tilde{x}'' + k_x(s)\tilde{x} - \frac{K}{2(\tilde{x} + \tilde{y})} - \frac{\tilde{\varepsilon}_x^2}{\tilde{x}^3} = 0 \quad (1.11)$$

$$\tilde{y}'' + k_y(s)\tilde{y} - \frac{K}{2(\tilde{x} + \tilde{y})} - \frac{\tilde{\varepsilon}_y^2}{\tilde{y}^3} = 0 \quad (1.12)$$

Here  $\tilde{x}$  and  $\tilde{y}$  are the rms beam sizes,  $\tilde{\varepsilon}_x$  and  $\tilde{\varepsilon}_y$  are the rms emittances and prime denotes derivatives with respect to path length  $s$ . However, the emittance in the rms envelope equations is an unknown function of path length  $s$  except for K-V distribution. Such envelope models are typically solved when the variation of statistical beam emittance is negligible or sufficiently slow [22, 23].

### 1.5.3 Beam Dynamics during Bunching

In many practical applications such as rf accelerators, free electron lasers and microwave tubes, one requires bunching of the intense beams. A systematic study of transverse and longitudinal dynamics during beam bunching results in better understanding of the processes and in improved design schemes. The collective processes in intense beams are three dimensional in nature and are difficult to solve analytically. However, considerable theoretical progress has been made in the development and application of one dimensional Vlasov-Maxwell model, warm fluid model and cold fluid model to describe the longitudinal beam dynamics of long beam bunch. Such one dimensional Vlasov descriptions rely heavily on using a quasi self-consistent  $g$ -factor model to incorporate the average effects of transverse beam geometry and the surrounding wall structure. The longitudinal space-charge electric field is given by [15]

$$E_z = \frac{g}{4\pi\varepsilon_0\gamma^2} \frac{\partial\lambda}{\partial z} \quad (1.13)$$

here  $\lambda$  is the line charge density,  $g = 2\ln(b/R)$  is the geometry factor which depends on radii  $b$  and  $R$  of conducting pipe and beam respectively. The term  $\partial\lambda/\partial z$  indicate the variation of line charge density along the bunch.

The transverse dynamics during the bunching is described by the transverse K-V envelope equation. The perveance of the beam bunch becomes function of path length  $s$  and increases as the beam bunching takes place. The evolution

of beam radius for an axisymmetric beam is described by,

$$R'' + k(s)R - \frac{K(s)}{R} - \frac{\varepsilon^2}{R^3} = 0 \quad (1.14)$$

The effective perveance  $K(s)$  includes the increase in the beam current during the bunching. The longitudinal and transverse beam dynamics are either solved independently or coupled by the geometric factor  $g$ . The  $g$ -factor model is used when the gradient of line charge density is very small and the longitudinal bunch size is large compared to the transverse beam size.

#### 1.5.4 Self-consistent Approach

The major shortcomings of K-V and rms beam envelope models are the fact that they do not provide any information on the emittance growth due to nonlinear forces from both the applied fields as well as from the space-charge forces. In cases where nonlinear forces are present the theoretical investigation becomes very difficult, and one has to rely on computer simulations using realistic beam distribution.

Several advanced numerical tools are available for the self-consistent investigation of nonlinear collective processes in intense charged particle beams. Few popular methods are particle-in-cell (PIC) simulation methods [24], particle-particle method, Vlasov method [25, 26, 27],  $\delta f$  simulation method [16] etc. Among them, PIC methods are most widely used. Realistic many particle simulations provide more insights into the various complexities associated with intense self field and also help in the design of the accelerator systems. PIC simulations follow the motion of a large number of charged particles in their self-consistent electric and magnetic fields. When appropriate methods are used, even few thousand macroparticles are sufficient to describe adequately the collective effects in a beam. However, to perform such numerical simulations, considerable computational power is often required.

## 1.6 Thesis Overview

In this thesis, detailed analytical formulations, numerical and PIC simulations have been performed to understand the dynamics of space-charge-dominated beam (single species and multispecies) propagating through a low energy beam transport line.

In **Chapter 2** a self-consistent kinetic description is presented to understand the dynamics of a space-charge-dominated beam in aligned and misaligned solenoid based beam transport line. A general equation for the centroid motion is derived using the nonlinear Vlasov-Maxwell equation. As we know that there exists Vlasov equilibrium for intense beam known as K-V distribution in the case of aligned transport elements. It has been shown that for misaligned channel there also exists a self-consistent Vlasov equilibrium distribution for the beam dynamics in the case of a uniform beam density around the beam centroid. The beam envelope equation that determines the evolution of outer radius of equilibrium beam around the beam centroid is similar in form to the well known K-V envelope equation. It is independent of the centroid equation when the conducting beam pipe is considered very far away from the beam. Finally, a self-consistent two dimensional PIC model is used to investigate the evolution of rms beam quantities, centroid motion, and phase space distribution of particles. In addition, the beam loss during the transport for different types of initial beam distributions has also been estimated for misaligned system.

In the first part of **Chapter 3** a beam envelope model for an axisymmetric space-charge-dominated multispecies beam is presented for the evolution of the radius of each species along a solenoid based beam transport line. Circular slits are introduced in the beam line for the selection of particular species. The effective values of the current and emittance of each species after the slit are

taken into account in the beam envelope model for further transport in case the radius of any species is larger than the slit size. In the later part of **Chapter 3** the evolution of multispecies beam is studied using self-consistent PIC method where each species of the beam is represented as a combination of large number of macroparticles. The evolution of beam size and emittance growth of the primary species is investigated in the presence of unwanted species. The real space distributions of the unwanted species are studied with and without the presence of a slit in the beam line. The formation of beam hollows of unwanted species is observed which are produced due to nonlinear space-charge effect. It has been shown that the rejection of unwanted species is very effective when the slit is placed after the hollow formation of unwanted species.

In **Chapter 4** an optimisation method is described to find the optimal beam line settings for the transport and matching of intense multispecies beam using the envelope model discussed in **Chapter 3**. The method is based on random search technique where the parameters are varied randomly during the optimisation. Using this method, the primary beam is matched at the final position and the losses of unwanted species are maximised at the location of the slit. To quantify the quality of the solution two cost functionals are used in the optimisation, one for the primary beam and other for the unwanted species. We have studied the transport of intense proton beam from ion source in the presence of  $H_2^+$  and  $H_3^+$  in the solenoid based beam transport line for various values of total beam current and different fractions of the species. The major advantage of this method is that it is very simple to apply and easy to include any number of constraints. It does not require any differentiation of the cost functional and is very fast.

In **Chapter 5** numerical simulations have been carried out to optimise the bunching performance of sinusoidal, two harmonic and double drift bunchers

in the presence of space charge. The main aim of this work is to find out a suitable buncher to bunch the high intensity beam for injection into the proposed cyclotron. Disc model has been used for the longitudinal dynamics and K-V envelope equations have been used for transverse dynamics. Numerical simulations and optimisation of buncher parameters have been performed for 100 keV proton beam. The effect of buncher voltage and drift length on the bunching efficiency and density distribution of the beam at the time focus have been studied for various values of the beam current.

In **Chapter 6** a theoretical model has been developed for bunch size comparable to transverse beam size to study the beam dynamics during the beam bunching for different types of distributions. As the beams from the ion source can never be monoenergetic, the finite longitudinal energy spread is also included in the analysis. The beam envelope equation has been modified to take into account the longitudinal space-charge effect on transverse motion which arises when the beam size is comparable to the bunch size. During the bunching as the beam drifts the line charge density along the beam bunch does not remain uniform. As a result different portions of the bunch evolve differently during the transport. In order to include the variation of beam radius along the length of the beam and to understand the behaviour of projected emittance during the bunch compression, the total length of the beam is divided into thick slices. The evolution of radius of individual slice is then found out under the influence of space charge and external forces. Finally, self-consistent PIC simulations have been carried out to understand the beam dynamics in more detail.

The details of the development of two-dimensional and three dimensional particle-in-cell (PIC) codes which are used in the previous chapters is described in **Chapter 7**. The 2D PIC code can handle self-consistent evolution of a space-

charge dominated single as well as multispecies beam propagating through a beam transport system. The developed 3D PIC can help to understand the complete description of collective behavior in intense charged particle beams during the beam bunching. In this chapter the details behind the structures of the two dimensional and three dimensional PIC codes are described. The code handles the misalignment (displacement as well as tilt) of the focussing element, higher order nonlinearity of the focussing elements and the off-centring of the beam.

Finally, **Chapter 8** summarizes the conclusions drawn from the earlier chapters and identifies possible areas of future research.

## Chapter 2

# Beam Dynamics in the Aligned and Misaligned LEBT System

### 2.1 Introduction

It is becoming increasingly important to understand the self-field effects on determining the detailed equilibrium, stability, and transport properties of high-intensity beams in a fully self-consistent manner from the nonlinear Vlasov-Maxwell equations [16]. In an uncoupled and perfectly aligned lattice, the Kapchinskij-Vladimirskij (K-V) distribution is the only known exact self-consistent solution of the nonlinear Vlasov-Maxwell equations for high-intensity beams [17]. There also exists a rigid-rotor Vlasov equilibrium for an intense axisymmetric beam with uniform density in the radial direction propagating through a periodic solenoidal focusing field [18]. Recently, Qin and Davidson have generalized the K-V distribution function to describe high-intensity beam dynamics in a coupled transverse focusing lattice [28] using the generalized Courant-Snyder invariant [29, 30]. In all the cases it has been assumed that the beam and the focusing elements are perfectly aligned to the symmetry axis. In a recent article, Moraes *et al.* [19] have studied the propagation of off-axis intense beam in an aligned periodically focusing solenoidal channel and obtained a Vlasov

equilibrium distribution.

One critical but unavoidable problem in the beam transport lines is the presence of undesired imperfections in the beam line components [31, 32, 33, 34, 35]. In practical beam transport systems there is always a possibility that solenoid magnets are placed with finite displacement and rotational alignment errors with respect to the ideal symmetry axis. The dipole field terms induced by misalignments of the solenoid can significantly deviate an aligned centroid orbit away from the designed axis of the beam. It is therefore, of practical importance to investigate the physics of beams in a misaligned focusing channel [36, 37, 38, 39].

In this chapter we provide a self-consistent kinetic description to understand the dynamics of a space-charge-dominated beam in a misaligned solenoid based low energy beam transport line [40]. At first the magnetic field components of the misaligned solenoid is obtained in the laboratory frame in terms of misalignment parameters and single particle equation of motion is derived. Then a general equation for the centroid motion of continuous, intense charged particle beam is derived using the kinetic nonlinear Vlasov-Maxwell equation.

Most beams extracted from the ion sources are in the energy range of 10 - 150 keV and current in the range of 10 - 20 mA with stronger repulsive space-charge force. It is therefore, important to understand the effect of space charge on beam dynamics at low energy since the initial beam state can affect the quality of the beam downstream. The nonlinear space-charge field of an intense beam is a serious concern and needs special attention to avoid emittance growth and halo formation during the transport [41, 42, 43, 44, 45]. The problem of matching of the nonuniform density distributed beam in a linear uniform channel as well as nonlinear focussing channel is discussed in Refs. [15, 46, 47, 48]. However, due

to some practical constraints, it is not always possible to use nonlinear focusing channel.

In the later part of the chapter, a PIC code has been used to investigate the evolution of rms beam quantities, centroid, and phase space distribution in the cases of aligned and misaligned focussing magnets. The details of PIC code are discussed in **Chapter 7**. We have used five types of phase space distributions of the beam and investigated the behaviour of beam propagation in real and phase spaces. In addition, loss of beam during the transport for different types of initial beam distributions are also estimated.

## 2.2 Vlasov Equilibrium in Misaligned Focussing Channel

We consider a continuous, axisymmetric charged-particle beam propagating in the laboratory coordinate system  $(x, y, z)$  with axial velocity  $\beta_b c \hat{z}$  in a solenoid based beam transport line. The magnetic field in the case of an aligned solenoid for small transverse excursions is given by,

$$B_r(r, s) = -\frac{r}{2} \frac{dB_z(s)}{ds} + \frac{r^3}{16} \frac{d^3 B_z(s)}{ds^3} + O(r^5) \quad (2.1a)$$

$$B_z(r, s) = B_z(s) - \frac{r^2}{4} \frac{d^2 B_z(s)}{ds^2} + O(r^4) \quad (2.1b)$$

where,  $s = z$  is the axial coordinate along the beam propagation,  $r = \sqrt{x^2 + y^2}$  is the radial distance from the solenoid axis and prime denotes derivative with respect to  $s$ . In a realistic beam transport system, there can be a finite displacement and rotational (tilt) mechanical alignment errors of the magnets. We now use coordinate system for the misaligned solenoid as  $x_D, y_D, z_D$ , with  $z_D$  as the longitudinal axis of symmetry for the solenoid as shown in Fig. 2.1. Let us assume that the geometric center of the magnet is translationally displaced by  $\vec{\Delta} = \Delta_x \hat{x} + \Delta_y \hat{y} + \Delta_z \hat{z}$  relative to the laboratory frame. The solenoid axis of

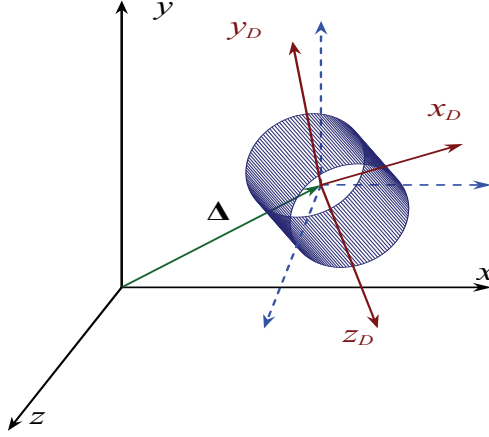


Figure 2.1: Schematic of a misaligned solenoid described by a two-step transformation. First, translation of center by  $\vec{\Delta} = \Delta_x \hat{x} + \Delta_y \hat{y}$ , and then a rotation of the axis of symmetry in the translated system.

symmetry  $\hat{z}_D$  is then rotated through a polar angle  $\phi$  with respect to  $z$  axis and an azimuthal angle  $\theta$  with respect to  $x$  axis. It is to be noted here that before the rotation, unit vectors in the displaced coordinate system are parallel to the laboratory coordinate system. The projection of  $\hat{z}_D$  in the laboratory system can be written as [34]

$$\hat{z}_D = \sin \phi \cos \theta \hat{x} + \sin \phi \sin \theta \hat{y} + \cos \phi \hat{z} \quad (2.2)$$

whereas the coordinate transformation in component form can be expressed as

$$x_D = x - \Delta_x - \theta_x (s - s_0 - \Delta_z) \quad (2.3a)$$

$$y_D = y - \Delta_y - \theta_y (s - s_0 - \Delta_z) \quad (2.3b)$$

$$z_D = z - \Delta_z + \theta_x x + \theta_y y \quad (2.3c)$$

in which we have used  $\theta_x = \phi \cos \theta$  and  $\theta_y = \phi \sin \theta$  for the rotational parameters assuming that the value of  $\phi$  is very small i.e.  $|\phi| \ll 1$ . The magnetic field components at location  $(r, z)$  in the laboratory frame for a misaligned solenoid

in linear approximation can be expressed as [34],

$$B_x(r, s) = -\frac{1}{2} \frac{dB_z(s)}{ds} (x - \Delta_x - \theta_x(s - s_0)) + B_z(s)\theta_x \quad (2.4a)$$

$$B_y(r, s) = -\frac{1}{2} \frac{dB_z(s)}{ds} (y - \Delta_y - \theta_y(s - s_0)) + B_z(s)\theta_y \quad (2.4b)$$

$$B_z(r, s) = B_z(s) - \frac{dB_z(s)}{ds} \Delta_z \quad (2.4c)$$

These equations represent the leading order magnetic field components of an ideal solenoid which is misaligned with displacement parameters  $\Delta_x, \Delta_y, \Delta_z$  and the rotational parameters  $\theta_x, \theta_y$ . It is easy to see that the misaligned solenoid generates an  $s$  dependent dipole field in  $x$  and  $y$  directions together with a shift in the longitudinal field component. The equations of motion for a particle of charge  $q$  and mass  $m_b$  in the presence of solenoidal magnetic field and self field of the beam are given by

$$\gamma_b m_b \frac{d^2 x}{dt^2} = -\frac{q}{\gamma_b^2} \frac{\partial \phi^s}{\partial x} + q (v_y B_z - v_b B_y) \quad (2.5a)$$

$$\gamma_b m_b \frac{d^2 y}{dt^2} = -\frac{q}{\gamma_b^2} \frac{\partial \phi^s}{\partial y} - q (v_x B_z - v_b B_x) \quad (2.5b)$$

here  $\phi^s$  is the usual self-field electrostatic potential and  $v_b = \beta_b c$ . Using Eq. (2.4) in Eq. (2.5) and using  $s = \beta_b ct$  it is straight forward to obtain

$$x'' - 2ky' + 2k'y'\Delta_z - k'y + \partial\psi^s/\partial x = -k'(\Delta_y + \theta_y(s - s_0)) - 2k\theta_y \quad (2.6a)$$

$$y'' + 2ky' - 2k'x'\Delta_z + k'x + \partial\psi^s/\partial y = k'(\Delta_x + \theta_x(s - s_0)) - 2k\theta_x \quad (2.6b)$$

Here  $\psi^s = q\phi^s/(m_b\gamma_b^3\beta_b^2c^2)$  is the normalised self-field potential of the beam and  $k = qB_z(s)/(2m_b c\beta_b\gamma_b)$  is the focussing field strength of the solenoid. For a solenoidal focussing, the cross coupled form of Eq. (2.6) results in a macroscopic rotation of the beam about the longitudinal axis. These equations can be simplified by transforming the coordinates to the rotating Larmor frame which rotates with angular velocity  $d\phi_L/ds = -k(s)$ . The Larmor frame coordinates

$x_L(s)$  and  $y_L(s)$  and laboratory frame coordinates  $x(s)$  and  $y(s)$  are related as,

$$\begin{bmatrix} x_L(s) \\ y_L(s) \end{bmatrix} = \begin{bmatrix} \cos \phi_L(s) & \sin \phi_L(s) \\ -\sin \phi_L(s) & \cos \phi_L(s) \end{bmatrix} \begin{bmatrix} x(s) \\ y(s) \end{bmatrix} \quad (2.7)$$

Equations (2.6), after some straightforward algebra, can be expressed in the Larmor frame as,

$$x_L'' + k^2 x_L + \partial\psi^s/\partial x_L = G^m \quad (2.8a)$$

$$y_L'' + k^2 y_L + \partial\psi^s/\partial y_L = H^m \quad (2.8b)$$

where,

$$\begin{aligned} G^m &= -k'(\Delta_y + \theta_y(s - s_0)) \cos \phi_L(s) - 2k\theta_y \cos \phi_L(s) \\ &\quad + k'(\Delta_x + \theta_x(s - s_0)) \sin \phi_L(s) - 2k\theta_x \sin \phi_L(s) \end{aligned}$$

$$\begin{aligned} H^m &= k'(\Delta_x + \theta_x(s - s_0)) \cos \phi_L(s) + 2k\theta_x \cos \phi_L(s) \\ &\quad + k'(\Delta_y + \theta_y(s - s_0)) \sin \phi_L(s) - 2k\theta_y \sin \phi_L(s) \end{aligned}$$

In the derivation of Eq. (2.8), we have neglected the higher order terms such as  $2k'y'\Delta_z$  and  $2k'x'\Delta_z$ . Since from here only Larmor frame will be used throughout in this chapter we drop the subscript  $L$  for convenience. In the paraxial approximation, the beam distribution function  $f_b(x, y, v_x, v_y, s)$  evolves according to the Vlasov-Maxwell equations [16]

$$\frac{\partial f_b}{\partial s} + v_x \frac{\partial f_b}{\partial x} + v_y \frac{\partial f_b}{\partial y} - (k^2 x + \partial\psi^s/\partial x - G^m) \frac{\partial f_b}{\partial v_x} - (k^2 y + \partial\psi^s/\partial y - H^m) \frac{\partial f_b}{\partial v_y} = 0 \quad (2.9)$$

$$\nabla^2 \psi^s = -(2\pi K/N_b) n_b(x, y, s) \quad (2.10)$$

In the above equation  $n_b(x, y, s) = \int f_b dv_x dv_y$  is the beam density,  $N_b = \int f_b d\mathbf{r} dv$  is the line density of the beam particles and  $K = 2N_b q^2 / (\gamma_b^3 m_b \beta_b^2 c^2)$  is the beam self-field perveance.

Our objective is to find a self-consistent solution of Eq. (2.9) and Eq. (2.10). Using Eq. (2.9) and averaging over the distribution function we have,

$$\langle x \rangle' = \langle v_x \rangle, \quad \langle y \rangle' = \langle v_y \rangle \quad (2.11)$$

$$\langle x \rangle'' = \langle v_x \rangle' = -k^2 \langle x \rangle - \langle \partial \psi^s / \partial x \rangle + G^m \quad (2.12a)$$

$$\langle y \rangle'' = \langle v_y \rangle' = -k^2 \langle y \rangle - \langle \partial \psi^s / \partial y \rangle + H^m \quad (2.12b)$$

Above equations describe the evolution of the beam centroid  $\langle x \rangle$  and  $\langle y \rangle$  in response to the solenoidal magnetic field, the average self-field components  $\langle \partial \psi^s / \partial x \rangle$ ,  $\langle \partial \psi^s / \partial y \rangle$  and the dipole field terms due to misaligned solenoid. Since  $\partial \psi^s / \partial x$  and  $\partial \psi^s / \partial y$  correspond to the self-force exerted on beam particles by themselves, their average over the beam distribution must vanish due to pair wise inter-particle interaction [19] i.e.  $\langle \partial \psi^s / \partial x \rangle = \langle \partial \psi^s / \partial y \rangle = 0$ . The equations of motion for the centroid, thus become

$$\langle x \rangle'' + k^2 \langle x \rangle = G^m \quad (2.13a)$$

$$\langle y \rangle'' + k^2 \langle y \rangle = H^m \quad (2.13b)$$

It is to be noted here that so far we have not made any assumption on the particular form of the beam distribution. Therefore, the equations of centroid stated above are always valid as long as the beam evolves according to the Vlasov-Maxwell system.

The self-field potential  $\psi^s$  and the distribution function  $f_b$  are nonlinearly coupled in the Vlasov-Maxwell equations. In order to construct the equilibrium solution, we first assume a specific form for the self-field potential, and then find the invariants of the particle motion in the presence of external field as well as the self field. A distribution function constructed in terms of the invariants of

single particle motion in the phase space will satisfy the Vlasov equation. However, any arbitrary choice of distribution function may not be useful. One needs to choose a specific distribution function of the invariants so that it generates the initially assumed self-field potential. This enables one to derive a set of differential equations for the beam envelopes using the self-consistent distribution function and the Vlasov-Maxwell equations.

In order to construct the self-consistent solution of the nonlinear Vlasov-Maxwell equations, we first assume a circular beam with a uniform distribution around the centre  $(\langle x \rangle, \langle y \rangle)$  as,

$$n_b(x, y, s) = \begin{cases} N_b / (\pi R^2(s)) & r_b < R(s) \\ 0 & r_b > R(s) \end{cases} \quad (2.14)$$

so that it will generate linear self-field force in the beam. Here  $r_b = (x_b^2 + y_b^2)^{1/2}$  is the radial distance of a particle,  $R(s)$  is the beam envelope with respect to the centroid,  $x_b = x - \langle x \rangle$  and  $y_b = y - \langle y \rangle$ . The normalised self potential in the interior of the beam is given by  $\psi^s = -K(x_b^2 + y_b^2) / 2R^2$ . The equations of motion of a beam particle in the Larmor frame located at  $(x, y)$  and subjected to the external focussing force and the self-field force are therefore, evolve according to

$$x'' + k^2 x - K x_b / R^2 = G^m \quad (2.15a)$$

$$y'' + k^2 y - K y_b / R^2 = H^m \quad (2.15b)$$

The equations of motion of beam particle in Larmor frame with respect to the beam centroid  $(\langle x \rangle, \langle y \rangle)$  can be easily obtained by subtracting Eqs. (2.13) from Eqs. (2.15) and given by

$$x_b'' + k^2 x_b - (K/R^2) x_b = 0 \quad (2.16a)$$

$$y_b'' + k^2 y_b - (K/R^2) y_b = 0 \quad (2.16b)$$

The solution for  $x_b$  and  $y_b$  can be expressed as [16]

$$x_b = A_x w(s) \cos \left( \int w^{-2}(s) ds + \phi_{0x} \right) \quad (2.17a)$$

$$y_b = A_y w(s) \cos \left( \int w^{-2}(s) ds + \phi_{0y} \right) \quad (2.17b)$$

in which  $A_x, A_y, \phi_{0x}, \phi_{0y}$  are constants and the envelope function  $w(s)$  can be obtained by solving  $w'' + (k^2 - K/R^2)w = w^{-3}$ .  $A_x$  and  $A_y$  can be expressed in the form

$$A_x^2 = (x_b/w)^2 + (wx'_b - w'x_b)^2 = \text{const.} \quad (2.18a)$$

$$A_y^2 = (y_b/w)^2 + (wy'_b - w'y_b)^2 = \text{const.} \quad (2.18b)$$

Since  $A_x$  and  $A_y$  are the constants of motion, any function of the form  $f_b(A_x^2, A_y^2)$  is a solution of the nonlinear Vlasov equation. If we choose the distribution function

$$f_b = N_b (\pi^2 \varepsilon)^{-1} \delta (A_x^2 + A_y^2 - \varepsilon) \quad (2.19)$$

it satisfies Eq. (2.14) provided  $R = \sqrt{\varepsilon}w$ , where  $\varepsilon$  is the emittance of the beam and is a constant. The beam radius  $R(s)$  obeys familiar envelope equation

$$R'' + k^2 R - (K/R) - (\varepsilon^2/R^3) = 0 \quad (2.20)$$

The above treatment can also be generalised for a uniformly distributed circular beam which rigidly rotates in the Larmor frame as it propagates along the beam line. From Eqs. (2.17) it is easy to see that  $d(x_b y'_b - y_b x'_b)/ds = 0$  which corresponds to the conservation of canonical angular momentum  $p_\theta$ . The generalised distribution function for a rigidly rotated circular beam [18] which satisfies the Vlasov-Maxwell equation can be expressed as

$$f_b = N_b (\pi^2 \varepsilon_T)^{-1} \delta (A_x^2 + A_y^2 - 2\omega p_\theta - (1 - \omega^2)\varepsilon_T) \quad (2.21)$$

In this case  $\varepsilon_T$  is the effective emittance,  $\omega$  ( $-1 < \omega < 1$ ) is the rotation parameter and both are constants and we obtain  $R = \sqrt{\varepsilon_T}w$  with an envelope equation similar to Eq. (2.20).

It is also possible to construct a Vlasov equilibrium for an elliptical beam with zero angular momentum assuming the distribution function given by

$$f_b = N_b (\pi^2 \varepsilon_x \varepsilon_y)^{-1} \delta (A_x^2/\varepsilon_x + A_y^2/\varepsilon_y - 1) \quad (2.22)$$

where  $\varepsilon_x$  and  $\varepsilon_y$  are the emittances of the beam in  $x$  and  $y$  directions respectively. This distribution function also yields coupled envelope equations similar to the K-V beam envelope equations. A Vlasov equilibrium distribution, therefore, can be formed for space-charge-dominated beam even when the solenoid magnets in the beam transport lines are misaligned with respect to the symmetry axis. To verify the conservation of beam emittances in such cases, we have performed a self-consistent simulation using particle-in-cell (PIC) [24] method discussed in **Chapter 7**. As the beam propagates, we compute the self-consistently obtained beam sizes and the rms transverse emittances from

$$X_{rms} = \sqrt{\langle x_b^2 \rangle}, \quad \varepsilon_{x rms} = \sqrt{\langle x_b^2 \rangle \langle x_b'^2 \rangle - \langle x_b x_b' \rangle^2} \quad (2.23)$$

where  $\langle \dots \rangle$  represents averages over macroparticles in the Larmor frame. We can have a similar expression for  $y$  plane also.

## 2.3 Numeical Results

Though the theoretical description presented in the previous sections is general in nature, however, it is developed mainly to study the dynamics of space-charge-dominated beam in our low energy beam injection line of 10 MeV cyclotron. The detail of low energy beam transport line are given in **Chapter 1**. Its consist of a microwave ion source and two solenoid magnets S1 and S2 of

physical length 40 cm each to transport and match the beam [49]. A schematic of beam transport system with misaligned solenoids is shown in Fig. 2.2.

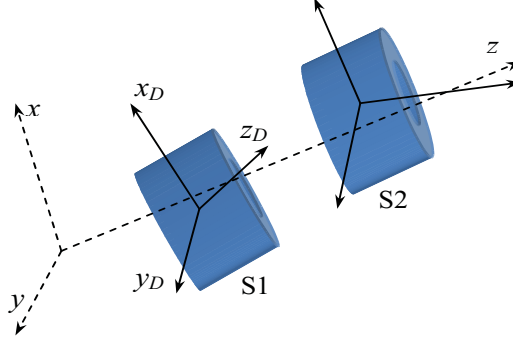


Figure 2.2: A schematic of beam transport system with misaligned solenoid magnets showing the laboratory coordinate system  $(x, y, z)$  and the local coordinate system  $(x_D, y_D, z_D)$  of the solenoids.

### 2.3.1 Computation of Solenoid Field and its Derivatives

In practical calculations, it is common to use a hard edge model for solenoids, however, a more realistic calculation can be done with accurate smooth field profile of the solenoids. We have calculated the magnetic field of the solenoid using 3D MagNet code [50] and fitted the calculated normalised field (magnetic field divided by the central field) by an analytical function given by,

$$B_n = \frac{B_z(s)}{B_0} = \begin{cases} \frac{1}{1+\exp(a(s-s_0-b))} & \text{for } s > s_0 \\ 1 - \frac{1}{1+\exp(-a(s-s_0-b))} & \text{for } s < s_0 \end{cases} \quad (2.24)$$

in which  $s_0$  is the axial coordinate of the centre of the solenoid. We obtained the values for the parameters  $a = 0.4986$  and  $b = 22.3712$  after fitting which has been used in Eq. (2.24) to compute the first, second and third derivatives of the field as needed in the simulation. We have defined a function  $\chi$ , the ratio of nonlinear to linear term to know the strength of the nonlinear term as given

by,

$$\chi = \left| \frac{r^2}{8} \frac{d^3 B_z}{ds^3} \cdot \left( \frac{dB_z}{ds} \right)^{-1} \right| \quad (2.25)$$

The normalised magnetic field and its first, second and third derivatives are shown in Fig. 2.3. It can be readily seen that the nonlinear terms are appreciable only at the both edges of the solenoid and the strengths are very small for higher order derivatives.

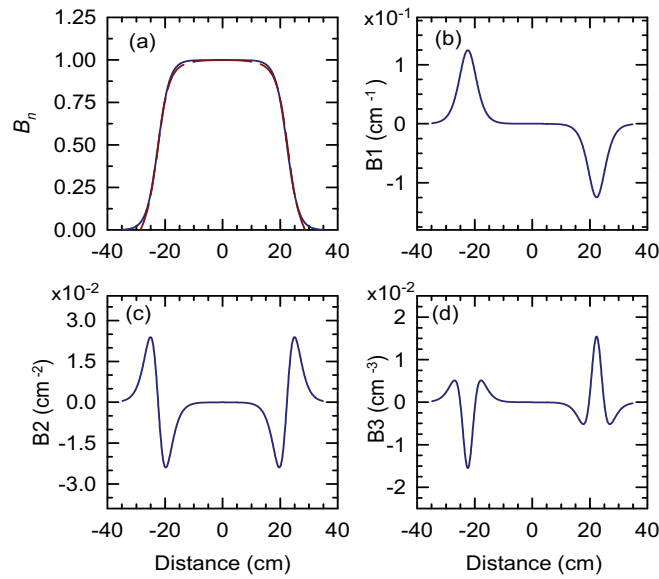


Figure 2.3: Variation of axial ( $r = 0$ ) (a) normalised axial magnetic field  $B_n$  of solenoid obtained from simulation (dotted) and analytical approximation (solid) (b) first  $B1 = dB_n/ds$ , (c) second  $B2 = d^2B_n/ds^2$ , and (d) third  $B3 = d^3B_n/ds^3$  derivatives along the length of the solenoid.

### 2.3.2 Vlasov Equilibrium in Misaligned Channel

In this subsection we compare the analytical results obtained in the previous section with the PIC simulation results. In Fig. 2.4(a) we have shown the evolution of beam centroid  $\langle x \rangle$  and  $\langle y \rangle$  as the beam propagates in the misaligned solenoids. The numerical solution to the beam centroid equations (solid curves) shows a good agreement with the self-consistent simulation result (dashed curves). The

input parameters are: beam current  $I = 10$  mA, normalized emittance  $\varepsilon_n = 0.8\pi$  mmmrad,  $\langle x \rangle = \langle y \rangle = 0$  and  $\langle x \rangle' = \langle y \rangle' = 0$ , the rms beam sizes  $X_{rms} = 1.25$  mm and  $Y_{rms} = 1.25$  mm at  $s = 0$ . The centre of solenoids S1 and S2 are located at 60 cm and 210 cm respectively. The peak values of the magnetic field of solenoids S1 and S2 are 3.035 kG and 2.883 kG respectively. The misaligned parameters of S1 are  $\Delta_x = 3$  mm,  $\Delta_y = -3$  mm,  $\theta_x = 0$  mrad,  $\theta_y = 0$  mrad and for S2 are  $\Delta_x = -5.225$  mm,  $\Delta_y = 5.225$  mm,  $\theta_x = -1.6$  mrad,  $\theta_y = 1.6$  mrad. Other important parameters for the numerical simulations are:  $N = 77000$ , step size along the axial direction  $\Delta s = 1$  mm,  $N_x = N_y = 128$ . Here we have assumed that the beam pipe is of square cross-section  $12.8$  cm  $\times$   $12.8$  cm.

It can be readily seen from Fig. 2.4(a) that initially the beam centroid which is aligned to the beam propagation axis, gets deviated from the ideal axis as it enters the dipole field region of the misaligned solenoid. The excursion of the centroid oscillation reaches to a very large value  $\sim 2$  cm at the second solenoid S2 for the chosen set of the parameters. Figure 2.4(b) shows the evolution of percentage change of rms beam emittances  $\varepsilon_{x_{rms}}$  and  $\varepsilon_{y_{rms}}$  as a function of drift length  $s$  obtained with PIC simulation for the cases of misaligned (dashed curves) and aligned (dotted curves) solenoids. It can be readily seen that the beam emittances are well conserved in the case of misaligned solenoids and the evolution of emittances is similar to the aligned solenoids. This confirms that the chosen K-V beam distribution function is the equilibrium distribution. The comparison of the rms beam envelope sizes shown in Fig. 2.4(c) indicates that there is hardly any difference in the evolution of the beam envelopes for the cases of misaligned and aligned solenoids. We also see that the beam envelopes are stable, though the beam centroid excursions along the beam line are very large. It is to be noted here that for the confinement of the beam both centroid

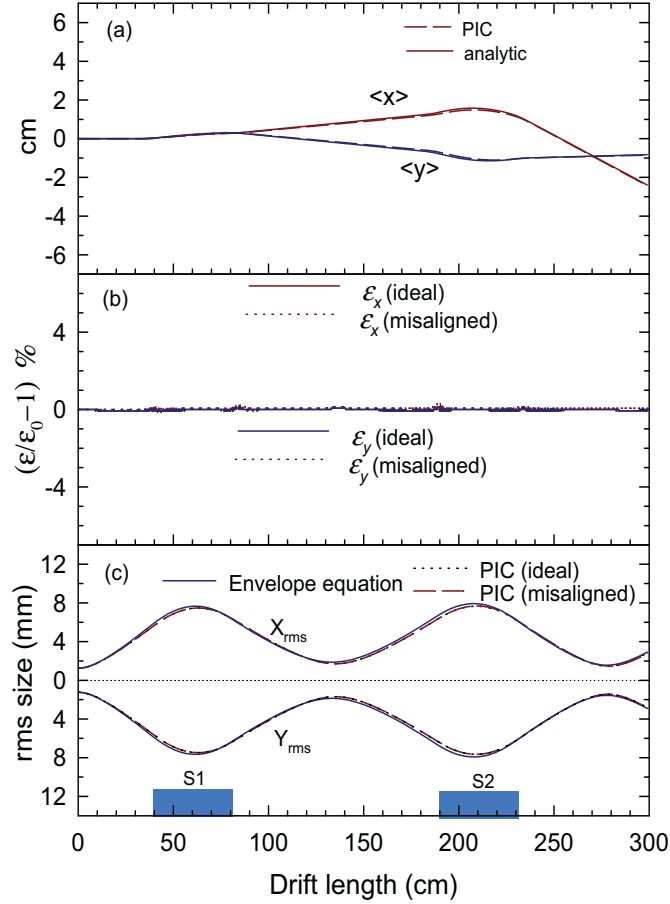


Figure 2.4: Plots show the evolution of (a) beam centroid  $\langle x \rangle$  and  $\langle y \rangle$  (b) percentage change in rms beam emittances and (c) rms beam sizes  $X_{rms}$  and  $Y_{rms}$  as a function of drift distance  $s$ .

and envelope have to be stable.

### 2.3.3 PIC Simulation in Aligned Solenoid System

In this subsection, we present the self-consistent particle-in-cell (PIC) simulation results carried out for the case of aligned solenoid transport system with different beam density distributions. In Fig. 2.5 we have shown the evolution of the rms envelopes and rms emittances for 10 mA with the same beam and transport parameters as used in Fig. 2.4. The beam is loaded initially according to five different distributions: K-V (KV), waterbag (WB), parabolic (PA), semi-

Gaussian (SG) and Gaussian (GA). It is readily seen from Fig. 2.5(a) that the variation of beam sizes along  $s$  is almost similar for all the distributions, indicating that evolution of the rms beam sizes is weakly dependent on the form of the initial beam distribution.

The evolution of emittance along the beam transport line is shown in Fig. 2.5(b). It is interesting to note that beam emittance for all the distributions except the K-V distribution shows an oscillating pattern and there is an overall increase in the emittance, more for Gaussian and semi-Gaussian distributions. The emittance increases in the initial part of the beam line, reaches its first maximum at  $s \sim 112$  cm just before the first waist, decreases with  $s$  and again starts increasing for all the distributions and reaches to maximum before the second waist. The reduction in the emittance for the semi-Gaussian distribution between the region  $s = 0$  to  $s = 40$  cm is not surprising because emittance can decrease during the relaxation.

In order to investigate the effect of nonlinear terms of solenoid fields on the emittance growth, we have compared the simulations with and without including the nonlinear term (as given in Eq. (2.1)). We did not observe any appreciable difference between the two cases. The third order nonlinear term is strong only in the fringe region near the edges of the solenoids (shown in Fig. 2.4(d)) where the beam size is  $\sim 1.5$  cm. In the fringe field region the maximum value of parameter  $\chi$ , the ratio of the nonlinear over linear term is only  $\sim 0.035$  which means the nonlinear force experienced by a particle at such radius is at most,  $\sim 3.5\%$  of the linear focussing force. The effect of nonlinearity of solenoid field on the emittance growth is thus negligibly small for the present case. Therefore emittance growth during transport is mainly an effect of the nonlinear beam space charge. Emittance growth is seen to be greater in the converging part of the beam, where the strength of nonlinear

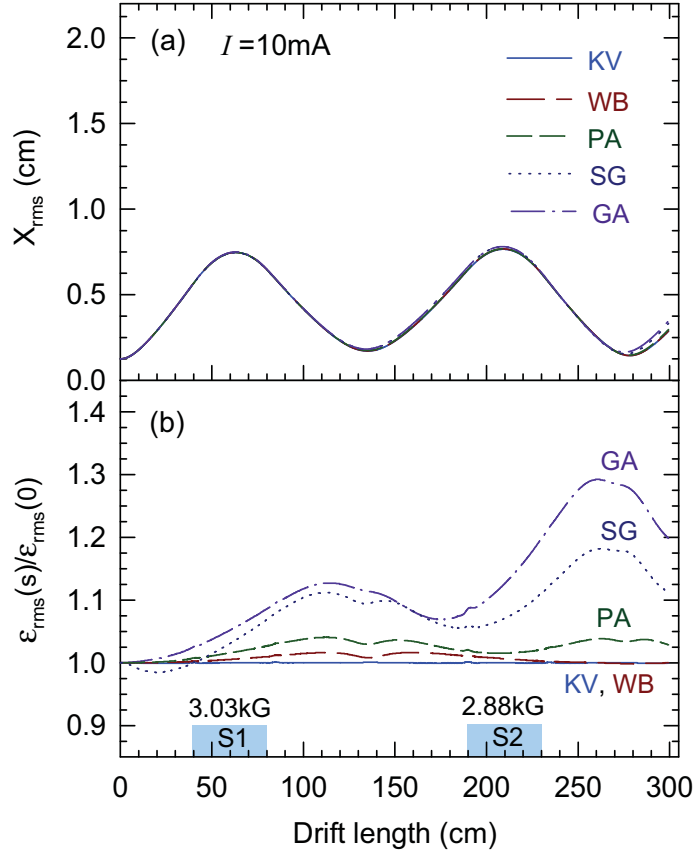


Figure 2.5: Evolution of (a) rms beam size  $X_{rms}(s)$  and (b) ratio of rms emittance  $\varepsilon_{rms}(s)/\varepsilon_{rms}(0)$  in Larmor frame as a function of drift length  $s$  using the self-consistent particle-in-cell method for five different initial distributions K-V (KV), waterbag (WB), parabolic (PA), semi-Gaussian (SG) and Gaussian (GA) of the beam.

space-charge term is more. The maximum emittance occurs at  $s = 270$  cm and the ratios  $\varepsilon_{rms}(270)/\varepsilon_{rms}(0)$  are 1.3, 1.175 and 1.05 for Gaussian, semi-Gaussian and parabolic distributions respectively.

In Fig. 2.6 the evolution of rms beam size and rms emittance is compared for axisymmetric and non-axisymmetric beam with  $I = 10$  mA. The initial beam distribution is Gaussian with following input conditions (i) axisymmetric  $X_{rms}(0) = Y_{rms}(0) = 0.125$  cm and  $\varepsilon_{x_{rms}}(0) = \varepsilon_{y_{rms}}(0) = 13\pi$  mmmrad, (ii) non-axisymmetric  $X_{rms}(0) = 0.125$  cm,  $Y_{rms}(0) = 0$ ,  $\varepsilon_{x_{rms}}(0) = 13\pi$  mmmrad

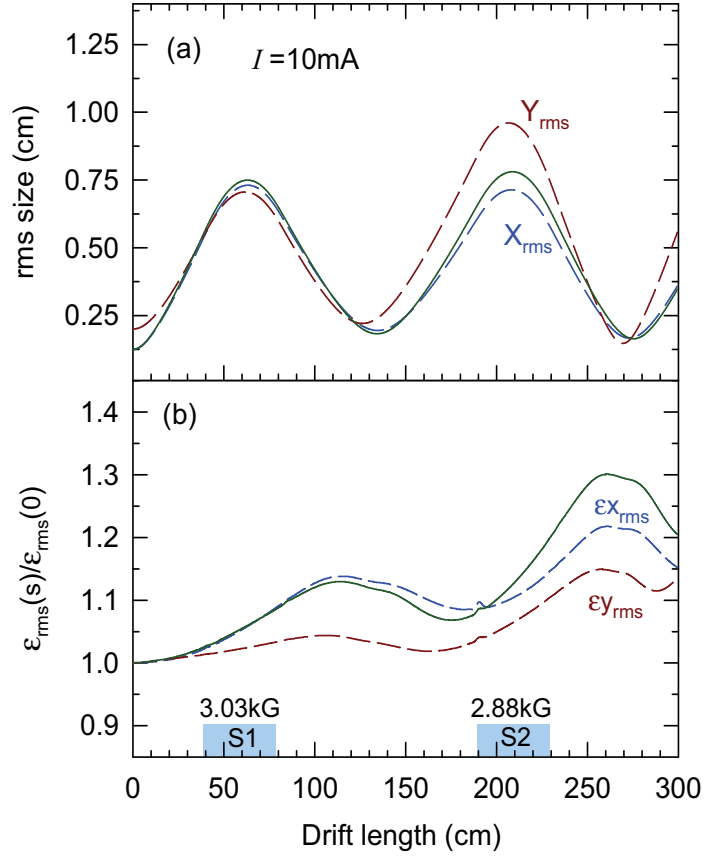


Figure 2.6: Evolution of rms beam size and rms emittance in Larmor frame for axisymmetric (solid) and non-axisymmetric (dashed) beam with Gaussian distribution. The input parameters are: (i) axisymmetric:  $X_{rms}(0) = Y_{rms}(0) = 0.125$  cm and  $\epsilon x_{rms}(0) = \epsilon y_{rms}(0) = 13\pi$  mmmrad, (ii) non-axisymmetric:  $X_{rms}(0) = 0.125$  cm,  $Y_{rms}(0) = 0.2$  cm,  $\epsilon x_{rms}(0) = 13\pi$  mmmrad and  $\epsilon y_{rms}(0) = 19.5\pi$  mmmrad.

and  $\epsilon y_{rms}(0) = 19.5\pi$  mmmrad. In the case of axisymmetric beam the behaviour of beam size and emittance in both the  $x$  and  $y$  planes is similar as shown by solid curve. It is interesting to note that in the case of non-axisymmetric beam the emittance growth is more in the plane where the beam envelope size is small and vice-versa. Initially the beam size and beam emittance in  $x$  plane follows the same behaviour as in the case of axisymmetric case however, as the beam leaves the first solenoid where the beam starts converging, the behaviour is changed. This is due to the inter plane coupling effect triggered by the beam

space-charge force. We also see that there is an exchange of emittance from one plane to the other plane in the case of non-axisymmetric beam which is common to the coupled motions.

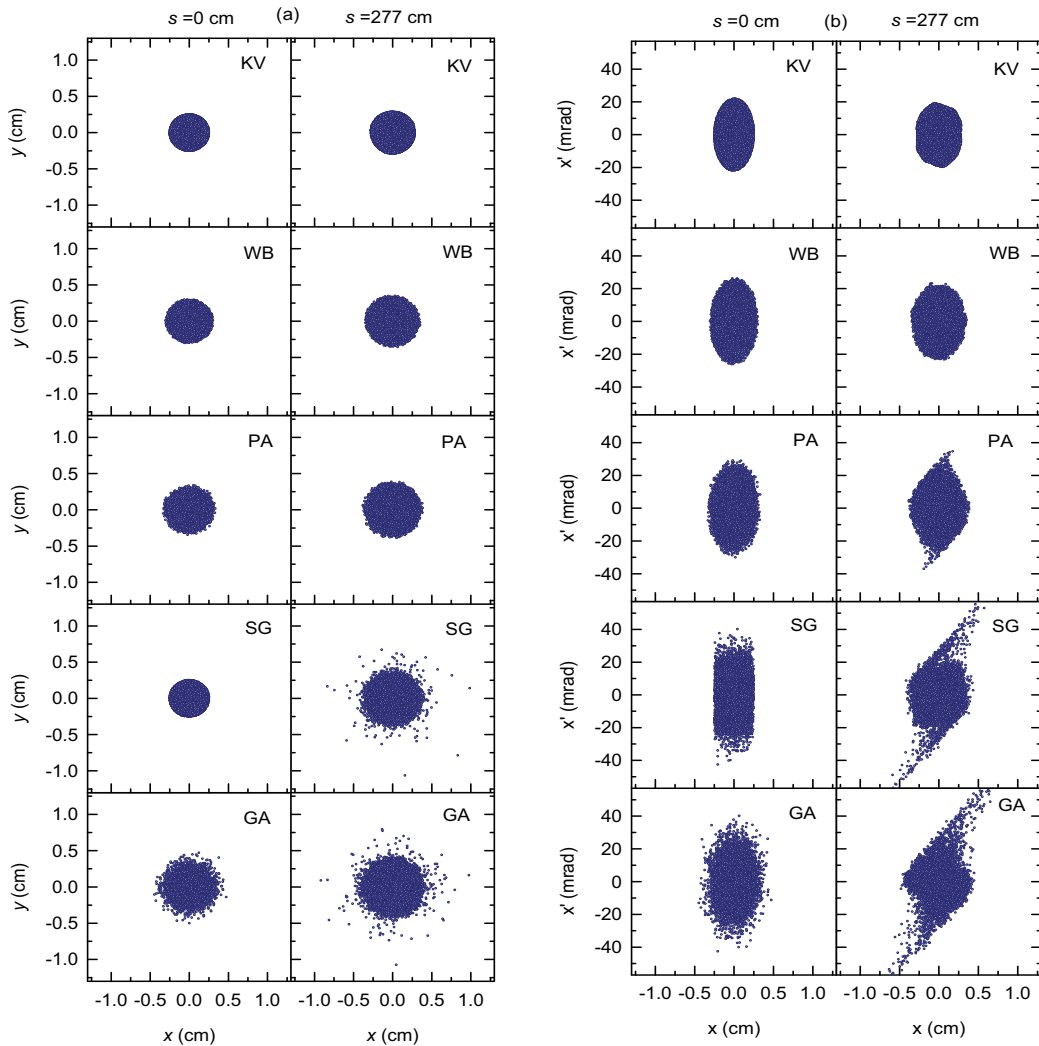


Figure 2.7: Plots of transverse (a) real space  $(x, y)$  and (b) phase space  $(x, x')$  of the beam at locations  $s = 0$  cm and  $s = 277$  cm for five initial distributions K-V (KV), waterbag (WB), parabolic (PB), semi-Gaussian (SG), and Gaussian (GA).

The distributions of beam in the real space and phase space in the transverse plane at the two locations  $s = 0$  and  $s = 277$  cm obtained by performing simulations with 10000 macroparticles for five different initial distributions K-V (KV), waterbag (WB), parabolic (PA), semi-Gaussian (SG) and Gaussian

(GA) are shown in Fig. 2.7. In this case both the solenoids are aligned with the beam propagation axis and other beam parameters are same as used in Fig. 2.5. From the simulation results we see that K-V and waterbag distributions yield almost similar real and phase space distributions at the final location. In the case of parabolic distribution where the beam density is non-uniform, it is easy to notice a slight deformation in the phase space and diffusion of particles in the outer region of the real space. The simulation results of semi-Gaussian and Gaussian distributions show a redistribution of the beam with large distortion in the phase space together with generation of many halo particles. We believe that such kind of behaviour is mainly caused by the nonlinear space-charge force which is stronger in these cases compared to the parabolic distribution.

### 2.3.4 PIC Simulation in Misaligned Solenoid System

In order to investigate the effect of misalignment of solenoid magnets on the beam dynamics, we have used various values of misalignment parameters of solenoids. Here we have studied the motion of centroid and the behaviour of beam envelopes around the centroid. Simulation results are shown in Fig. 2.8 to Fig. 2.12. The evolution of the centroid displacements  $x_0 = \langle x \rangle$  and  $y_0 = \langle y \rangle$  from the ideal beam axis has been calculated from the macroparticles positions  $x$  and  $y$ , where brackets indicate average over the distribution of macroparticles. We have considered three different sets of misalignment parameters of solenoids  $[\Delta_x(\text{mm}), \Delta_y(\text{mm}), \theta_x(\text{mrad}), \theta_y(\text{mrad})]$ : (i)  $[2, -2, 0, 0]$  for S1 and  $[0, 0, 0, 0]$  for S2, (ii)  $[5, 0, 0, 0]$  for S1 and  $[0, 0, 0, 0]$  for S2, (iii)  $[2, 2, 20, 0]$  for S1 and  $[2, 2, 20, 0]$  for S2.

Figure 2.8 shows the comparison of beam centroid motion  $x_0, y_0$  for different sets of misaligned parameters. We performed the simulation with all the five distributions and observed that the motion of centroid for a given set of mis-

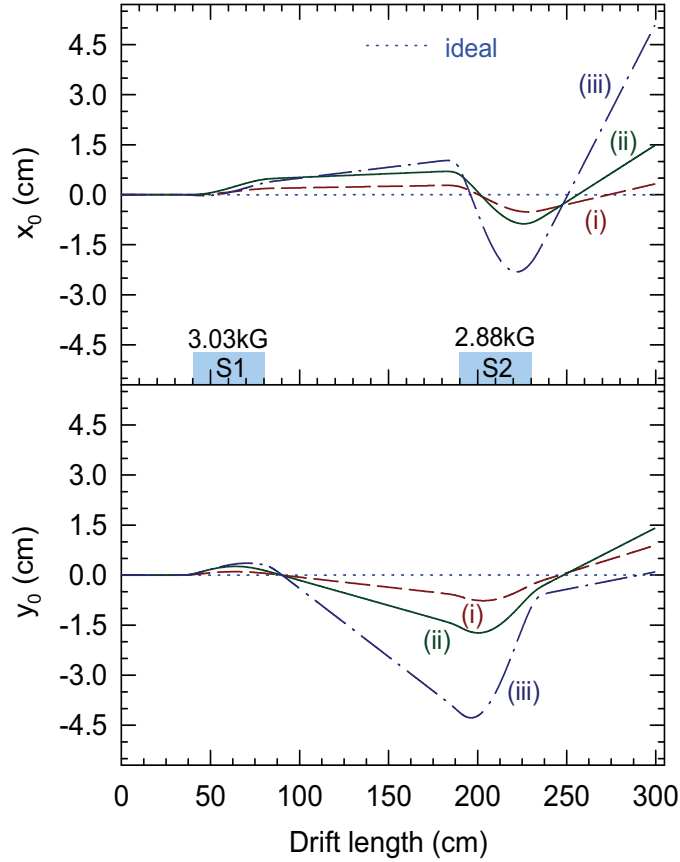


Figure 2.8: Evolution of the beam centroid  $\langle x \rangle$  and  $\langle y \rangle$  in laboratory frame using self-consistent model in the case of initial K-V distribution for four different cases: ideal  $[0, 0, 0, 0]$  for S1 and  $[0, 0, 0, 0]$  for S2, case (i)  $[2, -2, 0, 0]$  for S1 and  $[0, 0, 0, 0]$  for S2, case (ii)  $[5, 0, 0, 0]$  for S1 and  $[0, 0, 0, 0]$  for S2, case (iii)  $[2, 2, 20, 0]$  for S1 and  $[2, 2, 20, 0]$  for S2. Centroid motion for a given set of misalignment is independent of beam distribution.

aligned parameter is independent of the form of the initial beam distribution. It is easy to see from the figure that even for a small misalignment (case (ii)) the centroid oscillation amplitude reaches upto 1.5 cm at the end of the beam line. When the misalignment is large (case (iii)), the centroid motion is unstable and its value reaches to more than 4.5 cm at the end of the beam line. Any further transport of the beam without any control of the centroid motion leads to the loss of the whole beam on the beam pipe. The simulation was also done with and without including the higher order nonlinear field of the solenoid as

expressed in Eqs. (2.1) and we found no appreciable effect on the motion of centroid. This may be due to the small strength of nonlinear terms in the case of our solenoids as mentioned earlier.

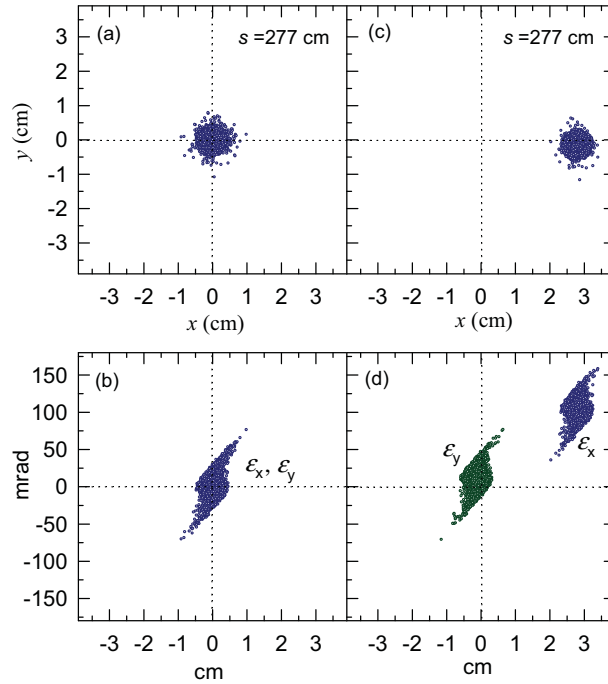


Figure 2.9: Real space and phase space distributions of initial 10 mA beam with Gaussian distribution at the second waist ( $s = 277$  cm) in the case (a), (b) aligned and (c), (d) misaligned solenoids of case (iii)  $[2, 2, 20, 0]$  for  $S1$  and  $[2, 2, 20, 0]$  for  $S2$ .

Figure 2.9 shows the real space and phase space distributions of initial 10 mA beam with Gaussian distribution at the second waist ( $s = 277$  cm) for aligned and misaligned solenoids. In Figs. 2.9(a) and 2.9(b) we have shown the beam behaviour in the case of aligned solenoids where both real space and phase space distributions are centered around the ideal beam propagation axis. The distribution in  $y - y'$  phase plane is similar as shown for  $x - x'$  plane. In Figs. 2.9(c) and 2.9(d), we have plotted the real space  $x - y$  distribution and phase space distribution in  $x - x'$  and  $y - y'$  planes for misaligned solenoids with parameters stated in case (iii). As obvious, the beam distribution is centred

around the location of the centroid at  $s = 277$  cm. We also see that real space and phase space distributions in this case are different mainly in the outer region due to the formation of halo and loss of the particles. A detailed analysis shows a loss of beam particles  $\sim 0.6\%$  in the present case of misaligned solenoids.

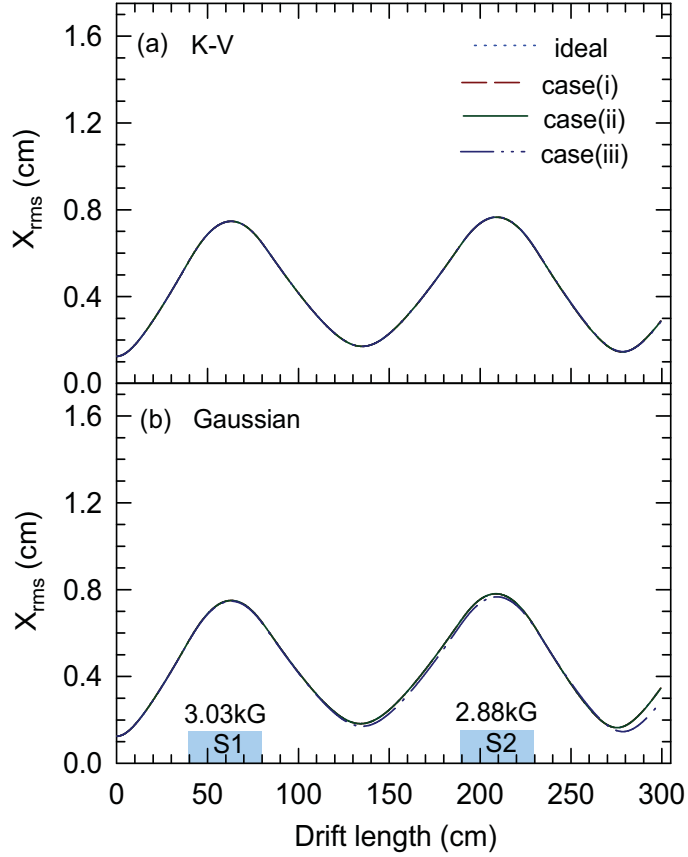


Figure 2.10: Evolution of rms beam envelope  $X_{rms}$  in Larmor frame around the centroid with drift length  $s$  in the case of misaligned solenoids for (a) K-V and (b) Gaussian distributions. Misalignment parameters are: ideal  $[0, 0, 0, 0]$  for S1 and  $[0, 0, 0, 0]$  for S2, case(i)  $[2, -2, 0, 0]$  for S1 and  $[0, 0, 0, 0]$  for S2, case(ii)  $[5, 0, 0, 0]$  for S1 and  $[0, 0, 0, 0]$  for S2, case(iii)  $[2, 2, 20, 0]$  for S1 and  $[2, 2, 20, 0]$  for S2.

The evolution of beam envelopes around the centroid for K-V and Gaussian distributions for various values of misalignment parameters is compared in Fig. 2.10. It can be readily seen that the beam envelope around the centroid is independent of the misalignment parameters in the case of K-V distribution.

For the Gaussian distribution there is a slight change in the envelope behavior for case (iii). It is interesting to note here that the evolution of envelope for both the distribution is independent of the centroid motion. This fact is also supported by the simulation result of case (iii) where we see that envelope is stable, although the centroid motion is unstable. The evolution of envelopes is also checked with other distributions and the envelope behavior is found almost identical when the misaligned parameters are small. We have also evaluated

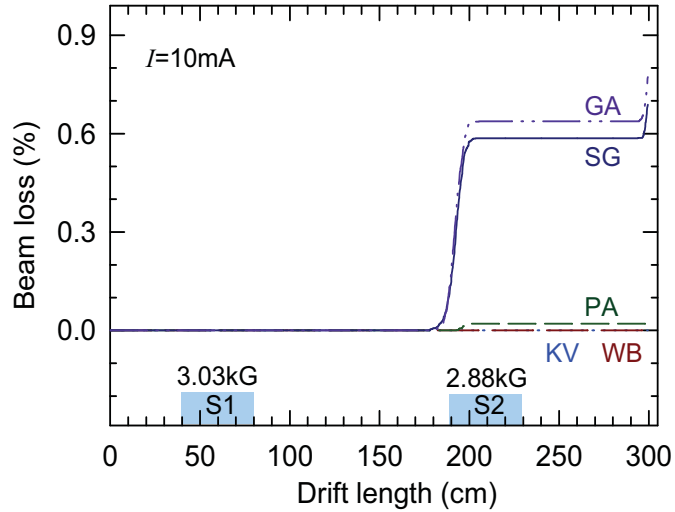


Figure 2.11: *Beam loss as a function of drift length  $s$  for five distributions with misalignment parameters of case (iii):  $[2, 2, 20, 0]$  for S1 and  $[2, 2, 20, 0]$  for S2.*

the percentage of beam loss as a function of drift distance  $s$  for various beam distributions using the misaligned parameters of case (iii)  $[2, 2, 20, 0]$  for S1 and  $[2, 2, 20, 0]$  for S2. Results shown in Fig. 2.11 indicate that beam loss is very small for KV, WB and PA distributions. However in the case of GA and SG distributions, the loss increases rapidly from  $s = 180$  cm to  $s = 200$  cm and saturates to a value of  $\sim 0.6\%$  in the case of GA distribution and  $\sim 0.55\%$  in the case of SG distribution. We believe that this loss is mainly due to the nonlinear space-charge force that generates more number of halo particles (see

Fig. 2.7). These halo particles ultimately hit the beam pipe when the centroid excursion is large from the symmetry axis.

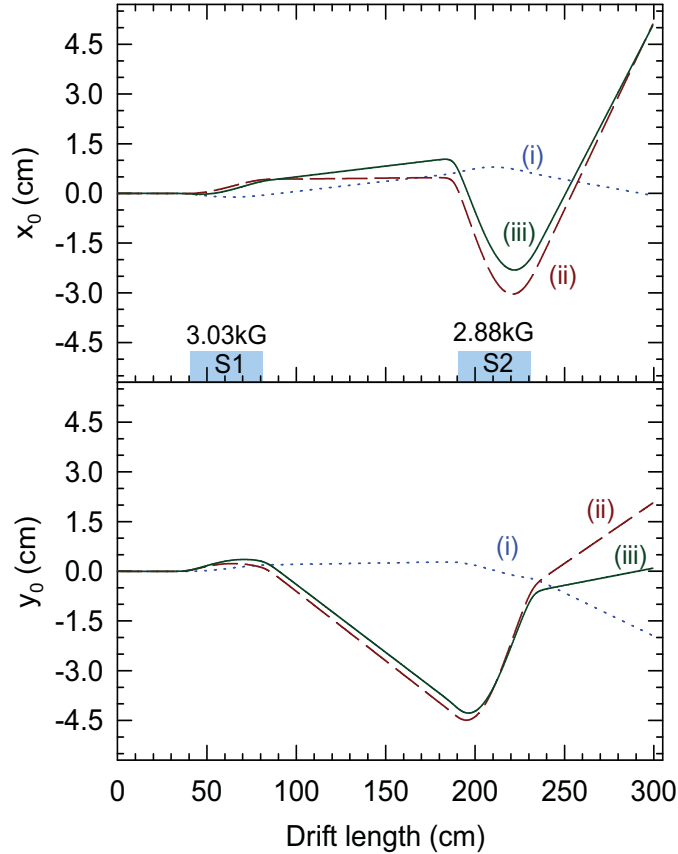


Figure 2.12: Evolution of the beam centroid in the laboratory frame for different misalignment parameters set (i)  $[0, 2, 0, 0]$  for S1 and  $[2, 0, 20, 0]$  for S2, set (ii)  $[2, 0, 20, 0]$  for S1 and  $[2, 0, 0, 0]$  for S2, set (iii)  $[2, 2, 20, 0]$  for S1 and  $[2, 2, 20, 0]$  for S2.

In order to control the centroid motion and beam oscillations generally steering magnets are used in the beam transport lines. For low beam current methodology applied is as follows. First the actual solenoid misaligned parameters are evaluated using the experimental measurement of the centroids at different locations in the beam line. Then centroid are manipulated using dipole steering field. This procedure is based on the fact that the resultant of several misalignments can be obtained by using the superposition principle [34]. In order to

show that such superposition is also valid for the case of space-charge-dominated beam, the PIC simulation is performed with following three sets of misaligned solenoids: set (i):  $[0, 2, 0, 0]$  for S1 and  $[2, 0, 20, 0]$  for S2, set (ii):  $[2, 0, 20, 0]$  for S1 and  $[2, 0, 0, 0]$  for S2, set (iii):  $[2, 2, 20, 0]$  for S1 and  $[2, 2, 20, 0]$  for S2. Here set (iii) is the resultant which combines the misalignments of set (i) and set (ii). From the simulation results shown in Fig. 2.12, it is seen that at any location  $s$  the value  $\mathbf{x}_1(s) + \mathbf{x}_2(s) = \mathbf{x}_3(s)$  where  $\mathbf{x}_1(s) = (x_1, y_1)$ ,  $\mathbf{x}_2(s) = (x_2, y_2)$  and  $\mathbf{x}_3(s) = (x_3, y_3)$  are the coordinates of centroid at location  $s$  obtained with misaligned set (i), set (ii) and set (iii). The results indicate that the superposition method is also valid here. The method developed in Ref. [34] to control the centroid motion due to misalignment can also be utilised in the case of space-charge-dominated beam with small centroid excursion.

## 2.4 Summary and Discussion

To summarize, we have derived equations of motion for the centroid of the beam in the Larmor frame in terms of focussing strength and misaligned parameters of the solenoid magnets using nonlinear Vlasov-Maxwell equation. We have constructed a self-consistent Vlasov equilibrium for the case of uniform density beam moving in a misaligned solenoidal focussing channel. It has been shown that the beam envelope obeys the familiar envelope equation, independent of the centroid motion and the misaligned parameters of the magnet. The self-consistent PIC simulation supports the analytical results.

A self-consistent PIC model has been utilized to study the dynamics of space-charge-dominated beam through aligned and misaligned solenoid based transport system. In the case of aligned solenoids, it is shown that the evolution of the rms beam sizes is weakly dependent on the form of the initial beam distribution. It is observed that the growth in the emittance is more in the

converging region of the beam where the strength of nonlinear space-charge term is comparatively more. There is an exchange of emittance from one plane to the other plane when the initial beam is non-axisymmetric.

In the case of misaligned solenoids, the simulation results with different distributions indicate that the motion of centroid is independent of the beam distribution. It is shown that the beam envelope around the centroid obeys the familiar envelope equation, and is independent of the centroid motion for small centroid oscillation. For large misalignment, particularly tilt, the envelope evolution depends on the form of beam distribution. It is also found that the envelope is stable although the centroid motion is unstable. Large excursion of centroid without any control leads to the loss of the beam on the beam pipe particularly in the case of nonuniform beam distribution. This reveals the importance of centroid motion to the overall beam confinement properties.

# Chapter 3

## Dynamics of Multispecies Beam in the LEBT System

### 3.1 Introduction

One of the earliest works on the beam envelope equations for transverse motion of intense charged particle beams having elliptical cross section and uniform density are the well known Kapchinskij-Vladimirskij (K-V) equations [17]. Later Sacherer and Lapostolle extended the work for the elliptically symmetric more general beam density profile [15, 20, 21]. However, the above mentioned equations are valid only when the beam contains particles of same species (electron or single ion).

Beam transport presents major difficulties in the cases when the beam contains more than one species. For example, the typical value of the proton fraction from the microwave ion sources is of the order of 80 - 85% of the extracted beam [51, 52, 53]. The other major unwanted components in the beam are  $H_2^+$  and  $H_3^+$ . The effect of unwanted species has to be taken into account for the matching of primary species which is very important in limiting the generation of beam halo [41, 42, 43, 44, 45] and particle losses.

In this chapter equations for the beam envelope of a cylindrically symmet-

ric space-charge-dominated multispecies beam transported through a solenoid based beam transport line are derived [49]. We have also discussed the beam selection using slits in the beam line. In the envelope equations, only the effective values of the current and emittance of each species are considered after the slit for further transport in case the radius of any species is larger than the slit.

The envelope model gives a good description about the evolution of beam sizes of different species and helps in quick optimisation of beam line parameters. However, it does not provide any information about the behaviour of beam distribution and emittance growth caused due to nonlinear effects during the transport. In order to investigate more deeply the dynamics of multispecies beam, the self-consistent PIC simulation has been performed. We have studied the emittance growth of the primary species due to other unwanted species present in the beam for various beam parameters. The real and phase space distributions of all the species are investigated with and without placing a slit in the beam line. It is observed that there is a formation of beam hollows of unwanted species which are produced due to nonlinear space-charge effect. The selection of the primary species has been carried out and it is shown that the rejection of unwanted species is very effective when one places the slit after the hollow formation of unwanted species. The numerical simulation result of the transport of protons from 2.45 GHz microwave ion source in the presence of  $H_2^+$ ,  $H_3^+$  species has been presented for various values of the total beam current and different fractions of  $p$ ,  $H_2^+$ ,  $H_3^+$  species.

## 3.2 Envelope Model for Multispecies Beam

In this section, we derive the differential equation for the envelope of multispecies beam propagating through a solenoid based beam transport system. It is assumed that beam is axisymmetric and the density distributions of all the

species are uniform.

### 3.2.1 Space Charge Field

We consider a thin, axisymmetric continuous intense multispecies charged particles beam propagating through the drift space and applied focussing fields. We use  $s = z$  as the axial coordinate measuring the distance along beam axis and  $r = \sqrt{x^2 + y^2}$  as the radial distance from the beam axis. In order to determine the self-electric and self-magnetic fields of the beam, we consider the density profile of different species of the beam to be uniform so that [18]

$$n_j(r, s) = \begin{cases} N_j / (\pi r_j^2(s)) & 0 < r \leq r_j(s) \\ 0 & r > r_j(s) \end{cases} \quad (3.1)$$

where  $r_j(s)$  is the beam radius of species  $j$  and  $N_j$  ( $N_j = \int_0^\infty n_j(r, s) 2\pi r dr$ ) is the number of particles of species  $j$  per unit axial length. In order to develop the equation of motion for individual test particles, the paraxial approximation has been used. In this approximation the Budker parameter of the beam is very small compared with unity i.e.,  $(q_j^2 N_j) / (m_j c^2) \ll 1$ , the beam is thin and the transverse kinetic energy of the particles is small compared to the axial kinetic energy i.e.,  $vx_j^2 + vy_j^2 \ll vz_j^2 \approx \beta_j^2 c^2$ . Here,  $c$  is the speed of light in vacuum,  $q_j, m_j$  are the charge and rest mass of species  $j$  respectively.  $\beta_j$  is the relativistic parameter for particle of species  $j$ . The scalar potential  $\phi_j^{sc}$  for the self-electric field can be obtained from Poisson's equation

$$\left( \frac{\partial^2}{\partial x^2} + \frac{\partial^2}{\partial y^2} \right) \phi_j^{sc}(x, y, s) = -\frac{q_j n_j(r, s)}{\epsilon_0} \quad (3.2)$$

Since we have assumed that beam is cylindrically symmetric, we can easily solve Eq. (3.2) in the cylindrical coordinate system with boundary condition  $\phi^{sc} = 0$  at  $r = b$  ( $b$  is the radius of beam pipe), and the solution is [15]

$$\phi_j^{sc}(r, s) = \begin{cases} \frac{q_j N_j}{4\pi\epsilon_0} \left( 1 + 2 \ln \frac{b}{r_j(s)} - \frac{r^2}{r_j^2(s)} \right) & \text{for } r \leq r_j(s) \\ \frac{q_j N_j}{2\pi\epsilon_0} \ln \frac{b}{r} & \text{for } r_j(s) < r \leq b \end{cases} \quad (3.3)$$

### 3.2.2 Single Particle Equation

The total force acting on a particle can be obtained by adding the external forces and the self-electric and magnetic forces due to all the components of the beam. The  $x$ -component of force on a particle of species  $j$  can be written as,

$$Fx_j = Fx_j^{ext} + Fx_j^{sc} \quad (3.4)$$

$Fx_j^{sc}$  is the force due to self-electric and magnetic fields of all the components of the beam and is given by

$$Fx_j^{sc} = q_j (Ex_j^{sc} - \beta_j c By_j^{sc}) + q_j \sum_{\substack{k=1 \\ k \neq j}}^n (Ex_k^{sc} - \beta_j c By_k^{sc}) \quad (3.5)$$

In Eq. (3.5) the first term on the right side represents the force due to  $j^{th}$  species whereas the summation term represents forces due to all other species  $k$ . Here  $n$  is the total number of species present in the beam. After simplification we have,

$$Fx_j^{sc} = q_j (1 - \beta_j^2) Ex_j^{sc} + q_j \sum_{\substack{k=1 \\ k \neq j}}^n (1 - \beta_j \beta_k) Ex_k^{sc} \quad (3.6)$$

The equation of motion for a particle of species  $j$  can be written as,

$$\gamma_j m_j \beta_j^2 c^2 x'' = Fx_j^{ext} + \frac{q_j Ex_j^{sc}}{\gamma_j^2} + q_j \sum_{\substack{k=1 \\ k \neq j}}^n (1 - \beta_j \beta_k) Ex_k^{sc} \quad (3.7)$$

in which the differentiation is with respect to the axial distance  $s$  and  $\gamma_j$  is the usual relativistic term for species  $j$ . The expression for  $Ex_j^{sc}$  can be obtained from Eq. (3.3) as

$$Ex_j^{sc} = \begin{cases} \frac{I_j}{2\pi\epsilon_0\beta_j cr_j^2} \cdot x & \text{for } |x| \leq r_j(s) \\ \frac{I_j}{2\pi\epsilon_0\beta_j c} \cdot \frac{x}{r^2} & \text{for } |x| > r_j(s) \end{cases} \quad (3.8)$$

where  $I_j$  is the current due to species  $j$  of the beam. The total current of the beam is simply the sum of the currents due to all the components i.e.

$$I = \sum_{j=1}^n I_j.$$

The equation of motion for a particle of species  $j$  can be written as,

$$\begin{aligned} \gamma_j m_j \beta_j^2 c^2 x'' &= F x_j^{ext} + \frac{q_j I_j}{2\pi \epsilon_0 c \beta_j \gamma_j^2 r_j^2} x \\ &+ q_j \sum_{\substack{k=1 \\ k \neq j}}^n \left[ (1 - \beta_j \beta_k) \frac{I_k}{2\pi \epsilon_0 c \beta_k} \left( \frac{x}{r_k^2} \Theta(r_k - r) + \frac{x}{r^2} \Theta(r - r_k) \right) \right] \end{aligned} \quad (3.9)$$

in which  $\Theta(y)$  is the Heaviside step function with the property  $\Theta(y) = 1$  for  $y \geq 0$  and  $\Theta(y) = 0$  for  $y < 0$ . Rearranging above equation we have

$$x'' = g x_j^{ext} + a_j \frac{x}{r_j^2} + \sum_{\substack{k=1 \\ k \neq j}}^n b_{jk} \left( \frac{x}{r_k^2} \Theta(r_k - r) + \frac{x}{r^2} \Theta(r - r_k) \right) \quad (3.10)$$

with  $a_j = \frac{q_j I_j}{2\pi \epsilon_0 m_j \beta_j^3 \gamma_j^3 c^3}$ ,  $g x_j^{ext} = \frac{F x_j^{ext}}{m_j \gamma_j \beta_j^2 c^2}$ ,  $b_{jk} = \frac{q_j (1 - \beta_j \beta_k) I_k}{2\pi \epsilon_0 m_j \beta_j^2 \gamma_j \beta_k c^3}$ .

### 3.2.3 Equation of Motion in the Larmor Frame

In the present analysis we consider that the external field is generated by the solenoid magnets only. The solenoid focusing field in the paraxial limit can be approximated by [54]

$$B^{ext}(r, s) = B_z(s) \hat{e}_z - \frac{r}{2} B'_z(s) \hat{e}_r$$

which yields the expression for  $g x_j^{ext}$  as [55]

$$g x_j^{ext} = k l'_j(s) y + 2 k l_j(s) y' \quad (3.11)$$

where,  $k l_j(s) = q_j B_z(s) / (2 m_j \gamma_j \beta_j c)$ . For solenoid focussing, the coupled form of the equations of motion causes a macroscopic rotation of the beam about the longitudinal axis. These equations take a simpler form in the Larmor frame which rotates at Larmor frequency with respect to the laboratory frame. The coordinates  $x_L, y_L$  in the Larmor frame can be obtained from coordinates  $x, y$  by a rotation of laboratory frame through Larmor angle  $\theta(s)$  about the  $z$  axis. The

rotation angle will be different for different species of the beam. If we denote the rotation for species  $j$  by  $\theta_j(s)$ , then we can write the relation between the coordinates of two frames as [16, 55]

$$x_L(s) = x(s) \cos \theta_j(s) + y(s) \sin \theta_j(s) \quad (3.12a)$$

$$y_L(s) = -x(s) \sin \theta_j(s) + y(s) \cos \theta_j(s) \quad (3.12b)$$

The rotation angle  $\theta_j(s)$  is given by

$$\theta_j(s) = - \int_{s_i}^s kl_j(s') ds' \quad (3.13)$$

Consistent with this Larmor transform, the divergences  $x'(s)$  and  $y'(s)$  transform as [55]

$$x'_L(s) = x'(s) \cos \theta_j + y'(s) \sin \theta_j + kl_j(s) (x(s) \sin \theta_j - y(s) \cos \theta_j) \quad (3.14a)$$

$$y'_L(s) = -x'(s) \sin \theta_j + y'(s) \cos \theta_j + kl_j(s) (x(s) \cos \theta_j + y(s) \sin \theta_j) \quad (3.14b)$$

Using these transformation relations and dropping the suffix in  $x_L$  for simplicity i.e.  $x_L \rightarrow x$ , the equation of motion of species  $j$  in the Larmor frame can be written as

$$x'' = -kl_j^2(s)x + a_j \frac{x}{r_j^2} + \sum_{\substack{k=1 \\ k \neq j}}^n b_{jk} \left( \frac{x}{r_k^2} \Theta(r_k - r) + \frac{x}{r^2} \Theta(r - r_k) \right) \quad (3.15)$$

where  $r^2 = x^2 + y^2 = x_L^2 + y_L^2$ . We have a similar equation for  $y$  motion also.

### 3.2.4 Beam Envelope Equation

In order to analyse the behaviour of the beam with any arbitrary distribution during the transport, it is more appropriate to use the rms quantities. Multiply the Eq. (3.15) by  $x$  and averaging over the distribution of species  $j$ , we obtain

$$\overline{xx''} + kl_j^2(s)\overline{x^2} - a_j \frac{\overline{x^2}}{r_j^2} - \sum_{\substack{k=1 \\ k \neq j}}^n b_{jk} \left( \overline{\frac{x^2}{r_k^2} \Theta(r_k - r)} + \overline{\frac{x^2}{r^2} \Theta(r - r_k)} \right) = 0 \quad (3.16)$$

with  $j = 1, 2, \dots, n$ . where  $\overline{x^2} = \frac{\int \int x^2 f_j(\mathbf{r}, \mathbf{p}, s) d\mathbf{r} d\mathbf{p}}{\int \int f_j(\mathbf{r}, \mathbf{p}, s) d\mathbf{r} d\mathbf{p}}$  and similar for other quantities.

Now we have the following relations [15]

$$\begin{aligned}\tilde{x}^2 &= \overline{x^2}, & \tilde{x}'^2 &= \overline{x'^2} \\ (\overline{x^2})' &= 2\overline{xx'} = (\tilde{x}^2)' = 2\tilde{x} \cdot \tilde{x}' \\ (\overline{x^2})'' &= (\tilde{x}^2)'' = 2(\tilde{x} \cdot \tilde{x}')' = 2(\tilde{x} \cdot \tilde{x}'' + \tilde{x}'^2)\end{aligned}$$

where tilde  $\sim$  indicates the rms quantities. Furthermore,

$$\begin{aligned}(\overline{xx'})' &= \overline{x'^2} + \overline{x \cdot x''} \\ &= \overline{x'^2} - kl_j^2(s)\overline{x^2} + a_j \frac{\overline{x^2}}{r_j^2} + \sum_{\substack{k=1 \\ k \neq j}}^n b_{jk} \left( \overline{\frac{x^2}{r_k^2} \Theta(r_k - r)} + \overline{\frac{x^2}{r^2} \Theta(r - r_k)} \right) = 0\end{aligned}\tag{3.17}$$

Using above relations and rearranging the terms of Eq. (3.17) we have

$$\tilde{x}'' + kl_j^2(s) \frac{\overline{x^2}}{\tilde{x}} - a_j \frac{\overline{x^2}}{r_j^2 \tilde{x}} - \frac{1}{\tilde{x}} \sum_{\substack{k=1 \\ k \neq j}}^n b_{jk} \left( \overline{\frac{x^2}{r_k^2} \Theta(r_k - r)} + \overline{\frac{x^2}{r^2} \Theta(r - r_k)} \right) - \frac{\tilde{\varepsilon}_j^2(s)}{\tilde{x}^3} = 0\tag{3.18}$$

In Eq. (3.18),  $\tilde{\varepsilon}_j(s)$  is the rms emittance of species  $j$  of the beam defined as,

$$\tilde{\varepsilon}_j^2(s) = \overline{x^2} \cdot \overline{x'^2} - \overline{xx'^2}\tag{3.19}$$

In order to find out the beam size of all the components of the beam, we need to calculate the average values of Eq. (3.18) and the evolution of the beam emittance along the transport line for each species. In the present envelope model we have used a fixed shape uniform density profile for all the species to study the behaviour of the beam keeping the emittance term constant. Substituting these average values and using  $\overline{x^2} = \tilde{x}^2$  in Eq. (3.18) we obtain

$$\tilde{x}'' + kl_j^2(s) \frac{\overline{x^2}}{\tilde{x}} - a_j \frac{\overline{x^2}}{r_j^2 \tilde{x}} - \frac{1}{\tilde{x}} \sum_{\substack{k=1 \\ k \neq j}}^n b_{jk} (f(r_j, r_k) + g(r_j, r_k)) - \frac{\tilde{\varepsilon}_j^2(s)}{\tilde{x}^3} = 0\tag{3.20}$$

where, the functions  $f(r_j, r_k)$  and  $g(r_j, r_k)$  are given by (see **Appendix A**)

$$f(r_j, r_k) = \begin{cases} \frac{r_j^2}{4r_k^2} & \text{if } r_j < r_k \\ \frac{r_k^2}{4r_j^2} & \text{if } r_j > r_k \end{cases} \quad (3.21)$$

and

$$g(r_j, r_k) = \begin{cases} 0 & \text{if } r_j < r_k \\ \frac{1}{2} \left(1 - \frac{r_k^2}{r_j^2}\right) & \text{if } r_j > r_k \end{cases} \quad (3.22)$$

For a uniform distribution, the beam radius  $r_j(s) = 2\tilde{x}$  and  $\varepsilon_j = 4\tilde{\varepsilon}_j$ . Therefore, the equation for the beam radius can be written as,

$$r_j'' + kl_j^2(s)r_j - \frac{a_j}{r_j} - \frac{4}{r_j} \sum_{\substack{k=1 \\ k \neq j}}^n b_{jk} (f(r_j, r_k) + g(r_j, r_k)) - \frac{\varepsilon_j^2(s)}{r_j^3} = 0 \quad (3.23)$$

It is very easy to show that envelope Eq. (3.23) developed here, reduces to the well known envelope equation for single species as discussed in the literature, for  $I_k = 0$  and  $j \neq k$ .

### 3.2.5 Beam Selection by Slit

In practical accelerator applications, out of many species only one component of the beam is required. In order to select a particular component of multispecies beam one has to put slits at appropriate places in the beam line. The current as well as the emittance of a particular species of the beam will be reduced if radius of the beam of that particular species at the slit position is larger than the radius of the slit. After passing through the slit, the resultant current of species  $j$  is given by

$$I_j = \begin{cases} I_j & \text{if } p \geq 1 \\ I_j p^2 & \text{if } p < 1 \end{cases} \quad (3.24)$$

where  $p = r_{slit}/r_j(slit)$ ,  $r_j(slit)$  is the radius of the species  $j$  at the slit and  $r_{slit}$  is the radius of the slit. The effective emittance of species  $j$ , can be obtained

by evaluating the phase space area that passes through the slit. The effective phase space area which passes through the slit is given by (see **Appendix A**)

$$\varepsilon j_{eff} = \frac{2\varepsilon_j}{\pi} \left[ p\sqrt{1-p^2} + \sin^{-1} p \right] \quad (3.25)$$

where  $\varepsilon_j$  is the emittance of species  $j$  of the beam before the slit. If there is any loss in any species at the slit the current of that species also reduces as given by the Eq. (3.24). So, in general the quantity  $a_j, b_{jk}$  in Eq. (3.23) varies along the transport line. To calculate the orientation of the effective phase ellipse after the slit, first we need to calculate the rms emittance as well as the twiss parameters  $\alpha_{s_j}, \beta_{s_j}$  and  $\gamma_{s_j}$  of the ellipse just after the slit. The rms quantities just after the slit are given by (see **Appendix A**)

$$\overline{x^2} = \frac{\varepsilon_j r_{slit}^2}{2\pi p^2 \varepsilon j_{eff}} \left[ p\sqrt{1-p^2} - 2p \cdot q^{3/2} + \sin^{-1} p \right] \quad (3.26)$$

$$\overline{x'^2} = \frac{\varepsilon_j^3 p^2}{6\pi r_{slit}^2 \varepsilon j_{eff}} \left[ 3\beta_j \gamma_j \sin^{-1} p + 3\beta_j \gamma_j p\sqrt{q} + 2p(1 - 3\alpha_j^2)q^{3/2} \right] \quad (3.27)$$

$$\overline{xx'} = -\frac{\alpha_j \varepsilon_j^2}{2\pi \varepsilon j_{eff}} \left[ p\sqrt{q} - 2p \cdot q^{3/2} + \sin^{-1} p \right] \quad (3.28)$$

where  $\alpha_j, \beta_j$  and  $\gamma_j$  are the Twiss parameters of the beam just before the slit and  $q = (1 - p^2)$ . The rms emittance of the species  $j$  after the slit can be obtained from

$$\tilde{\varepsilon}_{s_j} = \sqrt{\overline{x^2} \cdot \overline{x'^2} - (\overline{xx'})^2} \quad (3.29)$$

The Twiss parameters  $\alpha_{s_j}, \beta_{s_j}$  and  $\gamma_{s_j}$  are now given by  $\beta_{s_j} = \overline{x^2}/\tilde{\varepsilon}_{s_j}$ ,  $\gamma_{s_j} = \overline{x'^2}/\tilde{\varepsilon}_{s_j}$  and  $\alpha_{s_j} = -\overline{xx'}/\tilde{\varepsilon}_{s_j}$ .

### 3.3 Numerical Results

As mentioned earlier there is a slit system between the two solenoids of the LEBT line to reject unwanted species from the proton beam. The emittance

of the beam from the ion source is mainly dictated by the ions temperature, slit size of the plasma electrode and the magnetic field in the extraction region.

The normalised emittance of the extracted beam is given by [56, 57],

$$\varepsilon_n = \frac{4}{m_i c} \frac{R}{2} \sqrt{m_i k T_i + \frac{q^2 B_{ex}^2 R^2}{16}} \quad (3.30)$$

where  $B_{ex}$  is the axial magnetic field at the extraction slit,  $R$  is the slit radius,  $T_i$  is the ion temperature,  $m_i$  is the mass of the ion and  $k$  is the Boltzmann constant. Typical values of normalised emittances for  $p$ ,  $H_2^+$  and  $H_3^+$  ion species used in the numerical calculations are  $\varepsilon_n(p) = 0.8\pi$  mmmrad,  $\varepsilon_n(H_2^+) = 0.4\pi$  mmmrad and  $\varepsilon_n(H_3^+) = 0.27\pi$  mmmrad respectively.

### 3.3.1 Results using Envelope Model

In this subsection, we present numerical results using beam envelope model for multispecies beam with various beam currents and species fractions. We have used the soft edge profile of the solenoids (Eq. (2.24), **Chapter 2**) for the calculation. We have solved Eq. (3.23) using 4<sup>th</sup> order R-K method and the detailed procedure is given in **Appendix A**.

In Fig. 3.1 the envelopes of proton beam along the axial direction are plotted for various proton fractions (60%, 80% and 100%) in the total beam current of 10 mA. Other components of the beam are  $H_2^+$  and  $H_3^+$ . The centres of the solenoids S1 and S2 are located at  $s = 60$  cm and  $s = 210$  cm respectively and a circular slit of radius 5 mm at 135 cm. The location of the slit is indicated by an arrow. The initial beam has radius of 2.5 mm which expands rapidly due to space-charge forces. The first solenoid focuses the beam to a waist around the slit. The second solenoid brings the beam to another waist at the matching point which is  $\sim 280$  cm. We can see that for different fractions of proton, the envelope of proton beam behaves differently in the presence of other components. Before solenoid S1, the radii of  $H_2^+$  and  $H_3^+$  are smaller than the

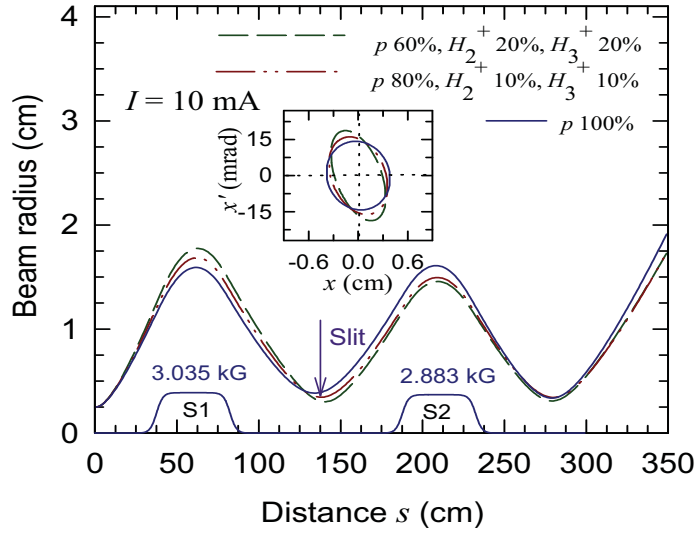


Figure 3.1: Evolution of the envelope radii of proton beam having three different fractions 60%, 80% and 100% in the total beam of 10 mA at 100 keV, for an axisymmetric beam in the transport line. The initial beam parameters are  $r(0) = 2.5$  mm,  $r'(0) = 0$ . The centres of the solenoids S1 and S2 are located at  $s = 60$  cm and  $s = 210$  cm respectively. The orientations of the phase ellipses at the slit location are also shown for the three different fractions of proton.

proton radius. Due to the space-charge forces of  $H_2^+$  and  $H_3^+$  the beam radius of proton diverges rapidly where the proton fraction is less. At the slit  $H_2^+$  and  $H_3^+$  fractions are reduced drastically with a substantial reduction in the space-charge force on proton beam due to these components. As a result the proton radius diverges more in the cases where the proton fraction is large. In all cases beam envelope passes through the slit and thus there is no reduction in the current and emittance of the proton beam.

The evolution of beam envelopes of  $H_2^+$  and  $H_3^+$  are shown in Fig. 3.2 for total beam current of 10 mA in which proton current is 6 mA and currents due to  $H_2^+$  and  $H_3^+$  are 2 mA from each. Both beams diverge initially and the growth rate slowed down when they are subjected to the focussing force of solenoid S1 at 60 cm. At the slit the beam radius of  $H_2^+$  is reduced from 2.5

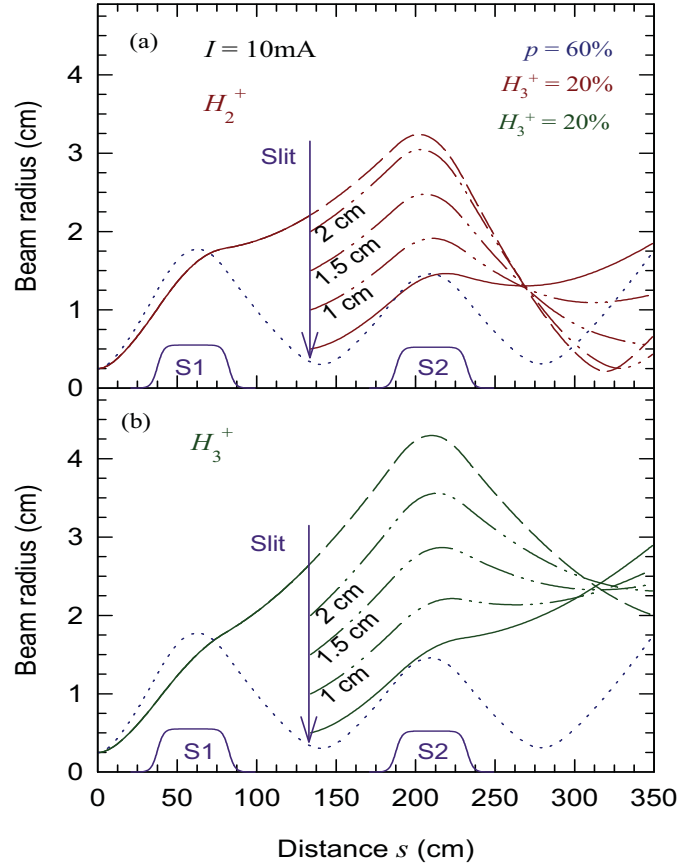


Figure 3.2: Variation of envelope radii of a)  $H_2^+$  beam and b)  $H_3^+$  beam without slit (dashed line) and with slit of radius 5 mm (solid line). Slit is located at  $s = 135\text{ cm}$ . The strengths of the solenoids S1 and S2 are 3.035 kG and 2.833 kG respectively. The evolution of  $H_2^+$  and  $H_3^+$  envelope radii after selection by three different slit sizes are also shown. The dotted curves represent the proton envelope.

cm to 0.5 cm (Fig. 3.2(a)) with a substantial reduction in the current as well in the emittance. The radius of  $H_2^+$  beam diverges again (shown by solid line) due to the action of its emittance and space-charge forces of proton,  $H_2^+$  and  $H_3^+$ . At solenoid S2 it again experiences the focussing force and thus the rate of divergence of its envelope is reduced. For this beam the focussing force due to solenoid is not enough and thus the beam diverges after forming a waist. The situation is same for  $H_3^+$  beam as shown in Fig. 3.2(b).

In order to understand the evolution of beam envelopes in more detail, the

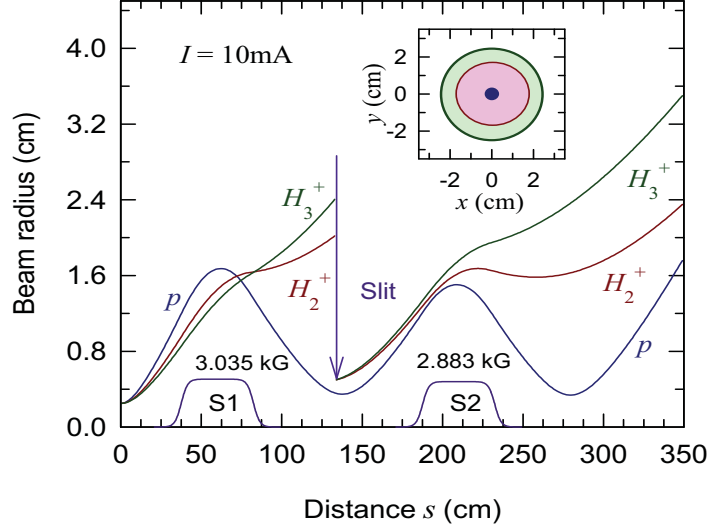


Figure 3.3: Evolution of envelope radii of  $p$ ,  $H_2^+$  and  $H_3^+$  having fractions of 80%, 15% and 5% respectively in the total initial beam current of 10 mA at 100 keV. The initial beam parameters are  $r(0) = 2.5$  mm,  $r'(0) = 0$  for all the species. Beam spots of  $p$ ,  $H_2^+$  and  $H_3^+$  near the second waist of proton beam are also shown.

envelopes of  $H_2^+$  and  $H_3^+$  are also plotted for three different slit sizes in Fig. 3.2(a) and 3.2(b). As the slit size increases the envelope radii also increases at the slit and evolves under the action of space charge and emittance forces. The beam with larger radius at the solenoid S2, experiences comparatively stronger focussing force and reduced space-charge force. The beam radius therefore evolves accordingly under the action of these focussing and defocussing forces as beam advances in the drift length. The major portions of the  $H_2^+$  and  $H_3^+$  beams are rejected at the slit and out of 4 mA beam, only 0.172 mA passes through the slit. There is also reduction in the emittances of both species.

Figure 3.3 shows the beam envelopes of  $p$ ,  $H_2^+$  and  $H_3^+$  having fractions of 80%, 15% and 5% respectively in the total initial beam current of 10 mA. At the slit most of the  $H_2^+$  and  $H_3^+$  beams are rejected whereas proton beam passes through the slit without any loss. The estimated fractions of  $p$ ,  $H_2^+$  and  $H_3^+$  after the slit are 98.6%, 1.13% and 0.27% respectively. The estimated beam

spot of these three beams near the second waist of proton beam is also shown in Fig. 3.3. A second slit at this location having radius equal to the radius of proton beam (7 mm), can further reduce the fraction of other components. The estimated fractions of  $p$ ,  $H_2^+$  and  $H_3^+$  after the second slit are 99.94%, 0.054% and 0.006% respectively.

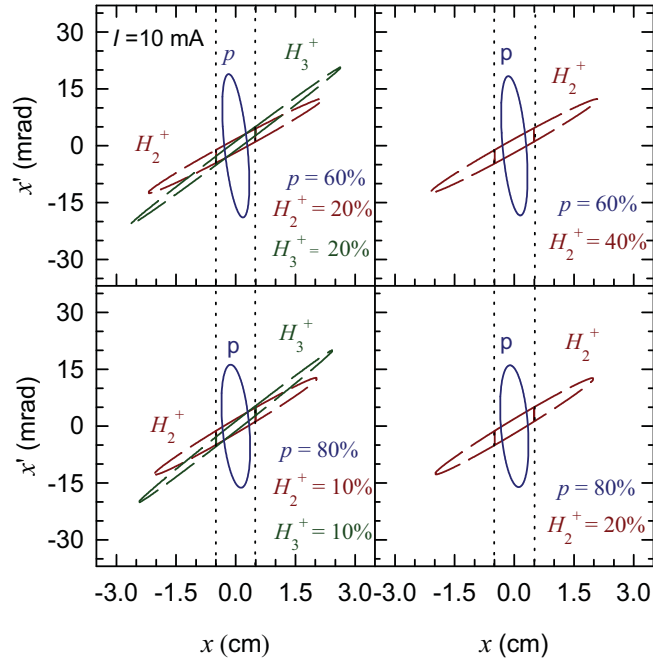


Figure 3.4: The orientation of phase space ellipses of different species of the beam at the position of the slit for various beam parameters. In each case the phase space region occupied between the two dotted lines (representing the edges of the slit in phase space), will pass through the slit of radius 5 mm.

The orientations of phase ellipses of  $p$ ,  $H_2^+$  and  $H_3^+$  beams at the slit location are shown in Fig. 3.4 for various fractions of  $p$ ,  $H_2^+$  and  $H_3^+$  in the beam current of 10 mA. As discussed earlier, only those portions of phase ellipses of  $H_2^+$  and  $H_3^+$  which are within the edges of the slit in the phase space represented by dotted lines, will pass through the slit. The emittance and current of  $H_2^+$  and  $H_3^+$  of the beam after passing through the slit for various values of proton fractions in the 10 mA and 20 mA of total beam current are given in Table 3.1.

Table 3.1: Emittances and currents of different components of the beam after the slit of radius 5 mm. The initial emittances in  $\pi$ mmmrad are; 54.7948 ( $p$ ), 38.7463 ( $H_2^+$ ) and 31.6376( $H_3^+$ ).

Total current (mA)	Beam species (%)			After passing through the slit			
				Emittance of species ( $\pi$ mmmrad)		Current of species (mA)	
	$p$	$H_2^+$	$H_3^+$	$H_2^+$	$H_3^+$	$H_2^+$	$H_2^+$
10	60	40	—	11.5911	—	0.224	—
	60	20	20	11.0869	7.5495	0.102	0.07
	80	20	—	12.2323	—	0.124	—
	80	10	10	11.9217	8.1996	0.059	0.041
	100	—	—	—	—	—	—
20	60	40	—	8.7806	—	0.247	—
	60	20	20	8.4597	5.4535	0.114	0.069
	80	20	—	9.2941	—	0.136	—
	80	10	10	9.0958	5.9969	0.065	0.04
	100	—	—	—	—	—	—

### 3.3.2 Results of PIC Simulation

We have developed a PIC method for multispecies beam to study the beam dynamics self-consistently. The details are given in **Chapter 7**. In the PIC method, each species of the beam is represented as a combination of large number of macroparticles. We have calculated the rms beam sizes  $\tilde{X}_j, \tilde{Y}_j$  and rms emittances  $\tilde{\epsilon}_{j_x}, \tilde{\epsilon}_{j_y}$  of all the species in their Larmor frame. The rms beam sizes and rms emittances for species  $j$  are given by,

$$\tilde{X}_j = \langle x_{ji}^2 \rangle^{1/2}, \quad \tilde{\epsilon}_{j_x} = [\langle x_{ji}^2 \rangle \langle x'_{ji}{}^2 \rangle - \langle x_{ji} x'_{ji} \rangle^2]^{1/2} \quad (3.31)$$

here  $x_{ji}$  is the  $i^{\text{th}}$  macroparticle of the  $j^{\text{th}}$  species. In Eq. (3.31),  $\langle \dots \rangle$  denotes the ensemble average over the beam particle distribution. We have similar expressions for  $y$  coordinate also.

The calculation region is divided into uniform rectangular meshes of dimension  $N_x = N_y = 128$ . We have used 77000 macroparticles for each species and step size  $\Delta s = 1$  mm in the axial direction. The charge on the macroparti-

cle of each species is distributed according to species fraction and number of macroparticles. We like to point out here that we have chosen the number of macroparticles and step size after running a large number of test simulations.

In Fig. 3.5 we have plotted the evolution of beam envelopes and emittances obtained from PIC simulation (dashed line) for the following choice of parameters: total beam current  $I = 10$  mA, species fractions  $p = 80\%$ ,  $H_2^+ = 15\%$ ,  $H_3^+ = 5\%$ , rms beam sizes  $X_{rms} = 1.25$  mm at  $s = 0$  for all the species, magnetic fields at the centre of the solenoids S1 and S2 equal to 3.03 kG and 2.88 kG respectively same as used in the envelope model. A slit of radius 5 mm is used at  $s = 135$  cm for the selection of proton. For comparison we have also shown the beam envelopes obtained by solving multispecies envelope equations (solid line). We have considered that all the species are K-V distributed at  $s = 0$ . It is evident from Fig. 3.5(a) that the results of the beam size obtained from the envelope equations agree well with the results of PIC simulations for the primary beam. However, the beam sizes predicted by the envelope model for  $H_2^+$  and  $H_3^+$  beams differ by  $\sim 12\%$ (maximum) near the centre of solenoid S2 although the qualitative behaviour of the envelope is almost similar.

The evolution of beam emittances of  $p$ ,  $H_2^+$  and  $H_3^+$  beams obtained from multispecies PIC simulation is shown in Fig. 3.5(b). The small growth in emittance of proton is because of the fact that initially the rms beam size of proton is larger than rms sizes of  $H_2^+$  and  $H_3^+$  and hence particles of the proton beam experience nonlinear space-charge force due to  $H_2^+$  and  $H_3^+$ . It is evident from the figure that there is a rapid increase in the emittances of  $H_2^+$  and  $H_3^+$  beams after  $s = 100$  cm. The emittance growth is due to the nonlinear space-charge force of converging intense proton beam. At the slit major portions of the  $H_2^+$  and  $H_3^+$  beams are rejected together with the substantial reduction in their emittances. We see a sharp increase in the emittances of  $H_2^+$  and  $H_3^+$

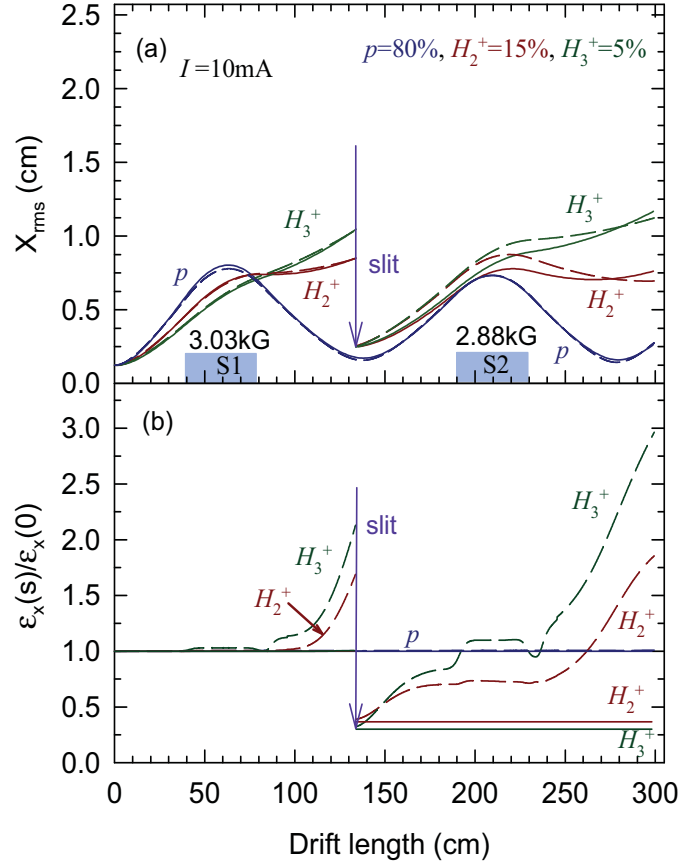


Figure 3.5: Comparison of the evolution of (a) rms beam sizes and (b) rms emittances of  $p$ ,  $H_2^+$  and  $H_3^+$  obtained from the multispecies envelope model (solid curve) and the self-consistent PIC simulation (dashed curve) for  $I = 10$  mA. A slit of radius 5 mm is placed at  $s = 135$  cm.

after the slit in the region where the proton beam size is small, remain almost constant in the region where the proton beam size is comparable to the beam sizes of  $H_2^+$  and  $H_3^+$  and then increase again as the proton beam converges. It is to be noted that the emittance of all the species is calculated in their own Larmor frame.

To further investigate the effect of the distribution of unwanted species  $H_2^+$  and  $H_3^+$  on the dynamics of proton beam, we have done the PIC simulation with different types of distribution for  $H_2^+$  and  $H_3^+$  keeping the distribution

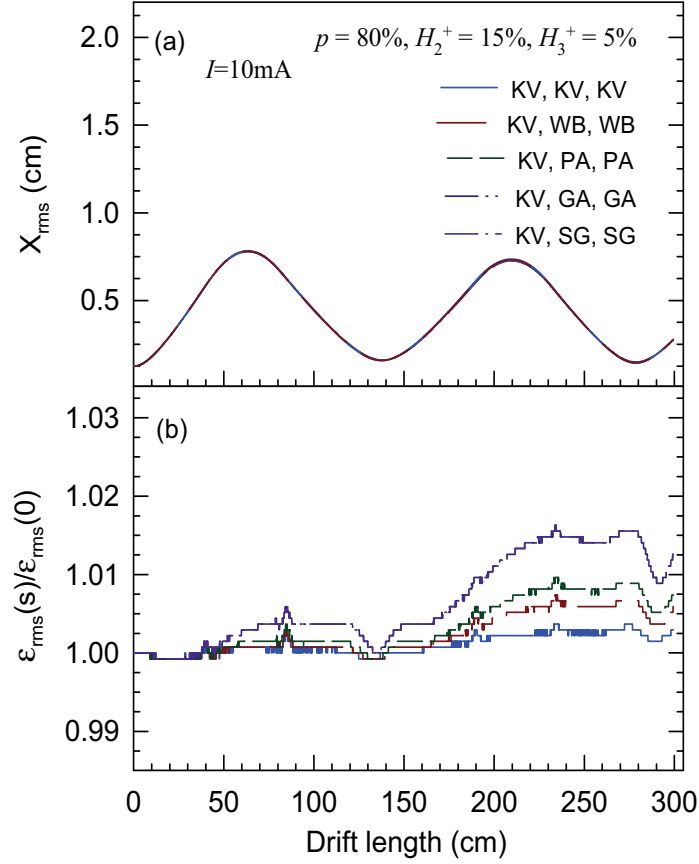


Figure 3.6: Plot shows the comparison of the variation of (a) rms beam size and (b) rms emittance of initially K-V distributed proton beam and with different types of beam distribution for  $H_2^+$  and  $H_3^+$ . We have considered five different types of distribution for  $H_2^+$  and  $H_3^+$ : K-V (KV), waterbag (WB), parabolic (PA), semi-Gaussian (SG) and Gaussian (GA) distributions.

of the proton beam same as K-V distribution. Figure 3.6(a) and 3.6(b) show, respectively, the evolution of the rms beam size and the rms emittance of proton beam along the transport line. Parameters are same as in Fig. 3.5. It is readily seen from the figure that the evolution of rms beam size of proton is independent to the form of the distribution function of  $H_2^+$  and  $H_3^+$ , however, there is a small growth in the emittance of the proton beam when the nonuniformity of the distributions of  $H_2^+$  and  $H_3^+$  is increased.

Up till now, we have presented the results of simulation considering the

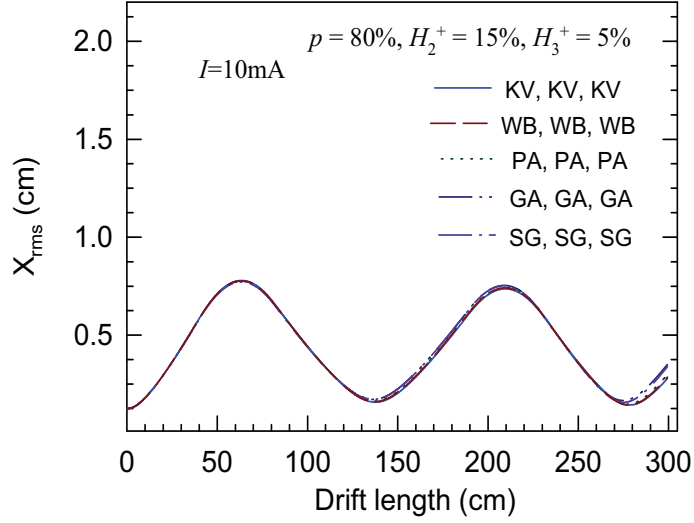


Figure 3.7: Evolution of rms beam size of proton along the distance  $s$  with different types of initial distribution for all the species. We have considered five different types of distributions for all the species  $p$ ,  $H_2^+$  and  $H_3^+$ : K-V (KV), waterbag (WB), parabolic (PA), semi-Gaussian (SG) and Gaussian (GA) distributions.

distribution of the proton beam as K-V and with various types of distribution for the  $H_2^+$  and  $H_3^+$  beam species. Now we study the beam dynamics of all the species considering different types of distribution. We have considered five different types of distribution for the simulation which are K-V, waterbag, parabolic, semi-Gaussian and Gaussian distribution and for the same choice of system parameters as in Fig. 3.5. We did not observe any appreciable change in the rms beam size of proton as shown in Fig. 3.7 by changing the distribution function of  $H_2^+$  and  $H_3^+$  beams.

Figure 3.8 shows evolution of beam envelopes of  $H_2^+$  and  $H_3^+$  for different types of initial distributions. It is evident from the figure that there is a slight difference in the evolution of the beam size of  $H_3^+$  before the slit location. Since after the slit major portion of this species is rejected we see that the difference is negligibly small.

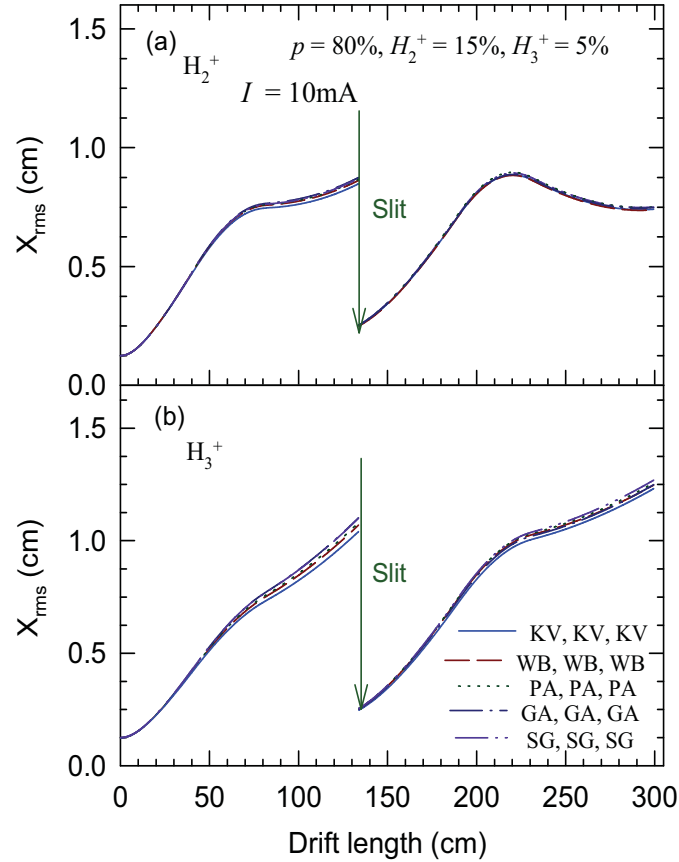


Figure 3.8: The variation of the rms beam size of (a)  $H_2^+$  and (b)  $H_3^+$  along the beam transport line. A circular slit of aperture 5 mm is placed at a distance  $s = 135$  cm.

Figure 3.9(a) and 3.9(b) show respectively, the evolution of the emittances of  $H_2^+$  and  $H_3^+$  as a function of distance  $s$ . It is readily seen from Fig. 3.9 that there is a significant change in the evolution of the emittances of  $H_2^+$  and  $H_3^+$  species when the distribution of the species are different. The emittance growth rate increases when the distribution of the proton beam changes from K-V to other distributions such as waterbag, parabolic, semi-Gaussian and Gaussian. This effect is more pronounced just before the slit within the region of  $s = 100$  cm to  $s = 135$  cm where the beam size of the proton beam is small and hence the strength of the space-charge defocusing force is more. After the slit the growth

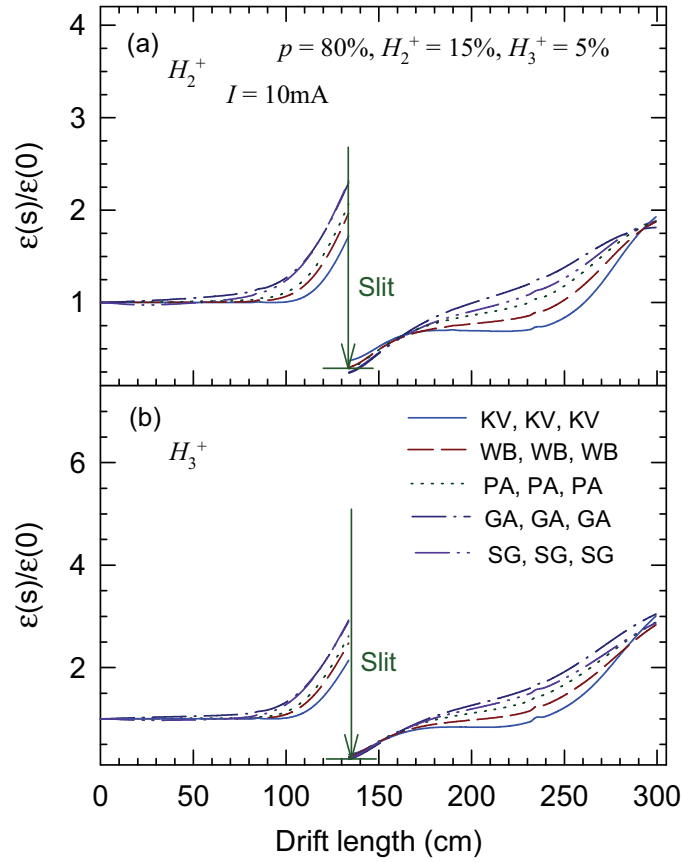


Figure 3.9: The variation of the rms emittance of (a)  $H_2^+$  and (b)  $H_3^+$  along the beam transport line before and after a slit of aperture 5 mm with different distributions of species. Slit is located at  $s = 135$  cm.

rate is small. This is due to the fact that most of the particles of  $H_2^+$  and  $H_3^+$  are within the proton beam. After  $s = 240$  cm where the proton beam starts converging, the rate of growth of emittance of  $H_2^+$  and  $H_3^+$  increases rapidly.

In Fig. 3.10, we have plotted the real space and phase space distributions of all the species at the final location  $s = 277$  cm without using any slit in the beam line. It is evident from the real space plot that the species are separated from each other in the case of uniform distribution whereas, in the case of Gaussian distribution, both  $p$  and  $H_2^+$  distributions overlapping each other. Figure 3.11 shows the final particle distributions in phase space and in real space at  $s =$

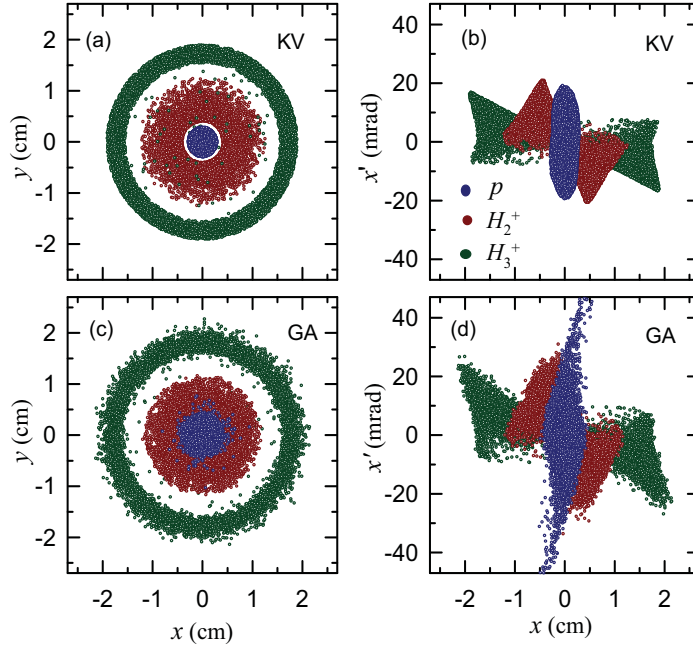


Figure 3.10: Phase space  $(x, x')$  and real space  $(x, y)$  distributions of  $p$ ,  $H_2^+$  and  $H_3^+$  at  $s = 277$  cm without any slit in the beam line for K-V and Gaussian distributions of all the species. Species fractions are:  $p = 80\%$ ,  $H_2^+ = 15\%$  and  $H_3^+ = 5\%$ .

277 cm, with circular aperture and square aperture for the case of K-V and Gaussian distributions for all the species. Both the diameter of the circular aperture as well as sides of the square aperture are kept equal to 1 cm. It is evident from the real space plot that the distributions of  $H_2^+$  and  $H_3^+$  form hollows around the proton beam. We can also see from the real space plot that the distribution of  $H_2^+$  beam is four fold symmetric which is arising due to the square slit whereas the distribution of  $H_3^+$  beam is almost axisymmetric. In Fig. 3.12, variation of the rms beam envelope size and rms emittances of proton beam are shown as a function of distance  $s$  for various proton fractions in the total beam current of 10 mA. Here Gaussian distribution is used for all the species in the simulation. From Fig. 3.12(a) we also see here that the proton envelopes for different fractions of proton behave differently in the presence of other component as predicted by the beam envelope model. Figure 3.12(b)

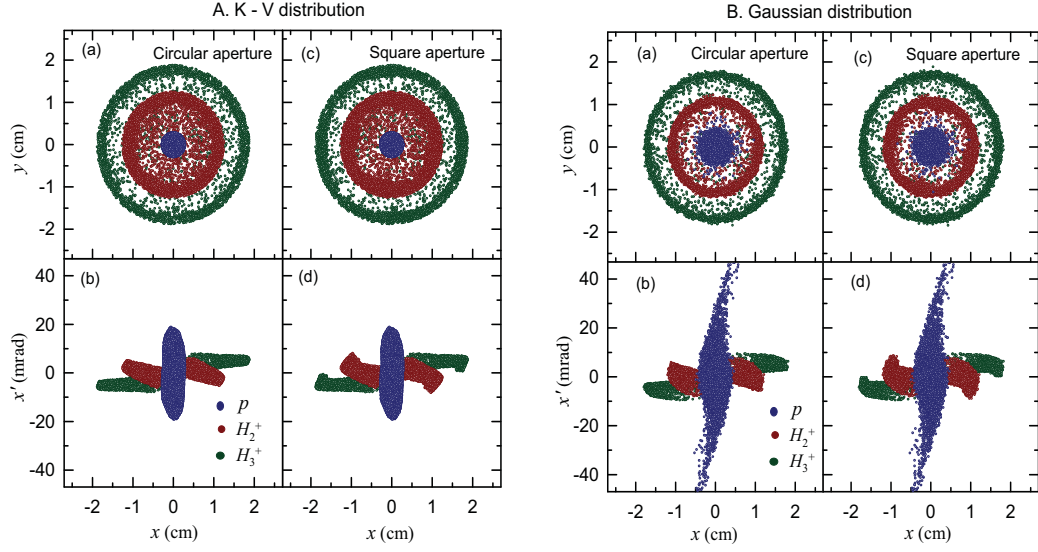


Figure 3.11: Comparison of phase space and real space distributions of  $p$ ,  $H_2^+$  and  $H_3^+$  at location  $s = 277$  cm for circular and square aperture placed at  $s = 135$  cm. We have considered K-V and Gaussian distributions of all the species.

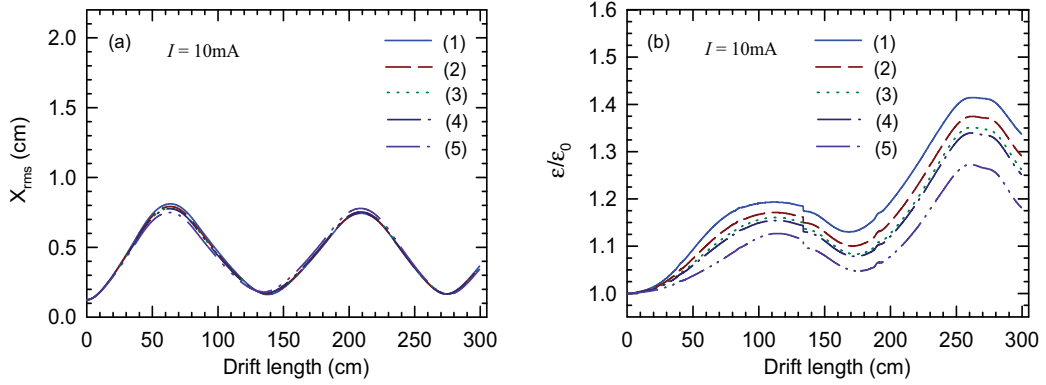


Figure 3.12: Evolution of (a) rms envelope size and (b) rms emittance of proton having different species fractions in the total beam of 10 mA at 100 keV. Different percentage fraction in 10 mA are (1): [60, 20, 20], (2): [70, 20, 10], (3): [80, 10, 10], (4): [80, 15, 5] and (5): [100, 0, 0].

shows the evolution of emittance of proton beam. The growth in the emittance of proton increases as the fraction of unwanted species is increased.

Self-consistent PIC simulation shows the formation of hollow of unwanted

species around the primary beam which become more distinct after the second solenoid. Inspecting the behaviour of beam evolution, we have chosen two location for the slit (i) at  $s = 135$  cm at the first waist of proton and (ii)  $s = 257$  cm just before the second waist of proton where the distribution of  $H_2^+$  and  $H_3^+$  become hollow. We have performed PIC simulations considering uniform and Gaussian distributions with initial species fraction as  $p = 80\%$ ,  $H_2^+ = 15\%$ ,  $H_3^+ = 5\%$  in both the cases.

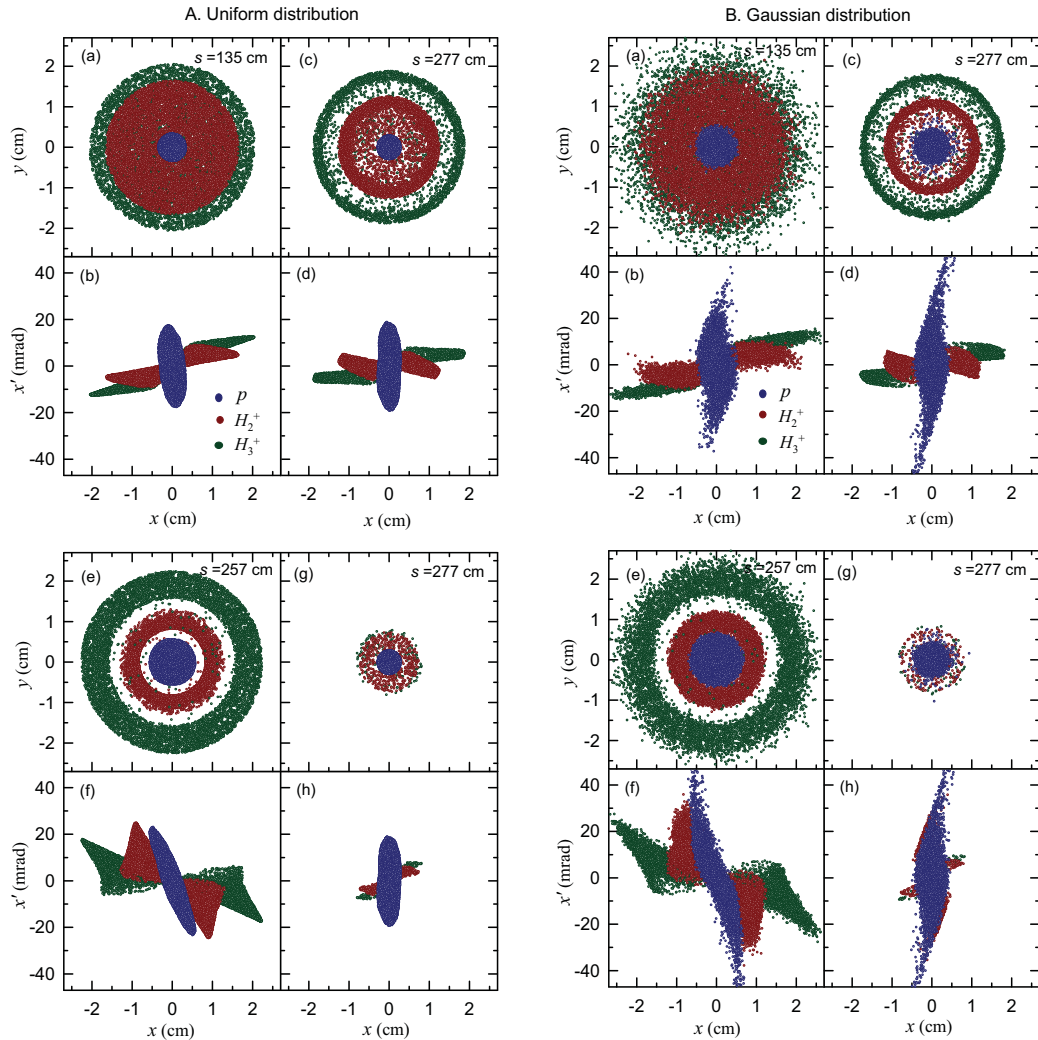


Figure 3.13: Phase space  $(x, x')$  and real space  $(x, y)$  distributions of  $p$ ,  $H_2^+$  and  $H_3^+$  at different locations during the beam transport for two types of distributions (A) K-V and (B) Gaussian for all the species.

The PIC simulation results of using slit at two locations with uniform distribution are shown in Fig. 3.13A(a) to (h). Figure 3.13A(a) and 3.13A(c) represent the real space distribution of the particles at the slit ( $s = 135$  cm) and at location  $s = 277$  cm where the second waist of proton is formed whereas Fig. 3.13A(b) and 3.13A(d) show the corresponding phase space plots. Similar plots of real and phase spaces when the slit is placed at  $s = 257$  cm are shown in Fig. 3.13A(e) to (h). The beam selection using a slit of radius 5 mm at  $s = 135$  cm results in further formation of hollows of unwanted species at the second waist of proton (Fig. 3.13A(c)). This indicates that the beam selection is not very efficient. It can be readily seen from Fig. 3.13A(e) that species at  $s = 257$  cm are well separated and putting a slit of size approximately equal to the size of proton beam (7 mm) at this location rejects most of the unwanted species efficiently. The estimated fractions of  $p$ ,  $H_2^+$  and  $H_3^+$  for the first case (slit at  $s = 135$  cm) are 98.38%, 1.34% and 0.28% respectively whereas for the second case (slit at  $s = 257$  cm), fractions are equal to 99.86%, 0.125%, 0.015% respectively. It is very easy to observe that phase space distributions of  $H_2^+$  and  $H_3^+$  beams are highly distorted at the slit as well as at the final location whereas, the phase space of proton at the final location is almost similar for both the cases.

As we know, every realistic particle distribution at finite temperature has a diffusive tail. The Gaussian beam is more realistic and it constitutes a bridge between the ideal K-V beam and the laboratory beam. Therefore, we have also shown the results of self-consistent PIC simulation with Gaussian distribution in Fig. 3.13B(a) to (h) for comparison. In this case the beam edges are not sharp and phase space distributions of all the species including proton are highly distorted at the slit position as well as at the final location, clearly indicating the effect due to nonlinear space-charge force of the species. A comparison of

results using these two distributions will provide valuable help in understanding the experimental data.

### 3.4 Summary and Discussion

In this chapter we have derived the transverse envelope equations to improve the modelling of a space-charge-dominated beam in the presence of unwanted species. The formulations for beam selection using slit system have been developed to obtain the phase ellipse and its orientation after the slit to calculate the beam transport downstream. We have studied the transport of proton from 2.45 GHz microwave ion source in the presence of  $H_2^+$ ,  $H_3^+$  species. We have observed that envelope of the proton beam behaves differently in the presence of different fractions of the other components.

Finally, self-consistent analysis has been performed using PIC method for different distributions of the species. The emittance growth of the primary species due to other unwanted species is studied for various beam parameters. We have observed the formation of beam hollows of unwanted species which are produced due to nonlinear space-charge effect. The selection of the primary species is performed and shown that the rejection of unwanted species is very effective when the slit is placed after the hollow formation of unwanted species.

The results of evolution of the rms beam envelopes obtained from envelope model show a reasonably good agreement with the PIC simulation. Thus the envelope model discussed in this chapter can be utilised for more precise estimate of the beam envelope without the use of large simulations in the case of a multispecies beam where the beam current is in the range of 5 - 30 mA. However in the case of beam current more than 30 mA the beam excursion becomes large, difficult to focus the beam to small waist, and the required solenoid fields are comparatively large. In the case of high beam current 30 - 100 mA,

one needs to introduce a desired gas deliberately in the beam transport line for space-charge compensation. This way one can reduce the space-charge defocusing force and control the beam excursion. The method developed in this chapter can still be used when the space-charge compensation is present by replacing the beam current  $I$  with  $I(1 - f)$  in the envelope equation where  $f$  is the average neutralization factor.

# Chapter 4

## Optimisation of LEBT Parameters for Multispecies Beam

### 4.1 Introduction

A key issue in the design of beam transport system for intense beam is to prevent the loss of the beam particles, emittance growth and halo formation [41, 58, 59, 60]. The situation becomes more difficult when the beam contains more species and various charge states. In the previous chapter, we have presented the beam envelope model for transport and selection of primary beam from the multispecies beam. As an example, we have discussed the transport of proton beam from 2.45 GHz microwave ion source in the presence of  $H_2^+$  and  $H_3^+$  beam in the solenoid based beam transport system. The values of proton fraction from these sources [52, 53] are in the range of 75% to 85% of the total extracted beam. The matching of primary beam in the presence of other unwanted species carries a practical importance in the case of space-charge-dominated beam to preserve the quality of the primary beam. Although numerical solutions to the beam envelope equations can be easily obtained in a given layout of a transport line, the question remains as to whether the best possible setting of the parameters (position and strength of the focussing elements) has been chosen in the sense

of providing the minimum beam radius all over the beam transport line.

Optimization problems arise in different fields of science and engineering [12, 61, 62, 63, 64, 65, 66, 67, 68, 69]. There are many optimization techniques discussed in the literature for designing and tuning of beam transport lines [70, 71, 72, 73, 74, 75, 76] using the well known K-V beam envelope equations [17], originally formulated to model a uniform density beam with elliptical cross section. These equations can also be applied to equivalent beams having different elliptically symmetric particle distributions with same second moments [15, 20, 77]. A semi analytical approach has been presented in Ref. [73] to find the best possible setting of magnetic lenses for a chosen layout of the transport line. The method is based on a piecewise minimisation of the beam radius using thin lens approximation for focussing magnets. The optimisation techniques presented in Refs. [74, 75, 76] utilize the principles of optimal control theory to aid in the design of beam transport and matching systems. However, above mentioned optimisation techniques are suitable for beam containing only single specie such as electron or single ion with constant beam emittance throughout the transport line.

In this chapter we describe a method to find the optimal beam line settings for the transport and matching of primary beam from the space-charge-dominated multispecies beam [78]. It is based on random search technique where the primary beam is matched at the final position and the loss of unwanted species is maximised at the location of a circular slit by choosing the parameters randomly. In general, the practical constraints in the matching section are (i) the maximum beam excursions dictated by the acceptance aperture of focussing elements and (ii) the beam pipe radius. The first constraint is imposed by the nonlinearities in the focussing fields of magnets which leads to the beam quality degradation. The second constraint is related to the interference

of image forces. To remove these difficulties, we have used a reference trajectory for the beam envelope along the transport line to restrict the excursion of beam radius [74] and a cost functional to quantify the quality of the solution. Numerical results of the beam selection and optimized transport parameters have been presented for various values of total beam current and different fractions of  $p$ ,  $H_2^+$  and  $H_3^+$  species for the LEBT system.

## 4.2 Mathematical Model

### 4.2.1 Dynamics of Multispecies Beam

Detailed derivations of space-charge-dominated beam envelope equations for a thin, axisymmetric, continuous intense multispecies beam and the beam selection using circular slit in a solenoid based transport line have been discussed in **Chapter 3**. The derivation of envelope equations is based on the assumption that beam density distribution of all the species will remain uniform (i.e. K-V distribution) [49]. Here we outline only important results relevant for the present optimisation. The envelope equations of each species of the beam, in its own Larmor frame, propagating through a solenoid focussing channel, is given by (Eq. (3.23), **Chapter 3**)

$$r_j'' + kl_j^2(s)r_j - \frac{a_j}{r_j} - \frac{4}{r_j} \sum_{\substack{k=1 \\ k \neq j}}^n b_{jk} (f(r_j, r_k) + g(r_j, r_k)) - \frac{\varepsilon_j^2(s)}{r_j^3} = 0 \quad (4.1)$$

Here  $j = 1, 2, \dots, n$ ,  $s$  is the axial coordinate in the laboratory frame,  $kl_j(s)$  is the applied external force experienced by species  $j$ ,  $r_j$  and  $\varepsilon_j$  are the envelope radius and emittance of the species  $j$  of the beam respectively and  $n$  is the number of species in the beam. The terms in the summations are the space-charge coupling terms due to other species. The quantities  $f(r_j, r_k)$  and  $g(r_j, r_k)$  are

defined in Eq. (3.21) and Eq. (3.22).  $a_j(s)$  and  $b_{jk}(s)$  are given by

$$a_j = \frac{q_j I_j}{2\pi\epsilon_0 m_j \beta_j^3 \gamma_j^3 c^3}, \quad b_{jk} = \frac{q_j (1 - \beta_j \beta_k) I_k}{2\pi\epsilon_0 m_j \beta_j^2 \gamma_j \beta_k c^3} \quad (4.2)$$

in which,  $I_j$  is the current,  $m_j$  is the mass,  $\beta_j$  and  $\gamma_j$  are the usual relativistic terms of species  $j$  of the beam. Similarly subscript  $k$  represents these quantities for species  $k$ . Though the envelope equation presented here is based on uniform density distribution it can also be utilized for any beam distribution using the concept of equivalent beams [15, 20]. According to this concept, the beam must have the same second moment as the actual beam distribution. In such cases one has to use the rms quantities in the envelope equation.

At the location of the circular aperture, the current as well as the emittance of species are reduced if envelope sizes of those species are larger than the aperture size. After passing through a circular slit the resultant current of the species  $j$  is given by

$$I_j = \begin{cases} I_j & \text{if } p \geq 1 \\ I_j p^2 & \text{if } p < 1 \end{cases} \quad (4.3)$$

where  $p = r_{slit}/r_j(\text{slit})$ . Here  $r_{slit}$  is the radius of the slit and  $r_j(\text{slit})$  is the radius of species  $j$  at the slit location. If the beam radius of the species  $j$  is larger than the radius of the slit then there is also a reduction in the emittance of species  $j$ . The value of effective emittance of species  $j$  just after the slit can be obtained from the phase space area that passes through the aperture of the slit and is given by (see **Appendix A**)

$$\varepsilon j_{eff} = \frac{2\varepsilon_j}{\pi} \left[ p\sqrt{1-p^2} + \sin^{-1} p \right] \quad (4.4)$$

The orientation of the phase ellipse after the slit can be obtained by evaluating the twiss parameters  $\alpha s_j$ ,  $\beta s_j$  and  $\gamma s_j$  of the species  $j$  just after the slit. These quantities can be obtained by evaluating the second moments of the beam distribution. The expression of the twiss parameters  $\alpha s_j$ ,  $\beta s_j$  and  $\gamma s_j$  are given as

(see **Appendix A**)

$$\beta s_j = \frac{\overline{x^2}}{\tilde{\varepsilon} s_j}, \quad \gamma s_j = \frac{\overline{x'^2}}{\tilde{\varepsilon} s_j}, \quad \alpha s_j = -\frac{\overline{xx'}}{\tilde{\varepsilon} s_j} \quad (4.5)$$

The rms emittance of the species  $j$  after the slit can be obtained from

$$\tilde{\varepsilon} s_j = \sqrt{\overline{x^2} \cdot \overline{x'^2} - (\overline{xx'})^2} \quad (4.6)$$

Since we have considered the uniform density distribution of the beam in our analysis the total effective emittance of species  $j$  of the beam just after the slit will be  $\varepsilon_j = 4\tilde{\varepsilon} s_j$ .

## 4.2.2 Boundary Condition

The initial conditions for each species of the beam such as radius, divergence, current, energy, emittance etc. at the entrance location  $s = s_i$  of the transport system are known. These conditions characterise the beam coming from the preceding device in the transport or accelerator system. For species  $j$  we specify the initial envelope radius and divergence as  $r_j(s_i)$  and  $r'_j(s_i)$ . In the case of matching, we are also given desired final condition at  $s = s_f$  for the desired primary component of the beam. We denote these conditions as  $r_{pm}, r'_{pm}$ . Thus the following boundary conditions must be satisfied for the desired primary component at the final location:

$$r_p(s_f) = r_{pm}, \quad r'_p(s_f) = r'_{pm} \quad (4.7)$$

Mathematically, the matching section has several adjustable parameters  $\mathbf{k} = (k_0, k_1, \dots)$  for example the strengths, position and length of focussing elements, drift spaces, location of slit etc. in the beam line. The beam radius and slope of the primary species  $(r_p, r'_p)$  at the matching point, which are functions of the beam line parameters  $\mathbf{k}$  can be obtained by integrating the  $n$  (number of species) number of coupled second order differential equations Eq. (4.1) simultaneously.

Beam envelope equations Eq. (4.1) must be solved along with Eq. (4.3) to Eq. (4.6) to take care reduction in beam emittance, change in the orientation of phase ellipses after the slit, reduction in the beam current of different species etc. The matching error can thus be expressed as  $f(\mathbf{k}) = (r_p - r_{pm}, r'_p - r'_{pm})$ . The total effective beam current of the unwanted species after the slit is

$$I_{eff}(\mathbf{k}) = \sum_{\substack{k=1 \\ k \neq j}}^n I_k \cdot \frac{r_{slit}^2}{r_k^2(slit)} \quad (4.8)$$

The matching problem is therefore equivalent to find a solution set  $\{\mathbf{k}_{opt}\}$  such that  $\|f(\mathbf{k}_{opt})\| = 0$  for the case of primary species and the total beam current  $I_{eff}(\mathbf{k})$  of the unwanted species be as minimum as possible at the slit location.

### 4.2.3 The Reference Trajectory and Cost Functional

In most of the cases we have more variables or parameters than the terminal conditions in a beam transport systems which lead multiple solutions to the matching problem. In order to quantify the quality of each solution we generally define a cost functional. The optimal solution is one for which the cost functional is optimum in the specified domain of parameter space. Initially we define a reference trajectory guided by the initial design for the primary component which we want to match into the injection point of the accelerator or in another transport system. The reference trajectory represents the optimal path through the transport channel and consequently we need that the actual beam envelope trajectory tracks the path as close as possible to the reference trajectory. Therefore, we choose the cost functional of the primary beam as the least square distance between the actual beam trajectory and the reference trajectory. We define a cost functional for the primary species in terms of the solution of the primary component  $(r_p(s), r'_p(s))$  and the reference trajectory

$(r_{ref}(s), r'_{ref}(s))$  as

$$J_p(\mathbf{k}) = \int_{s_i}^{s_f} (r_p(s) - r_{ref}(s))^2 ds \quad (4.9)$$

### 4.3 Optimisation using Random Search Method

The main aim in any optimization problem is to minimize a set of objective functions by tuning several variables under certain given constraints. For the present case, the optimisation problem can be stated as

$$\begin{aligned} &\text{minimise} && \|f(\mathbf{k})\|, \quad I_{eff}(\mathbf{k}) \quad \text{and} \quad J_p(\mathbf{k}) \\ &\text{subject to} && r_p(slit) < r_{slit} \quad \text{and} \quad r_p(s) < r_{max} \\ &\text{with} && k_i^L \leq k_i < k_i^U \end{aligned} \quad (4.10)$$

where  $k_i^L$  and  $k_i^U$  are the lower and upper limit of the parameter  $k_i$ , and  $r_{max}$  is the maximum allowed radius of the primary species. In the random search technique we start with an initial value of the parameters of the beam line elements. The upper and lower limits of each parameter are also defined. We then solve the  $n$  (number of species) number of coupled second order differential equations Eq. (4.1) simultaneously along with Eq. (4.3) to Eq. (4.6) for all the species with initially chosen set of parameters. The values of matching error  $\|f(\mathbf{k})\|$  and the effective current of the unwanted species at the location of the slit  $I_{eff}(\mathbf{k})$  as well as the cost functional  $J_p(\mathbf{k})$  defined for the primary species are then calculated for the initial set of parameters. In the next step, the new values of all the parameters are randomly chosen within the predefined range of each parameter [12, 79]. The values of  $\|f(\mathbf{k})\|$ ,  $I_{eff}(\mathbf{k})$  and  $J_p(\mathbf{k})$  are again calculated for these chosen random set of parameters and compared with those obtained with the previous set of parameters. If these values are smaller than the previous trial then this gives an intermediate set of parameters  $\mathbf{k}$ . The

process is repeated and after a number of successful trials we check whether the value of a parameter is increased or decreased over the previous trials and accordingly we shift the parameter space.

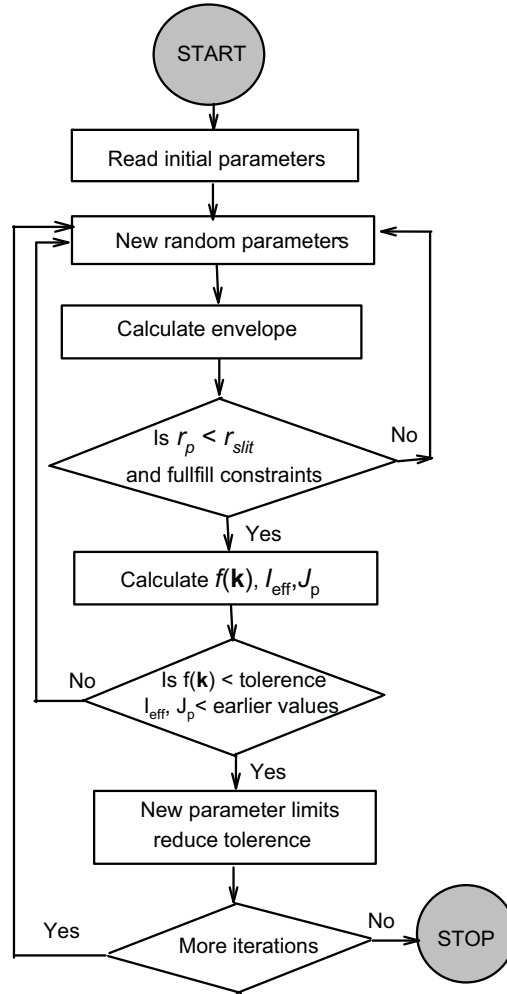


Figure 4.1: The flow chart of the optimisation code using random search technique.

In order to reduce the range of each parameter during the optimization the following technique has been adopted. The lower and upper values  $k_i^L$  and  $k_i^U$  of parameter  $k_i$  are chosen initially along with the starting value of the parameter  $k_0$ . After each successful trial we first check whether the value of the parameter  $k_i$  is increased or decreased from the previous trial and we take

it as  $k_{temp}$ . Then we define the range with respect to this temporary value and also reduce the parameter space from the previous parameter range using  $k_i^L(new) = k_{temp} - \alpha(k_{temp} - k_i^L)$  and  $k_i^U(new) = k_{temp} + \alpha(k_i^U - k_{temp})$ . Here  $\alpha < 1$ , is the user defined parameter chosen suitably. Depending on the value of  $\alpha$  the parameter space is reduced. Now during the optimization the values of the parameters are varied from  $k_i^L(new)$  and  $k_i^U(new)$ . This way it is possible to locate the optimised set of parameters more accurately. This procedure helps in reducing the total number of trials needed for the optimisation. In this technique one can easily introduce any number of constraints in the problem and it does not require any differentiation of the objective function. It arrives at a solution quite fast and can locate the global minimum within the specified range of the parameters if the random jump is chosen sufficiently large initially. We have written a program in Fortran to optimise the transport line parameters for matching of space-charge-dominated multispecies beam. The flow chart of the program is shown in Fig. 4.1.

## 4.4 Numerical Results

The schematic diagram of our injection system of 10 MeV cyclotron, indicating the location of various components is shown in Fig. 4.2. The system is axisymmetric, consisting of two solenoid magnets S1 and S2, with physical lengths of  $l_{s1} = l_{s2} = 40$  cm. The radius of the slit  $r_{slit}$  is equal to 5 mm and is placed at 135 cm from the ion source. The total length of the beam line  $ld_1 + ld_2 + ld_3$  is fixed and equal to 280 cm. In the optimisation, the soft edge profile of the solenoid magnet (Eq. (2.24)) has been used. Typical values of normalised emittances for  $p, H_2^+$  and  $H_3^+$  ion species used in the numerical calculations are  $\varepsilon_n(p) = 0.8\pi$  mmmrad,  $\varepsilon_n(H_2^+) = 0.4\pi$  mmmrad and  $\varepsilon_n(H_3^+) = 0.27\pi$  mmmrad which corresponds to emittance (in  $\pi$  mmmrad) of  $\varepsilon(p) = 54.7948$ ,

$\varepsilon(H_2^+) = 38.7463$  and  $\varepsilon(H_3^+) = 31.6376$  respectively at energy of 100 keV.

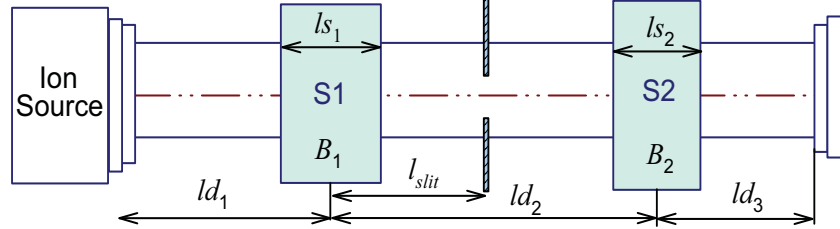


Figure 4.2: Schematic diagram of the matching system.

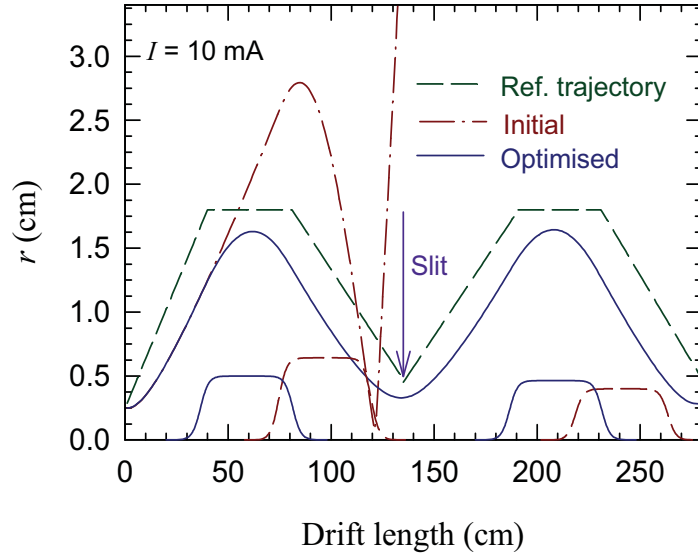


Figure 4.3: Plots of unmatched (dash-dotted line) and matched (solid line) beam envelopes of proton for total initial beam current of 10 mA at 100 keV. Dashed line represents the reference trajectory of the proton beam. The initial beam parameters for all the species are  $r(0) = 2.5$  mm,  $r'(0) = 0$ . The fractions of  $p$ ,  $H_2^+$  and  $H_3^+$  are 80%, 15% and 5% respectively. The initial beam transport parameters are:  $B_1 = 3.97$  kG,  $B_2 = 2.47$  kG,  $ld_1 = 97$  cm,  $ld_2 = 144$  cm and  $ld_3 = 39$  cm. The optimised beam transport parameters are:  $B_1 = 3.09$  kG,  $B_2 = 2.87$  kG,  $ld_1 = 59$  cm,  $ld_2 = 150$  cm and  $ld_3 = 71$  cm. The optimised locations of solenoid magnets are also shown by solid curve.

In the optimisation problem the matching section has seven adjustable parameters. The parameters are  $\mathbf{k} = (B_1, B_2, ls_1, ls_2, ld_1, ld_2, l_{slit})$ . Here,  $B_1$  and

$B_2$  are the peak magnetic fields,  $ls_1$  and  $ls_2$  are the physical lengths,  $ld_1$  and  $ld_2$  are the location of the centre of the first and second solenoids respectively as shown in Fig. 4.2. In the present example we have fixed the lengths  $ls_1$  and  $ls_2$  of the solenoids S1 and S2 and the location of the slit from the ion source. So, there are four free parameters with two conditions to be satisfied at the target plane i.e. beam envelope size and divergence. This means that the matching problem is under constrained. However, in the practical situation there are some constraints in the transport systems which are very common and need to be taken into consideration. The most important constraint is the maximum beam envelope excursion dictated by the linearity of the acceptance aperture of the focussing elements. In the optimisation problem we have introduced a constraint such that the beam excursion in the solenoid magnet and beam line does not exceed 50% of the available aperture radius. Our goal is to match the proton beam to the final state  $r_{pm} = 2.5$  mm,  $r'_{pm} = 0$  mrad and maximise the loss of other undesired components of the beam at the slit. In order to calculate the cost functional for the proton beam we have chosen a reference trajectory  $r_{ref}$  in units of cm (dashed line in Fig. 4.3) as a piecewise linear function of  $s$  defined along the transport line as,

$$r_{ref}(s) = \begin{cases} 0.25 + \frac{(1.8-0.25)}{40} \cdot s & \text{if } s < 40 \\ 1.8 & \text{if } 40 \leq s < 80 \\ 1.8 - \frac{(1.8-0.45)}{55} \cdot s & \text{if } 80 \leq s < 135 \\ 0.45 + \frac{(1.8-0.45)}{55} \cdot s & \text{if } 135 \leq s < 190 \\ 1.8 & \text{if } 190 \leq s < 230 \\ 1.8 - \frac{(1.8-0.45)}{50} \cdot s & \text{if } 230 \leq s < 280 \end{cases} \quad (4.11)$$

The matched beam envelopes (solid line) and the beam envelope obtained with initial setting (dash-dotted line) of the proton beam along the transport line for 10mA total beam current are shown in Fig. 4.3. The initial beam radius and divergence of all the species are same i.e.  $r(0) = 2.5$  mm,  $r'(0) = 0$  with fractions of  $p$ ,  $H_2^+$  and  $H_3^+$  as 80%, 15% and 5% respectively. It is evident from

Fig. 4.3 that for the initial set of parameters the trajectory of the proton beam does not satisfy the matching conditions at the final point and the radius of the proton beam at the slit location is larger than the slit size. The radius of proton beam is also beyond the allowed set value of  $r_{max} = 2$  cm along the beam line.

The beam envelope for  $H_2^+$  and  $H_3^+$  beams before the slit and after the selection by slit is shown in Fig. 4.4 for both the initial and optimised beam line parameters. It is readily seen that beam sizes of  $H_2^+$  and  $H_3^+$  at the position of the slit are larger in the case of optimised set of the parameters compared to the beam sizes with initial parameters. This indicates a loss of large fraction of total beam current due to  $H_2^+$  and  $H_3^+$  species at the slit position.

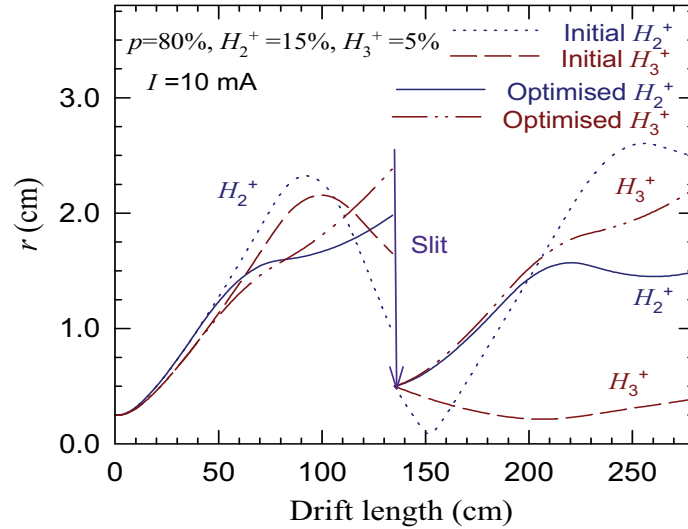


Figure 4.4: Plots of envelope radii of  $H_2^+$  beam (dotted line),  $H_3^+$  beam (dashed line) before optimisation and  $H_2^+$  beam (solid),  $H_3^+$  beam (dash-dotted) after optimisation of the beam line parameters. The initial and optimised transport parameters are same as in Fig. 4.3.

Figure 4.5(a) shows the optimised beam envelopes of  $p$ ,  $H_2^+$  and  $H_3^+$  having fractions of 80%, 15% and 5% respectively in the total initial beam current of 10 mA. At the slit most of the  $H_2^+$  and  $H_3^+$  beams are rejected whereas proton

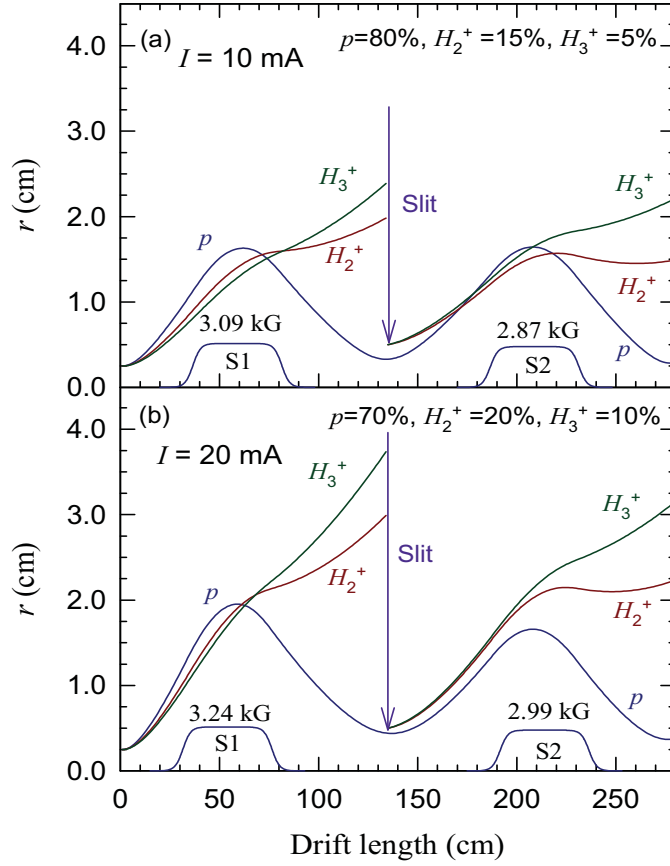


Figure 4.5: Evolution of envelope radii of  $p$ ,  $H_2^+$  and  $H_3^+$  beams for 10 mA and 20 mA beam current for two different fractions. The initial beam parameters for all the species are  $r(0) = 2.5$  mm,  $r'(0) = 0$  in both the cases.

beam passes through the slit without any loss in its beam current. The final beam parameters obtained for proton are  $r(278) = 2.83$  mm,  $r'(278) = 0$  which are very close to the values set in the matching condition as  $r_{pm} = 2.5$  mm,  $r'_{pm} = 0$ . The estimated fractions of  $p$ ,  $H_2^+$  and  $H_3^+$  after the slit are 98.6%, 1.15% and 0.25% respectively. A second slit at the waist position of proton having radius equal to the radius of proton beam (2.83 mm), can further reduce the beam of the other components. The estimated fractions of  $p$ ,  $H_2^+$  and  $H_3^+$  after the second slit are 99.95%, 0.043% and 0.007% respectively. The evolution of envelopes of  $p$ ,  $H_2^+$  and  $H_3^+$  with fractions 70%, 20% and 10% at 20 mA beam

current are also shown in Fig. 4.5(b) for comparison. The optimised beam line parameters for different fractions of  $p$ ,  $H_2^+$  and  $H_3^+$  at total beam current of 10 mA and 20 mA are given in Table 4.1.

Table 4.1: Optimised parameters for 10 mA total beam current with different fraction of  $p$ ,  $H_2^+$  and  $H_3^+$ . The initial emittances in  $\pi$ mmrad are; 54.7948 ( $p$ ), 38.7463 ( $H_2^+$ ) and 31.6376 ( $H_3^+$ ). ( $ld_1 + ld_2 + ld_3 = 280$  cm)

Beam current (mA)	Parameter	Initial values	Optimised values			
			1	2	3	4
			p=60% $H_2^+=20\%$ $H_3^+=20\%$	p=70% $H_2^+=20\%$ $H_3^+=10\%$	p=80% $H_2^+=10\%$ $H_3^+=10\%$	p=80% $H_2^+=15\%$ $H_3^+=5\%$
10	$B_1$ (kG)	3.97	3.05	3.05	3.04	3.09
	$B_2$ (kG)	2.47	2.95	2.94	2.92	2.87
	$ld_1$ (cm)	97	60	61	60	59
	$ld_2$ (cm)	144	152	150	153	150
20	$B_1$ (kG)	3.97	3.23	3.24	3.23	3.24
	$B_2$ (kG)	2.47	2.92	2.99	2.98	2.96
	$ld_1$ (cm)	97	57	54	55	55
	$ld_2$ (cm)	144	147	155	154	159

We have also done the calculation at higher beam current upto 40 mA and found that optimization technique works well. However for fixed length of the transport system the solenoid field and the amplitude of the envelope in the beam line increases with the higher value of the beam current. It is also difficult to get the desired beam waist size of the proton at the defined location. In order to transport higher current say in the range of 40 mA to 100 mA, one therefore needs to use the space-charge compensation to reduce the space-charge defocusing force. In that case the effective beam current will be reduced to  $I(1 - f)$  where  $f$  is the neutralization factor and the procedure discussed in this chapter can be easily utilized.

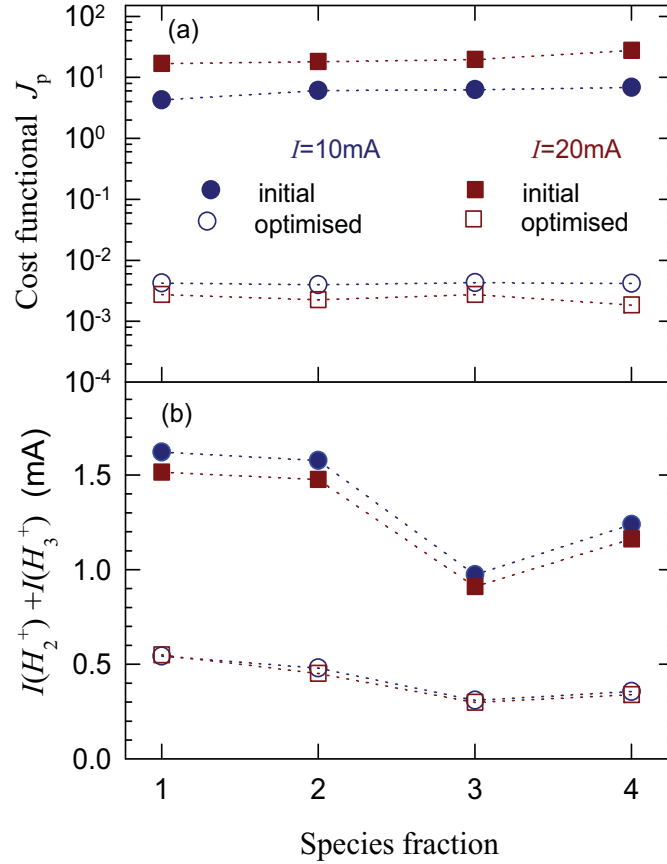


Figure 4.6: Cost functional of proton beam and total beam current of unwanted species just after selection by the slit for different fractions 1, 2, 3 and 4 of species as mentioned in Table 4.1. Results are presented for the optimised and unoptimised beam transport parameter for 10 mA and 20 mA.

The cost functional  $J_p$  defined in Eq. (4.9) as the least square distance between the actual trajectory and the reference trajectory over the entire transport line is shown in Fig. 4.6(a) for 10 mA and 20 mA of total beam current and at four different fractions 1, 2, 3 and 4 as mentioned in Table 4.1. It is evident from the figure that there is a substantial reduction almost by a factor of  $\sim 10^4$  in the cost functional in all the cases. It is to be noted here that the value of cost functional depends upon the choice of reference trajectory and one can further reduce it by a better choice of reference trajectory. The advantage of this method is that one can choose the reference trajectory as desired for the

transport of the beam and the program optimises the parameters accordingly. Figure 4.6(b) shows the reduction in the beam current of the unwanted species after the slit. Since the beam size of  $H_3^+$  at the slit is larger than  $H_2^+$ , the loss of  $H_3^+$  will be more compare to  $H_2^+$  at the slit. This fact is evident in Fig. 4.6(b) for the cases of fractions 3 and 4 where total beam current due to both the  $H_2^+$  and  $H_3^+$  are same but they have different fractions. The initial beam currents of unwanted species just before the slit, which are 4 mA, 3 mA, 2 mA and 2 mA for fractions 1, 2, 3 and 4 in the case of total beam current of 10 mA, are reduced to less than 0.5 mA in all the cases after the selection by the slit. It is interesting to note that the beam current of unwanted species after the slit for 20 mA total beam current are also same as in the case of 10 mA, though the values of beam current of these unwanted species before the slit are twice for 20 mA compare to the values in the case of 10 mA.

## 4.5 Summary and Discussion

The procedure outlined in this chapter provides a method to find optimal beam line settings for a space-charge-dominated multispecies beam using random search optimisation technique. We have used this technique and studied the transport of the high current proton beam in the presence of unwanted  $H_2^+$  and  $H_3^+$  species. The optimum magnetic fields and the positions of the two solenoid magnets have been obtained to transport and match the proton beam and maximise the reduction of the unwanted species at the position of the slit. In the optimisation, we have defined two cost functionals, one for the primary beam and other for the unwanted species. The major advantage of this method is that it is very simple to apply, easy to include any number of constraints without calculating any differentiation of the cost functional and is very fast.

# Chapter 5

## Beam Bunching in the Presence of Space Charge

### 5.1 Introduction

Most of the ion sources produce continuous beam of charged particles. In a cyclotron using such an external ion source, only a small fraction of the injected continuous beam is accepted in the central region for further acceleration. By transforming the continuous beam into a suitably bunched beam using a buncher prior to injection, the amount of accepted particles can be increased.

An ideal voltage waveform for a buncher is a sawtooth, however, it is very difficult to generate it at the required frequency and power level. Therefore, bunchers are fed with either a sinusoidal waveform or a nearly saw tooth like waveform obtained by combining the fundamental wave with its various higher harmonics. Sinusoidal bunchers, using the fundamental of sinusoidal voltage waveform at a gap, are the most frequently used bunchers in the axial injection system of the cyclotron. They typically bunch about 50% of the original dc beam in a phase width of  $30^\circ$  of rf [80]. Harmonic bunchers [81, 82, 83] where higher harmonics together with the fundamental rf are superimposed on a single bunching gap, capture as much as 60% - 80% of the dc beam depending upon

the number of harmonics used. In a double drift buncher, the beam is over-bunched by the first buncher operating at the fundamental frequency of the rf, allowed to drift a short distance, and then modulated again by a second buncher operating at twice the frequency of the first buncher and out of phase by  $180^\circ$ . The maximum efficiency obtainable with this technique depends on the voltages of two bunchers as well as on the ratio of the separation of two bunchers to the total drift length. These types of bunchers give a bunching efficiency slightly better than what is obtainable with three harmonics on a single bunching gap. Many workers have carried out detailed theoretical studies and optimization of parameters of such bunchers but their results are applicable only for low beam current.

As mentioned earlier, the axial injection system of the cyclotron consists of two solenoids to transport the beam together with a buncher and a spiral inflector [84]. In order to find out a suitable buncher as per our requirement in the limited space, we have carried out studies using a numerical technique to optimise the parameters of a sinusoidal, two harmonics and double drift bunchers and evaluated the performances as a function of beam current. In the case of a sinusoidal buncher for a given drift length and low beam current, one can achieve optimum bunching efficiency by varying only the voltage on the buncher electrode (assuming negligible energy spread in the beam). Same procedure does not work as we increase the beam current. For high beam current ( $I > 1$  mA), it is necessary to optimize both buncher voltage and as well as drift length to get the optimum performance. In the case of a double drift buncher (DDB), the distance between the two bunchers is another parameter requires to be optimised.

The phase acceptance of most of the cyclotron is roughly 10% of the rf cycle. The local beam current just before injection becomes  $\sim 10$  times higher

than the average beam current. This leads to large space-charge effects on the transverse beam size and affects the longitudinal bunching efficiency for average beam current more than 1 mA. Most of the high current cyclotrons are designed and developed for medical isotope productions and they produce average beam current in the range of 100 - 500  $\mu\text{A}$ . Since at this current level and for a nominal beam sizes  $\sim 5$  mm to 8 mm, the beam envelope is still dominated by the emittance, one can observe a very small space-charge effect on bunching.

The dependence of bunching efficiency of a double drift double harmonic buncher on beam intensity has been investigated experimentally at TRIUMF cyclotron up to 700  $\mu\text{A}$  of proton at injection voltage of 300 kV [85]. In the experimental results, a small but gradual drop in the bunching efficiency has been observed with the beam current. A detailed analysis of bunching using a sinusoidal buncher for 870 keV protons has been presented in Ref. [86] relevant only to the injector cyclotron at PSI. In compact cyclotrons, it is not possible to use such high injection energy because of the space problem in the central region for a high voltage inflector. An analysis of bunching performance related with cyclotron TR30 (injection energy 25 keV) [87] indicates that one needs to carefully optimize the drift distance to get good bunching efficiency in the case of high intensity beams. Further one should also use high injection energy in a compact cyclotron.

In this chapter we have carried out numerical simulation to optimise the bunching performance of sinusoidal, two harmonic and double drift bunchers in the presence of space charge. We have used disc model in the longitudinal direction and K-V envelope equation in the transverse direction. We have performed the numerical results at 100 keV proton beam and optimised the buncher parameters. The effect of buncher voltage and drift length on the bunching efficiency and the density distribution at the time focus has been studied for various

values of the beam current. The details of the buncher to be used in the axial injection system together with the results of simulations are also discussed.

## 5.2 Theory

In a buncher, an axial rf electric field generates a time dependent modulation of the ions velocity. This velocity modulation leads to a density modulation after a drift space. The buncher parameters are optimised to get the maximum number of ions in a given bunch width at the time focus. As long as the beam current is small, this optimisation can be easily done analytically [83]. At high beam current where space-charge-effect dominates, an analytical description becomes difficult and one rely on numerical simulation.

We have written a computer code using the well-known disc model [88, 89] in the longitudinal direction as used by many workers for sinusoidal bunchers to incorporate the effect of space charge and extended it for other kind of bunchers [90]. For the estimation of transverse beam size during bunching, we have used the K-V beam envelope equation. A length of the beam corresponding to the bunch spacing  $\beta\lambda_{rf}$ , is divided into a number of discs, where  $\beta$  is the relativistic term and  $\lambda_{rf}$  is the free space wavelength of applied rf. In order to improve the accuracy, a  $\beta\lambda_{rf}/2$  period is also included in both sides of the period  $\beta\lambda_{rf}$ . The average electric field of disc  $j$  on disc  $i$  is given by [88, 89]

$$E_{ij} = E_0 \sum_{n=1}^{\infty} \exp(-\beta_n |z_i - z_j|) \left( \frac{2J_1(\beta_n R)}{\alpha_n J_1(\alpha_n)} \right)^2 \text{sign}(z_i - z_j) \quad (5.1)$$

here  $E_0 = Q/(2\pi\epsilon_0 R^2)$ ,  $Q$  is the charge on each disc and  $R$  is the radius of disc.  $z_i, z_j$  are the positions of discs  $i$  and  $j$  respectively from the central disc.  $J_0$  and  $J_1$  are the Bessel functions,  $\alpha_n$  being the zero of order  $r$  of  $J_0$  and  $\beta_n = \alpha_n/b$  where  $b$  is the radius of the beam pipe. The total force acting on disc  $i$  can be

obtained by summing the effect of all the discs i.e.

$$F_i = Q \sum_{j=1}^N E_{ij}, \quad j \neq i \quad (5.2)$$

where  $N$  is the total number of discs in the length  $2\beta\lambda_{rf}$ . The total force on any disc due to all other discs depends only on the positions of the other discs. Since the positions of discs change along the drift length, it is necessary to divide the total drift distance into discrete steps. In the case of sinusoidal buncher, when discs pass through the buncher gap they receive voltage impulse and for the disc  $i$ , it is given by,

$$\Delta V_i = -V_1 \sin\left(\frac{4\pi(i-1)}{(N-1)}\right) \quad (5.3)$$

where  $V_1$  is the amplitude of the buncher voltage. In the case of two harmonic buncher, rf of frequencies  $\omega$  and  $2\omega$  are applied at the same gap. The voltage  $V_2$  of the rf of frequency  $2\omega$  is set  $180^\circ$  out of phase with respect to the voltage  $V_1$  of the rf of frequency  $\omega$ . The resultant voltage impulse on disc  $i$  after passing through such buncher gap is,

$$\Delta V_i = -V_1 \sin\left(\frac{4\pi(i-1)}{(N-1)}\right) + V_2 \sin\left(\frac{8\pi(i-1)}{(N-1)}\right) \quad (5.4)$$

The increase in the kinetic energy  $T_0$  of disc  $i$  after passing the buncher gap is given by,

$$T_i = T_0 + Q\Delta V_i \quad (5.5)$$

In the present calculation, the effect of the initial beam energy spread is not considered. The position and velocity of all discs have been calculated with respect to the central disc, which gets no impulse from the buncher. The position and velocity of disc  $i$  at distance  $L$  from the buncher in the absence of space-charge effect can be easily obtained using,

$$\delta\beta_i = (\beta_i - \beta_0), \quad z_i = (i - (N+1)/2)h + \delta\beta_i \frac{L}{\beta_0} \quad (5.6)$$

where,  $h = 2\beta\lambda_{rf}/N$ , is the width of each disc and  $\beta_i$  and  $\beta_0$  are the velocity parameters of disc  $i$  and that of the central disc respectively. In order to calculate the effect of space charge, it is necessary to divide the total drift length into many small intervals of length  $d$ , and can be chosen suitably to improve the numerical accuracy. The position of disc  $i$  after travelling a small distance  $d$ , as a result of velocity modulation by buncher voltage, is given by

$$z1_i = z_i + \delta\beta_i \frac{d}{\beta_0} \quad (5.7)$$

The space-charge force on a disc due to all other discs changes with the position of disc and thus modifies the velocity and energy of the disc at each step. The modified velocity (with respect to central disc) of disc  $i$  having mass  $M$ , after the first step is,

$$\delta\beta_{s_i} = \delta\beta_i + \frac{F_i}{M} \frac{d}{\beta_0 c^2} \quad (5.8)$$

The new position of disc  $i$  due to the velocity change caused by the space-charge force and velocity modulation is given by,

$$zn_i = z_i + \frac{\delta\beta_i + \delta\beta_{s_i}}{2} \frac{d}{\beta_0} \quad (5.9)$$

It is to be noted here that the effect of space-charge term has been averaged over small distance  $d$ . The above-mentioned steps are then repeated for all discs from  $i = 1$  to  $N$ . The position and velocity of all discs are then calculated at distances  $2d, 3d, 4d \dots$  till the central disc completes the total drift length  $L$ .

In a double drift beam buncher the fundamental rf voltage is applied at one gap and the second harmonic of rf voltage is applied at an another gap at a suitable distance from the first gap. In this case, disc  $i$  gets the voltage impulse and energy at the first gap as given by Eq. (5.3) and Eq. (5.5) and moves ahead. When it reaches the second gap it receives another voltage impulse given by,

$$\Delta V'_i = V_2 \sin \left( \frac{8\pi}{(N-1)} \frac{zn_i}{h} \right) \quad (5.10)$$

and

$$Tn_i = T_i + Q\Delta V'_i \quad (5.11)$$

where  $zn_i$  is the position of the disc  $i$  at the second buncher gap situated at a distance  $l = n.d$  from the first buncher. We then calculate the position and velocity of discs at distances  $(n+1)d, (n+2)d, \dots$  and so on till the central disc completes the total drift length  $L$ .

In order to know the beam radius along the transport line which is required in Eq. (5.1) we have used K-V beam envelope equation [15]. In our transport line there are two solenoid magnets for focussing the beam in the transverse direction. Since the focussing force due to the solenoid magnet is axially symmetric, the size of the beam in the transverse direction remains symmetric as the beam traverses along the axial direction. The K-V beam envelope equation for instantaneous beam radius  $R$  is given by

$$R'' + k^2(s)R - \frac{K(s)}{R} - \frac{\varepsilon^2}{R^3} = 0 \quad (5.12)$$

with

$$K(s) = K \frac{n(s)}{n} \quad (5.13)$$

Here  $\varepsilon$  is the transverse emittance of the beam,  $k(s) = qB_z(s)/(2mc\beta\gamma)$  is the focussing strength for the solenoid and  $B_z(s)$  is the axial magnetic field of the solenoid.  $\beta$  and  $\gamma$  are the usual relativistic factors.  $K = 2I/(I_0\beta^3\gamma^3)$  is known as the generalised perveance with  $I_0 = 31$  MA for proton and  $I$  is the average beam current. For a continuous beam perveance is constant. In the case of bunching, voltage modulation at the buncher gap leads to the density modulation as the beam advances and thus at each step current in the bunch changes. We have introduced this effect in our calculation by multiplying  $K$  with the ratio of the number of discs  $n(s)$  in the specified bunch width at location  $s$  in the drift to the number of discs  $n$  in the specified bunch width at the buncher location.

### 5.3 Numerical Results

In this section, we present the results of optimisation of the above-mentioned bunchers for 100 keV proton beam with normalised emittance of  $0.8\pi$  mmmrad. The operating frequency of the 10 MeV cyclotron is 42 MHz (4<sup>th</sup> harmonic operation) which gives the value of bunch spacing  $\beta\lambda_{rf}$  equal to  $\sim 10.5$  cm. We have written a computer code, which calculates the position and velocity of all the discs including the space-charge forces at any specified position along the drift length. In the present calculation we have taken 360 discs in one bunch spacing, but this can be changed as required. Before performing the simulation, the force on a disc due to all other discs for 5000 disc separations have been calculated in advance and stored in a file for interpolation. This helps in reducing the computational time. Figure 5.1 shows the plot of normalised electric field as a function of disc separation. We can see that the influence of electric field is almost negligible when the discs separation are more than  $\beta\lambda_{rf}/4$ . Numerical calculations indicate that one disc per degree gives a good accuracy. We have calculated the efficiency of all the bunchers for a bunch width of  $30^\circ$  of rf at the time focus. In the initial calculations, it has been assumed that the beam radius will remain approximately constant ( $R = 5$  mm, can be adjusted by focusing with a long solenoid) during the drift.

Figure 5.2 shows the optimised bunching efficiency for a sinusoidal buncher as a function of the buncher voltage and the drift length. The bunching efficiency is the ratio of the number of discs in the specified phase width to the number of discs in one  $\beta\lambda_{rf}$ . It is observed that at low beam current ( $< 1$  mA), the bunching efficiency remains almost constant and is independent of the drift length. However, the optimum buncher voltage increases as the drift length is decreased. This behaviour is similar to the bunching process as observed in the absence of space-charge effects. For higher currents ( $> 1$  mA), the bunching

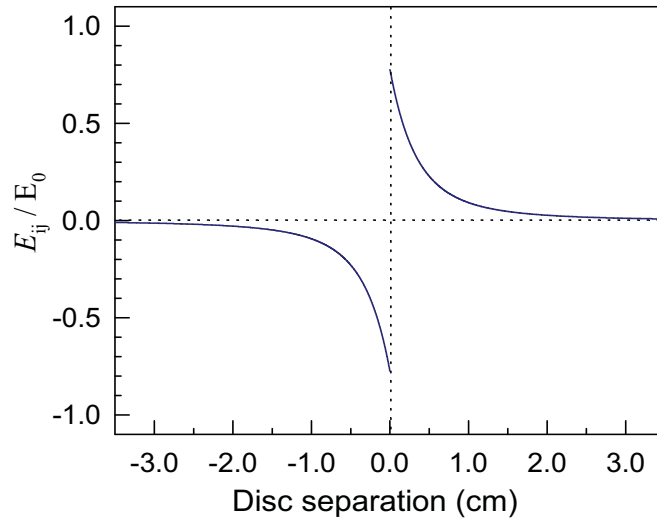


Figure 5.1: Normalised electric field  $E_{ij}/E_0$  as a function of the disc separation. The bunch spacing  $\beta\lambda_{rf}$  is equal to 10.5 cm.

efficiency remains almost constant up to a certain drift length and then decreases rapidly as the drift length is increased. This decrease in bunching efficiency is sharper at higher beam currents. This behaviour is independent of the voltage on the buncher and is shown in Fig. 5.2 for several values of beam current optimised for the beam phase width  $30^\circ$  of rf.

We have found that for a given beam current and a fixed phase width there is an optimum drift length below which the bunching efficiency remains almost constant. However, the buncher voltage increases as we decrease the drift length from the optimum value. It is obvious that one should use the buncher voltage as minimum as possible to save the rf power as well as to restrict the spread in the beam energy in the bunch. We define an optimum drift length which requires minimum buncher voltage for bunching efficiency of 90% of the maximum bunching efficiency. The optimum drift length decreases as we increase the beam current. Figure 5.3 shows the variation of the optimum drift length and optimised buncher voltage for various values of the beam current for beam

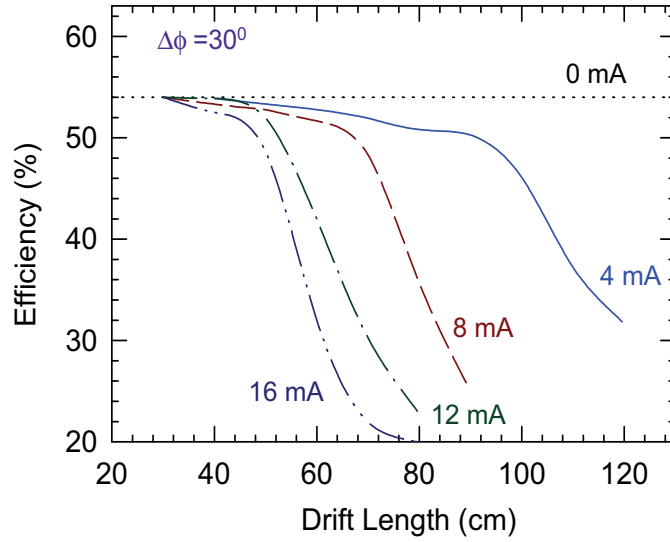


Figure 5.2: Optimised bunching efficiency of a sinusoidal buncher as a function of the drift length for various values of the beam current of 100 keV proton beam. The beam radius is 5 mm and the phase width at time focus is  $30^\circ$  of rf for all the cases.

radii of 5 mm and 8 mm. It is clear that the beam radius plays a crucial role and a large beam radius is advantageous. It requires not only the less buncher voltage but also gives more flexibility in the choice of the drift length for a given beam current.

In two harmonics buncher, the rf voltage of frequency  $\omega$  and  $2\omega$  are applied at the same gap. The voltage  $V_2$  of second harmonic ( $2\omega$ ) of rf is adjusted  $180^\circ$  out of phase with respect to the voltage  $V_1$  of the fundamental ( $\omega$ ) of rf. We have optimised the bunching efficiency by varying the voltages of the two harmonics. For the double drift bunching system, the bunching efficiency has been optimised by varying the voltages and the separation between  $\omega$  and  $2\omega$  bunchers. It has been observed that for a particular value of the beam current, the optimum drift length  $L$  remains same for sinusoidal, two harmonic and double drift bunchers. Thus the drift length  $L$  between the buncher and the time focus is a crucial parameter to obtain a good bunching efficiency for a

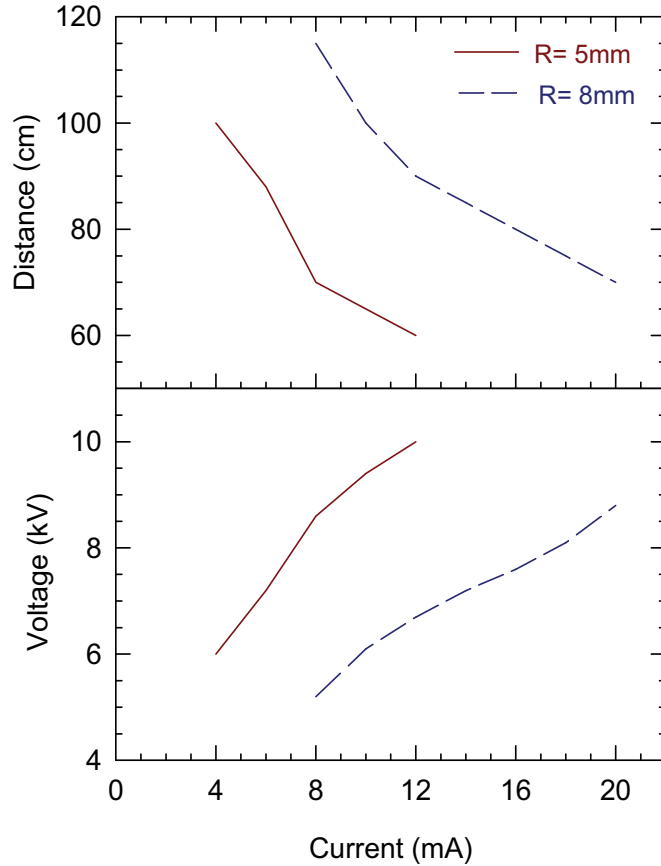


Figure 5.3: Variation of the optimum drift length and buncher voltage as a function of the beam current. The beam phase width at the time focus is  $30^\circ$  of rf.

given beam current.

The variations of buncher voltage  $V_1(\omega)$  and the ratio of voltages  $V_2(2\omega)$  and  $V_1(\omega)$  for two harmonic buncher are shown in Fig. 5.4 as a function of beam current. In all the cases bunching efficiency is  $\sim 73\%$  for phase width  $30^\circ$  of rf. The variation of the bunching efficiency of double drift buncher with  $l/L$  is shown in Fig. 5.5 for three values of beam current and optimum drift length. Here  $l$  is the distance between the two buncher gaps and  $L$  is the distance of time focus from the first buncher. As it appears, the ratio  $l/L$  for maximum bunching efficiency is approximately equal to 0.22 for all cases.

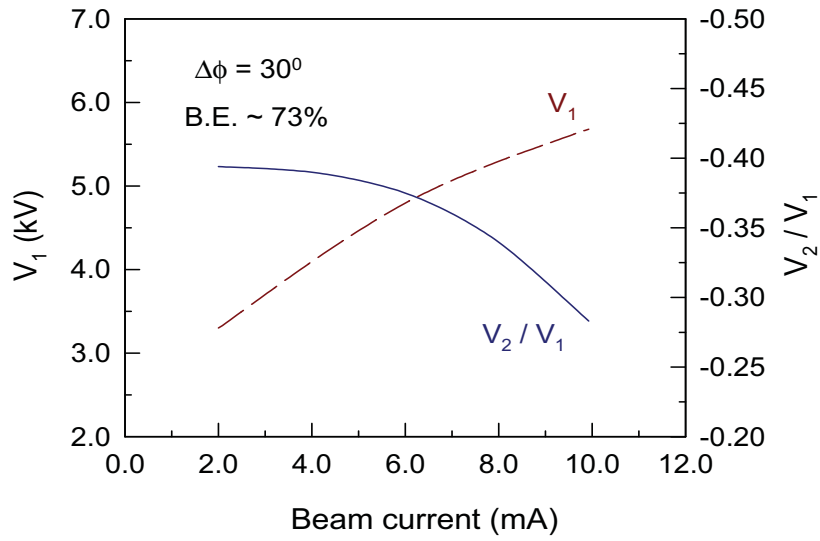


Figure 5.4: Variation of the parameters of a two harmonic buncher with the beam current. The bunch width at the time focus is  $30^\circ$  of rf and the beam radius is 5 mm.

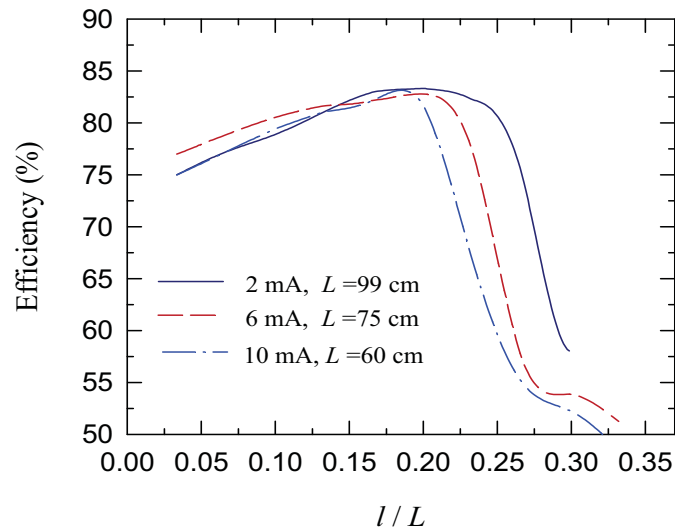


Figure 5.5: Variation of the bunching efficiency for a double drift buncher as a function of  $l/L$  for three different values of the beam current. The beam bunch width at the time focus is  $30^\circ$  of rf and the beam radius is 5 mm.

As mentioned earlier the axial injection system of the proposed 10 MeV, 5 mA proton cyclotron consists of a 2.45 GHz microwave ion source to deliver 100 keV, 20 mA (maximum) proton beam, two solenoids (S1 and S2) with

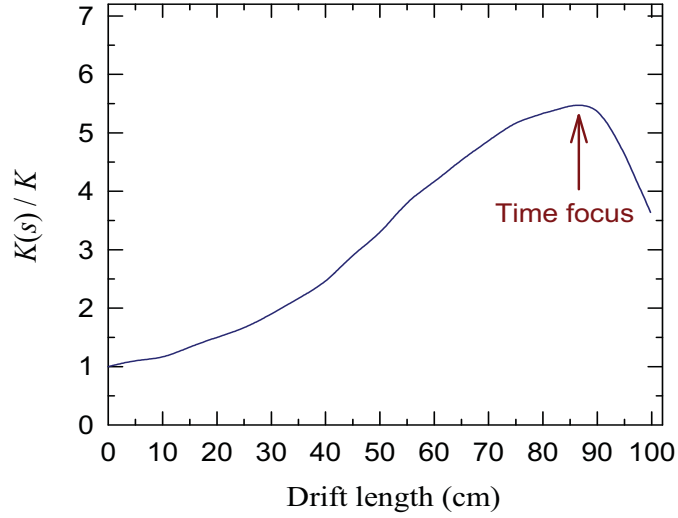


Figure 5.6:  $K(s)/K$  as a function of drift length showing the effect of increasing beam current in the bunch on the perveance.

physical length 40 cm to transport the beam together with a buncher and a spiral inflector. The length of the Low Energy Beam Transport (LEBT) is  $\sim 2.8$  meter. In between the two solenoids there is a slit to remove the undesired part of the beam and a faraday cup to measure the beam current. As we have already mentioned that in the case of bunching, the voltage modulation at the buncher gap leads to the density modulation as the beam advances and thus at each step perveance of the bunch  $K(s)$  assumes a new value. The numerical estimate of the  $K(s)/K$  as a function of drift length (Fig. 5.6) shows the effect of density modulation on perveance as the beam advances in the drift.

The optimised beam envelope for 10 mA of beam current, obtained by solving K-V beam envelope equation is shown in Fig. 5.7 (dash-dotted line). The maximum drift distance available in the transport line is  $\sim 100$  cm (from the end of the buncher) with one solenoid magnet S2 in between the buncher and the time focus. We have carried out the optimisation of a sinusoidal buncher for this particular case using the above mentioned disc model in the longitudinal

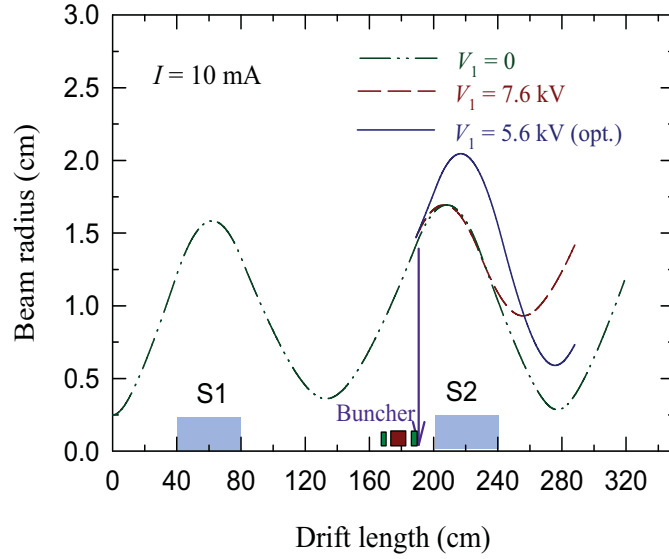


Figure 5.7: *Beam envelopes for 10 mA proton beam in the injection line. (a) dash-dotted line: without buncher, magnetic field of S1 and S2 are 3.034 kG and 2.88 kG respectively, beam radius at time focus is 2.85 mm. (b) dashed line: with buncher on and unoptimised, (c) solid line: with buncher on and optimised, magnetic field of S1 and S2 are 3.034 kG and 2.96 kG respectively and the beam radius at time focus is 6.03 mm. The beam phase width is  $30^\circ$  of rf.*

direction and K-V beam envelop equations in the transverse direction. This way we have taken care of the change in beam radius within the phase width during the bunching as the beam travels in the drift space. In this optimisation we have varied the position and strength of the solenoid S2 to get the beam waist at the same location. The dashed curve in Fig. 5.7 shows the beam envelope with buncher on. As it appears the waist of the beam is formed earlier and the size of the beam is also increased. It was not possible to form the waist at the desired location with a reasonable beam size by varying the buncher voltage and the magnetic field of the solenoid magnet S2. In order to get the beam waist at the same location as in the case of continuous beam, we have to shift the location of the solenoid S2 by 15 cm. In the optimisation, we have taken care that beam waist and time focus both are formed at the same location. As

seen in Fig. 5.7 (solid line) there is an increase in the beam size in the solenoid and at the waist also. Figure 5.8 shows the density distribution of the discs at the time focus. The bunching efficiency in this case is  $\sim 47\%$  for phase width of  $\pm 15^\circ$  of rf and the energy width within the bunch is  $\pm 2.0$  keV.

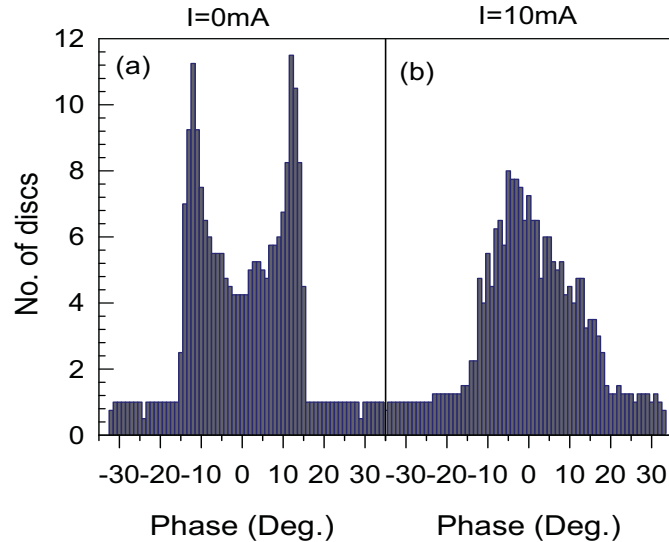


Figure 5.8: Density distribution of discs at the time focus for beam phase width of  $30^\circ$  of rf. (a) Without space charge: buncher voltage  $V_1 = 5.32$  kV and bunching efficiency is equal to 54%. (b) With space charge (10 mA beam current): optimized buncher voltage  $V_1 = 5.6$  kV and bunching efficiency is 47%. The restricted energy width  $\Delta E = \pm 2.0$  keV.

## 5.4 Summary and Discussion

In this chapter we have presented the results of numerical simulations carried out for sinusoidal, two harmonic and double drift bunchers in the presence of space charge. We have shown that the location of buncher from the time focus is a very crucial parameter in the case of high beam current. For a given beam current there is an optimum drift length beyond which the bunching efficiency decreases rapidly and is independent of buncher voltage. This decrease in bunching efficiency is sharper at higher beam currents. We have also seen

that the optimum drift length remains the same whether one uses a sinusoidal or a double harmonic or a double drift buncher. A prior knowledge of the buncher parameters is useful in setting up and tuning a bunching system without much experimentation and the results presented here will help in this regard. The method of optimization based on disc model has helped us to obtain the required buncher parameters and configuration for our injection system. This method can be easily applied to any type of bunchers used in the accelerator laboratories.

# Chapter 6

## Dynamics of Intense Beam during Bunching

### 6.1 Introduction

The longitudinal compression of space-charge-dominated beam has been studied extensively in theory, simulations [91, 92, 93, 94, 95, 96, 97] and experiments [98, 99, 100]. Considerable progress has been made in the development and application of one dimensional Vlasov-Maxwell model [91, 92, 93, 94], warm-fluid model [101, 102, 103] and cold-fluid model [104] to describe the longitudinal beam dynamics of intense beams for long bunch. Such models rely heavily on using a quasi self-consistent  $g$ -factor model [105, 106, 107] to incorporate the average effects of transverse beam geometry. In a situation, where the bunch size becomes comparable to the beam radius, the  $g$ -factor model is no longer valid. In such situation one needs to include the effect of longitudinal electric field in the transverse motion.

In this chapter we have developed a model to study the beam dynamics of intense beams during the bunching for the cases when the bunch size is comparable to beam radius [90, 108]. Since ion beams from the ion source can never be monoenergetic, the finite longitudinal energy spread in the beam is

also included in the simulation. During the bunching, the line charge density along the beam bunch does not remain uniform, as a result different portions of the beam in the bunch evolve differently along the transport line. We have included this effect in the analytical formulation [109]. Finally, we have carried out simulations using a 3D PIC method to investigate the beam dynamics self-consistently in more detail.

## 6.2 Longitudinal Dynamics

In order to study the beam dynamics, we have divided the beam into large number of discs and slices. A schematic illustration of the beam frame and laboratory frame is shown in Fig. 6.1. Here,  $s$  is the longitudinal coordinate of the bunch centre from the buncher gap,  $z$  is the longitudinal coordinate in the bunch frame,  $z_i$  is the coordinate of thin disc  $i$  used for longitudinal dynamics and  $Z_i$  is the coordinate of the centre of thick slice  $i$  from the bunch centre. The thick slices are used for numerical modelling of the transverse envelope equation describing the evolution of the bunch radius  $R(z, s)$ . Here  $z_i = 0$  and  $Z_i = 0$  correspond to the location of the bunch centre. The positions of thin discs  $z_i$  evolve during the bunching, whereas the position of thick slice  $Z_i$  is fixed in the beam frame.

### 6.2.1 Beam Energy Spread

Apart from ion temperature, fluctuations in the extraction voltage, a physical limitation on the minimum energy spread in the beam also results from the space-charge effect of the beam during the transport in a conducting beam pipe. The electrostatic potential distribution [15] for a beam having uniform density in the radial direction in a beam pipe of radius  $b$  (with  $\phi(b) = 0$ ) is

$$\phi(r) = \frac{30I}{\beta} \left( 1 + 2 \ln \frac{b}{R} - \frac{r^2}{R^2} \right), r \leq R, \quad (6.1)$$

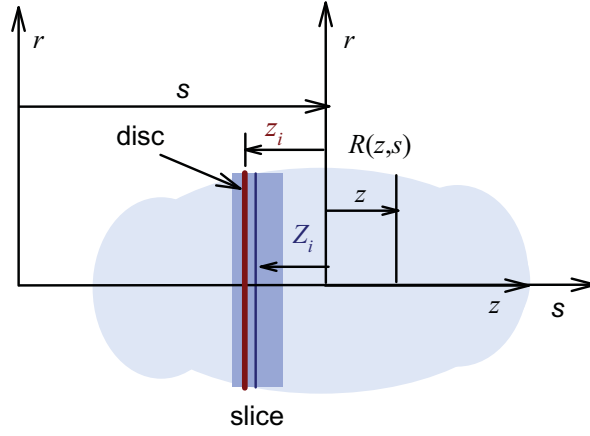


Figure 6.1: A schematic illustration of beam frame and laboratory frame.

Here  $R$  is the beam radius and  $I$  is the beam current. Due to the space-charge field, part of the kinetic energy of the particle inside the beam is converted into electrostatic potential energy. The magnitude of the energy spread can be estimated by taking difference of potentials at  $r = 0$  and  $r = R$  which is equal to  $30I/\beta$ . The minimum value of the energy spread due to the space-charge effect is  $\sim 20$  eV for 100 keV, 10 mA protons.

In order to study the finite longitudinal energy spread on the beam dynamics we have assumed that the longitudinal energy distribution in the continuous beam is Gaussian before entering the buncher gap with

$$f(E) = \frac{1}{\sqrt{2\pi}\sigma_E} \exp\left(-\frac{(E - E_0)^2}{2\sigma_E^2}\right) \quad (6.2)$$

Here  $\sigma_E$  is the resultant energy spread due to all the effects discussed earlier. After crossing the buncher gap the velocity of the beam will be modulated depending upon the time of arrival of the beam particle at the buncher gap. For a sinusoidal voltage applied at the buncher gap, the resulting velocity modulation

is given by

$$\Delta v(z) = -\frac{eV_b}{mv} \sin\left(\frac{\omega z}{v}\right) \quad (6.3)$$

where  $V_b$  is the amplitude of the buncher voltage of frequency  $\omega$  and  $z$  is the longitudinal coordinate in the beam frame from the centre of the bunch and has a span of  $-\beta\lambda_{rf}/2$  to  $\beta\lambda_{rf}/2$ .

## 6.2.2 Average Longitudinal Electric Field

In order to obtain the longitudinal electric field of the beam having different density profiles in the transverse direction we have used the Green function method and assumed that the beam is axisymmetric. The beam potential  $\phi(r, z)$  inside a conducting pipe with radius  $b$  is given by

$$\phi(r, z) = \int \int G(r, z; r_s, z_s) \rho(r_s, z_s) r_s dr_s dz_s \quad (6.4)$$

where  $G(r, z; r_s, z_s)$  is the Green function and  $\rho(r_s, z_s)$  is the charge density of the beam at the source point  $(r_s, z_s)$ . The coordinates  $(r, z)$  denote the field point where potential  $\phi(r, z)$  is to be calculated. The Green's function  $G$  for an axisymmetric charge distribution can be obtained from a Bessel series expansion [108, 110, 111, 112] as

$$G(r, z; r_s, z_s) = \frac{1}{\varepsilon_0 b} \sum_{n=1}^{\infty} \frac{J_0(\beta_n r) J_0(\beta_n r_s)}{\alpha_n J_1^2(\alpha_n)} \exp(-\beta_n |z - z_s|) \quad (6.5)$$

where,  $\beta_n = \alpha_n/b$  and  $\alpha_n$ 's are the zeros of the Bessel function  $J_0$ . The longitudinal component of the space-charge field is given by  $E_z = -\partial\phi/\partial z$ . The electric field  $E_{ij}(r, s)$  at a position  $(r, z_i, s)$  due to a thin disc of width  $w$  and fixed charge  $Q$  located at  $z_j$  is given by

$$\begin{aligned} E_{ij}(r, s) &= \frac{1}{\varepsilon_0 b^2} \sum_{n=1}^{\infty} \exp(-\beta_n |z_i - z_j|) \frac{J_0(\beta_n r)}{J_1^2(\alpha_n)} \\ &\times \int_0^{R_j} J_0(\beta_n r') \sigma(r', R_j) w r' dr' \text{sign}(z_i - z_j) \end{aligned} \quad (6.6)$$

where  $R_j = R(z_j, s)$  is the radius of disc  $j$  at the position  $z_j$  when the bunch centre is at location  $s$  and  $\sigma(r', R_j)$  is the charge density of disc  $j$  per unit length. The integration over  $z$  is not required because discs are infinitesimally thin. Since we have assumed that the total charge  $Q$  in a disc will remain fixed, we have  $Q = \lambda w$ , where  $\lambda$  is the constant line charge density of a disc given by

$$\lambda = \int_{r=0}^{R_j} \sigma(r, R_j) 2\pi r dr \quad (6.7)$$

The average longitudinal electric field on disc  $i$  due to disc  $j$  is given by

$$\langle E_{ij}(r, s) \rangle = \frac{\int_{r=0}^{R_i} \int_{\phi=0}^{2\pi} E_{ij}(r, s) \sigma(r, R_i) r dr d\phi}{\int_{r=0}^{R_i} \int_{\phi=0}^{2\pi} \sigma(r, R_i) r dr d\phi} \quad (6.8)$$

Equation (6.6) and Eq. (6.8) can be used to evaluate a close expression for the average electric field  $\langle E_{ij}(r, s) \rangle$  for a wide range of choices of beam density profile  $\sigma(r, R)$ . In the following section we discuss two types of fixed shape density profiles, one is of the bell shape type and other is of hollow shape type.

### 6.2.3 Fixed Shape Density Profile $\sigma(r, R)$

Let us assume the transverse beam density profile  $\sigma(r, R)$  as [16]

$$\sigma(r, R) = \begin{cases} \lambda f\left(\frac{r}{R}\right) & 0 \leq r \leq R \\ 0 & R < r \leq b \end{cases} \quad (6.9)$$

where  $f(r/R)$  is a smooth function that depends on scaled radial variable  $r/R$ . There are many choices for density distribution function  $f(r/R)$  in Eq. (6.9).

In order to generate bell shape density distribution, we assume

$$f\left(\frac{r}{R}\right) = \sigma_B(p, R) \left(1 - \frac{r^2}{R^2(p)}\right)^p \quad 0 \leq r \leq R \quad (6.10)$$

and for the hollow shape density distribution, we consider

$$f\left(\frac{r}{R}\right) = \sigma_H(p, R) \left(1 + \frac{r^2}{R^2(p)}\right)^p \quad 0 \leq r \leq R \quad (6.11)$$

where  $p = 0, 1, 2, \dots$  is a positive integer. It decides the peakedness and hollowness of the beam distribution. The value of  $p = 0$  corresponds to the uniform

distribution in both the cases. The terms  $\sigma_B(p, R)$  and  $\sigma_H(p, R)$  for the bell shape and hollow shape distributions respectively, are to be determined from the normalisation condition. In order to analyse and compare the behaviour of uniform, bell shape and hollow shape beam distributions during bunching, we consider the concept of equivalent beams [15, 113]. According to this concept the equivalent beam must have the same second moments as the actual beam. Thus for rms-matched beams we have  $\langle x^2 \rangle_0 = \langle x^2 \rangle_p$ . The expression of  $\langle x^2 \rangle_p$  for the bell shape density distribution and  $\langle x^2 \rangle_0$  for uniform density distribution are given by

$$\langle x^2 \rangle_p = \frac{R^2(p)}{2(p+2)}, \quad \langle x^2 \rangle_0 = \frac{R^2(0)}{4} \quad (6.12)$$

It then follows that

$$R^2(p) = \frac{(p+2)R^2(0)}{2} \quad (6.13)$$

Using the normalisation condition defined in Eq. (6.7), we can easily obtain

$$\sigma_B(p, R) = \frac{p+1}{\pi R^2(p)} \quad (6.14)$$

Similarly, for the hollow shape distribution we have

$$\langle x^2 \rangle_p = \frac{(p2^{p+1} + 1) R^2(p)}{2(p+2)(2^{p+1} - 1)} \quad (6.15)$$

$$R^2(p) = \frac{(p+2)(2^{p+1} - 1) R^2(0)}{2(p2^{p+1} + 1)} \quad (6.16)$$

$$\sigma_H(p, R) = \frac{p+1}{\pi(2^{p+1} - 1) R^2(p)} \quad (6.17)$$

Figure 6.2 compares the function  $f(r/R)\pi R^2$  as a function of normalised beam radius  $r/R$  for bell shape and hollow shape distributions at different values of parameter  $p$ .

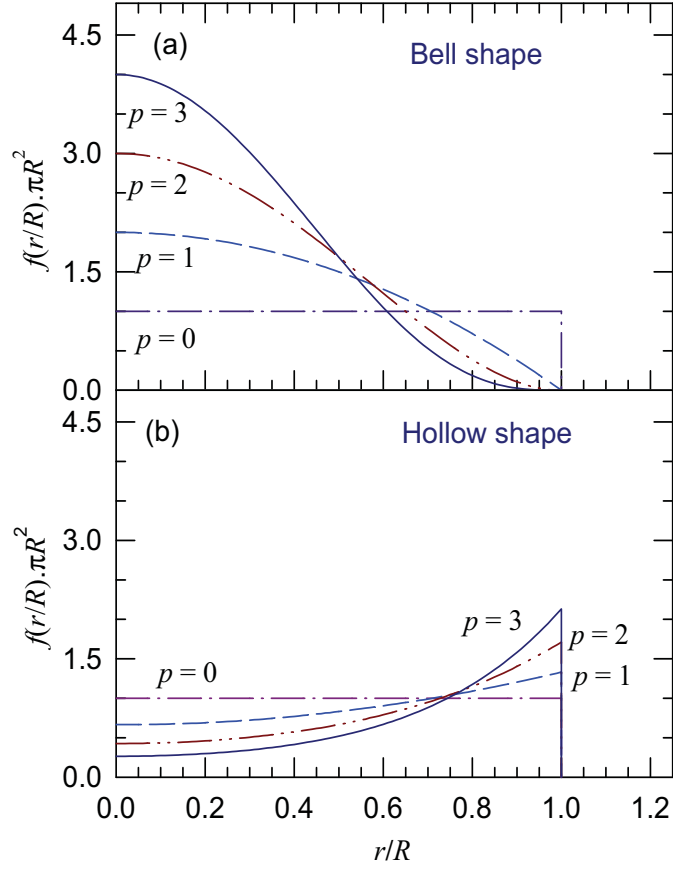


Figure 6.2: Plot of distribution function  $f(r/R)\pi R^2$  as a function of  $r/R$  for (a) bell shape and (b) hollow shape distributions with  $p = 0, 1, 2, 3$ .

#### 6.2.4 Evaluation of $\langle E_{ij} \rangle$ for Fixed Shape Density Profile

In this subsection we will derive expressions for the average electric field  $\langle E_{ij} \rangle$  on disc  $i$  due to disc  $j$  for the class of fixed shape density profiles described in Eq. (6.10) and Eq. (6.11) for the bell shape and hollow shape distributions. Using Eq. (6.6) and Eq. (6.10) we can write the expression for electric field on disc  $i$  due to disc  $j$  for the case of bell shape distribution as,

$$\begin{aligned}
 E_{ij}(r, p, s) &= \frac{\lambda \sigma_B(p, R_j) w}{\epsilon_0 b^2} \sum_{n=1}^{\infty} \exp(-\beta_n |z_i - z_j|) \frac{J_0(\beta_n r)}{J_1^2(\alpha_n)} \\
 &\times \int_0^{R_j} J_0(\beta_n r') \left(1 - \frac{r'^2}{R_j^2}\right)^p r' dr' \cdot \text{sign}(z_i - z_j) \quad (6.18)
 \end{aligned}$$

here  $R_j = R(p, z_j, s)$  is the radius of the  $j^{\text{th}}$  disc. Using Eq. (6.10) and Eq. (6.18) in Eq. (6.8), we can obtain the average longitudinal electric field on disc  $i$  due to disc  $j$  as (see **Appendix B**)

$$\begin{aligned} \langle E_{ij}(r, p, s) \rangle &= \frac{Q2^{2p+1} ((p+1)!)^2 b^{2p}}{\pi\epsilon_0 R_i^{p+1} R_j^{p+1}} \sum_{n=1}^{\infty} \frac{\exp(-\beta_n |z_i - z_j|)}{J_1^2(\alpha_n)} \\ &\times \frac{J_{p+1}(\beta_n R_i) J_{p+1}(\beta_n R_j)}{\alpha_n^{2p+2}} \text{sign}(z_i - z_j) \end{aligned} \quad (6.19)$$

A similar exercise for hollow shape distribution yields (see **Appendix B**)

$$\begin{aligned} \langle E_{ij}(r, p, s) \rangle &= B_H 2^{2p} b^2 \sum_{n=1}^{\infty} \frac{\exp(-\beta_n |z_i - z_j|)}{J_1^2(\alpha_n)} \left[ \frac{R_i}{\alpha_n} J_1(\beta_n R_i) - \frac{pb}{\alpha_n^2} J_2(\beta_n R_i) \right. \\ &+ \frac{p \cdot (p-1) b^2}{\alpha_n^3 R_i} J_3(\beta_n R_i) - \dots + \frac{(-1)^p p! b^{p-1}}{\alpha_n^{p+1} R_i^{p-1}} J_{p+1}(\beta_n R_i) \left. \right] \\ &\times \left[ \frac{R_j}{\alpha_n} J_1(\beta_n R_j) - \frac{pb}{\alpha_n^2} J_2(\beta_n R_j) + \frac{p \cdot (p-1) b^2}{\alpha_n^3 R_j} J_3(\beta_n R_j) \right. \\ &\left. - \dots + \frac{(-1)^p p! b^{p-1}}{\alpha_n^{p+1} R_j^{p-1}} J_{p+1}(\beta_n R_j) \right] \cdot \text{sign}(z_i - z_j) \end{aligned} \quad (6.20)$$

where,  $B_H = \frac{2Q(p+1)^2}{\pi\epsilon_0(2^{p+1}-1)^2 R_i^2 R_j^2 b^2}$ .

Using Eq. (6.19) and Eq. (6.20) one can calculate the average electric field on disc  $i$  due to disc  $j$  for various kind of beam distributions.

## 6.2.5 Equation of Motion

In the disc model each disc, identified by index  $i$ , is characterized by fixed charge  $Q$ , mass  $M$ , an axial velocity  $v_i$ , longitudinal position  $z_i$ . The longitudinal equation of motion of each disc in the beam frame can be written as,

$$\frac{dz_i}{ds} = \frac{v_i}{v} \quad (6.21)$$

$$\frac{dv_i}{ds} = \frac{Q}{\gamma M v} [E^{rf} + E^{sc}(z_i, s)] \quad (6.22)$$

where,  $E^{sc}(z_i, s) = \sum_j \langle E_{ij}(r, s) \rangle$ ,  $j \neq i$  is the total space-charge field on disc  $i$ . Here,  $v$  is the velocity with which the central disc in the defined bunch width

moves. The field  $E^{sc}(z_i, s)$  which is due to the space charge will be experienced by the discs throughout the motion whereas the field  $E^{rf}$  will act only once on a disc at the buncher gap.

## 6.3 Transverse Dynamics

The transverse beam dynamics has been studied by employing the beam envelope equation. Since the longitudinal electric field depends upon the beam radius, an accurate calculation of the radius is necessary to simulate the longitudinal beam dynamics correctly. In order to include the possible variation of beam radius along the length of the beam and to understand the behaviour of projected emittance during the bunch compression, we have divided the length  $\beta\lambda_{rf}$  of the beam into thick slices, where  $\lambda_{rf}$  is the wavelength of the rf. The position of the slices is fixed with respect to the beam centre. The evolution of the radius of the slices is then found out under the influence of external force and space-charge force of the beam during the bunch compression.

### 6.3.1 Beam Envelope Equation

We now begin with the rms envelope equation of each slice for a cylindrically symmetric beam in a beam transport line. The equation for rms envelope  $\tilde{x}(Z, s)$  is given by

$$\tilde{x}'' + k(Z, s)\tilde{x} - \frac{\langle xF_x \rangle}{m\gamma v^2 \tilde{x}} - \frac{\tilde{\epsilon}^2(Z, s)}{\tilde{x}^3} = 0 \quad (6.23)$$

here,  $Z$  is the position of a slice with respect to the bunch centre and in this case it covers a span of  $-\beta\lambda_{rf}/2 \leq Z \leq \beta\lambda_{rf}/2$ . The prime denotes differentiation with respect to the variable  $s$ .  $F_x$  is the space-charge force and  $\tilde{\epsilon}(Z, s)$  is the rms emittance of the slice and  $k(Z, s)$  represents the focussing strength of the external force. Furthermore, the rms emittance also includes the contribution due to the time dependent rf force applied at the buncher gap. For an

axisymmetric beam, we have from Maxwell's equation

$$\frac{1}{r} \frac{\partial}{\partial r}(rE_r) + \frac{\partial E_z}{\partial z} = \frac{\rho(r, z)}{\epsilon_0} \quad (6.24)$$

Using Taylor series expansion [15, 108] and keeping only first order term in the expansion of  $\partial E_z(r, z)/\partial z$  we can write,

$$E_r(r, z) \approx \frac{1}{\epsilon_0 r} \int_0^r r \rho(r, z) dr - \frac{r}{2} \frac{\partial E_z(0, z)}{\partial z} \quad (6.25)$$

After substituting the expression of  $E_r(r, z)$  in Eq. (6.23) and using some algebra, we can write the envelope equation of each slice as [109]

$$\tilde{x}'' + k(Z, s)\tilde{x} - \frac{K(Z, s)}{4\tilde{x}} + \frac{q}{2mc^2\beta^2\gamma^2} \frac{\partial E_z(Z, s)}{\partial Z} \tilde{x} - \frac{\tilde{\epsilon}^2(Z, s)}{\tilde{x}^3} = 0 \quad (6.26)$$

Here  $K(Z, s) = 2I(Z, s)/(I_0\beta^3\gamma^3)$ ,  $I(Z, s)$  being the current in the slice given by  $N_d(Z, s)Q\beta c/\Delta g$ , where  $N_d(Z, s)$  is the number of discs in the slice at location  $(Z, s)$  and  $\Delta g$  is the width of the slice.  $I_0$  is the characteristics current and for proton  $I_0 = 31$  MA. Using the expression of the rms beam size in terms of total beam radius  $R(p, Z, s)$  as given in Eq. (6.12) for the case bell shape density distribution, we can write

$$R'' + k(Z, s)R - \frac{(p+2)}{2} \frac{K(Z, s)}{R} + \Lambda(Z, s)R - \frac{\epsilon^2(Z, s)}{R^3} = 0 \quad (6.27)$$

where  $\epsilon = 2(p+2)\tilde{\epsilon}$  and  $\Lambda(Z, s) = \frac{q}{2mc^2\beta^2\gamma^2} \frac{\partial E_z(Z, s)}{\partial Z}$ . The term  $\Lambda(Z, s)R$  in the envelope equation is the force in the radial direction due to the axial variation of the longitudinal electric field. Similarly for the hollow shape density distribution, we can use Eq. (6.15) and write the envelope equation as

$$R'' + k(Z, s)R - \frac{2(p+2)(2^{p+1}-1)}{4(p2^{p+1}+1)} \frac{K(Z, s)}{R} + \Lambda(Z, s)R - \frac{\epsilon^2(Z, s)}{R^3} = 0 \quad (6.28)$$

with  $\epsilon = \frac{2(p+2)(2^{p+1}-1)}{(p2^{p+1}+1)}\tilde{\epsilon}$ . The number of discs in a given slice and hence  $I(Z, s)$  can be obtained by evaluating the position of discs using longitudinal dynamics.

The projected emittance of the bunch can be obtained by summing over the ensemble of beam slices covering the bunch and is given by

$$\varepsilon p(s) = \sqrt{\langle R^2 \rangle \langle R'^2 \rangle - \langle RR' \rangle^2} \quad (6.29)$$

where

$$\begin{aligned} \langle R^2 \rangle(s) &= \frac{1}{N_s} \sum_{j=1}^{N_s} R^2(Z_j, s), & \langle R'^2 \rangle(s) &= \frac{1}{N_s} \sum_{j=1}^{N_s} R'^2(Z_j, s), \\ \langle RR' \rangle(s) &= \frac{1}{N_s} \sum_{j=1}^{N_s} R(Z_j, s) R'(Z_j, s). \end{aligned} \quad (6.30)$$

Here  $N_s$  is the number of slices within the specified bunch width. Since the bunch size is very small, typically one tenth of the total beam size in one rf period, the projected transverse emittance will be small for the emittance dominated beam. But for space-charge-dominated beam the projected emittance can be quite large. The total emittance of the beam will therefore, be the combination of this projected and the thermal emittances.

### 6.3.2 Evaluation of the Axial Derivative of $\langle E_{ij} \rangle$

In order to solve the transverse envelope Eq. (6.27) and Eq. (6.28), first we need to evaluate the average value of axial derivative of the longitudinal electric field. Here we present the method of calculation of the axial derivative of longitudinal field for different types of density distributions in the transverse direction. Using Eq. (6.6) we can write the axial longitudinal electric field at the position of slice  $i$  slice due to disc  $j$  as,

$$\begin{aligned} E_{ij}(0, Z_i, s) &= \frac{1}{\varepsilon_0 b^2} \sum_{n=1}^{\infty} \frac{\exp(-\beta_n |Z_i - z_j|)}{J_1^2(\alpha_n)} \\ &\times \int_0^{R_j} J_0(\beta_n r') \sigma(r', R_j) w r' dr' \text{sign}(Z_i - z_j) \end{aligned} \quad (6.31)$$

So, the axial electric field at the position  $Z_i$  of slice  $i$  due to all other discs in the beam is

$$E_i(0, Z_i, s) = \sum_j E_{ij}(0, Z_i, s) \quad (6.32)$$

Since a given slice contains many discs, we have evaluated the axial electric field at the midpoint of the thick slices for the present case. Using Eq. (6.10), Eq. (6.31) and Eq. (6.32) the general expression for the axial electric field in the case of bell shape density distribution is given by (see **Appendix B**)

$$\langle E_i(0, Z_i, s) \rangle = \frac{Q2^{p+1}(p+1)!b^{p-1}}{\epsilon_0} \sum_{n=1}^{\infty} \frac{\exp(-\beta_n|Z_i - z_j|) J_{p+1}(\beta_n R_j)}{\alpha_n^{2p+2} J_1^2(\alpha_n)} \frac{J_{p+1}(\beta_n R_j)}{R_j^{p+1}} \text{sign}(z_i - z_j) \quad (6.33)$$

In a similar way, using Eq. (6.11), Eq. (6.31) and Eq. (6.32) the axial electric field for hollow shape distribution can be obtained as (see **Appendix B**)

$$\begin{aligned} \langle E_i(r, Z_i, s) \rangle &= \frac{2Q(p+1)2^p}{\epsilon_0(2^{p+1}-1)} \sum_{n=1}^{\infty} \frac{\exp(-\beta_n|Z_i - z_j|)}{J_1^2(\alpha_n)} \left[ \frac{R_j}{\alpha_n} J_1(\beta_n R_j) - \frac{pb}{\alpha_n^2} J_2(\beta_n R_j) \right. \\ &+ \left. \frac{p(p-1)b^2}{\alpha_n^3 R_j} J_3(\beta_n R_j) - \dots + \frac{(-1)^p p! b^{p-1}}{\alpha_n^{p+1} R_j^{p-1}} J_{p+1}(\beta_n R_j) \right] \text{sign}(Z_i - z_j) \end{aligned} \quad (6.34)$$

The derivative of the axial electric field at the midpoint of each thick slice can be obtained from

$$\frac{dE_i(0, Z_i, s)}{dZ} = \frac{E_{i+1}(0, Z_{i+1}, s) - E_{i-1}(0, Z_{i-1}, s)}{2\Delta g} \quad (6.35)$$

where  $\Delta g$  is the width of each thick slice.

The average behaviour of the bunch can be found by replacing the quantity  $K(Z, s)$  by  $\langle K(Z, s) \rangle$ ,  $\Lambda(Z, s)$  by  $\langle \Lambda(Z, s) \rangle$  and  $\varepsilon(Z, s)$  by  $\langle \varepsilon(Z, s) \rangle$ . Here the average  $\langle \dots \rangle$  is over the bunch length  $\Delta z$ . So, the envelope equation of the bunch can be written as [108]

$$\bar{R}'' + k(s)\bar{R} - \frac{K(s)}{\bar{R}} + \frac{q\bar{R}}{2m\beta^2\gamma^2c^2} \left\langle \frac{\partial E_z(0, z, s)}{\partial z} \right\rangle - \frac{\varepsilon^2(s)}{\bar{R}^3} = 0 \quad (6.36)$$

We can write the above equation as

$$\bar{R}'' + k(s)\bar{R} - \frac{K_{eff}(s)}{\bar{R}} - \frac{\varepsilon^2(s)}{\bar{R}^3} = 0 \quad (6.37)$$

where we have defined,

$$K_{eff}(s) = K(s) - \Lambda(s)\bar{R}^2 \quad (6.38)$$

and

$$\Lambda(s) = \frac{q}{2m\beta^2\gamma^2c^2} \left\langle \frac{\partial E_z(z, s)}{\partial z} \right\rangle \quad (6.39)$$

### 6.3.3 Emittance Growth due to RF Field

In Eq. (6.27) and Eq. (6.28) the quantity  $\varepsilon(Z, s)$  is the effective value of the transverse emittance of the thick slice at location  $s$  from the buncher gap. In beam bunching, the rf field at the buncher gap modulates the velocity of the beam longitudinally as well as it provides focussing or defocussing impulse in the transverse direction. Depending upon the phase  $\phi$ , the value of the divergence will be different for different discs. As the beam drifts, these discs with different orientation of phase ellipse will start overlapping each other which leads to the emittance growth in the transverse direction. The phase  $\phi$  is uniformly distributed on discs before crossing the buncher gap and is equal to zero when the centre of the bunch crosses the rf gap. After crossing the buncher gap, the transverse position of a particle in disc  $n$  is [108, 114]

$$x_f = x_i, \quad x'_f = x'_i + \frac{\pi V_b x_i}{2T\beta\lambda_{rf}} (1 - \beta^2) \cos \phi_n \quad (6.40)$$

where  $V_b$  is the applied peak voltage at the buncher gap,  $T$  is the kinetic energy of the beam and  $\phi_n$  is the rf phase when the disc  $n$  crosses the gap. The initial and final rms emittances of a slice at location  $Z$  from the bunch centre can be written as

$$\tilde{\varepsilon}_i^2(Z, s) = \overline{x_i^2} \cdot \overline{x_i'^2} - \overline{x_i x_i'}^2, \quad \tilde{\varepsilon}_f^2(Z, s) = \overline{x_f^2} \cdot \overline{x_f'^2} - \overline{x_f x_f'}^2 \quad (6.41)$$

The change  $\Delta\tilde{\varepsilon}_{rf}^2(Z, s) = \tilde{\varepsilon}_f^2(Z, s) - \tilde{\varepsilon}_i^2(Z, s)$  in the emittance of the slice at location  $(Z, s)$  after simplification is given by

$$\Delta\tilde{\varepsilon}_{rf}^2(Z, s) = \bar{x}^2 \left( \frac{\pi V_b}{2T\beta\lambda_{rf}} \right)^2 \left[ \overline{\cos^2 \phi_n}|_Z - \overline{\cos \phi_n^2}|_Z \right] \quad (6.42)$$

The terms  $\overline{\cos^2 \phi_n}$  and  $\overline{\cos \phi_n^2}|_Z$  are average values of  $\cos^2 \phi_n$  and  $\cos \phi_n$  of the discs which are within the slice at the location  $(Z, s)$ . The change in the emittance  $\Delta\tilde{\varepsilon}_{rf}^2(s)$  of the bunch at location  $s$  can be obtained from Eq. (6.42) by taking the averages of the discs which are within the specified bunch width  $\Delta z$  and is given by [108]

$$\Delta\tilde{\varepsilon}_{rf}^2(s) = (\varepsilon_f^2 - \varepsilon_i^2) = \bar{x}^2 \left( \frac{\pi V_b}{2T\beta\lambda_{rf}} \right)^2 \left[ \overline{\cos^2 \phi_n}|_s - \overline{\cos \phi_n^2}|_s \right] \quad (6.43)$$

The total effective rms emittance of the bunch is therefore given by

$$\tilde{\varepsilon}_{eff}^2(s) = \tilde{\varepsilon}^2 + \tilde{\varepsilon}p^2(s) + \Delta\tilde{\varepsilon}_{rf}^2(s) \quad (6.44)$$

## 6.4 Numerical Results

The theoretical formulations of the beam dynamics in the previous sections indicate that the transverse and longitudinal motions are coupled to each other. Thus, to calculate the dynamics of each disc, it is necessary to solve the transverse and longitudinal motions simultaneously. In this section we present the results of studies on a sinusoidal beam bunching system to be used in the injection line of the 10 MeV compact cyclotron (see Fig. 1.1, Chapter 1). The expected normalized emittance of the beam is  $0.8\pi$  mmmrad. The diameter of the beam pipe is 11.0 cm. The buncher is placed before the solenoid S2 in the beam line. The operating rf frequency of the buncher is 42 MHz, which gives the bunch spacing  $\beta\lambda_{rf} = 10.45$  cm at 100 keV injection energy and bunch width  $\Delta\phi$  is  $30^\circ$  of rf.

### 6.4.1 Simulation Results using Analytical Model

At first we present the simulation results of beam bunching for a beam having uniform density distribution in the transverse direction. Figure 6.3(a) shows how the longitudinal part which is due to the axial variation of longitudinal electric field, contributes in the transverse envelope equation as the beam moves along the drift length. This effect decreases with the increase in the energy spread and is more dominant near the time focus where the number of discs in the specified bunch width is large. Figure 6.3(b) compares the variation of the effective perveance as a function of drift length with and without longitudinal part with zero energy spread. We see that in the case of short bunches the inclusion of axial variation of longitudinal electric field is necessary in the transverse dynamics, because it reduces the effective perveance by a considerable amount.

The simulation results on emittance growth due to rf field applied at the buncher gap for different values of energy spread in the beam for 0 mA and 10 mA are shown in Fig. 6.4. The effect of energy spread on emittance dilution is almost negligible at low beam current. As the beam current increases, emittance dilution also increases and the effect is more dominant when the energy spread is large. Since this effect is due to the overlapping of discs with different orientations of transverse phase space, the emittance dilution is maximum at the time focus.

The relative density distribution  $N(\phi)/N_0$  of discs at the time focus is shown in Fig. 6.5.  $N(\phi)$  and  $N_0$  are the number of disc per unit phase at the time focus when the buncher voltage is on and off respectively. Figure 6.6 shows the phase space plot of the beam at the time focus for various conditions. The indicated bunching efficiencies  $\eta$  in both the figures present the values for bunch width  $\pm 15^\circ$  of rf ( $\Delta\phi = 30^\circ$  of rf). The bunching efficiency decreases as we increase the beam current. For  $I = 10$  mA, the bunching efficiency decreases to 42% for

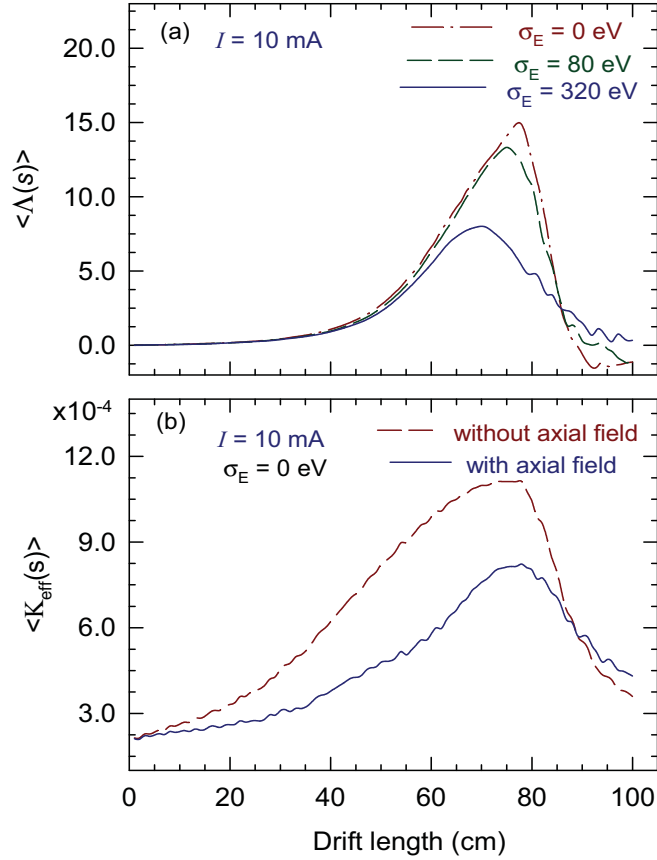


Figure 6.3: (a) Evolution of the quantity  $\langle \Lambda(s) \rangle$  due to the axial variation of longitudinal electric field during the bunch compression for 100 keV, 10 mA beam at various values of energy spread. (b) Variation of the perveance  $\langle K(s) \rangle$  of the beam bunch during longitudinal bunch compression, with and without the inclusion of  $\langle \Lambda(s) \rangle$ . The optimised drift length  $L = 77$  cm and buncher voltage  $V_b = 6$  kV are used in the simulation.

energy spread of 80 eV and it further decreases to 29% when the energy spread is 320 eV. We see here that space-charge affects the bunching process adversely and it is more severe when the energy spread is large.

It is evident from Fig. 6.6 that the phase space plot of the beam is different when the beam current is high. For  $I = 0$  mA, discs which are behind the bunch centre at buncher gap having positive impulse tend to overtake discs which are ahead during the drift and cross through the bunch centre at the time focus

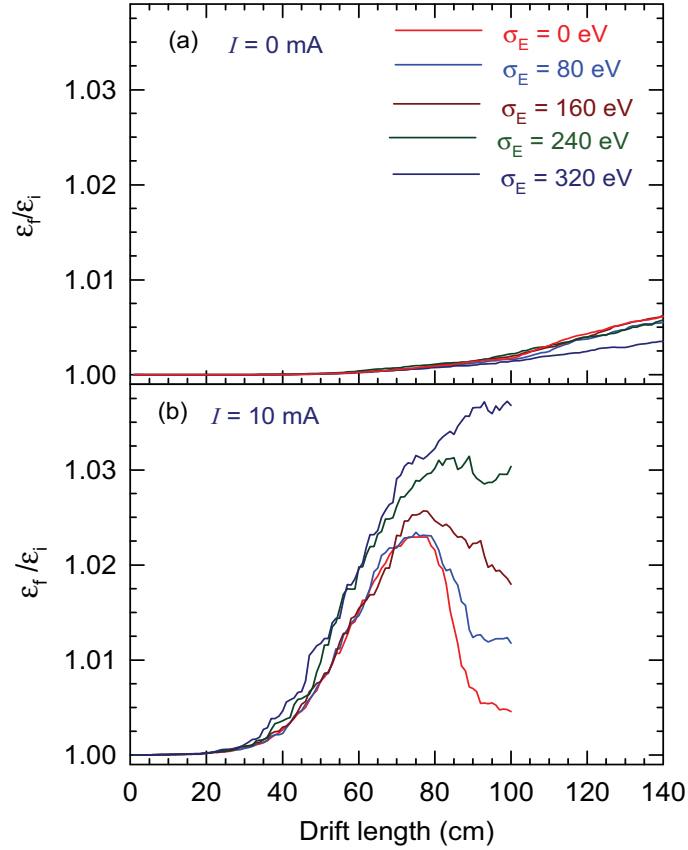


Figure 6.4: Evolution of the emittance growth during the beam transport with bunch compression for three different values of beam current and at different energy spread ;  $\sigma_E = 0, 80, 160, 240, 320$  eV. The beam injection energy is 100 keV.

and vice versa. In the case of high beam current the motions of the discs are dominated by both rf field as well as the space-charge field of the beam. The space-charge force of the beam increases during the bunch compression and act against the velocity modulation initially given by the rf field. As a result discs are repelled by the space-charge force with less number of discs crossing centre of the bunch at the time focus. At sufficiently high current space-charge force dominates and prevents the disc crossing with substantial reduction in the bunching efficiency.

In order to study the dynamics inside the bunch in more detail during

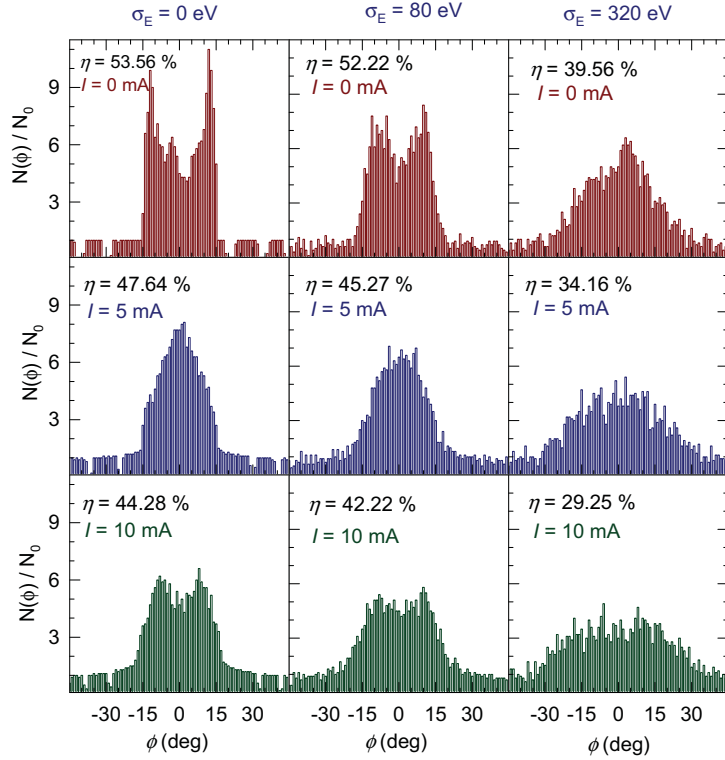


Figure 6.5: Relative density distribution of discs at the time focus as a function of phase  $\phi$  for 100 keV beam at beam current of  $I = 0$  mA ( $L = 100$  cm),  $I = 5$  mA ( $L = 87$  cm) and  $I = 10$  mA ( $L = 77$  cm) and for three different values of initial beam energy spread (column 1 for  $\sigma_E = 0$  eV, column 2 for  $\sigma_E = 80$  eV and column 3 for  $\sigma_E = 320$  eV).

the bunching process we have divided the beam into slices as discussed in **Section 6.3** and considered different density distribution for the discs in the transverse direction. Figure 6.7 shows the variation of rms radius and rms divergence of the beam in one  $\beta\lambda_{rf}$  consisting of 72 slices near the entrance of the buncher gap obtained from the data of optimise beam envelope in the transport line. The number of slices in the chosen bunch width of  $30^\circ$  of rf is 6. It can be readily seen from the figure that the rms radius of slices in one  $\beta\lambda_{rf}$  varies from 6.85 mm at the beginning to 8.35 mm at the end. The radius of slice decides the radius of discs, and any variation in the radius of discs changes its space-charge contribution on the other discs. As the beam propagates the radius and diver-

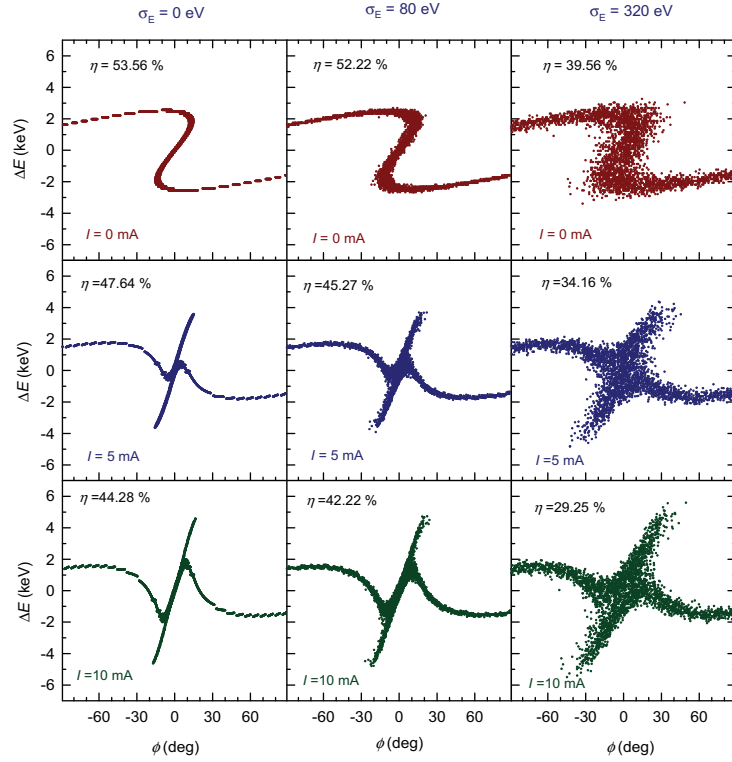


Figure 6.6: The longitudinal phase space distribution of the beam at the time focus for three different value of beam current and energy spread at 100 keV. The indicated bunching efficiencies  $\eta$  are for bunch width  $\Delta\phi = 30^\circ$  of rf.

gence of the slices change according to the transverse beam envelope equation.

We first simulated the evolution of envelope radius and divergence of slices as a function of drift length and phase ellipse of different slices at the time focus (longitudinal focus) with low beam current. The calculation is then repeated the same calculation with 10 mA beam current for uniform and nonuniform density distributions of the beam in the transverse direction. The evolution of the rms radius of different slices numbered as 1 to 6 starting from the beginning of bunch to the end, are shown in Fig. 6.8 as a function of drift distance for two different values of beam currents  $I = 0$  mA and  $I = 10$  mA respectively. It

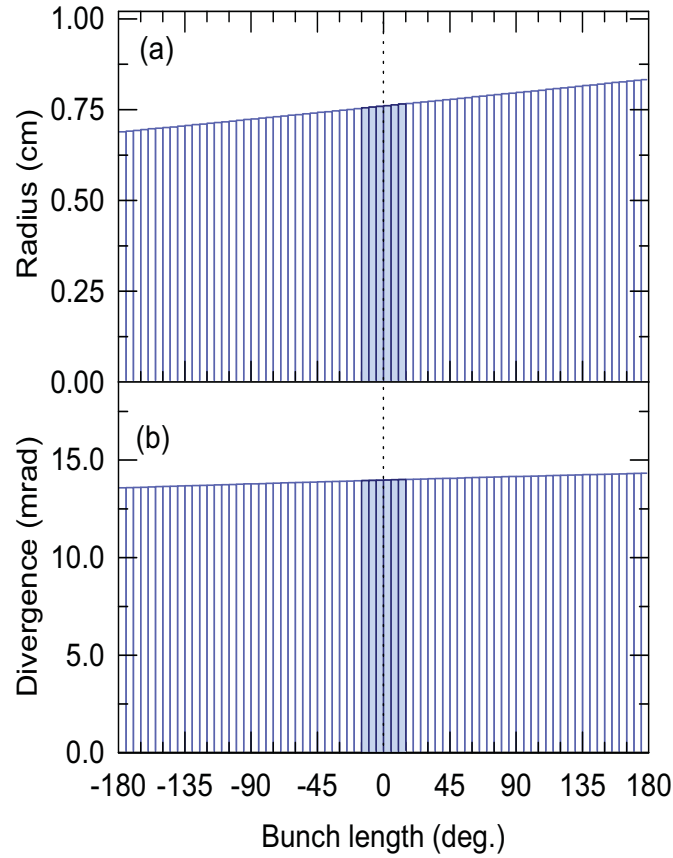


Figure 6.7: Variation of (a) rms radius and (b) rms divergence of beam in one  $\beta\lambda_{rf}$  consisting of 72 slices at the entrance of the buncher gap. The slices in the chosen bunch width are indicated by dark shades.

can be readily seen that there is very small difference in the radius of different slices along the transport line when the beam current is very small. It is evident from Fig. 6.8(b) that for 10 mA beam current the evolution of the rms beam size of the slices are quite different. This is because of the fact that these slices receive different space-charge forces during the bunch compression. The radii of central slices 3 and 4 indicate as if they have received comparatively stronger transverse space-charge force compared to the those slices which are away from the centre of the bunch. The dotted curve in Fig. 6.8(b) compares the result where the bunch radius is assumed as constant. It is also evident from the Fig.

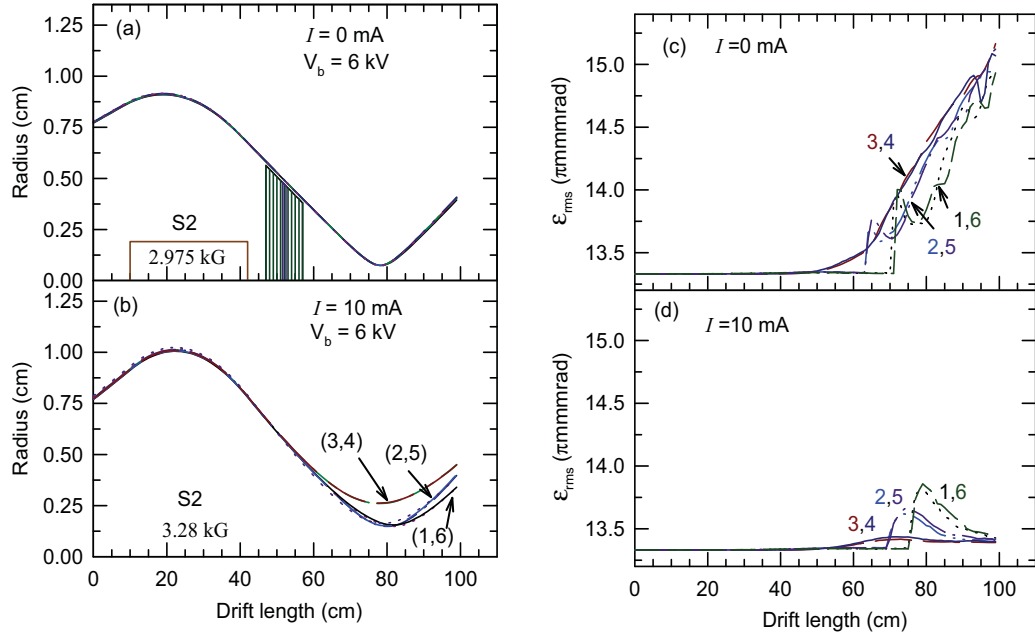


Figure 6.8: Variation of rms radius and rms emittance of different slices in the bunch width as a function of drift length for  $I = 0$  mA and  $I = 10$  mA. Six slices of the bunch are numbered as 1 to 6 starting from the beginning of the bunch to the end. The location and length of solenoid magnet S2 together with strengths are also indicated.

6.8(b) that the waist of central slices and outer slices are formed at different locations compared to the position of the waist of the bunch of constant radius.

Figures 6.8(c) and 6.8(d) show the effect of phase dependent rf field on the emittance of different slices as the beam drifts for 0 mA and 10 mA. The evolution of emittance of slices is quite different in these two cases which is due to the fact that in the first case discs cross the bunch centre whereas in the second case discs are repelled by the space-charge force with a reduction in the disc crossing near the time focus. The emittance growth is at peak near the time focus and decreases afterwards for all the slices in the case of 10 mA beam current whereas the emittance growth of different slices keeps on increasing even after the time focus when the beam current is very low.

A plot of the projected rms emittance of the bunch for uniform, bell shape

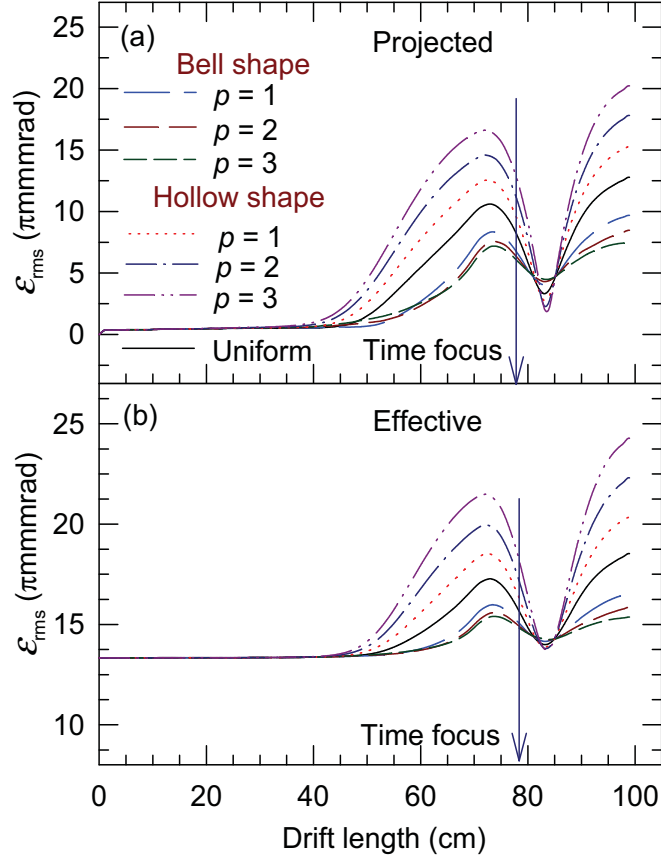


Figure 6.9: Evolution of (a) projected rms emittance due to space-charge effect and (b) total effective rms emittance for different distributions. The total effective rms emittance (Eq. (6.44)) includes the thermal and growth due to the space charge and rf fields.

and hollow shape distributions are shown in Fig. 6.9(a). The variation of total effective rms emittance (as defined in Eq. (6.44)) as a function of drift length is shown in Fig. 6.9(b). The total effective rms emittance includes thermal part as well as growth due to the space charge effect and time dependent rf force. A comparison of results indicates that an increase in the non uniformity of density leads to an increase in the rms emittance for hollow shape distribution and a decrease in the rms emittance of the bell shape distribution throughout the drift length. It is readily seen from Fig. 6.9 that the maximum growth in the emittance occurs just before the time focus whereas minimum growth is

just after the time focus in all the cases. Results show that the rms emittance growth at the time focus increases with increasing parameter  $p$  for hollow shape distribution and decreases with increasing parameter  $p$  for the case of bell shape distribution.

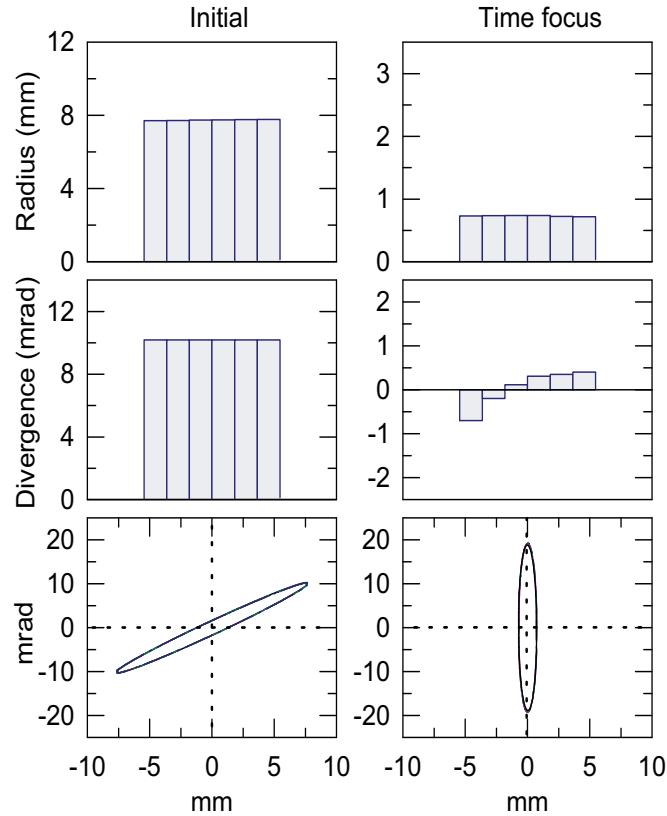


Figure 6.10: The rms radius, rms divergence and orientation of the phase ellipses of the slices 1 to 6 at the buncher location and at the time focus for  $I = 0$  mA.

In Fig. 6.10 we have plotted the rms beam radius, rms beam divergence and orientation of phase ellipses at the buncher gap and at the time focus for very low beam current i.e.  $I = 0$  mA. We see here that at the time focus the radius of different slices are almost same whereas the divergence of different slices, though small but changes from negative to positive values. Since the radius of six slices is almost same and the difference in divergence among the slices is

very small at the time focus, the orientation of phase ellipse for different slices is almost identical.

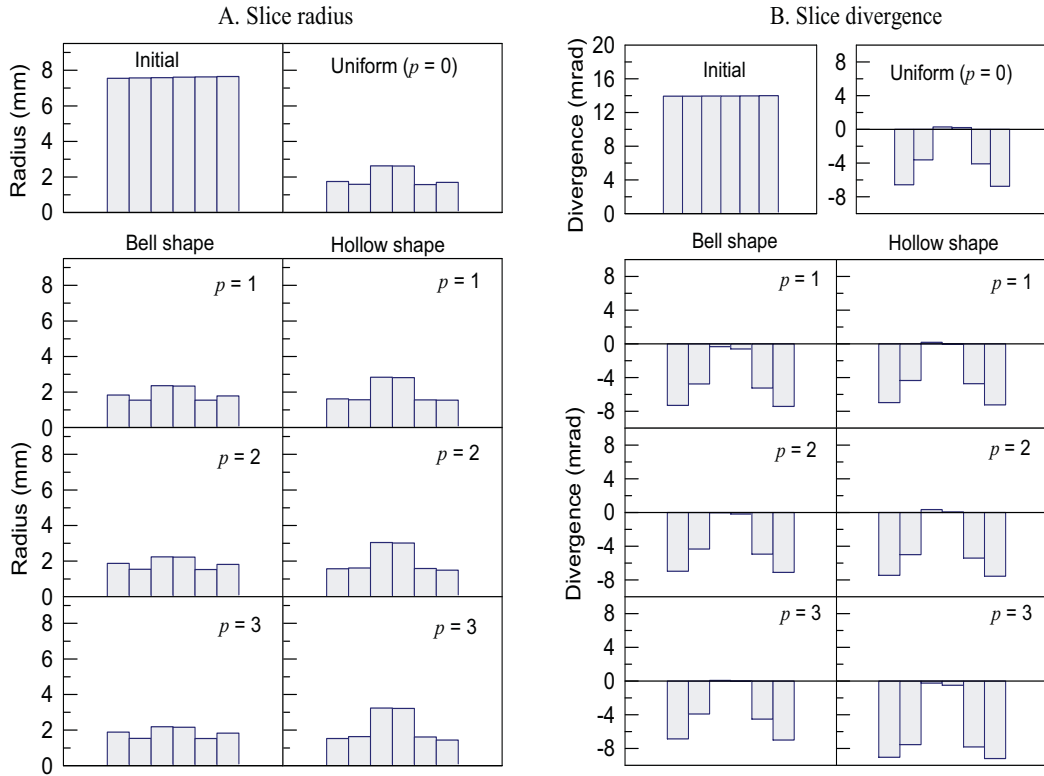


Figure 6.11: Plots show (A) rms radius and (B) rms divergence of slices 1 to 6 of the beam bunch at the time focus at 10 mA beam current having different density distributions in the radial direction. The term initial indicates the values at the buncher location.

The behaviour of slice radius at the time focus for the bell shape and hollow shape distributions at 10 mA beam current are shown in Fig. 6.11 from which three points are noteworthy. First, the radius of the six slices is not same at the time focus in the case of bell shape and hollow shape distributions. Second, the radius of slices near the bunch centre seems to be more affected by the space-charge force and thus become large compare to the radius of outer slices. This is due to the fact that the number of discs and hence the transverse space-charge force is more in the central slices compared to that of outer slices. Third,

the effect of parameter  $p$  is completely opposite in the two cases of density distribution. In the case of bell shape distribution, the rms radius of central slices decreases and outer slices increases with parameter  $p$  whereas the effect is just opposite in the case of hollow shape distribution.

Figure 6.11(B) compares the rms divergence of different slices at time focus for bell shape and hollow shape density distributions with different values of parameter  $p$  at 10 mA beam current. As mentioned earlier for the case of  $I = 0$  mA, the envelope divergence of slices starting from a small negative value goes through almost equal to zero for central slices and then become positive for the latter slices and all the slices more or less form a waist at the time focus. In the case of space-charge-dominated beam the divergence of central slices are also zero however slices on both sides of central slices have negative divergence in all the cases. We also see that the magnitude of divergence increases in the case of hollow shape distribution with parameter  $p$  whereas it decreases in the case of bell shape distribution.

In Fig. 6.12(A) we have shown the phase space orientations of all six slices at the time focus for three different values of parameter  $p$  together with the initial phase ellipses at the buncher location. It is readily seen from Fig. 6.12(A) that the phase space orientation of central and outer slices at the time focus are different in contrast to the case of  $I = 0$  mA, where all the slices form a waist at the time focus. It is also evident from these plots that the effective rms emittance decreases in the case of bell shape distribution as we increase the value of parameter  $p$  and it increases for the hollow shape distribution with  $p$  (also shown in Fig. 6.9).

The profile of the current in different slices around the bunch centre at the time focus for bell shape and hollow shape density distributions is presented in

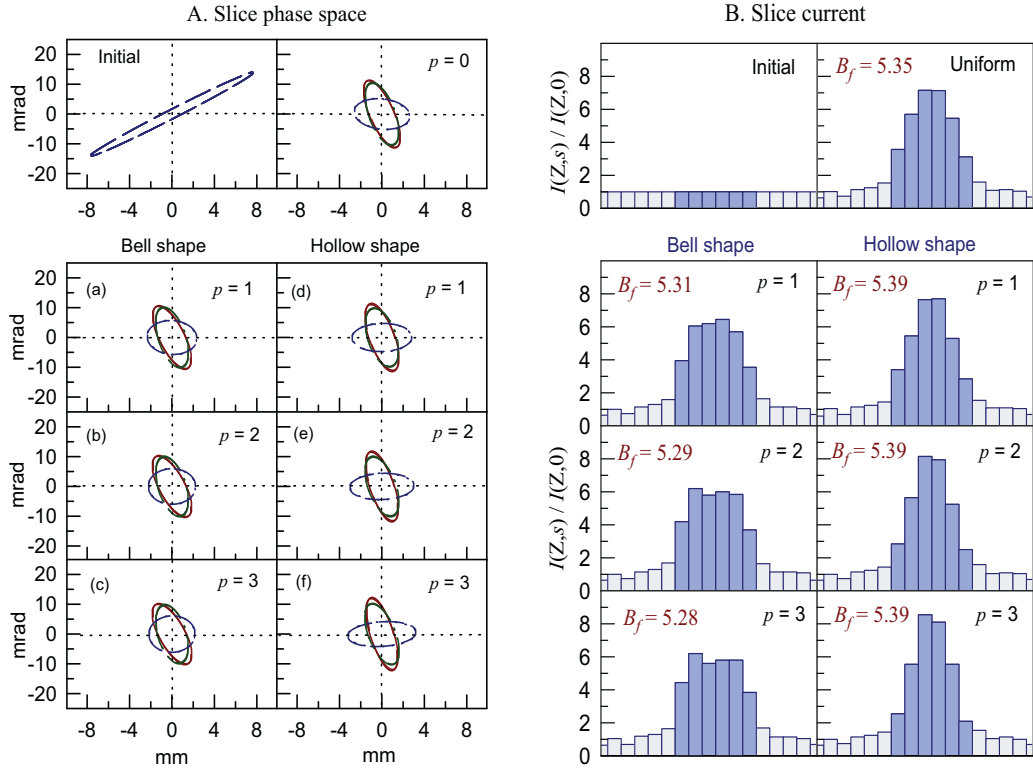


Figure 6.12: (A) Phase space ellipse and (B) current  $I(Z, s)/I(Z, 0)$  of all six slices in the bunch at the time focus for bell shape and hollow shape density distributions of the beam at three different values of parameter  $p$ . Initial indicates values at the buncher location. Slices in the specified bunch width of  $30^0$  of rf are shown in dark colour.

Fig. 6.12(B). In fact these plots represent the variation of the actual line charge density distribution of the beam at the time focus. The estimated bunching efficiencies for all the distributions is 44%. The slices in the specified bunch width are indicated by dark colour. The average bunching factor  $B_f$ , which we define by the ratio of total current in the slices in a given phase width at the time focus when the buncher is on to the total current in the slices in the same phase width when the buncher is off, is also indicated in the Fig. 6.12(B). We see that values of  $B_f$  are almost same in all the cases, but the shapes of the current pulses at the time focus vary with density distributions. These are comparatively sharper in the case of hollow shape density distribution. The

sharpness of current pulses increases with parameter  $p$  for hollow shape density distribution whereas it reduces in the case of bell shape distribution.

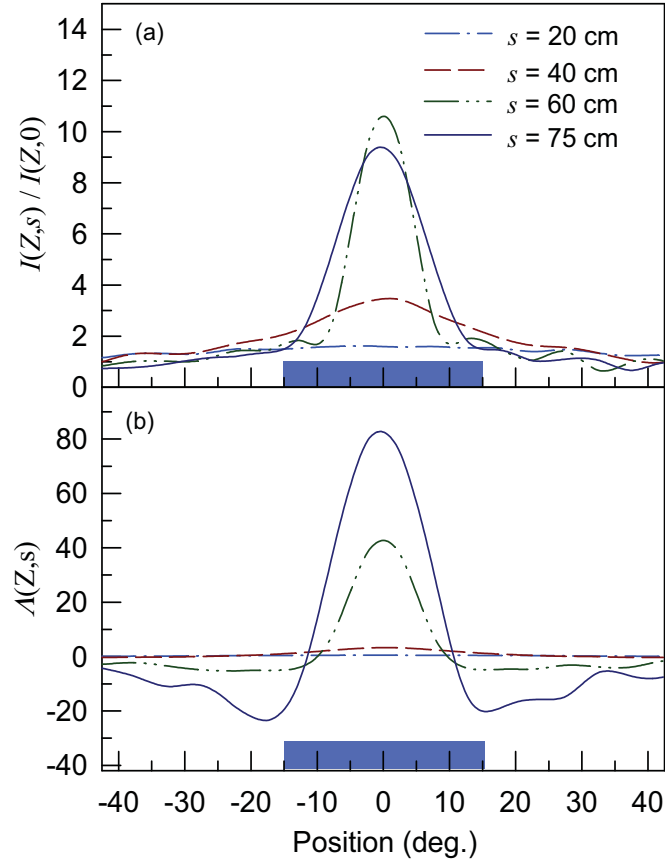


Figure 6.13: Variation of (a) current in the slices  $I(Z, s)/I(Z, 0)$  around the bunch centre and (b) the parameter  $\Lambda(Z, s)$  at four different axial locations  $s$  from the buncher gap in the case of uniform density profile. The shaded regions indicate the extent of specified bunch width ( $30^\circ$  of rf).

The profile of the current in the slices  $I(Z, s)/I(Z, 0)$  around the bunch centre and the parameter  $\Lambda(Z, s)$  defined in Eq. (6.27) and Eq. (6.28), are shown in Fig. 6.13 at four different locations  $s$  in the drift length from the buncher gap for the case of uniform density profile. The numerical results of these parameters show almost identical qualitative behaviour for hollow and bell shape density profiles. It is evident from Fig. 6.13(a) that the current is

large at the centre of the bunch and the maximum current in the central slice reaches before the time focus. However, the total current in the specified bunch width which also defines the bunching efficiency reaches its maximum value at the time focus. It is readily seen from Fig. 6.13(b) that the value of parameter  $\Lambda(Z, s)$  which is proportional to the axial derivative of the longitudinal electric field, reaches its maximum value at the time focus. The appearance of the negative value of  $\Lambda(Z, s)$  at the bunch edges as the beam approaches the time focus is due to the change in the behaviour of the electric field at the bunch edges. Thus the inclusion of this effect in the transverse dynamics is essential for more accurate estimation of the bunch behaviour.

### 6.4.2 Simulation Results using PIC Model

In the analysis of beam bunching presented in previous sections of this chapter it is assumed that the transverse emittance of each disc remains constant during the transport. But in real situation during the bunching the beam emittance evolve along the transport line and therefore one needs a self-consistent simulation for prediction of the beam behavior more accurately. In this section, we employ a PIC method to study the beam dynamics self-consistently. The details of the PIC simulation method are given in **Chapter 7**. The macroparticles used in the simulation have following distribution in the transverse 4D phase space: K-V, waterbag, parabolic, semi-Gaussian and Gaussian. The initial distribution of the macroparticles in the longitudinal direction is taken as uniform in space and Gaussian distributed in energy with respect to the mean value.

The evolution of the average rms radius of the bunch is shown in Fig. 6.14(a) as a function of drift distance for 10 mA beam current. For comparison, the rms radius obtained from the disc-envelope model is also plotted [109]. In Fig.

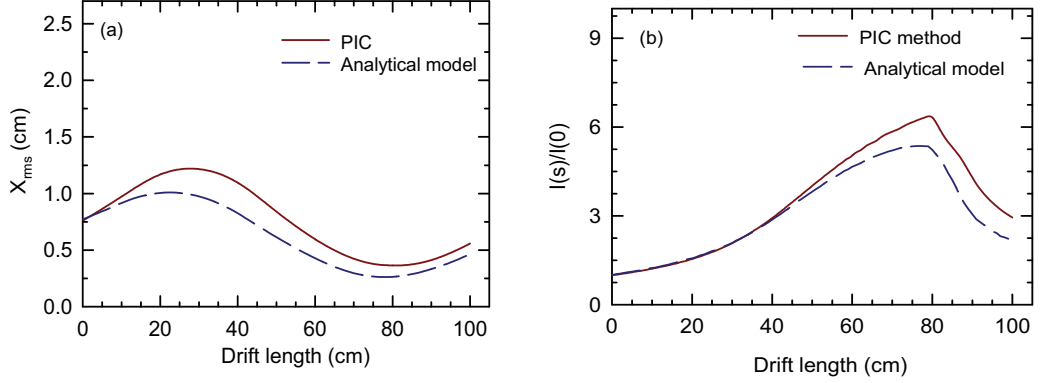


Figure 6.14: Comparison of the evolution of (a) the rms beam size and (b) the relative increase in bunch current  $\langle I(s) \rangle / I(s = 0)$  along the drift length during the bunching obtained with PIC simulation (solid) and analytical formulations.

6.14(b) we have compared the variation of the bunch current  $\langle I(s) \rangle / I(s = 0)$  in the defined phase width ( $\pm 15^\circ$ ) along the drift length obtained from 3D PIC model and envelope-disc model for monoenergetic beam.

In Fig. 6.15A(a) and Fig. 6.15B(b), we have plotted the evolution of emittances of different slices numbered as 1 to 6 along the beam transport line during the bunch compression with K-V and Gaussian distribution in the transverse phase space respectively. The increase in emittance occurs mainly due to transverse-longitudinal space charge coupling. We can see from Fig. 6.15A(a) that the emittance of the central slices increases with a slow rate. The emittance of end slices is almost constant up to 60 cm and then increases very rapidly. After  $s = 80$  cm, the emittance of all the slices saturates at higher value than the initial values.

For the Gaussian beam, the behaviour is different than the K-V beam and the results of PIC simulation is shown in Fig. 6.15A(b). For Gaussian distribution, the emittance of the central slices grows slowly and reaches to maximum value at  $s = 60$  cm and then starts decreasing and saturates at a lower value

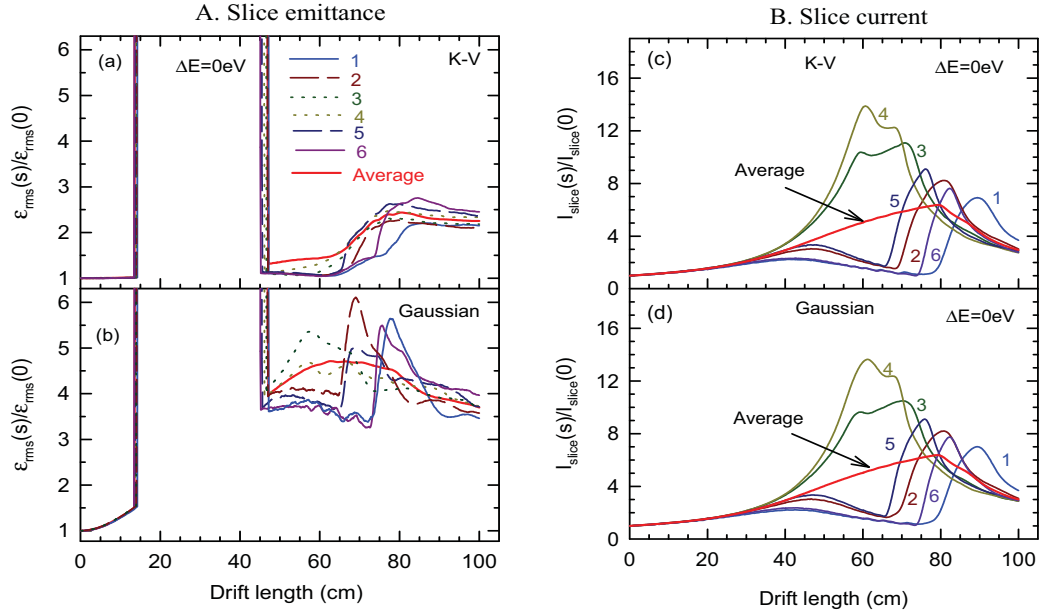


Figure 6.15: Evolution of the (A) slice emittances and (B) slice current as a function of drift distance  $s$  with initial K-V and Gaussian distributions. The thick solid line indicated by average represents the average value of parameter of the bunch.

than the peak value. The emittance of the slices at the edges (1 and 6) is almost constant up to  $s = 80$  cm and then increases abruptly to a very high value and then decreases slowly and reaches to a lower value. The saturation value of final rms emittance of different slices is 2 to 2.5 times of the initial value in the case of K-V beam whereas it is 3.5 to 4 times in the case of Gaussian beam indicating a considerable emittance growth.

The evolution of the relative increase in current in the slices as a function of drift distance is shown in Fig. 6.15B(c) and Fig. 6.15B(d) for a monoenergetic beam with K-V and Gaussian distribution in the transverse direction respectively. It is easy to observe that up to  $s = 40$  cm there is very little change in the current in slices. After  $s = 40$  cm, current in the central slices increase, whereas the current in the slices at the edges decreases. The current of the central slices (3 and 4) increase to a very high value almost by a factor of  $\sim$

12 at  $s = 60$  cm and then it decreases. The current of other slices also show the increasing behaviour at different drift locations. It is interesting to observe that decrease of the current in the central slices and increase in the slice at the outer slices happen in such way that the average current in the bunch becomes maximum at the time focus. We can see that this behaviour is similar for both the distributions.

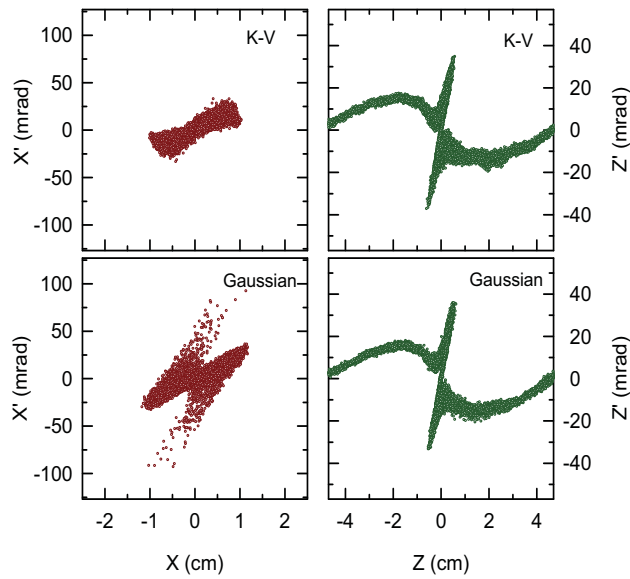


Figure 6.16: *Transverse and longitudinal phase space distributions at the time focus with initial K-V and Gaussian distributions.*

The phase space distributions of the beam in the transverse and longitudinal planes at the time focus are shown in Fig. 6.16. The results of PIC simulation show that particles are more diffused and occupied large phase space area in the transverse plane for Gaussian distribution in comparison with that of K-V distribution. However, the distribution of particles in the longitudinal phase space is almost identical for both the distributions. This is because of the fact that beam is monoenergetic and has identical distribution in the longitudinal distribution for both the cases.

## 6.5 Summary and Discussion

In this chapter, we have developed a method to study the dynamics of the rf beam bunching under the influence of space charge for the cases where the bunch size is comparable to the beam radius. We have modified the beam envelope equation to take into account the longitudinal space charge effect on transverse motion which arises due to the finite bunch size. We have shown that for intense beam, different part of the bunch evolve in a different way due to the unequal amount of space-charge force experienced during the bunching in contrast to the cases where the beam current is very low. For beams with bell shape distribution, it has been observed that the increase in non-uniformity in density distribution reduces the total projected rms emittance as well as sharpness of the beam pulse at the time focus. For beams with hollow shape distribution, it has been found that the increased non-uniformity in density distribution increases the total rms projected emittance and the sharpness of the beam pulse at the time focus. We have also observed that when the beam current is high, the projected rms emittance of the bunch dominates over the rms emittance growth caused due to the rf phase mixing.

Finally we have compared the results of analytical model with the PIC simulation. The evolution of rms size and current in the bunch obtained from disc-envelope model agrees reasonably well with PIC simulation results. Simulation of emittance growth with PIC code shows a saturation value of final rms emittance of different slices. As expected, the beam with Gaussian distribution shows a comparatively large emittance growth with respect to K-V distribution.

# Chapter 7

## PIC Simulation Methods for Space Charge Dominated Beam

### 7.1 Introduction

The estimation of the average behavior of intense single and multispecies beam can be found using beam envelope model [15, 17, 20, 49, 115, 116, 117]. Although, these models can provide a good estimate of the average behavior of the beam, these methods are not self-consistent. In most of the cases, it is impossible to investigate the dynamics analytically with strong nonlinear space-charge forces and misaligned magnets. For the self-consistent description of an intense beam, there are several advanced numerical tools such as particle-in-cell (PIC) simulation methods [24, 118, 119, 120, 121, 122, 123, 124], Vlasov method [25, 26, 27],  $\delta f$  simulation method [16, 125, 126, 127] etc. Among them PIC simulations are widely used to provide insights into the various complexities associated with high space-charge conditions.

In order to understand the detailed dynamics of space-charge-dominated beam with different density distributions in the injection line, a two-dimensional PIC code has been developed. To include the effect of bunching, a three dimensional PIC code has also been developed for the self-consistent study during

the longitudinal compression. The 2D PIC code can handle the misalignment (displacement as well as tilt), higher order nonlinearity of the focusing element and the off-centering of the beam.

## 7.2 Computational Procedure for PIC Method

In PIC method small number of macroparticle (compared to the number of real particles) are used to represent the beam and the self-field are calculated self-consistently from them. Each macroparticle represents many individual charge particle respectively while maintaining the charge to mass ratio of a single charge particle.

The PIC algorithm is outlined in Fig. 7.1. The interior is divided into a computational mesh. At each time step in the PIC simulation, the charge densities at the grid points are calculated from the distributions of macroparticles. The potential is solved at the grid points from the Poisson's equation. The electric field is calculated at each particle position from the known values of the electric field at the nearest grid points. The particle positions and velocities are advanced in time in the presence of self field and external field by the leap-frog method. Any particles which are found to hit the boundary are removed from the simulation. The process is repeated for the next time step. The separate steps implemented in the PIC algorithm are described in detail in the following sections. The code is written in Fortran.

## 7.3 2D PIC Method for Single Species

In this section we discuss briefly each step of a 2D PIC method for the case when the beam contains single species.

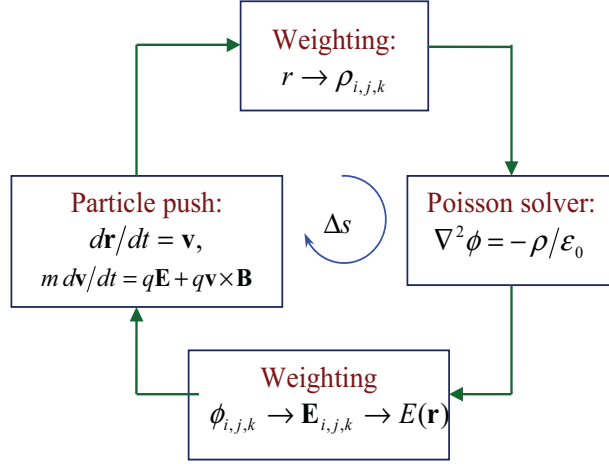


Figure 7.1: Particle-in-cell simulation algorithm.

### 7.3.1 Charge Assignment to the Grid Points

The first part of the PIC algorithm is to set up the charge density for the Poisson solver. The region occupied by ensemble of particles is divided into uniform rectangular meshes of dimension  $N_x \times N_y$ . Since Poisson's equation is solved on a mesh, the charge density needs to be known at the grid points, however, the particles are free to be anywhere in the computational region. Therefore, one must interpolate charge density from the particle's position to the computational grid. The charge of every particle is distributed to its four nearest grid points as shown in Fig. 7.2. We have used the area weighting method which is also known as particle-in-cell or bilinear weighting [122]. The charge density  $Q_{ij}$  at grid points  $(i, j)$  is a combination of contributions from all particles which are inside the given elementary mesh and is given by

$$Q_{ij} = \sum_{n=1}^N Q_{xy} \left(1 - \frac{|x_n - x_i|}{h_x}\right) \left(1 - \frac{|y_n - y_j|}{h_y}\right) \quad (7.1)$$

where  $Q_{xy}$  is the dimensionless space-charge density of individual particle and  $h_x, h_y$  are mesh sizes in  $x$  and  $y$  direction respectively,  $(x_n, y_n)$  is the coordinate of the particle  $n$ . We can write the beam current  $I = \lambda v$ , where  $\lambda$  is the charge

per unit length. In grid weighting method, one particle occupies an area of  $h_x \times h_y$ . Space-charge density of each macroparticle is

$$Q_{xy} = \frac{\lambda}{Nh_x h_y} \quad (7.2)$$

where  $N$  is the total number of macroparticle in the simulation.

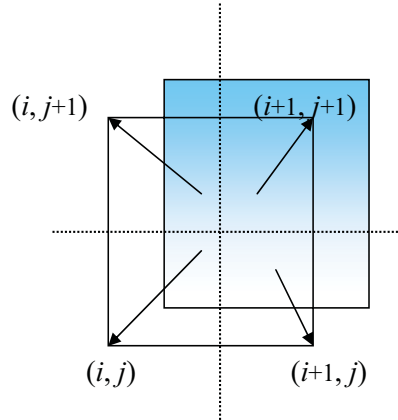


Figure 7.2: Charge deposition in two dimensional rectangular grid.

Since charge is distributed to neighbouring grid points, the area weighting scheme has the effect of introducing finite size particles, rather than point particles into the simulation. It results in smoothing of particle distribution and the singularity associated with the Coulomb interaction between point particles is removed implicitly in PIC simulations.

### 7.3.2 Poisson Solver

We consider that the continuous beam is transported in a straight focussing channel within a conducting rectangular beam pipe. The potential  $\phi$  at the boundary of the beam pipe is zero (shown in Fig. 7.3) and on grid points it is solved using Poisson's equation. We have calculated the potential of the beam in the beam frame using fast Fourier transform (FFT) method.

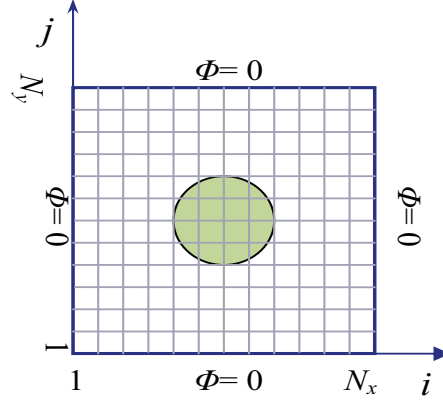


Figure 7.3: 2D Cartesian grid for the solution of Poisson's equation for continuous beam in the case two dimensional problem.

The Poisson equation in Cartesian coordinate is given by

$$\frac{\partial^2 \phi}{\partial x^2} + \frac{\partial^2 \phi}{\partial y^2} = -\rho(x, y) \quad (7.3)$$

Here the potential and density are normalised. The unknown potential of the beam and space-charge density at grid points can be represented by the Fourier series as,

$$\phi_{ij} = \sum_{m=1}^{N_x-1} \sum_{n=1}^{N_y-1} \bar{\phi}_{mn} \sin\left(\frac{\pi m i}{N_x}\right) \sin\left(\frac{\pi n j}{N_y}\right) \quad (7.4a)$$

$$\rho_{ij} = \sum_{m=1}^{N_x-1} \sum_{n=1}^{N_y-1} \bar{\rho}_{mn} \sin\left(\frac{\pi m i}{N_x}\right) \sin\left(\frac{\pi n j}{N_y}\right) \quad (7.4b)$$

The terms  $\bar{\phi}_{mn}$  and  $\bar{\rho}_{mn}$  are found from inverse Fourier transform and given by,

$$\bar{\rho}_{mn} = \frac{4}{N_x N_y} \sum_{i=1}^{N_x-1} \sum_{j=1}^{N_y-1} \rho_{ij} \sin\left(\frac{\pi m i}{N_x}\right) \sin\left(\frac{\pi n j}{N_y}\right) \quad (7.5a)$$

$$\bar{\phi}_{mn} = \frac{4}{N_x N_y} \sum_{i=1}^{N_x-1} \sum_{j=1}^{N_y-1} \phi_{ij} \sin\left(\frac{\pi m i}{N_x}\right) \sin\left(\frac{\pi n j}{N_y}\right) \quad (7.5b)$$

Substituting the expression of  $\phi_{ij}$  and  $\rho_{ij}$  in the Poisson's equation (7.3), we obtain,

$$\bar{\phi}_{mn} = \frac{\bar{\rho}_{mn}}{\left(\frac{\pi m}{a}\right)^2 + \left(\frac{\pi n}{b}\right)^2} \quad (7.6)$$

So the space-charge potential  $\phi_{ij}$  can be calculated utilising expansion of Eq. (7.4). We have used a centered difference scheme to calculate electric field at the grid points as given by,

$$Ex_{ij} = -\frac{\phi_{i+1j} - \phi_{i-1j}}{2h_x}, \quad Ey_{ij} = -\frac{\phi_{ij+1} - \phi_{ij-1}}{2h_y} \quad (7.7)$$

### 7.3.3 Interpolation of Fields to the Particle Location

The electric fields at all particle positions are calculated by interpolating from the electric field at the grid points using the same area weighting scheme as described for the calculation of the charge density matrix and it is given by,

$$Ex_n = Ex_{ij}W_{ij} + Ex_{i+1j}W_{i+1j} + Ex_{ij+1}W_{ij+1} + Ex_{i+1j+1}W_{i+1j+1} \quad (7.8a)$$

$$Ey_n = Ey_{ij}W_{ij} + Ey_{i+1j}W_{i+1j} + Ey_{ij+1}W_{ij+1} + Ey_{i+1j+1}W_{i+1j+1} \quad (7.8b)$$

where  $W_{ij}, W_{i+1j}, W_{ij+1}, W_{i+1j+1}$  are the weighting factor at the grid points  $(i, j), (i + 1, j), (i, j + 1), (i + 1, j + 1)$  respectively. The weighting factor  $W_{ij}$  is given by

$$W_{ij} = \left(1 - \frac{|x_n - x_i|}{h_x}\right) \left(1 - \frac{|y_n - y_j|}{h_y}\right) \quad (7.9)$$

Similarly one can calculate other weighting factors.

### 7.3.4 Particle Distribution Generator in Phase Space

At first we require the phase space coordinates of all the macroparticles for the simulation. For the generation of particle distribution in transverse 4D phase space  $(x, x', y, y')$ , we consider a class of distributions with elliptical symmetry.

The distribution function  $f(x, x', y, y', s)$  depends on a parameter which describes the hyper ellipsoid surface in 4D phase space. The linear field Courant-Snyder invariant distribution is specified as

$$f_{\perp}(x_{\perp}, x'_{\perp}, s) = \frac{\lambda}{q} f(A^2) \quad (7.10)$$

where

$$\lambda = q \int d^2x_{\perp} \int d^2x'_{\perp} f_{\perp} \quad (7.11)$$

and  $f(A^2)$  is any function of the single particle amplitude parameter given by

$$A^2 = \left(\frac{x}{r_x}\right)^2 + \left(\frac{r_x x' - r'_x x}{\epsilon_x}\right)^2 + \left(\frac{y}{r_y}\right)^2 + \left(\frac{r_y y' - r'_y y}{\epsilon_y}\right)^2 \quad (7.12)$$

The functions  $f(A^2)$  for K-V, waterbag, parabolic, Gaussian, semi-Gaussian distribution are given by [15, 122, 128]

$$\text{K-V : } f(A^2) = \frac{1}{\pi^2 \epsilon_x \epsilon_y} \delta(A^2 - 1) \quad (7.13)$$

$$\text{Waterbag : } f(A^2) = \frac{8}{9\pi^2 \epsilon_x \epsilon_y} \Theta\left(1 - \frac{2}{3}A^2\right) \quad (7.14)$$

$$\text{Parabolic : } f(A^2) = \frac{3}{2\pi^2 \epsilon_x \epsilon_y} \left(1 - \frac{1}{2}A^2\right) \Theta\left(1 - \frac{1}{2}A^2\right) \quad (7.15)$$

$$\text{Gaussian : } f(A^2) = \frac{4}{\pi^2 \epsilon_x \epsilon_y} e^{-2A^2} \quad (7.16)$$

Here,  $\Theta(x) = 1$  for  $x > 0$  and  $\Theta(x) = 0$  for  $x < 0$  is a Heaviside unit-step function.

The semi-Gaussian distribution is taken to be of the form [27, 119, 129]

$$\begin{aligned} f_{\perp}^{SG}(x, x', y, y') &= \frac{2\lambda}{q\pi^2 \epsilon_x \epsilon_y} \Theta\left[1 - \left(\frac{x^2}{r_x^2} + \frac{y^2}{r_y^2}\right)\right] \\ &\quad \times \exp\left[-2\left(\frac{r_x x' - r'_x x}{\epsilon_x}\right)^2 - 2\left(\frac{r_y y' - r'_y y}{\epsilon_y}\right)^2\right] \end{aligned} \quad (7.17)$$

An important feature of Eq. (7.17) is that the corresponding number density of beam particles  $n_b(x, y) = q \int d^2x'_{\perp} f_{\perp}^{SG}$  has the uniform-density step-function

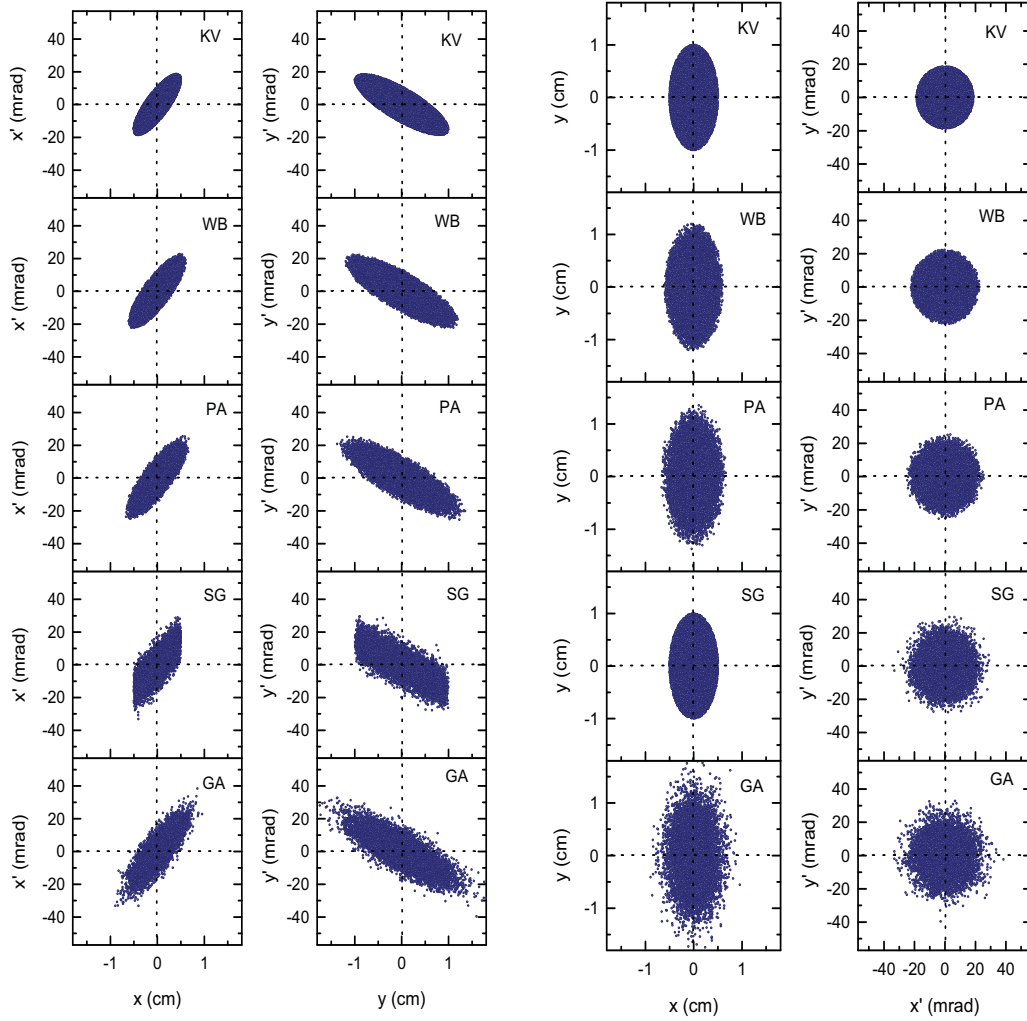


Figure 7.4: Generation of particle distributions in real, phase and momentum spaces for K-V (KV), waterbag (WB), parabolic (PA), semi-Gaussian (SG) and Gaussian (GA) distributions.

profile. The projections of 4D distribution function in phase spaces  $(x, x')$  and  $(y, y')$ , real space  $(x, y)$  and momentum space  $(x', y')$  are shown in Fig. 7.4 for five different distributions. The parameters used are: number of macroparticle  $N = 10000$ , rms normalized emittances  $\tilde{\epsilon}_{nx} = 0.2\pi$  mmmrad and  $\tilde{\epsilon}_{ny} = 0.8\pi$  mmmrad, rms beam sizes  $X_{rms} = 2.5$  mm and  $Y_{rms} = 5$  mm, rms envelope angles  $X'_{rms} = 7.5$  mrad and  $Y'_{rms} = -7.5$  mrad.

### 7.3.5 Equation of Motion

The equations of motion of each macroparticle are given by,

$$\frac{d\mathbf{x}}{dt} = \mathbf{v} \quad (7.18a)$$

$$\gamma \frac{d\mathbf{v}}{dt} = \frac{q}{m} (\mathbf{E}^{ext}(\mathbf{x}, \Delta, \theta, s) + \mathbf{E}^{sc} + \mathbf{v} \times (\mathbf{B}^{ext}(\mathbf{x}, \Delta, \theta, s) + \mathbf{B}^{sc})) \quad (7.18b)$$

here  $\Delta$  and  $\theta$  are the displacement and rotational misalignment parameters of the focussing elements. We have solved the set of first order ordinary differential equations using the second order, time centred leap-frog method [24]. The leap-frog scheme is shown in the Fig. 7.5. If the external focussing force is only electric field then the differential equations can be written in finite difference form as

$$\gamma \frac{\mathbf{v}_{i+1/2} - \mathbf{v}_{i-1/2}}{\Delta t} = \frac{q}{m} \mathbf{E}(\mathbf{x}_i) \quad (7.19a)$$

$$\frac{\mathbf{x}_{i+1} - \mathbf{x}_i}{\Delta t} = \mathbf{v}_{i+1/2} \quad (7.19b)$$

In Eq. (7.19),  $\mathbf{E}(\mathbf{x}_i) = \mathbf{E}^{ext}(\mathbf{x}_i) + \gamma^{-2} \mathbf{E}^{sc}(\mathbf{x}_i)$ . If the external magnetic field is

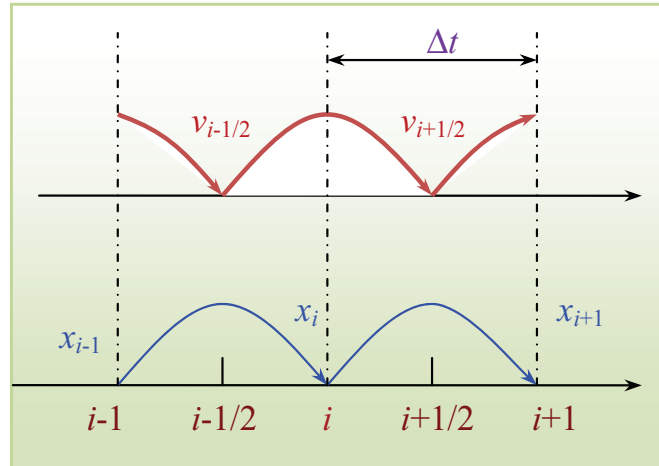


Figure 7.5: Leap-frog method.

present a complication in the motion of macroparticles arises because of the velocity dependent terms in the Lorentz force. This complication results because

$x$  and  $v$  are advanced out of phase in the leap-frog method. A commonly implemented time centred scheme for magnetic forces is the following 3-step Boris method [24]. At the first stage, the particle performs a half-step acceleration in the electric field given by,

$$\mathbf{v}_{i+1/2}^{(1)} = \mathbf{v}_{i-1/2} + \frac{q}{m} \frac{\Delta t}{2\gamma} \mathbf{E}(\mathbf{x}_i) \quad (7.20)$$

At the second stage the velocity vector of the particle rotates in the magnetic field given by

$$\mathbf{v}_{i+1/2}^{(2)} = \mathbf{v}_{i+1/2}^{(1)} + \left( \mathbf{v}_{i+1/2}^{(2)} + \mathbf{v}_{i+1/2}^{(2)} \right) \times \frac{\Omega_i \Delta t}{2} \quad (7.21)$$

where,  $\Omega_i = \frac{q\mathbf{B}(\mathbf{x}_i, s_i)}{m\gamma}$  and  $s_i = i\beta c\Delta t$ . The above equation can be simplified as,

$$\mathbf{v}_{i+1/2}^{(2)} = \mathbf{v}_{i+1/2}^{(1)} + \frac{2}{1 + \left(\frac{\Omega_i \Delta t}{2}\right)^2} \mathbf{v}_{i+1/2}^{(3)} \times \Omega_i \quad (7.22)$$

Where,  $\mathbf{v}_{i+1/2}^{(3)} = \mathbf{v}_{i+1/2}^{(1)} + \mathbf{v}_{i+1/2}^{(1)} \times \frac{\Omega_i \Delta t}{2}$ . At the third stage, the particle perform half step acceleration in the electric field

$$\mathbf{v}_{i+1/2} = \mathbf{v}_{i+1/2}^{(2)} + \frac{q}{m} \frac{\Delta t}{2\gamma} \mathbf{E}(\mathbf{x}_i) \quad (7.23)$$

The rms emittances of the beam at each step are calculated using position and divergence of macroparticles and it is given by,

$$\tilde{\varepsilon}_x = \left[ \langle x_i^2 \rangle \langle x_i'^2 \rangle - \langle x_i x_i' \rangle^2 \right]^{1/2} \quad (7.24)$$

here  $\langle x_i^2 \rangle = \frac{1}{N} \sum_{i=1}^N x_i^2$ ,  $\langle x_i'^2 \rangle = \frac{1}{N} \sum_{i=1}^N x_i'^2$ ,  $\langle x_i x_i' \rangle = \frac{1}{N} \sum_{i=1}^N x_i x_i'$ . Similar expressions for  $y$  coordinates also.

## 7.4 PIC Model for Multispecies Beam

In this section, we describe the PIC method for multispecies beam. Each species of the beam is represented as a combination of large number of macroparticles and each macroparticle maintains the  $m_k/q_k$  of a single ion. We consider a

continuous, multispecies beam propagating in the  $z$ -direction, each of which is described by a distribution function, for example,  $f_j(x, p, t)$  for species  $j$ . Each component of the beam has characteristic axial momentum  $m_j \gamma_j V_j$ . Here,  $V_j = \beta_j c$  is the average axial velocity,  $\gamma_j$  is the relativistic factor,  $m_j$  is the rest mass of species  $j$  and  $c$  is the speed of light in vacuum. For illustration, in Fig. 7.6 we have shown the transverse cross section of the beam containing three species and the computational grids. The equations of motion for the particles are given by

$$\frac{dx_{ji}}{ds} = \frac{v_{ji}^x}{\beta_j c} \quad (7.25a)$$

$$\frac{dy_{ji}}{ds} = \frac{v_{ji}^y}{\beta_j} \quad (7.25b)$$

$$\begin{aligned} \frac{dv_{ji}^x}{ds} = & -\frac{q_j}{m_j \beta_j c \gamma_j} \left[ \frac{1}{\gamma_j^2} \frac{\partial \phi_j^s}{\partial x} + \sum_{\substack{k=1 \\ k \neq j}} \frac{\partial \phi_k^s}{\partial x} - v_{ji}^y (B_z^{ext} + \sum_{\substack{k=1 \\ k \neq j}} B_{zk}^s) \right. \\ & \left. + \beta_j c (B_y^{ext} + \sum_{\substack{k=1 \\ k \neq j}} B_{yk}^s) \right] \end{aligned} \quad (7.25c)$$

$$\begin{aligned} \frac{dv_{ji}^y}{ds} = & -\frac{q_j}{m_j \beta_j c \gamma_j} \left[ \frac{1}{\gamma_j^2} \frac{\partial \phi_j^s}{\partial y} + \sum_{\substack{k=1 \\ k \neq j}} \frac{\partial \phi_k^s}{\partial y} + v_{ji}^x (B_z^{ext} + \sum_{\substack{k=1 \\ k \neq j}} B_{zk}^s) \right. \\ & \left. - \beta_j c (B_x^{ext} + \sum_{\substack{k=1 \\ k \neq j}} B_{xk}^s) \right] \end{aligned} \quad (7.25d)$$

The subscript  $ji$  labels the  $i^{th}$  simulation particle and  $N_j$  is the total number of simulation particles for the  $j^{th}$  species. The term  $\phi_k^s, B_{xk}^s, B_{yk}^s, B_{zk}^s$  are the space-charge potential and magnetic field in the laboratory frame due to  $k^{th}$  species. The total current of the beam is the sum of the currents due to all the species. Let the current of the  $j^{th}$  species is  $I_j$ . We can write the current  $I_j = \lambda_j v_j$  for the species  $j$ , where  $\lambda_j$  is the charge per unit length. Space-charge density of each macroparticle for species  $j$  is

$$Q_{jxy} = \frac{\lambda_j}{N_j h_x h_y} \quad (7.26)$$

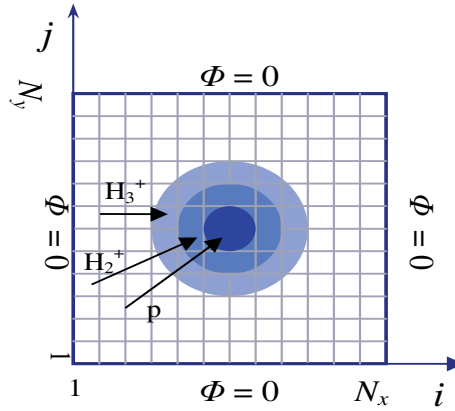


Figure 7.6: *Computational grid for the solution of Poisson's equation with beam spot of three different species.*

The electric field in the beam frame on the grids due to each species is calculated using FFT method as discussed in **Section 7.3.2**. The fields are then transformed in the laboratory frame using the Lorentz transformation. The above procedure is repeated for other species of the beam also. The total electric and magnetic fields in the laboratory frame are calculated by summing the electric and magnetic fields of each species respectively. Then fields at the position of the macroparticles are calculated by interpolating the field from the grid points to the particles position using the same area weighting scheme.

## 7.5 3D PIC Method for Beam Bunching

In order to study the bunching problem we have extended the 2D PIC code discussed in previous sections with the inclusion of a third longitudinal coordinate into the equations of motion. Here each particle occupies a position in 6D phase space depending on the specific particle distribution. The macroparticles are initially placed with different types of distribution in the transverse direction as discussed earlier and the longitudinal distribution corresponds to a  $z$ -continuous

beam with a finite spread of longitudinal momentum  $\Delta p_z$ . The generation of particle distributions in the transverse phase space is already discussed in 2D PIC model. Simulation of longitudinal phase space is performed by generating uniform particle distribution within the interval  $-\beta\lambda_{rf}/2 \leq z \leq \beta\lambda_{rf}/2$  and a Gaussian distribution in longitudinal energy around the average kinetic energy of the beam. Here  $\lambda_{rf}$  is the wavelength of rf. The Fourier transform method is used to solve Poisson equation with proper boundary condition in the longitudinal and transverse directions. The potential  $\phi$  is zero at the surface of a rectangular pipe and is periodic in the longitudinal direction with period  $\beta\lambda_{rf}$ .

### 7.5.1 Equation of Motion

The equation of motion along the longitudinal direction is given by

$$\frac{dz}{ds} = \frac{v_z}{V_z} \quad (7.27a)$$

$$\frac{dv_z}{ds} = \frac{q}{m\gamma V_z} (E_z^{rf} + E_z^{sc}) \quad (7.27b)$$

where  $v_z$  is the velocity of macroparticle with respect to average velocity  $V_z$ .  $E_z^{rf}, E_z^{sc}$  are the longitudinal component of electric field due to rf field and space-charge field respectively. Before entering the buncher gap the beam is continuous. At the buncher gap it received velocity modulation from the rf field which leads to density modulation as the beam advances and finally takes the form of a bunch.

### 7.5.2 Charge Assignment to the Grid Points

In this case the region occupied by ensemble of particles is divided into uniform rectangular meshes of dimension  $N_x \times N_y \times N_z$ . The charge of every particle is distributed to its eight nearest grid points as shown in Fig. 7.7. The charge density at grid points,  $Q_{ijk}$  is a combination of contributions from all particles

which are inside the given elementary mesh and is given by [122]

$$Q_{ijk} = \sum_{n=1}^N Q_{xyz} \left(1 - \frac{|x_n - x_i|}{h_x}\right) \left(1 - \frac{|y_n - y_j|}{h_y}\right) \left(1 - \frac{|z_n - z_k|}{h_z}\right) \quad (7.28)$$

where  $Q_{xyz}$  is the dimensionless space-charge density of individual particle and  $h_x, h_y, h_z$  are mesh sizes in  $x, y$  and  $z$  directions respectively.  $x_n, y_n, z_n$  are the coordinates of the particle  $n$ . Similarly the charge is distributed to the other grid points also.

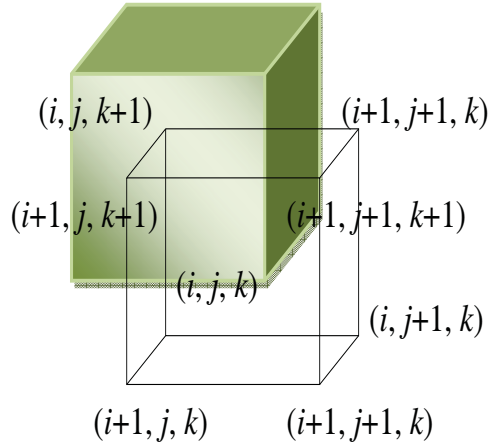


Figure 7.7: Charge deposition in three dimensional rectangular grid.

### 7.5.3 Calculation of the Space Charge Electric Field

To calculate the space-charge field, we have divided the continuous beam into several  $\beta\lambda_{rf}$  interval. Due to the periodic formation of bunches, it is possible to consider the motion of only one bunch. Space-charge fields of neighbouring bunches are taken into account by imposing periodic boundary conditions for potential and space-charge density in the longitudinal direction. Space-charge field of the train of bunches is calculated from the Poisson's equation in Carte-

sian coordinate system. The Poisson equation in 3D cartesian coordinate is

$$\frac{\partial^2 \phi}{\partial x^2} + \frac{\partial^2 \phi}{\partial y^2} + \frac{\partial^2 \phi}{\partial z^2} = -\rho(x, y, z) \quad (7.29)$$

With Dirchlet boundary conditions for potential  $\phi$  at the surface of an infinite pipe with rectangular cross-section of  $a \times b$  and periodic condition in  $z$ -direction i.e.,  $\phi(a/2, y, z) = \phi(-a/2, y, z) = \phi(x, b/2, z) = \phi(x, -b/2, z) = 0$  and  $\phi(x, y, z) = \phi(x, y, z + L_b)$ . Here,  $L_b$  is the distance between center of two consecutive bunches. In terms of rf wavelength, we can write  $L_b = \beta\lambda_{rf}$ . The computational mesh is shown in Fig. 7.8. Unknown potential of the beam and

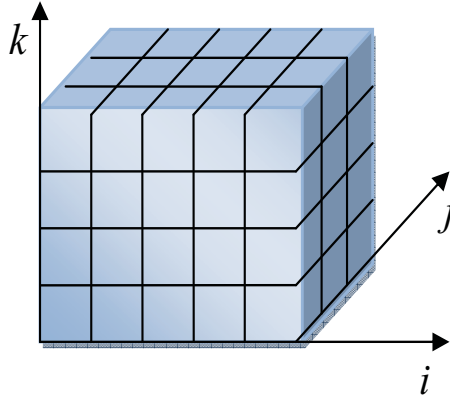


Figure 7.8: 3D rectangular grid for the solution of Poisson's equation for continuous beam and bunched beam respectively.

space-charge density at the grid points are represented as Fourier series as given by,

$$\phi_{ijk} = \sum_{m=1}^{N_x-1} \sum_{n=1}^{N_y-1} \sum_{p=1}^{N_z} \bar{\phi}_{mnp} \sin\left(\frac{\pi m i}{N_x}\right) \sin\left(\frac{\pi n j}{N_y}\right) \exp\left(-\frac{2\pi k p}{N_z}\right) \quad (7.30a)$$

$$\rho_{ijk} = \sum_{m=1}^{N_x-1} \sum_{n=1}^{N_y-1} \sum_{p=1}^{N_z} \bar{\rho}_{mnp} \sin\left(\frac{\pi m i}{N_x}\right) \sin\left(\frac{\pi n j}{N_y}\right) \exp\left(-\frac{2\pi k p}{N_z}\right) \quad (7.30b)$$

As a first step, Fourier coefficients in space-charge density expansion are calculated as

$$\bar{\rho}_{mnp} = \frac{4}{N_x N_y N_z} \sum_{i=1}^{N_x-1} \sum_{j=1}^{N_y-1} \sum_{p=1}^{N_z} \rho_{ijk} \sin\left(\frac{\pi m i}{N_x}\right) \sin\left(\frac{\pi n j}{N_y}\right) \exp\left(-\frac{2\pi k p}{N_z}\right) \quad (7.31)$$

Substitution of expressions of  $\phi_{ijk}$  and  $\rho_{ijk}$  into Poisson's equation, we obtain the relation between Fourier coefficients of space-charge  $\bar{\rho}_{mnp}$  and potential  $\bar{\phi}_{mnp}$ .

$$\bar{\phi}_{mnp} = \frac{\bar{\rho}_{mnp}}{\left(\frac{\pi m}{a}\right)^2 + \left(\frac{\pi n}{b}\right)^2 + \left(\frac{2\pi p}{L_b}\right)^2} \quad (7.32)$$

The potential  $\phi_{ijk}$  at the grid point  $(i, j, k)$  can be found using inverse Fourier transform as given by the expression Eq. (7.30). We used a centered difference scheme to calculate electric field at the grid points as given by,

$$E_{xijk} = -\frac{\phi_{i+1jk} - \phi_{i-1jk}}{2h_x}, E_{yijk} = -\frac{\phi_{ij+1k} - \phi_{ij-1k}}{2h_y}, E_{zijk} = -\frac{\phi_{ijk+1} - \phi_{ijk-1}}{2h_z} \quad (7.33)$$

#### 7.5.4 Interpolation of Fields to the Particles Position

The electric fields at all particle positions are calculated by interpolating from the electric field at the grid points using the same area weighting scheme as used for the calculation of the charge density matrix.

$$\begin{aligned} E_{x_n} = & E_{xijk}W_{ijk} + E_{x_{i+1}jk}W_{i+1jk} + E_{x_{ij+1}k}W_{ij+1k} \\ & + E_{x_{ijk+1}}W_{ijk+1} + E_{x_{i+1j+1k}}W_{i+1j+1k} + E_{x_{i+1jk+1}}W_{i+1jk+1} \\ & + E_{x_{ij+1k+1}}W_{ij+1k+1} + E_{x_{i+1j+1k+1}}W_{i+1j+1k+1} \end{aligned} \quad (7.34)$$

here  $W_{ijk}, W_{i+1jk}, W_{ij+1k}, W_{ijk+1}, W_{i+1j+1k}, W_{i+1jk+1}, W_{ij+1k+1}, W_{i+1j+1k+1}$  are the weighting factor at the grid points  $(i, j, k), (i+1, j, k), (i, j+1, k), (i, j, k+1), (i+1, j+1, k), (i+1, j, k+1), (i, j+1, k+1), (i+1, j+1, k+1)$  respectively. Similarly one can express the fields in  $y$  and  $z$  directions. The weighting factor  $W_{ijk}$  is

given by,

$$W_{ijk} = \left(1 - \frac{|x_n - x_i|}{h_x}\right) \left(1 - \frac{|y_n - y_j|}{h_y}\right) \left(1 - \frac{|z_n - z_k|}{h_z}\right) \quad (7.35)$$

And other weighting factors can also be found in a similar way.

## 7.6 Convergence Test and Benchmarking

There are two main sources of numerical errors relevant to beam dynamics simulation. First arises due to the finite accuracy of the arithmetic operations performed by the computer. Second one is due to the finite accuracy of the numerical methods used to calculate the fields at the grid points. The first type of errors can be minimised by using double precision arithmetics. At the same time we have used second order leap-from integrator with regards to the step size to increase the accuracy. The numerical stability of the integration scheme depends only on having sufficiently fine step size  $\Delta s$ . The most important condition in choosing a step size is to have enough steps to resolve the relevant length scales. Another issue that can affect the accuracy of PIC simulations is the number of macroparticles  $N$  used. The parameters  $N$  and number of grid points are not completely independent because a sensible charge density representation at the grid points is obtained only when there is a sufficient number of macroparticles per grid cell.

At first we found out the minimum number of macroparticles needed to represent the beam distributions. We have generated different initial distributions by varying the number of macroparticles. The rms normalised emittance is chosen equal to  $0.2\pi$  mmmrad which is same for all the distributions. The number of macroparticles is varied from  $10^2$  to  $10^5$ . At first, we have generated particles position and divergence for a particular number of macroparticles for all the distributions. Then using the values of position and divergence of the

macroparticles, we have again calculated rms emittance of the beam and estimated the error in the rms emittance. The process is repeated by varying the number of macroparticles.

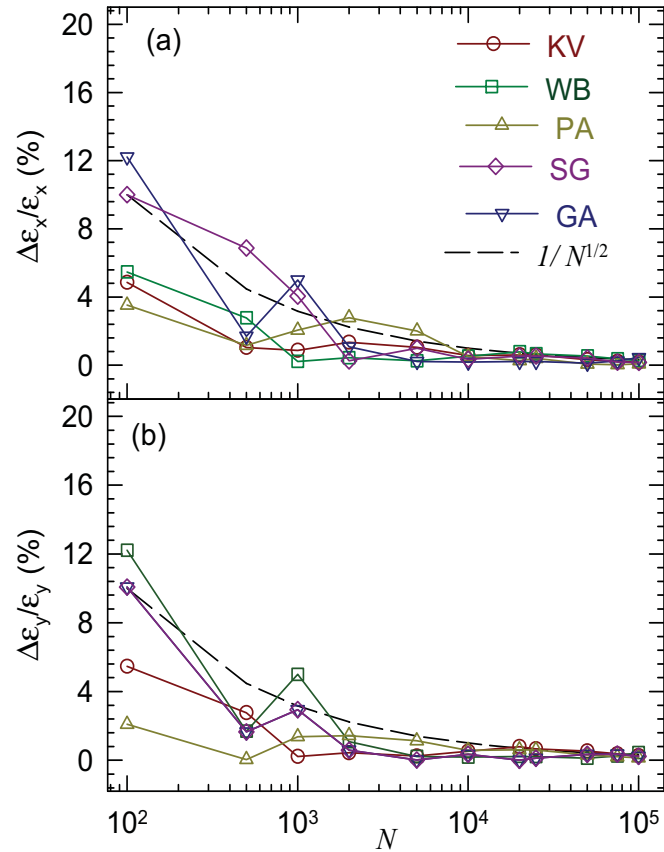


Figure 7.9: Variation of error in the generation of emittance against number of macroparticles.

Figure 7.9 shows the variation of percentage error in the calculated emittance as a function of number of macroparticles. It is easy to see that for number of macroparticles more than  $10^4$ , the error is within 1%. It can be also seen from the figure that the error follows the  $1/N^{1/2}$  pattern (shown by dashed curve).

In Fig. 7.10 beam density profiles are plotted for an initial K-V and Gaussian beam along the  $y$  axis for different values of number of grids and macroparticles.

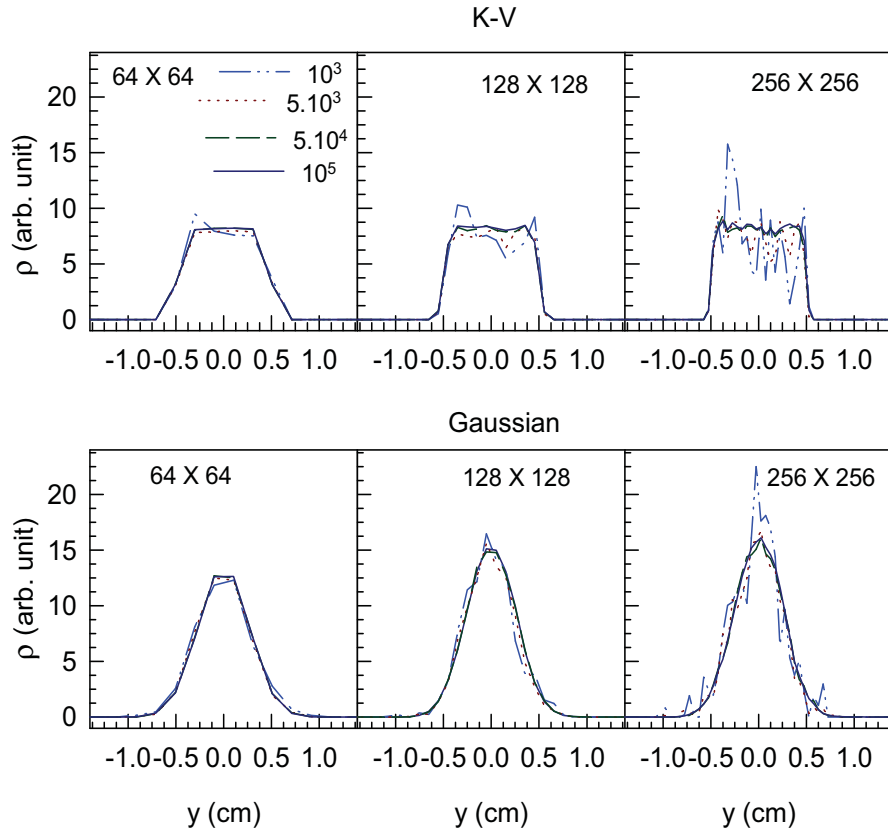


Figure 7.10: Plots of the beam density profiles along the  $y$  axis for different values of number of grids and macroparticles.

The number of grids are varied from  $64 \times 64$  to  $256 \times 256$ . For the number of grids  $64 \times 64$ , the outer boundary of the uniform density beam is not sharp even after using large number of macroparticles. With the number of grids  $128 \times 128$  we see that the beam boundary is comparatively sharp and the sharpness of the beam edge increases when the number of grids is increased to  $256 \times 256$ . With more number of grids one also needs more macroparticles to reduce the density fluctuation in the beam. It is readily seen that more than  $2 \cdot 10^4$  macroparticles are required for  $128 \times 128$  grids to get the smooth profile for the charge density whereas more than  $5 \cdot 10^4$  macroparticles are needed in the case of  $256 \times 256$  grids.

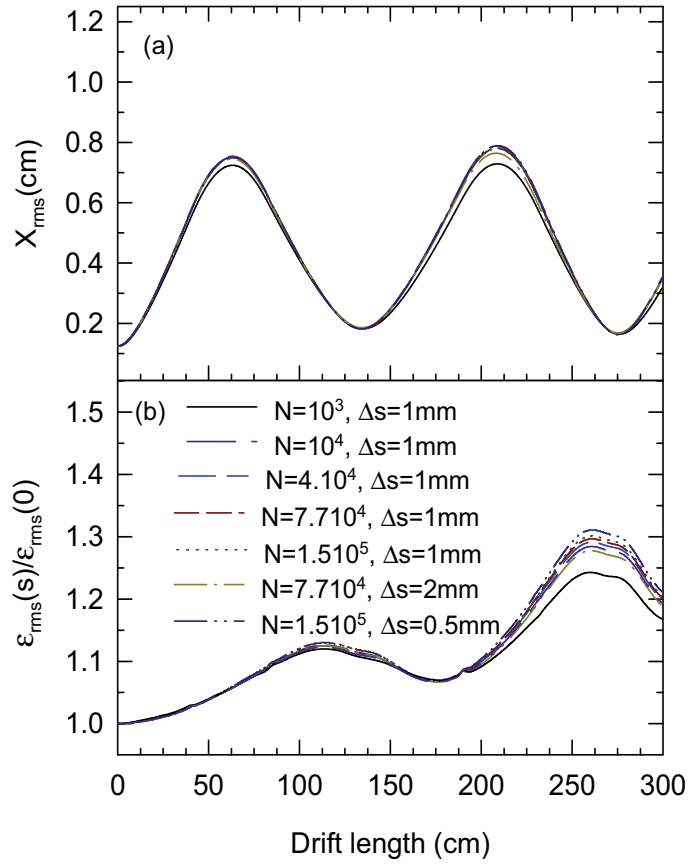


Figure 7.11: Evolution of (a) rms beam size and (b) rms emittance of an initial Gaussian distributed beam along the beam transport line for different values of  $N$ ,  $N_x$  and  $\Delta s$ .

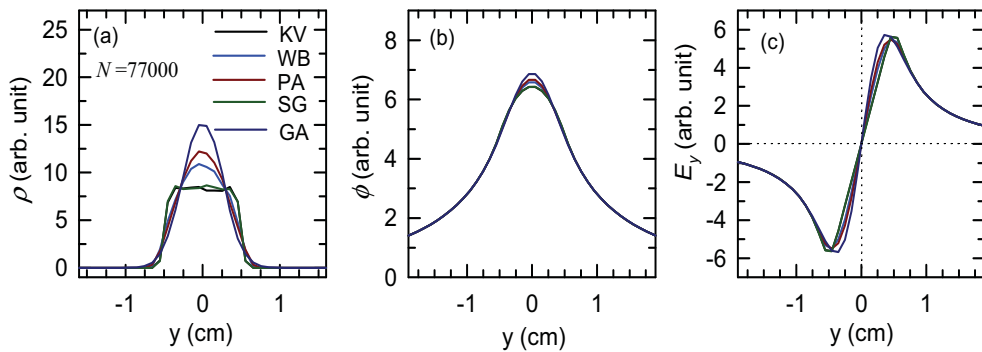


Figure 7.12: Variation of charge density, potential and  $y$ -component of electric field for different distributions.

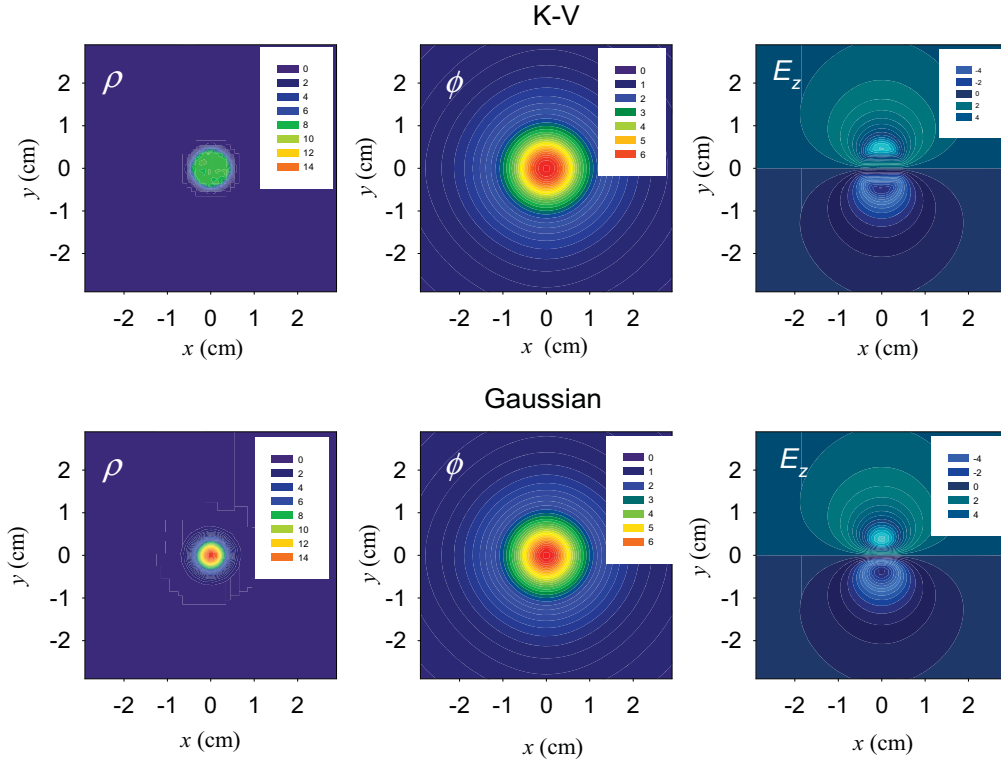


Figure 7.13: Contour plot for the charge density, potential and  $y$ -component of the electric field  $E_y$  for K-V and Gaussian distributions.

We now study the convergence properties with respect to the parameters  $\Delta s, N, N_x, N_y$  for the case of transport of proton beam in the solenoid based low energy beam transport line as discussed earlier. We consider the transport of 10 mA, 100 keV cw proton beam with Gaussian distribution and rms normalized emittances equal to  $0.2\pi$  mmmrad in the transverse planes. The simulation result for the evolution of rms beam size and rms emittance with initial Gaussian beam is shown in Fig. 7.11. Convergence studies included the following ranges of parameters:  $\Delta s = 5$  mm, 2 mm, 1 mm and 0.5 mm;  $N = 1000, 10000, 40000, 77000$  and 150000;  $N_x \times N_y = 64 \times 64, 128 \times 128$  and  $256 \times 256$ . It is evident from the figure that there is very small difference in the rms size and emittance when the number of macroparticles is more than 40000 and step size is less than

2 mm.

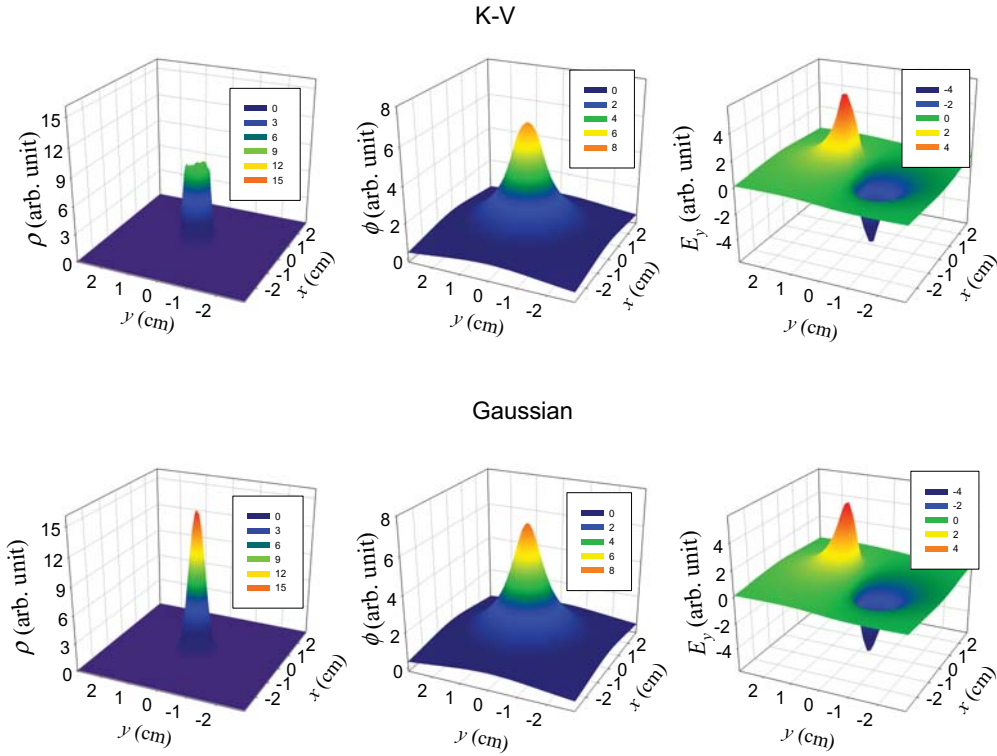


Figure 7.14: Three dimensional plot for the charge density, potential and  $y$ -component of the electric field  $E_y$  for K-V and Gaussian distributions.

Figure 7.12 shows the plots of density, potential and  $y$ -component of the electric field with 77000 macroparticles for K-V, waterbag, parabolic, Gaussian and semi-Gaussian distributions. The contour and the 3D plots of charge density, potential and  $y$ -component of electric field are also shown in Fig. 7.13 and Fig. 7.14 respectively for K-V and Gaussian distribution.

It is also important to validate the PIC simulation result with a wellknown analytical results. For this we have done the beam dynamics simulation for the same transport line using K-V distribution with PIC and wellknown beam envelope equation. Figure 7.15 shows the comparison of results obtained with PIC simulation (solid line) and solving the K-V beam envelope equations (dashed

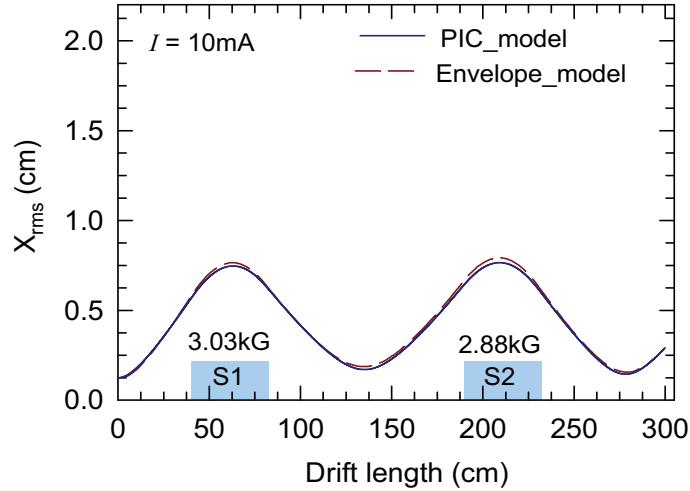


Figure 7.15: Plots of rms beam envelopes obtained with PIC method and envelope equation as a function of path length for  $I = 10$  mA. Beam input parameters are: rms beam size  $X_{rms}(0) = 1.25$  mm and rms divergence  $X'_{rms}(0) = 0$ , beam energy  $E_0 = 100$  keV, normalised rms emittance  $\varepsilon_{rms} = 0.2\pi$  mmmrad.

line). We have choose 77000 macroparticles and  $128 \times 128$  grids for this case. PIC simulation shows a good agreement.

## 7.7 Summary and Discussion

A PIC simulation method has been developed for the self-consistent evolution of a space-charge-dominated single and multispecies beam propagating through a beam transport system and the dynamics of intense beams during the longitudinal compression. In the 2D PIC model we have included the misalignment (displacement as well as tilt) and the higher order nonlinearity of the focussing element, off-centring of the beam. We have described the method in detail for 2D and 3D PIC codes. The convergence test and the benchmarking of the code have also been performed. The PIC codes developed in this chapter have been used extensively to study and understand the space-charge-dominated beam presented in previous chapters.

# Chapter 8

## Conclusions and Future Research

### 8.1 Conclusions

In this thesis, detailed analytical and numerical studies have been performed to study the dynamics of space-charge-dominated beam (single species and multi-species) propagating through a solenoid based low energy beam transport line. The main aim is to develop understanding of the dynamics of space-charge-dominated beam in the transport line and also providing valuable data for practical applications.

In **Chapter 2** of this thesis, a self-consistent kinetic description is described to understand the dynamics of a space-charge-dominated beam in a misaligned solenoidal channel. At first the magnetic field components of the misaligned solenoid in the laboratory frame have been obtained in terms of misalignment parameters and the single particle equation of motion has been developed. A general equation for the centroid motion of continuous, intense charged particle beam is derived using the kinetic nonlinear Vlasov-Maxwell equation. It has been shown that there exists a self-consistent Vlasov equilibrium distribution for the beam dynamics in the case of a uniform density around the centroid.

The beam envelope equation that determines the evolution of outer radius of equilibrium beam around the beam centroid is similar in form to the well known K-V envelope equation and is independent of the centroid equation when the conducting beam pipe is considered very far away from the beam. The self-consistent particle-in-cell (PIC) simulation supports the analytical results.

A self-consistent PIC model has been developed and utilized to study the dynamics of continuous space-charge-dominated beam through aligned and misaligned solenoid based transport system considering different kinds of initial beam distributions. In the case of aligned solenoids, it has been shown that the evolution of the rms beam sizes is weakly dependent on the form of the initial beam distribution. The emittance growth is seen to be greater in the converging part of the beam where the strength of nonlinear space-charge term is comparatively more. It is seen that there is an exchange of emittance from one plane to the other plane when the initial beam is nonaxisymmetric. In the case of misaligned solenoids, the simulation results with different distributions indicate that the motion of centroid is independent of the beam distribution. It is shown that the beam envelope around the centroid obeys the familiar envelope equation, and is independent of the centroid motion for small misaligned parameters. For large misalignment particularly tilt, the envelope evolution depends on form of the distribution of the beam. It is also found that the envelope is stable although the centroid motion is unstable. Large excursion of centroid without any control leads to the loss of the beam on the beam pipe particularly in the case of nonuniform beam distribution, revealing the importance of centroid motion to the overall beam confinement properties.

In the first part of **Chapter 3** of this thesis, a beam envelope model of an axisymmetric space-charge-dominated multispecies beam is presented for the evolution of the radius of each species in a solenoid based beam transport line.

Circular slit is used in the beam line for the selection of particular species. The effective values of the current and emittance of each species after the slit are taken into account in the beam envelope model for further transport in case the radius of any species is larger than the slit size. The analytical model has been used to transport proton from 2.45 GHz microwave ion source in the presence of  $H_2^+$ ,  $H_3^+$  species. Numerical results are presented for various values of the total beam current and different fractions of  $p$ ,  $H_2^+$ ,  $H_3^+$  species. It has been observed that envelope of the proton beam behaves differently in the presence of different fractions of the other components. The envelope model discussed in Chapter 3 can be utilised for more precise estimate of the beam envelope without the use of large simulations in the case of a multispecies beam.

In the later part of **Chapter 3**, the evolution of multispecies beam is studied using self-consistent 2D PIC method where each species of the beam is represented as a combination of large number of macroparticles. The evolution of beam size and emittance growth of the primary species due to other unwanted species for various beam parameters has been investigated. The real space distributions of the unwanted species have been investigated with and without the presence of a slit in the beam line. The formation of beam hollows of unwanted species is observed around the primary beam which is produced due to nonlinear space-charge effects. It has been shown that the rejection of unwanted species is very effective when we place the slit after the hollow formation of unwanted species.

In **Chapter 4** of this thesis, an optimisation method is discussed to find the optimal beam line settings for the transport and matching of multispecies beam using the multispecies beam envelope model described in Chapter 3. The optimisation method is based on random search technique where the transport parameters are varied randomly during the optimisation. Using this method,

the primary beam is matched at the desired position and the loss of unwanted species is maximised at the location of a circular slit. In the optimisation, two cost functionals are defined one for the primary beam and other for the unwanted species. The advantage of a random search technique over the other methods is that it is very simple to apply. In this technique one can easily introduce any number of constraints in the problem. It does not require any differentiation of the objective function with respect to the parameters. The technique is quite fast and can locate the global minimum within the specified range of the parameters if the random jump is chosen sufficiently large initially. To demonstrate the utility of the technique, the optimised parameters have been obtained for the transport and matching of intense proton beam from ion source in the presence of  $H_2^+$  and  $H_3^+$  in a solenoid based transport line. Numerical results of the beam selection and optimized transport parameters have been presented for various values of total beam current and different fractions of  $p$ ,  $H_2^+$  and  $H_3^+$  species. We have also tested the method at higher beam current upto 40 mA and found that optimization technique works well. For the transport of higher current say in the range of 40 – 100 mA, one needs space-charge compensation to restrict the beam envelope size within the reasonable limit. In that case the effective beam current will be reduced to  $I(1 - f)$  where  $f$  is the charge neutralization factor and the procedure discussed in Chapter 4 can be easily utilized.

In order to find out a suitable buncher in our injection system, numerical simulations have been carried out to study the bunching performance of sinusoidal, two harmonic and double drift bunchers in the presence of space charge. Methods and results are presented in **Chapter 5**. Disc model have been used for the longitudinal dynamics and K-V envelope equations have been used for transverse dynamics. Numerical simulations and optimisation of buncher pa-

rameters have been performed for 100 keV proton beam. It is found that the location of buncher from the time focus is a very crucial parameter in the case of high beam current. For a given beam current there is an optimum drift length beyond which the bunching efficiency decreases rapidly and is independent of buncher voltage. This decrease in bunching efficiency is very rapid at higher beam currents. We have also seen that the optimum drift length remains the same whether one uses a sinusoidal or a double harmonic or a double drift buncher. The simple disc model has helped us to obtain the required buncher parameters and configuration for our injection system. This method can be easily applied to any type of bunchers used in the accelerator laboratories.

In **Chapter 6** of this thesis, a model has been developed for the longitudinal and transverse beam dynamics of the bunch as it evolve under the influence of space charge and external force during the bunching. The longitudinal dynamics is studied using disc model and transverse dynamics is studied using envelope model. An analytical expression for the electric field experienced by a disc due to other disc inside a conducting pipe is derived using Green function technique for the case of bell shape and hollow shape density profiles in the transverse direction. The beam envelope equation has been modified to take into account the longitudinal space-charge effect on transverse motion, which arises when the beam size is comparable to the bunch size.

In order to include the variation of beam radius along the length of the beam and to understand the behaviour of projected emittance during the bunch compression, the total length of the beam is divided into thick slices. The evolution of radius of individual slice is then found out under the influence of space charge and external forces. For beams with bell shape distribution, it has been observed that the increased nonuniformity in density distribution reduces the total projected rms emittance as well as sharpness of the beam pulse at

the time focus. On the other hand, for beams with hollow shape distribution, the increased nonuniformity in density distributions increases the total rms projected emittance and the sharpness of the beam pulse at the time focus. It has also been observed that when the beam current is high the projected rms emittance of the bunch dominates over the rms emittance growth caused due to the phase mixing arising from the rf field.

Finally we have compared the results of analytical model with the 3D PIC simulations. The evolution of rms size and current in the bunch obtained from disc-envelope model agrees reasonably well with PIC simulation result. Simulation of emittance growth with PIC code shows a saturation value of final rms emittance of different slices. As expected, the beam with Gaussian distribution shows a considerably large emittance growth compared to case when K-V distribution is used.

In **Chapter 7** detail description of the 2D and 3D PIC simulation methods used in the previous chapters for the self-consistent evolution of space-charge-dominated (single and multispecies) beam have been described. In the 2D PIC model we have included the misalignment (displacement as well as tilt) and the higher order nonlinearity of the focussing element, off-centring of the beam. The convergence test and the benchmarking of the code have also been performed.

## 8.2 Future Research

Our studies on the dynamics of intense beam in low energy transport line open up the following directions of research which can be attempted in future. In the present thesis, we have considered only solenoid magnets (based on requirement of the project) for focussing of the intense beam. The analysis can be extended to study the beam dynamics in transport lines where solenoid and quadrupole magnets are present. The combination of both magnets can be used

for the matching of axisymmetric beam into nonaxisymmetric beam. It would be interesting to study the effect of misalignments of solenoid and quadrupole magnets on the beam behaviour.

In the thesis we have considered the uniform density distributions for all the species for the development of multispecies beam envelope equation. Though, we have predicted the evolution of rms beam sizes for all the species using PIC simulation for different distributions, the analysis can be extended analytically using different types of fixed shape density distribution. This analysis will predict the beam envelope evolution for realistic distribution. The PIC simulation method can also be extended to study the effect of misalignments of the focussing magnets on the primary beam in the presence of unwanted species, which has not been discussed in this thesis.

We have used 3D PIC code for the complete description of collective behavior in intense charged particle beams during the bunching. Since full 3D PIC method is very slow, an alternate fast method can be developed to study the transverse dynamics during the beam bunching by combining 2D PIC and disc model together. For simplicity many authors have taken linear increase in the bunch current along the beam transport line during the bunching. It would be more realistic if one takes the more realistic data for the increase in the beam current which one can obtain by using the beam envelope and disc model. This value can be easily included in the 2D PIC model to study the transverse beam dynamics.

We have developed an optimisation technique to obtain the parameters of beam transport lines for the matching of intense multispecies beam. The technique can be extended to carry out the analysis in the presence of bunching for single species. The evolution of transverse beam size will be different than

that of the continuous beam. This effect will be small in the case of low beam current but it will become important in the case of intense beam and will affect the matching at the target location. One can do it by varying the strength and position of the magnet. But sometimes due to the constraint of the available drift space, one may not be able to achieve the matching condition. Thus for the proper matching, one may need another parameter that is the variation in the length of the solenoid magnet together with the strength and the location, which we have not explored in the present thesis.

# Appendix A

## A.1 Calculation of $f(r_j, r_k)$ and $g(r_j, r_k)$

In this Appendix, we derive the term  $f(r_j, r_k)$  and  $g(r_j, r_k)$  as given in Eq. (3.21) and Eq. (3.22) for the case of uniform density distribution for all the species.

The functions  $f(r_j, r_k)$  and  $g(r_j, r_k)$  in Eq. (3.20) is defined as

$$f(r_j, r_k) = \overline{\frac{x^2}{r_k^2(s)} \Theta(r_k(s) - r)} \quad (\text{A.1})$$

$$g(r_j, r_k) = \overline{\frac{x^2}{r^2} \Theta(r - r_k(s))} \quad (\text{A.2})$$

where the average of the quantity  $h(\mathbf{r}, \mathbf{p}, s)$  is given by

$$\overline{h(\mathbf{r}, \mathbf{p}, s)} = \frac{\int \int h(\mathbf{r}, \mathbf{p}, s) f_j(\mathbf{r}, \mathbf{p}, s) d\mathbf{r} d\mathbf{p}}{\int \int f_j(\mathbf{r}, \mathbf{p}, s) d\mathbf{r} d\mathbf{p}} \quad (\text{A.3})$$

Here  $f_j(\mathbf{r}, \mathbf{p}, s)$  is the distribution function for species  $j$ . The number density of species  $j$  is

$$n_j(\mathbf{r}, s) = \int f_j(\mathbf{r}, \mathbf{p}, s) d\mathbf{p} \quad (\text{A.4})$$

For K-V distributed beam we can write

$$n_j(\mathbf{r}, s) = \begin{cases} n_j & 0 < r \leq r_j(s) \\ 0 & r > r_j(s) \end{cases} \quad (\text{A.5})$$

where,  $n_j = N_j / (\pi r_j^2(s))$ ,  $N_j$  is the number of particles per unit length. If  $r_j(s) < r_k(s)$  then

$$\overline{\frac{x^2}{r^2} \Theta(r - r_k(s))} = 0 \quad (\text{A.6})$$

and

$$\begin{aligned}
 \overline{\frac{x^2}{r_k^2(s)} \Theta(r_k(s) - r)} &= \frac{\int \frac{x^2}{r_k^2(s)} \Theta(r_k(s) - r) f_j(\mathbf{r}, \mathbf{p}, s) d\mathbf{r} d\mathbf{p}}{\int f_j(\mathbf{r}, \mathbf{p}, s) d\mathbf{r} d\mathbf{p}} \\
 &= \frac{\int \frac{x^2}{r_k^2(s)} \Theta(r_k(s) - r) n_j(\mathbf{r}, s) d\mathbf{r}}{\int n_j(\mathbf{r}, s) d\mathbf{r}} \\
 &= \frac{\int_0^{r_j(s)} \int_0^{2\pi} \frac{x^2}{r_k^2(s)} n_j r dr d\theta}{\int_0^{r_j(s)} \int_0^{2\pi} n_j r dr d\theta} = \frac{r_j^2(s)}{4r_k^2(s)} \quad (\text{A.7})
 \end{aligned}$$

(b) If  $r_j(s) > r_k(s)$  then average exists for both the terms i.e.

$$\overline{\frac{x^2}{r_k^2(s)} \Theta(r_k(s) - r)} = \frac{\int_0^{r_k(s)} \int_0^{2\pi} \frac{x^2}{r_k^2(s)} n_j r dr d\theta}{\int_0^{r_k(s)} \int_0^{2\pi} n_j r dr d\theta} = \frac{r_k^2(s)}{4r_j^2(s)} \quad (\text{A.8})$$

and

$$\overline{\frac{x^2}{r^2} \Theta(r - r_k(s))} = \frac{\int_{r_k(s)}^{r_j(s)} \int_0^{2\pi} \frac{x^2}{r^2} n_j(r, s) r dr d\theta}{\int_{r_k(s)}^{r_j(s)} \int_0^{2\pi} n_j(r, s) r dr d\theta} = \frac{1}{2} \left( 1 - \frac{r_k^2(s)}{r_j^2(s)} \right) \quad (\text{A.9})$$

Substituting above values in Eq. (A.1) and Eq. (A.2), we obtain

$$f(r_j, r_k) = \begin{cases} \frac{r_j^2}{4r_k^2} & \text{if } r_j < r_k \\ \frac{r_k^2}{4r_j^2} & \text{if } r_j > r_k \end{cases} \quad (\text{A.10})$$

and

$$g(r_j, r_k) = \begin{cases} 0 & \text{if } r_j < r_k \\ \frac{1}{2} \left( 1 - \frac{r_k^2}{r_j^2} \right) & \text{if } r_j > r_k \end{cases} \quad (\text{A.11})$$

## A.2 Beam Selection through Circular Slit

To solve the envelope Eq. (3.23), we need to calculate the phase space area that passes through the slit in the case when the beam size is larger than the radius of the slit. For illustration we have shown a typical phase space ellipse of a species of the beam at the location of the slit in Fig. A.1. The maximum opening of the slit is shown by two vertical solid lines. So the effective phase space area which passes through the slit is the shaded region. The effective

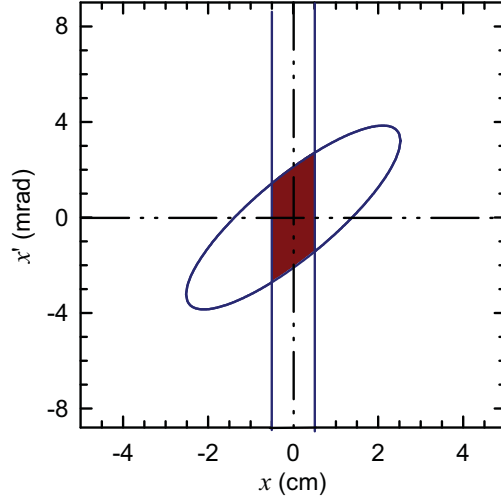


Figure A.1: Plot shows a typical phase space ellipse at the slit position. The edges of the slit are shown by two vertical solid lines.

emittance which passes through the slit can be easily obtained by using the steps given below. The equation of the ellipse at the slit position can be written as

$$\gamma_j x^2 + 2\alpha_j x x' + \beta_j x'^2 = \varepsilon_j \quad (\text{A.12})$$

where  $\varepsilon_j$  is the emittance of species  $j$  of the beam before the slit and  $\alpha_j, \beta_j$  and  $\gamma_j$  are the well known Twiss parameters. From the above equation we can write

$$x' = -\frac{\alpha_j}{\beta_j} x \pm \sqrt{\frac{\varepsilon_j}{\beta_j} - \frac{x^2}{\beta_j^2}}$$

The area of the shaded region is given by

$$\Delta A_j = \int_{-r_{slit}}^{r_{slit}} \int_{-\frac{\alpha_j}{\beta_j} x - \sqrt{\frac{\varepsilon_j}{\beta_j} - \frac{x^2}{\beta_j^2}}}^{-\frac{\alpha_j}{\beta_j} x + \sqrt{\frac{\varepsilon_j}{\beta_j} - \frac{x^2}{\beta_j^2}}} dx dx' = 2 \int_{-r_{slit}}^{r_{slit}} \sqrt{\frac{\varepsilon_j}{\beta_j} - \frac{x^2}{\beta_j^2}} dx$$

After simplification we obtain

$$\Delta A_j = 2\varepsilon_j \left[ p\sqrt{1-p^2} + \sin^{-1} p \right] \quad (\text{A.13})$$

where  $p = r_{slit}/r_j(\text{slit})$ . The effective emittance of species  $j$  after the slit is, therefore, given by  $\varepsilon_{j\text{eff}} = \Delta A_j/\pi$ . To calculate the orientation of the effective

phase ellipse after the slit, first we need to calculate the rms emittance of the new area as well as the twiss parameters  $\alpha s_j$ ,  $\beta s_j$  and  $\gamma s_j$  of the ellipse just after the slit. The rms quantities just after the slit are given by

$$\overline{x^2} = \frac{\int \int x^2 dx dx'}{\int \int dx dx'} = \frac{I_1}{\Delta A_j} \quad (\text{A.14})$$

$$\begin{aligned} I_1 &= \int \int x^2 dx dx' \\ &= \frac{\varepsilon_j r_{slit}^2}{2p^2} \left[ p\sqrt{1-p^2} - 2p(1-p^2)^{3/2} + \sin^{-1} p \right] \end{aligned}$$

$$\overline{x'^2} = \frac{\int \int x'^2 dx dx'}{\int \int dx dx'} = \frac{I_2}{\Delta A_j} \quad (\text{A.15})$$

$$\begin{aligned} I_2 &= \int \int x'^2 dx dx' \\ &= \frac{\varepsilon_j^3 p^2}{6r_{slit}^2} \left[ 3\beta_j \gamma_j \sin^{-1} p + 3\beta_j \gamma_j p\sqrt{1-p^2} + 2p(1-3\alpha_j^2)(1-p^2)^{3/2} \right] \end{aligned}$$

$$\overline{xx'} = \frac{\int \int xx' dx dx'}{\int \int dx dx'} = \frac{I_3}{\Delta A_j} \quad (\text{A.16})$$

$$\begin{aligned} I_3 &= \int \int xx' dx dx' \\ &= -\frac{\alpha_j \varepsilon_j^2}{2} \left[ p\sqrt{1-p^2} - 2p(1-p^2)^{3/2} + \sin^{-1} p \right] \end{aligned}$$

The rms emittance of the species  $j$  after the slit can be obtained from

$$\tilde{\varepsilon} s_j = \frac{\sqrt{I_1 I_2 - I_3^2}}{\Delta A_j} \quad (\text{A.17})$$

### A.3 Runge-Kutta Method

We have used 4<sup>th</sup> order Runge-Kutta method for solving the envelope equations of species as given in Eq. (3.23) in **Chapter 3**. At first, we converted the  $n$  number of second order equations into  $2n$  first order equations. We represented

the radii and divergence of the beam envelope by two vectors  $R$  and  $V$  i.e.

$R^T = [r_1, r_2, \dots, r_n]$  and  $V^T = [r'_1, r'_2, \dots, r'_n]$ . We can write Eq.(3.23) as

$$R' = V \tag{A.18a}$$

$$V' = F(R, I, \varepsilon, kl, s) \tag{A.18b}$$

where

$$I^T = [I_1(s), I_2(s), \dots, I_n(s)]$$

$$\varepsilon^T = [\varepsilon_1(s), \varepsilon_2(s), \dots, \varepsilon_n(s)]$$

$$kl^T = [kl_1(s), kl_2(s), \dots, kl_n(s)]$$

(A.19)

The solution at the  $(i + 1)$ th interval can be written as

$$R_{i+1} = R_i + \frac{1}{6} [K_1 + 2K_2 + 2K_3 + K_4] \tag{A.20a}$$

$$V_{i+1} = V_i + \frac{1}{6} [L_1 + 2L_2 + 2L_3 + L_4] \tag{A.20b}$$

where

$$K_1 = \Delta s \cdot V_i$$

$$L_1 = \Delta s \cdot F(R_i, I, \varepsilon, kl, s_i)$$

$$K_2 = \Delta s \cdot \left( V_i + \frac{L_1}{2} \right)$$

$$L_2 = \Delta s \cdot F\left( R_i + \frac{K_1}{2}, I, \varepsilon, kl, s_i + \frac{\Delta s}{2} \right)$$

$$K_3 = \Delta s \cdot \left( V_i + \frac{L_2}{2} \right)$$

$$L_3 = \Delta s \cdot F\left( R_i + \frac{K_2}{2}, I, \varepsilon, kl, s_i + \frac{\Delta s}{2} \right)$$

$$K_4 = \Delta s \cdot (V_i + L_3)$$

$$L_4 = \Delta s \cdot F(R_i + K_3, I, \varepsilon, kl, s_i + \Delta s)$$

In order to obtain the radius of each species of the beam, we have calculated the values of  $K_1, K_2, K_3, K_4, L_1, L_2, L_3, L_4$  at each step. At the slit position the effective beam current and emittance of each species were modified using the expressions as given in Eq. (3.24) and Eq. (3.25) respectively.

# Appendix B

In this Appendix, we have derived the expressions for the electric fields as used in Eq. (6.19) and in Eq. (6.20) for the case of bell shape and hollow shape density distributions respectively. Similarly these expressions can be utilised in Eq. (6.31) to get the final expressions Eq. (6.33) and Eq. (6.34).

## B.1 Evaluation of $\langle E_{ij} \rangle$ for Bell Shape Density Profile

The expression for electric field on disc  $i$  due to disc  $j$  for the case of bell shape distribution is

$$E_{ij}(r, p, s) = \frac{\lambda\sigma_B(p, R_j)w}{\epsilon_0 b^2} \sum_{n=1}^{\infty} \exp(-\beta_n |z_i - z_j|) \frac{J_0(\beta_n r)}{J_1^2(\alpha_n)} \times \int_0^{R_j} J_0(\beta_n r') \left(1 - \frac{r'^2}{R_j^2}\right)^p r' dr' \cdot \text{sign}(z_i - z_j) \quad (\text{B.1})$$

where  $R_j = R(p, z_j, s)$ .

The average longitudinal electric field on disc  $i$  due to disc  $j$  can be obtained using

$$\langle E_{ij}(r, p, s) \rangle = \frac{\int_{r=0}^{R_i} \int_{\phi=0}^{2\pi} E_{ij}(r, p, s) \lambda\sigma_B(p, R_i) \left(1 - \frac{r^2}{R_i^2}\right)^p r dr d\phi}{\int_{r=0}^{R_i} \int_{\phi=0}^{2\pi} \lambda\sigma_B(p, R_i) \left(1 - \frac{r^2}{R_i^2}\right)^p r dr d\phi} \quad (\text{B.2})$$

$$\begin{aligned}
 \langle E_{ij}(r, p, s) \rangle &= A_B \sum_{n=1}^{\infty} \frac{\exp(-\beta_n |z_i - z_j|)}{J_1^2(\alpha_n)} \left[ \int_0^{R_j} J_0(\beta_n r') \left(1 - \frac{r'^2}{R_j^2}\right)^p r' dr' \right] \\
 &\times \left[ \int_0^{R_i} J_0(\beta_n r) \left(1 - \frac{r^2}{R_i^2}\right)^p r dr \right] \text{sign}(z_i - z_j) \quad (\text{B.3})
 \end{aligned}$$

where  $A_B = \frac{2\pi Q \sigma_B(p, R_j) \sigma_B(p, R_i)}{\epsilon_0 b^2}$ . The above equation can be simplified as

$$\begin{aligned}
 \langle E_{ij}(r, p, s) \rangle &= B_B \sum_{n=1}^{\infty} \frac{\exp(-\beta_n |z_i - z_j|)}{J_1^2(\alpha_n)} \left[ \int_0^{R_j} J_0(\beta_n r') \left(1 - \frac{r'^2}{R_j^2}\right)^p r' dr' \right] \\
 &\times \left[ \int_0^{R_i} J_0(\beta_n r) \left(1 - \frac{r^2}{R_i^2}\right)^p r dr \right] \text{sign}(z_i - z_j) \quad (\text{B.4})
 \end{aligned}$$

where  $B_B = \frac{2Q(p+1)^2}{\pi \epsilon_0 b^2 R_j^2 R_i^2}$ . Here we have used the relation  $\sigma_B(p, R) = \frac{p+1}{\pi R^2(p)}$ .

Let us define

$$I_b(p, R) = (p+1) \int_0^R J_0(\beta_n r) \left(1 - \frac{r^2}{R^2}\right)^p r dr \quad (\text{B.5})$$

To calculate the integral we have used the relation  $\int t^\alpha J_{\alpha-1}(t) dt = t^\alpha J_\alpha(t)$

For  $p = 1$

$$\begin{aligned}
 I_b(1, R) &= 2 \int_0^R J_0(\beta_n r) \left(1 - \frac{r^2}{R^2}\right) r dr \\
 &= \frac{4}{\beta_n^2} J_2(\beta_n R)
 \end{aligned}$$

We can arrange it as

$$I_b(1, R) = \frac{2(1+1)!}{\beta_n^{1+1} R^{1-1}} J_{1+1}(\beta_n R) \quad (\text{B.6})$$

For  $p = 2$

$$\begin{aligned}
 I_b(2, R) &= 3 \int_0^R J_0(\beta_n r) \left(1 - \frac{r^2}{R^2}\right)^2 r dr \\
 &= 3 \int_0^R J_0(\beta_n r) \left(1 - \frac{2r^2}{R^2} + \left(\frac{r^2}{R^2}\right)^2\right) r dr \\
 &= \frac{24}{\beta_n^3 R} J_3(\beta_n R)
 \end{aligned}$$

We can arrange the expression as

$$I_b(2, R) = \frac{2^2(2+1)!}{\beta_n^{2+1}R^{2-1}}J_{2+1}(\beta_n R) \quad (\text{B.7})$$

For  $p = 3$

$$\begin{aligned} I_b(3, R) &= 4 \int_0^R J_0(\beta_n r) \left(1 - \frac{r^2}{R^2}\right)^3 r dr \\ &= 4 \int_0^R J_0(\beta_n r) \left(1 - \frac{3r^2}{R^2} + 3\left(\frac{r^2}{R^2}\right)^2 - \left(\frac{r^2}{R^2}\right)^3\right) r dr \\ &= \frac{192}{\beta_n^4 R^2} J_4(\beta_n R) \end{aligned}$$

We can arrange the expression as

$$I_b(3, R) = \frac{2^3(3+1)!}{\beta_n^{3+1}R^{3-1}}J_{3+1}(\beta_n R) \quad (\text{B.8})$$

So in general we can write

$$I_b(p, R) = \frac{2^p(p+1)!}{\beta_n^{p+1}R^{p-1}}J_{p+1}(\beta_n R) \quad (\text{B.9})$$

If we substitute the expression (B.9) of  $I_b(p, R)$  in Eq. (B.4) we obtain

$$\begin{aligned} \langle E_{ij}(r, p, s) \rangle &= \frac{Q2^{2p+1}((p+1)!)^2 b^{2p}}{\pi \epsilon_0 R_i^{p+1} R_j^{p+1}} \sum_{n=1}^{\infty} \frac{\exp(-\beta_n |z_i - z_j|)}{J_1^2(\alpha_n)} \\ &\quad \times \frac{J_{p+1}(\beta_n R_i) J_{p+1}(\beta_n R_j)}{\alpha_n^{2p+2}} \text{sign}(z_i - z_j) \end{aligned} \quad (\text{B.10})$$

## B.2 Evaluation of $\langle E_{ij} \rangle$ for Hollow Shape Density Profile

For hollow shape density distribution the average electric field on disc  $i$  due to disc  $j$  is

$$\begin{aligned} \langle E_{ij}(r, p, s) \rangle &= A_H \sum_{n=1}^{\infty} \frac{\exp(-\beta_n |z_i - z_j|)}{J_1^2(\alpha_n)} \left[ \int_0^{R_j} J_0(\beta_n r') \left(1 + \frac{r'^2}{R_j^2}\right)^p r' dr' \right] \\ &\quad \times \left[ \int_0^{R_i} J_0(\beta_n r) \left(1 + \frac{r^2}{R_i^2}\right)^p r dr \right] \text{sign}(z_i - z_j) \end{aligned} \quad (\text{B.11})$$

Where  $A_H = \frac{2\pi Q\sigma_H(p,R_j)\sigma_H(p,R_i)}{\epsilon_0 b^2}$ . The above equation can be simplified as

$$\begin{aligned} \langle E_{ij}(r, p, s) \rangle &= B_H \sum_{n=1}^{\infty} \frac{\exp(-\beta_n |z_i - z_j|)}{J_1^2(\alpha_n)} \left[ \int_0^{R_j} J_0(\beta_n r') \left(1 + \frac{r'^2}{R_j^2}\right)^p r' dr' \right] \\ &\times \left[ \int_0^{R_i} J_0(\beta_n r) \left(1 + \frac{r^2}{R_i^2}\right)^p r dr \right] \text{sign}(z_i - z_j) \end{aligned} \quad (\text{B.12})$$

where,  $B_H = \frac{2Q(p+1)^2}{\pi\epsilon_0(2^{p+1}-1)^2 R_i^2 R_j^2 b^2}$ . Here we have used the relation  $\sigma_H(p, r) = \frac{(p+1)}{\pi(2^{p+1}-1)R^2(p)}$ .

Let us define

$$I_h(p, R) = \int_0^R J_0(\beta_n r) \left(1 + \frac{r^2}{R^2}\right)^p r dr \quad (\text{B.13})$$

For  $p = 1$

$$\begin{aligned} I_h(1, R) &= \int_0^R J_0(\beta_n r) \left(1 + \frac{r^2}{R^2}\right) r dr \\ &= \frac{2R}{\beta_n} J_1(\beta_n R) - \frac{2}{\beta_n^2} J_2(\beta_n R) \end{aligned}$$

We can arrange the expression as

$$I_h(1, R) = 2^1 \left[ \frac{R}{\beta_n} J_1(\beta_n R) - \frac{1}{\beta_n^2} J_2(\beta_n R) \right] \quad (\text{B.14})$$

For  $p = 2$

$$\begin{aligned} I_h(2, R) &= \int_0^R J_0(\beta_n r) \left(1 + \frac{r^2}{R^2}\right)^2 r dr \\ &= \int_0^R J_0(\beta_n r) \left(1 + \frac{2r^2}{R^2} + \left(\frac{r^2}{R^2}\right)^2\right) r dr \\ &= \frac{4R}{\beta_n} J_1(\beta_n R) - \frac{8}{\beta_n^2} J_2(\beta_n R) + \frac{8}{\beta_n^3 R} J_3(\beta_n R) \end{aligned}$$

Arranging the above expression we can write

$$I_h(2, R) = 2^2 \left[ \frac{R}{\beta_n} J_1(\beta_n R) - \frac{2}{\beta_n^2} J_2(\beta_n R) + \frac{2!}{\beta_n^3 R} J_3(\beta_n R) \right] \quad (\text{B.15})$$

Similarly for  $p = 3$  we can write,

$$\begin{aligned}
 I_h(3, R) = & 2^3 \left[ \frac{R}{\beta_n} J_1(\beta_n R) - \frac{3}{\beta_n^2} J_2(\beta_n R) + \frac{3 \cdot 2}{\beta_n^3} J_3(\beta_n R) \right. \\
 & \left. - \frac{3!}{\beta_n^4 R^2} J_4(\beta_n R) \right] \tag{B.16}
 \end{aligned}$$

In general

$$\begin{aligned}
 I_h(p, R) = & 2^p \left[ \frac{R}{\beta_n} J_1(\beta_n R) - \frac{p}{\beta_n^2} J_2(\beta_n R) + \frac{p \cdot (p-1)}{\beta_n^3} J_3(\beta_n R) \right. \\
 & \left. - \dots + (-1)^p \frac{p!}{\beta_n^{p+1} R^{p-1}} J_{p+1}(\beta_n R) \right] \tag{B.17}
 \end{aligned}$$

Substituting the above expression (B.17) and using  $\beta_n b = \alpha_n$  in Eq. (B.12) we obtain,

$$\begin{aligned}
 \langle E_{ij}(r, p, s) \rangle = & B_H 2^{2p} b^2 \sum_{n=1}^{\infty} \frac{\exp(-\beta_n |z_i - z_j|)}{J_1^2(\alpha_n)} \left[ \frac{R_i}{\alpha_n} J_1(\beta_n R_i) - \frac{pb}{\alpha_n^2} J_2(\beta_n R_i) \right. \\
 & \left. + \frac{p \cdot (p-1) b^2}{\alpha_n^3 R_i} J_3(\beta_n R_i) - \dots + \frac{(-1)^p p! b^{p-1}}{\alpha_n^{p+1} R_i^{p-1}} J_{p+1}(\beta_n R_i) \right] \\
 & \times \left[ \frac{R_j}{\alpha_n} J_1(\beta_n R_j) - \frac{pb}{\alpha_n^2} J_2(\beta_n R_j) + \frac{p \cdot (p-1) b^2}{\alpha_n^3 R_j} J_3(\beta_n R_j) \right. \\
 & \left. - \dots + \frac{(-1)^p p! b^{p-1}}{\alpha_n^{p+1} R_j^{p-1}} J_{p+1}(\beta_n R_j) \right] \text{sign}(z_i - z_j) \tag{B.18}
 \end{aligned}$$

# Bibliography

- [1] H. Nifenecker, S. David, J. M. Loiseaux, and O. Meplan, Nucl. Instrum. Methods Phys. Res. A **463**, 428 (2001).
- [2] G. S. Bauer, Nucl. Instrum. Methods Phys. Res. A **463**, 505 (2001).
- [3] R. C. Arnold, Nature **276**, 19 (1978).
- [4] M. Abs *et al.*, arXiv: acc-ph/1207.4895v2.
- [5] A. Calanna, D. Campo, L. Calabretta, M. Maggiore, L. A. C. Piazza, and F. Meot, in *Proceedings of the 3rd International Particle Accelerator Conference*, New Orleans, Louisiana, USA (2012) p. 421.
- [6] C. Rubbia, P. Mandrillon, and N. Fietier, in *Proceedings of the 4th European Particle Accelerators Conference*, London, UK (1994) p. 270.
- [7] G. P. Lawrence, Nucl. Instrum. Methods Phys. Res. B **55/57**, 1000 (1991).
- [8] N. Fietier and P. Mandrillon, in *Proceedings of the 14th International Conference on cyclotrons and their Applications*, Cape Town, South Africa (1995) p. 598.
- [9] M. Seidel *et al.*, in *Proceedings of the 1st International Particle Accelerator Conference*, Kyoto, Japan (2010) p. 1309.
- [10] M. Seidel *et al.*, in *Proceedings of the 19th International Conference on cyclotrons and their Applications*, Lanzhou, China (2010) p. 275.
- [11] A. Goswami, P. Sing Babu, and V. S. Pandit, Nucl. Instrum. Methods Phys. Res. A **562**, 34 (2006).
- [12] P. Sing Babu, A. Goswami, P. R. Sarma, and V. S. Pandit, Nucl. Instrum. Methods Phys. Res. Sect. A **624**, 560 (2010).
- [13] A. Goswami, P. Sing Babu, and V. S. Pandit, Eur. Phys. J. Plus **127**: 47 (2012).

- [14] V. S. Pandit *et al.*, in *2nd International Workshop on ADS and Thorium Utilization*, BARC, Mumbai (2011).
- [15] M. Reiser, *Theory and Design of Charged Particle Beams* (John Wiley and Sons, New York, 1994).
- [16] R. C. Davidson and H. Qin, *Physics of Intense Charged Particle Beams in High Energy Accelerators* (World Scientific, Singapore, 2001).
- [17] I. M. Kapchinskij and V. V. Vladimirkij, in *Proceedings of the International Conference on High Energy Accelerators and Instrumentation*, CERN, Geneva (1959) p. 274.
- [18] C. Chen, R. Pakter, and R. C. Davidson, *Phys. Rev. Lett.* **79**, 225 (1997).
- [19] J. S. Moraes, R. Pakter, and F. B. Rizzato, *Phys. Rev. Lett.* **93**, 244801 (2004).
- [20] F. J. Sacherer, *IEEE Trans. Nucl. Sci.* NS-**18**, 1105 (1971).
- [21] P. M. Lapostolle, *IEEE Trans. Nucl. Sci.* NS-**18**, 1101 (1971).
- [22] B. L. Qian, J. Zhou, and C. Chen, *Phys. Rev. ST Accel. Beams* **6**, 014201 (2003).
- [23] J. Zhou, B. L. Qian, and C. Chen, *Phys. Plasmas* **11**, 4203 (2003).
- [24] R. W. Hockney and J. W. Eastwood, *Computer Simulation Using Particles* (Taylor & Francis, New York, 1988).
- [25] C. Z. Cheng and G. Knorr, *J. Comput. Phys.* **22**, 330 (1976).
- [26] E. Sonnendrucker, J. Roche, P. Bertrand, and G. Ghizzo, *J. Comput. Phys.* **149**, 201 (1999).
- [27] E. Sonnendrucker, J. J. Barnard, A. Friedman, D. P. Grote, and S. M. Lund, *Nucl. Instrum. Methods Phys. Res. Sect. A* **464**, 470 (2001).
- [28] H. Qin, M. Chung, and R. C. Davidson, *Phys. Rev. Lett.* **103**, 224802 (2009).
- [29] H. Qin and R. C. Davidson, *Phys. Plasmas* **16**, 050705 (2009).
- [30] H. Qin and R. C. Davidson, *Phys. Rev. ST Accel. Beams* **12**, 064001 (2009).

- [31] C. Papadopoulos, G. Bai, R. A. Kishek, I. Haber, M. Walter, B. Beaudoin, P. G. O'Shea, and M. Reiser, in *Proceedings of the 2007 Particle Accelerators Conference*, Albuquerque, New Mexico, USA (2007) p. 3567.
- [32] C. M. Celata, I. Haber, and D. P. Grote, in *Proceedings of the 2001 Particle Accelerators Conference*, (IEEE, Piscataway, NJ, 2001), p. 2926.
- [33] J. J. Barnard, in *Proceedings of the 1995 Particle Accelerators Conference*, (IEEE, Piscataway, NJ, 1996), p. 3241.
- [34] S. M. Lund, C. J. Wootton, and E. P. Lee, *Nucl. Instr. and Meth. A* **606**, 56 (2009).
- [35] J. E. Coleman, P. A. Seidl, E. Henestroza, M. A. Leitner, P. K. Roy, W. L. Waldron, D. Baca, I. Haber, A.W. Molvik, W. M. Sharp, and J. Armijo, *Phys. Rev. ST Accel. Beams* **11**, 050101 (2008).
- [36] L. C. Martins, F. B. Rizzato, and R. Pakter, *Journal of Appl. Phys.* **106**, 043305, (2009).
- [37] M. Hess and C. Chen, *Phys. Lett. A* **295**, 305 (2002); *Phys. Rev. ST Accel. Beams* **7**, 092002 (2004).
- [38] J. S. Moraes, R. Pakter, and F. B. Rizzato, *Phys. Plasmas* **12**, 023104 (2005).
- [39] K. Fiuza, F. B. Rizzato, and R. Pakter, *Phys. Plasmas* **13**, 023101 (2006).
- [40] P. Sing Babu, A. Goswami, and V. S. Pandit, *Phys. Plasmas* **19**, 080702 (2012).
- [41] R. L. Gluckstern, *Phys. Rev. Lett.* **73**, 1247 (1994).
- [42] M. Ikegami, *Phys. Rev. E* **59**, 2330 (1999).
- [43] Y. K. Batygin, *Nucl. Instrum. Methods Phys. Res. A* **618**, 37 (2010).
- [44] M. A. Dorf, R. C. Davidson, and E. A. Startsev, *Phys. Plasmas* **18**, 043109 (2011).
- [45] C. K. Allen, K. C. D. Chan, P. L. Colestock, K. R. Crandall, R. W. Garnett, J. D. Gilpatrick, W. Lysenko, J. Qiang, J. D. Schneider, M. E. Schulze, R. L. Sheffield, H. V. Smith, and T. P. Wangler, *Phys. Rev. Lett.* **89**, 214802 (2002).
- [46] J. Struckmeier and I. Hofmann, *Part. Accel.* **39**, 219 (1992).

- [47] Y. K. Batygin, *Phy. Rev. E* **53**, 5358 (1996).
- [48] Y. K. Batygin, *Phy. Rev. E* **54**, 5673 (1996).
- [49] P. Sing Babu, A. Goswami, and V. S. Pandit, *Phys. Plasmas* **18**, 103117 (2011).
- [50] *MagNet User Guide*, Infolytica Corporation, version **6.26**.
- [51] S. Gammino, G. Ciavola, L. Celona, L. Torrisci, D. Mascali, S. Passarello, and A. Galata, *Rev. Sci. instrum.* **77**, 03B511 (2006).
- [52] R. Xu, J. Zhao, S. X. Peng, Z. X. Yuan, Z. Z. Song, J. X. Yu, and Z. Y. Guo, *Rev. Sci. instrum.* **79**, 02B713 (2008).
- [53] Terence Taylor and John S.C. Wills, *Nucl. Instrum. Methods Phys. Res. A* **309**, 37 (1991).
- [54] C. Chen and R. C. Davidson, *Phy. Rev. E.* **49**, 5679 (1994).
- [55] S. M. Lund and B. Bukh, *Phys. Rev. ST Accel. Beams* **7**, 024801 (2004).
- [56] Y. Batygin, A. Goto, and Y. Yano, in *Proceedings of the 1995 Particle Accelerator Conference*, Texas (1995) p. 1001.
- [57] W. Krauss-Vogt, H. Beuscher, H. Hagedoorn, J. Reich, and P. Wucherer, *Nucl. Instrum. Methods Phys. Res. A* **268**, 5 (1988).
- [58] T. P. Wangler, K. R. Crandall, R. Ryne, and T. S. Wang, *Phys. Rev. ST Accel. Beams* **1**, 084201 (1998).
- [59] Tai-Sen, F. Wang, *Phys. Rev. E* **61**, 855 (2000).
- [60] Hiromi Okamoto and Masanori Ikegami, *Phys. Rev. E* **55**, 4694 (1997).
- [61] Jan Schumann-Bischoff and Ulrich Parlitz, *Phys. Rev. E* **84**, 056214 (2011).
- [62] P. Karimov, E. Z. Kurmaev, *Phys. Lett. A* **320**, 234 (2003).
- [63] Weiwei Gao, Lin Wang, and Weimin Li, *Phys. Rev. ST Accel. Beams* **14**, 094001 (2011).
- [64] Juan de Vicente, Juan Lanchares, and Roman Hermida, *Phys. Lett. A* **317**, 415 (2003).
- [65] C. Sun, D. S. Robin, H. Nishimura, C. Steier, and W. Wan, *Phys. Rev. ST Accel. Beams* **15**, 054001 (2012).

- [66] R. Bartolini, M. Apollonio, and I. P. S. Martin, Phys. Rev. ST Accel. Beams **15**, 030701 (2012).
- [67] R. Toma's, Phys. Rev. ST Accel. Beams **9**, 081001 (2006).
- [68] Juyong Lee, Steven P. Gross, and Jooyoung Lee, Phys. Rev. E **85**, 056702 (2012).
- [69] Lingyun Yang, Yongjun Li, Weiming Guo, and Samuel Krinsky, Phys. Rev. ST Accel. Beams **14**, 054001 (2011).
- [70] J. G. Wang and Y. Zhang, Nucl. Instrum. Methods Phys. Res. Sect. A **648**, 41 (2011).
- [71] R. Baartman, Nucl. Instrum. Methods Phys. Res. Sect. B **204**, 392 (2003).
- [72] E. Schuster, C. K. Allen, and M. Krstic, in *Proceeding of Particle Accelerator Conference*, Knoxville, Tennessee (2005) p. 4269.
- [73] Pedro F. Tavares, in *Proceeding of Particle Accelerator Conference*, Dallas, Texas (1995) p. 3352.
- [74] C. K. Allen and M. Reiser, Nucl. Instrum. Methods Phys. Res. Sect. A **384**, 322 (1997).
- [75] H. Li, S. Bernal, R.A. Kishek, I. Haber, Y. Zou, P.G. O'Shea, and M. Reiser, Nucl. Instrum. Methods Phys. Res. Sect. A **519**, 405 (2004).
- [76] S. Bernal, H. Li, R. A. Kishek, B. Quinn, M. Walter, M. Reiser, and P. G. O'Shea, Phys. Rev. ST Accel. Beams **9**, 064202 (2006).
- [77] Wilson Simeoni Jr., Phys. Lett. A **374**, 2750 (2010).
- [78] P. Sing Babu, A. Goswami, and V. S. Pandit, Phys. Lett. A **376**, 3192 (2012).
- [79] S. S. Rao, *Optimization: Theory and Application* (Wiley Eastern, New Delhi, 1978).
- [80] V. S. Pandit, P. R. Sarma, and R. K. Bhandari, Nucl. Instrum. Methods Phys. Res. A **276**, 21 (1989).
- [81] C. Goldstein and A. Laisne, Nucl. Instr. and Meth. **61**, 221 (1968).
- [82] F. J. Lynch, R. N. Lewis, L. M. Bollinger, W. Henning, and O. D. Despe, Nucl. Instr. and Meth. **159**, 245 (1979).

- [83] V. S. Pandit and P. R. Sarma, Nucl. Instrum. Methods Phys. Res. A **462**, 349 (2001).
- [84] V. S. Pandit, in *Proceedings of the 2005 Indian Particle Accelerator Conference*, Kolkata, India (2005) p. 13.
- [85] R. Baartman, Y. N. Rao, in *Proceedings of the 2003 Particle Accelerator Conference*, Portland, Oregon (2003) p. 1578.
- [86] Th. Stambach *et al.*, in *Proceedings of the 16th International Conference on Cyclotrons and Their Applications*, East Lansing, Michigan (2001) p. 423
- [87] R. Baartman, in *Proceedings of the 14th International Conference on Cyclotrons and Their Applications*, Cape Town ( 1995) p. 440.
- [88] R. Baartman, in *Proceedings of the 11th International Conference on Cyclotrons and Their Applications*, Tokyo (1986) p. 238.
- [89] C. B. Williams and M. H. McGregor, IEEE Trans. Nucl. Sci. NS-14 No.3, 1097 (1967).
- [90] P. Sing Babu, A. Goswami, and V. S. Pandit, Nucl. Instrum. Methods Phys. Res. A **603**, 222 (2009).
- [91] H. Schamel, Phys. Rev. Lett. **79**, 2811 (1997).
- [92] O. Boine-Frankenheim, I. Hofmann, and G. Rumolo, Phys. Rev. Lett. **82**, 3256 (1999).
- [93] R. C. Davidson, E. A. Startsev, Phys. Rev. ST Accel. Beams **7**, 024401 (2004).
- [94] R. C. Davidson, Phys. Rev. ST Accel. Beams **7**, 054402 (2004).
- [95] E. A. Startsev and R. C. Davidson, New Journal of Physics **6**, 141 (2004).
- [96] W. M. Sharp, J. J. Barnard, and S. S. Yu, Part. Accel. **37-38**, 205 (1992).
- [97] I. D. Kaganovich, S. Massidda, E. A. Startsev, R. C. Davidson, J. L. Vay, and A. Friedman, Nucl. Instrum. Methods Phys. Res. A **678**, 48 (2012).
- [98] P. K. Roy, S. S. Yu, W. L. Waldron, A. Anders, D. Baca, J. J. Barnard, F. M. Bieniosek, J. Coleman, R. C. Davidson, P. C. Efthimion, S. Eylon, A. Friedman, E. P. Gilson, W. G. Greenway, E. Henestroza, I. Kaganovich, M. Leitner, B. G. Logan, A. B. Sefkow, P. A. Seidl, W. M. Sharp, C. Thoma, and D. R. Welch, Nucl. Instrum. Methods Phys. Res. A **577**, 223 (2007).

- [99] S. Massidda, I. D. Kaganovich, E. A. Startsev, R. C. Davidson, S. M. Lidia, P. Seidl, and A. Friedman, *Nucl. Instrum. Methods Phys. Res. A* **678**, 39 (2012).
- [100] P. K. Roy *et al.*, *Phys. Rev. Lett.* **95**, 234801 (2005).
- [101] H. Qin and R. C. Davidson, *Phys. Rev. ST Accel. Beams* **5**, 034401 (2002).
- [102] H. Qin and R. C. Davidson, *Phys. Rev. ST Accel. Beams* **7**, 104201 (2004).
- [103] H. Qin and R. C. Davidson, J. J. Barnard, E. P. Lee, *Nucl. Instr. and Meth. A* **544**, 255 (2005).
- [104] M. J. L. de Hoon, E. P. Lee, J. J. Barnard, and A. Friedman, *Phys. Plasmas* **10**, 855 (2003).
- [105] J. G. Wang, D. X. Wang, and M. Reiser, *Appl. Phys. Lett.* **62**, 3232 (1993).
- [106] J. G. Wang, D. X. Wang, and M. Reiser, *Appl. Phys. Lett.* **62**, 645 (1993).
- [107] J. G. Wang, H. Suk, D. X. Wang, and M. Reiser, *Phys. Rev. Lett.* **72**, 2029 (1994).
- [108] P. Sing Babu, A. Goswami, and V. S. Pandit, *Nucl. Instrum. Methods Phys. Res. A* **642**, 1 (2011).
- [109] P. Sing Babu, A. Goswami, and V. S. Pandit, *Phys. Plasmas* **18**, 113104 (2011).
- [110] C. K. Allen and M. Reiser, *Physical Review E* **55**, 7591 (1997).
- [111] C. K. Allen, N. Brown, and M. Reiser, *Part. Accel.* **45**, 149 (1994).
- [112] C. K. Allen and M. Reiser, *Part. Accel.* **48**, 193 (1995).
- [113] Thomas P. Wangler, *RF Linear Accelerator* (Wiley- VCH Verlag-GmbH & co. KGaA, Weinheim, 2nd edition, 2008).
- [114] R. Baartman, *TRIUMF design note TRI-DN-85-37* (1985).
- [115] C. Chen and R. C. Davidson, *Phys. Rev. Lett.* **72**, 2195 (1994).
- [116] O. A. Anderson, *Phys. Rev. ST Accel. Beams* **10**, 034202 (2007).
- [117] S. M. Lund, S. H. Chilton, and E. P. Lee, *Phys. Rev. ST Accel. Beams* **9**, 064201 (2006).

- [118] R. A. Kishek, P. G. O'Shea, and M. Reiser, Phys. Rev. Lett. **85**, 4514 (2000).
- [119] S. Bernal, R. A. Kishek, M. Reiser, and I. Haber, Phys. Rev. Lett. **82**, 4002 (1999).
- [120] D. Stratakis, R. A. Kishek, I. Haber, S. Bernal, M. Reiser, and P. G. O'Shea, Phys. Rev. ST Accel. Beams **12**, 064201 (2009).
- [121] C. Chen and R. A. Jameson, Phys. Rev. E **52**, 3074 (1995).
- [122] Y. K. Batygin, Nucl. Instrum. Methods Phys. Res., Sect. A **539**, 455 (2005).
- [123] Ji Qiang, Robert D. Ryne, and Ingo Hofmann, Phys. Rev. Lett. **92**, 174801 (2004).
- [124] G. Franchetti, I. Hofmann, and D. Jeon, Phys. Rev. Lett. **88**, 254802 (2002).
- [125] P. H. Stoltz, R. C. Davidson, and W. Wei-li Lee, Phys. Plasmas **6**, 298 (1999).
- [126] E. A. Startsev, R. C. Davidson, and H. Qin, Phys. Plasmas **14**, 056705 (2007).
- [127] H. Qin, R. C. Davidson, and W.W. Lee, Phys. Lett. A **272**, 389 (2000).
- [128] S. M. Lund, T. Kikuchi, and R. C. Davidson, Phys. Rev. ST Accel. Beams **12**, 1148013(2009).
- [129] R. C. Davidson, H. Qin, and S. M. Lund, Phys. Rev. ST Accel. Beams **6**, 024402 (2003).

# List of Publications

- \*1. “*Simulation of beam bunching in the presence of space charge effects*”, **P. Sing Babu**, A. Goswami, and V. S. Pandit, **Nucl. Instrum. Methods Phys. Res. A** **603**, 222 (2009).
- \*2. “*Optimization of sector geometry of a compact cyclotron by random search and matrix methods*”, **P. Sing Babu**, A. Goswami, P. R. Sarma, and V. S. Pandit, **Nucl. Instrum. Methods Phys. Res. A** **624**, 560 (2010).
- \*3. “*Behavior of space charge dominated beam during longitudinal compression in a bunching system*”, **P. Sing Babu**, A. Goswami, and V. S. Pandit, **Nucl. Instrum. Methods Phys. Res. A** **642**, 1 (2011).
- \*4. “*Envelope equations for cylindrically symmetric space charge dominated multispecies beam*”, **P. Sing Babu**, A. Goswami, and V. S. Pandit, **Phys. Plasmas** **18**, 103117 (2011).
- \*5. “*Effect of nonuniform radial density distribution on space charge dominated beam bunching*”, **P. Sing Babu**, A. Goswami, and V. S. Pandit, **Phys. Plasmas** **18**, 113104 (2011).
- \*6. “*A Vlasov Equilibrium for Space Charge Dominated Beam in a Misaligned Solenoidal Channel*”, **P. Sing Babu**, A. Goswami, and V. S. Pandit, **Phys. Plasmas** **19**, 080702 (2012).
- \*7. “*Optimisation of beam line parameters for space charge dominated multi species beam using random search method*”, **P. Sing Babu**, A. Goswami, and V. S. Pandit, **Phys. Lett. A** **376**, 3192 (2012).
- \*8. “*Studies of space charge dominated multispecies beam in a solenoid based beam transport line*”, **P. Sing Babu**, A. Goswami, and V. S. Pandit, **Phys. Plasmas** **19**, 113112 (2012).
- \*9. “*Self consistent study of space charge dominated beam in a misaligned transport system*”, **P. Sing Babu**, A. Goswami, and V. S. Pandit, *Submitted to journal*.

---

\*Indicates publications related to this thesis.

- \*10. “*Effect of subdominant species on the evolution of intense primary beam in a low energy beam transport line*”, **P. Sing Babu**, A. Goswami, and V. S. Pandit, *Submitted to journal*.
- 11. “*Estimation of the transverse space charge limiting current in a compact isochronous cyclotron*”, V. S. Pandit, and **P. Sing Babu**, **Nucl. Instrum. Methods Phys. Res. A** **523**, 19 (2004).
- 12. “*Behavior of space charge dominated beam in a high current compact cyclotron*”, A. Goswami, **P. Sing Babu**, and V. S. Pandit, **Nucl. Instrum. Methods Phys. Res. A** **562**, 34 (2006).
- 13. “*Transfer matrix of a Glaser magnet to study the dynamics of non-axisymmetric beam*”, A. Goswami, **P. Sing Babu**, and V. S. Pandit, **Nucl. Instrum. Methods Phys. Res. A** **678**, 14 (2012).
- 14. “*Investigation on beam envelope oscillations and amplitude growth in a high current compact cyclotron*”, A. Goswami, **P. Sing Babu**, and V. S. Pandit, **Eur. Phys. J. Plus** **127**: 47 (2012).
- 15. “*Beam focusing characteristic of an elliptical solenoid magnet in the presence of space charge*”, A. Goswami, **P. Sing Babu**, and V. S. Pandit, **Nucl. Instrum. Methods Phys. Res. A** **685**, 46 (2012).
- 16. “*Space charge dominated beam dynamics in a spiral inflector for a compact cyclotron*”, A. Goswami, **P. Sing Babu**, and V. S. Pandit, **Eur. Phys. J. Plus** **127**: 79 (2012).
- 17. “*Self-consistent space charge dominated beam dynamics in a spiral inflector*”, A. Goswami, **P. Sing Babu**, and V. S. Pandit, **Nucl. Instrum. Methods Phys. Res. A** **693**, 276 (2012).
- 18. “*Transport characteristics of a glaser magnet for an axisymmetric and non-axisymmetric space charge dominated beam*”, A. Goswami, **P. Sing Babu**, and V. S. Pandit, **Phys. Plasmas** **19**, 123105 (2012).